Scale Dependent Electrical Properties of Sulphide Deposits

Andrew Fitzpatrick
B.Sc (Honours) Geophysics

Submitted in fulfilment of the requirements for the
Degree of Doctor of Philosophy

University of Tasmania
May, 2006

This thesis contains no material which has been accepted for a degree or diploma at the University or any other institution, except by way of background information and duly acknowledged in the thesis, and to the best of the candidate's knowledge and belief, no material previously published or written by another person, except where due acknowledgement is made, is in the text of the thesis.

Fitzpatrick

Date 12.5.06

This thesis may be made available for loan and limited copying in accordance with the *Copyright ACT 1968.*

Date 12.5.06

Abstract

The electrical properties of sulphide rocks are observed to be influenced by the scale of investigation. To test this scale-dependence an empirical study of in-situ and laboratory electrical properties was undertaken at three diverse economic sulphide ore deposits: Golden Grove - Scuddles, McArthur River – HYC and North Parkes – E27. Apparent resistivity and chargeability data were collected from decimetre to metre scales at a number of sites within homogenous sections of each deposit. Equivalent laboratory measurements were performed on prismatic samples collected from each site to ossess the suitability of laborotory meosurements for estimation of bulk-rock properties.

Chargeobility can vary significantly but does not display a consistent pattern of scale variobility from site to site or between deposits. However, in-situ and loboratory data for all deposits show a consistent trend of decreasing apparent resistivity with increasing scale of investigation. Apparent resistivity variations of up to three orders of magnitude were observed at some sites between small-scale measurements (0.1m electrode spacing) and bulk rock measurements (2m electrode spacing). Laboratory data generally correlates well with in-situ measurements at small electrode spacing but in some cases displays a bimodal distribution representative of resistive and conductive end members. In these cases the most conductive loboratory meosurements lie close to the bulk-rock apparent resistivity.

Although apparent resistivity consistently decreases with increasing observation scale, the degree and detoiled pottern of this variation is often difficult to predict even for related sites within a single deposit. No simple generic scaling rule is universally applicable for predicting bulk properties from loboratory or small-scale measurements. However, for all sites surveyed, a pragmatic best estimate of the bulk apparent resistivity from a set of laboratory measurements would be obtoined by odopting the minimum sample resistivity value rother than the orithmetic meon, geometric mean or median of the sample population.

Two new laboratory techniques, cantinuity mapping and current mapping, have been developed and refined to assess the influence of ore texture on sample resistivity. These methods provide detailed maps of electrical continuity on the sample surface and directly map the current path through the sample. Both techniques have been successfully applied to samples from Golden Grove and McArthur River and have highlighted the influence of small proportions of well-connected conductive phases on the bulk electrical properties of the rock mass.

The three main factors that appear to control the degree of scale variation of apparent resistivity are the resistivity contrast between mineral phases, the propartion of the most conductive phase and the ore texture. These factors, originally inferred from the empirical measurements, are supported directly by the results of three dimensional numerical modelling that predicts the most pronounced scale-variability for textures that include planar conductive components such as conductive sulphide veins. Scale variation in apparent resistivity will be significant where there is a large resistivity contrast between mineral phases and the conductive component is well connected even if it is present only in very small proportions.

Acknowledgments

I thank the Australian Research Council, and Strategic, Partnerships in Industry Research and Training for providing APA-I scholarship and project funding. Also, the numerous mining companies that sponsored this project, many of which now no longer exist under the same name, are hereby acknowledged: Rio Tinto, North, Western Metals, Normandy, Capper Mines of Tasmania, and MIM.

Many thanks go to June Pongratz, Di Edwards, and Lyn Starr for providing essential administrative and technical support.

Special cheers to the many University of Tasmania Honours, Masters and PhD students, who have become my close and dear friends, Matty G, Kev, Pat, Daz, Roman, Leeroy, Moose, Andrew R, Kieran, to name just a few...

Acknowledgements must also go to research assistants Ben Payne, Pat Fournier, and Scott Boulten. Special thanks to Vagn Jensen, for constructing my electronic circuits and giving me valuable technical advice. Also thank you to Peter Cornish and Simon Stephens for their industrious assistance with equipment construction and lapidary.

Thanks to Matilda Thomas for casting her expert eye over the final draft of this thesis.

I can only hope that I have done justice to the assistance, encouragement, and professional development I have received from my project supervisor Michael Roach, Senior Lecturer at the University of Tasmania. He has mentored me through out my research and passed on his invaluable knowledge in the field of exploration geophysics.

Thanks to Mum and Dad for teaching me to value education and supporting me during my studies.

And lastly, but not least, thank you to my very understanding partner, Tess for enduring the painful write-up.

Table of Contents

List of Figures

List of Tables

Chapter 1
Introduction

1.1. Preamble

The basis of geophysical exploration is to detect a response due to the contrast in physical properties between the target and its host. Electrical and electromagnetic geophysical techniques are commonly used for the detection of sulphide deposits, due to the anomalous electrical contrast observed between the conductive sulphide mineralisation, and the more resistive host sequence.

These electrical methods operate at low frequencies, where displacement currents can be ignored and conduction currents predominate. Thus resistivity, or its inverse conductivity, is the property fundamental to the majority of electrical geophysical prospecting methods. A secondary effect observed in galvanic measurements known as induced polarisation is also suitable for detecting disseminated sulphide mineralisation.

Electrical properties can be estimated by modelling and inversion of field-based data or by measurements of hand samples or drill-core collected from the field. However, in many cases the properties inferred from large-scale measurements do not closely correlate with laboratory-scale data. Although extensive studies into resistivity and induced polarisation effects of rocks have been conducted at microscopic, macroscopic and in-situ scales, detailed systematic investigations into scale variations of electrical properties of sulphide bearing rocks are lacking. Discrepancies of up to several orders of magnitude between laboratory and in-situ electrical resistivity measurements are observed in some cases (Schneider and Emerson, 1980), but other studies show minimal scaling effects (Hone, 1980; Tyne et al. 1981; Nelson and Van Voorhis, 1983). This is the first study that systematically investigates scaling effects in detail for sulphide-bearing rocks.

1.2. Scale variations in electrical physical properties

Despite the lack of detailed studies examining the scale dependence of electrical measurements, a number of authors have commented on such phenomena.

Hone (1980) examined the electrical response of the Elura ore body using a combination of soundings, electrical logging and laboratory measurements of drill-core. Hone cautions correlating laboratory data to the insitu data, as drilling and removal of the samples may change their properties to an unknown extent. Despite minor differences between the soundings, logging and sample measurements, all the data show consistent trends and absolute values of resistivity throughout the deposit. For fully saturated samples collected below the water-table the differences in laboratory and insitu measurements were small. For partially saturated samples above the water

table the differences in insitu and laboratory measured resistivity could be over one order of magnitude, depending on sample saturation. In contrast, Schneider and Emerson's (1980) study of the Elura deposit showed that for siliceous massive sulphide ore samples, laboratory resistivity measurements (34 Ωm) were several orders of magnitude greater than insitu measurements (0.1-0.3 Ωm).

Similarly, Tyne et al. (1981) in a petrophysical study of the Woodlawn ore body and host sequence, noted that resistivity measurements of silicious core samples could be an order of magnitude greater than the true insitu resistivity, which they attributed to the absence of normal electrolytic conduction through the rock. Tyne et al. (1981) state that the chargeability measurements of samples may not be representative of the entire polarisation process, as polarisation will predominantly occur at the upper and lower boundaries of the ore-body. However, when they compared resistivity and induced polarisation measurements between core and insitu samples a reasonable correlation was found.

It is important here to highlight the limitations of laboratory electrical measurements in predicting insitu properties. Emerson (1969) and Pelton et al. (1978) suggest samples are typically biased towards more coherent sections of the rock mass, and exclude larger scale conductive fractures and vein networks which occur in the field. Emerson and Smith (1969) suggest that resistivity values are lower in laboratory samples of sulphides compared to insitu values owing to pressure differences (although the difference is not stated). This pressure difference is likely to enhance laboratory polarisation as "the effect of pore diminution and closure with increase of pressure should equally affect the shunting ionic-bypass and the electrode polarisation pore paths" (Emerson and Smith, 1969). Emerson (1969) lists a number of studies that examine the relationship between pressure and electrical resistivity. For a range of saturated igneous and sedimentary rocks (Brace, et al.,1965) showed resistivity to increase with increasing pressure by up to one order of magnitude. Such pressures exerted would be the equivalent of depths of several kilometres. Pressure effects are likely to be insignificant for the depths encountered for economic sulphide deposits. Nelson and Van Voorhis (1983) comment that in-situ measurements provide a better basis for quantitative correlation between electrical parameters than laboratory measurements.

More recent work has attempted to find an explanation for the discrepancies observed between field and laboratory measurements. Jones (1989) completed a detailed study on in-situ scale electrical measurements in granite using borehole electrical techniques. He observed resistivity to decrease as the electrode spacing was increased from centimetres to several metres. The electrical data was fitted to a fractal model implying the scale dependence was attributed to fracturing in the granite. Emerson and Yang (1998) produced type curves to predict bulk insitu apparent resistivity from laboratory or drill-hole measurements for fractured rocks.

Other studies have shown the importance texture has on electrical conduction through rocks. Vanhala and Peltoniemi (1992) fitted Cole-Cole parameters to field data and correlated these to mineralogical descriptions and grain size. DaRocha and Habashy (1997) produced a model to interpret the electrical behaviour of rocks containing metallic or clay particles. Their model introduces a fractal roughness factor, a parameter which relates to

the texture of the rocks. They applied their techniques for complex resistivity and dielectric data of samples from various authors. Other studies have examined the relationship between rock fabric and electrical properties of metamorphic (eg: Siegsemend et al., 1991) and sedimentary rocks (eg: Wong et al., 1986; DeLima and Sharma 1990). The conduction in these rocks is largely electrolytic, occurring through groundwater pore spaces of rocks, and relationships between these two properties have been well established. The effect of minor chemical variation and microscale textures can be significant, as found by Losito et al. (2001). Losito et al. (2001) conducted laboratory electrical measurements on black shales from the Swiss Alps to account for variations observed in magnetotelluric field measurements. Two samples were found to have markedly different resistivities of several orders of magnitude, despite appearing to have near identical mineralogy. The difference was found to be related to minor variations in carbon content and microscale mineral connectivity.

1.3. Methodology

1.3.1. Objective

The intent of this dissertation is to investigate the extent to which the scale of measurement influences the electrical properties of a range of sulphide deposits. The study primarily employs an empirical methodology using insitu and laboratory electrical techniques to systematically assess scale variability. The empirical results are then compared and validated against the results of numerical models.

1.3.2. Field Sites

Insitu and laboratory studies were completed on sulphide-bearing rocks from three deposits: Golden Grove- Scuddles zinc-copper-lead massive sulphide deposit in Western Australia; McArthur River- HYC lead-zinc stratiform sediment hosted sulphide deposit in the Northern Territory; and North Parkes- E27copper-gold porphyry deposit located in New South Wales (Figure 1.1).

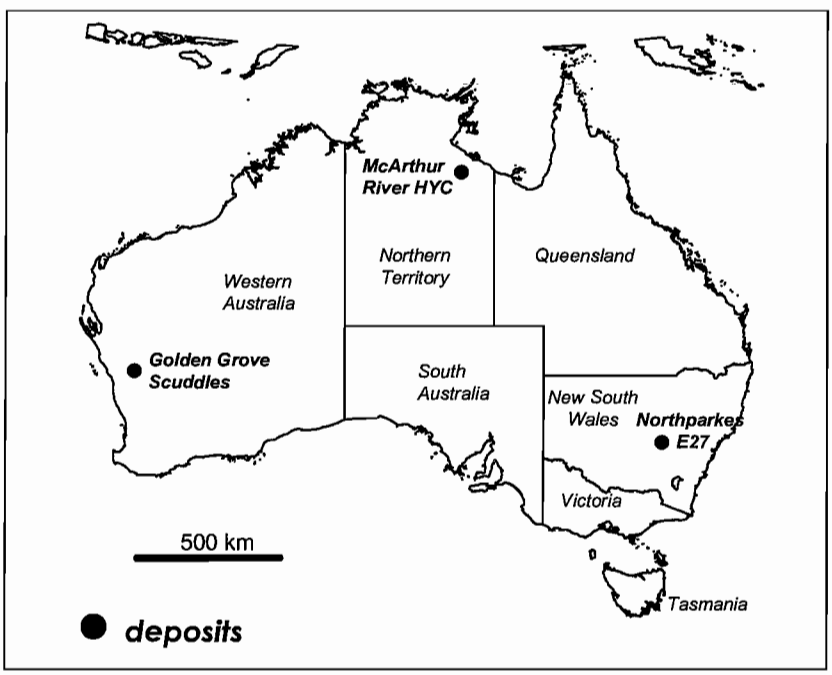

Figure 1.1. Location of field sites; Golden Grove- Scuddles zinc-copper-lead massive sulphide deposit; McArthur River lead-zinc stratiform sediment-hosted sulphide deposit; and North Parkes E27 copper-gold porphyry deposit, Australia.

1.3.3. Methodology

Field experiments were designed to collect data to test the hypothesis that rock electrical properties may exhibit scale dependent phenomena.

Insitu electrical resistivity and chargeability measurements were completed at a number of sites at each deposit using expanding Wenner arrays from centimetre to metre scales. Site selection was dependent on the deposit-type and ability to map lithological or ore-grade variation. For example, at the Golden Grove Scuddles deposit, measurements were completed in the vastly different ore types and host sequence of the deposit, where as at McArthur River, site selection was largely controlled by variation in ore-grade. At the North Parkes E27 deposit two main lithologies were examined.

Standard laboratory electrical measurements were then conducted on decimetre scale prismatic samples collected from all three deposits. In addition, two new laboratory techniques, continuity and current mapping were developed to image the connectivity of sulphide and oxide phases and map current flow within thin prismatic samples. The results can be directly compared to mesoscopic textural and mineralogical variations of samples. Geochemical, petrographic and textural analysis was completed on samples to aid in the interpretation of the electrical results.

Numerical modelling of a variety of synthetic ore textures was used in an attempt to replicate and validate the patterns of scale variations observed in field measurements.

1.4. Thesis Strategy

The overall approach of this work is as follows. First an overview of electrical properties of rocks is given in Chapter 2 as are references to background work. Field and laboratory methodology is described in Chapter 3. Chapter 4 describes two new laboratory techniques; continuity and current mapping used for assessing electrical heterogeneity of samples. Chapters 5, 6 and 7 document the three case studies; Golden Grove (Scuddles), McArthur River (HYC) and North Parkes (E27). Chapter 8 presents numerical modelling results of scale effects for a variety of ore textures. A synthesis of the field and synthetic models is incorporated into the conclusion chapter (Chapter 9) together with a discussion of the observed similarities between the scale variability of electrical and hydraulic properties.

Chapter 2

Low frequency electrical properties of rocks

2.1. Introduction

There are three primary properties that control the electrical conduction in a rock: resistivity, dielectric permittivity and magnetic permeability. The influence of these properties is largely controlled by the frequency of the applied current. At low frequencies, typically 0.1-1000 Hz (Vanhala, 1997), conduction currents predominate and resistivity determines the electrical characteristics of the medium. At high frequencies, displacement currents predominate and dielectric permittivity and magnetic permeability determine the electrical characteristics of the medium. The critical frequency defines the boundary between the two mechanisms (Collett and Katsube, 1973; Olhoeft, 1985).

Electrical geophysical prospecting for base-metal deposits is typically conducted using low frequency techniques. High frequency techniques have very limited depths of investigation, and are typically used for shallow geotechnical and environmental applications. At low frequencies the electrical resistivity of rocks may be frequency dependent. The principal cause of this effect is the storage of chemical energy due to variations in the mobility of ions or the presence of metallic minerals. This effect is known as induced polarisation (IP).

Low frequency methods are well suited for base-metal exploration, as these deposits typically form conductive and/or polarisable targets in comparison to their host geology. This chapter discusses the resistivity and induced polarisation properties of rocks, with particular emphasis on sulphide minerals and ores.

2.2. Electrical resistivity of rocks and minerals

Resistivity is a property defined as the ability to impede current flow within a material. The resistivity ρ of a prismatic sample of length L and cross section A, having resistance R, between the two end faces is given by;

$$\rho = \frac{RA}{L} \tag{2.1}$$

2.2.1. Electrical resistivity of minerals

In discussing the electrical resistivity of rocks it is important to consider the electrical resistivities of minerals. "While it may never be possible to measure the properties of an individual mineral with an exploration method, it often is of interest to attempt to build a rock conceptually from minerals for which the properties are known and to predict the properties of the aggregate." (Keller, 1989).

The electrical resistivities of minerals span a very large range of more than twenty orders of magnitude (eg: from conductive pyrrhotite: 10^{-6} Ωm to

resistive quartz: $10^{14}\ \Omega m$). The wide range of resistivities is largely attributed to the different electrical mechanisms that are responsible for electrical conduction in a mineral. The electrical properties of minerals and rocks are extensively covered in the literature (eg: Parkhomenko, 1967; Collett and Katsube, 1973; Saint-Amant and Strangway, 1970). The following provides a brief overview.

Minerals can be divided into three classes depending upon their mechanism of electrical conduction: (1) metals, (2) semiconductors, and (3) solid electrolytes (or dielectrics). Native metals include native gold, silver, platinum, copper and bismuth, and rarely occur in crustal rocks. The semiconductors include most of the sulphide and oxide ore minerals. Most of the rock-forming minerals such as silicates, phosphates, carbonates, nitrates and sulphates are solid electrolytes.

The conduction mechanism in metals and semiconductors involves the movement of electrons (i.e. electronic conduction). Metals have the lowest resistivities as they contain an abundance of free electrons, requiring little or no excitation energy. The resistivity of semiconductors is greater than metals, as fewer electrons are available for conduction. This means the energy level of conduction electrons needs to be increased in order for conduction to occur. This energy may be in the form of heat, hence semiconductors exhibit a negative temperature coefficient of resistivity, where as metals have a positive coefficient (Lewis, 1985). A similar process occurs in solid electrolytes, but in this case charge is carried by ions, rather than by electrons (i.e. ionic conduction). The energy barriers required to move ions are far greater than that of electrons, hence solid electrolytes are extremely resistive and may be considered as "insulators". From the perspective of exploration geophysics, metals and semiconductors are commonly grouped together as "conductive minerals".

Clay minerals, including illite, kaolinite and chlorite (Lewis, 1985) may also be conductive if they are in contact with water (Waxman and Smits, 1968). Saturated clay minerals exhibit negatively charged surfaces, due to the substitution of metallic ions in their structure for other ions of a lower valence (DaRocha and Habashy, 1997). Silicon is typically substituted by magnesium or aluminium ions. The negative charge attracts cations to the surface (from the electrolyte) to form a thick double layer of adsorbed cations, thus lowering the clay's resistivity.

The resistivity of metals and minerals are extensively described in the literature (eg: Harvey, 1928; Parasnis, 1957; Parkhomenko, 1967; Shuey, 1975; Keller, 1988; and Keller, 1989). The resistivity and mechanism of conduction for several metals and minerals is shown in Figure 2.1. Although the different conduction mechanisms result in markedly different resistivities, there is no distinct boundary which clearly defines them. Resistivity provides a quantitative measure of the electrical characteristics of a material, but does not directly discriminate the different mechanisms of conduction that may occur.

Even for a particular mineral the electrical resistivity is typically not constant, and variation of several orders of magnitude may occur, hence the range of resistivities reported for individual minerals (Figure 2.1). These variations are due to chemical impurities, foreign inclusions and micro-fractures, which

strongly affect electrical conduction in minerals (Harvey, 1928). This especially applies in semiconductor minerals, as impurities may lower the activation energy required for conduction. The semiconduction in sulphides is controlled by minor deviations from stoichiometry and impurity content, and hence by their geochemistry (Pridmore and Shuey, 1976). The effect of minor impurities and defects can typically vary the resistivity of a semiconductor by over two orders of magnitude. Micro-fractures in minerals can impede conduction, increasing the resistivity of a mineral (Keller, 1989). Although the range of resistivity for each mineral is large, many mineral resistivities do not overlap, thus making certain minerals electrically distinguishable from one another.

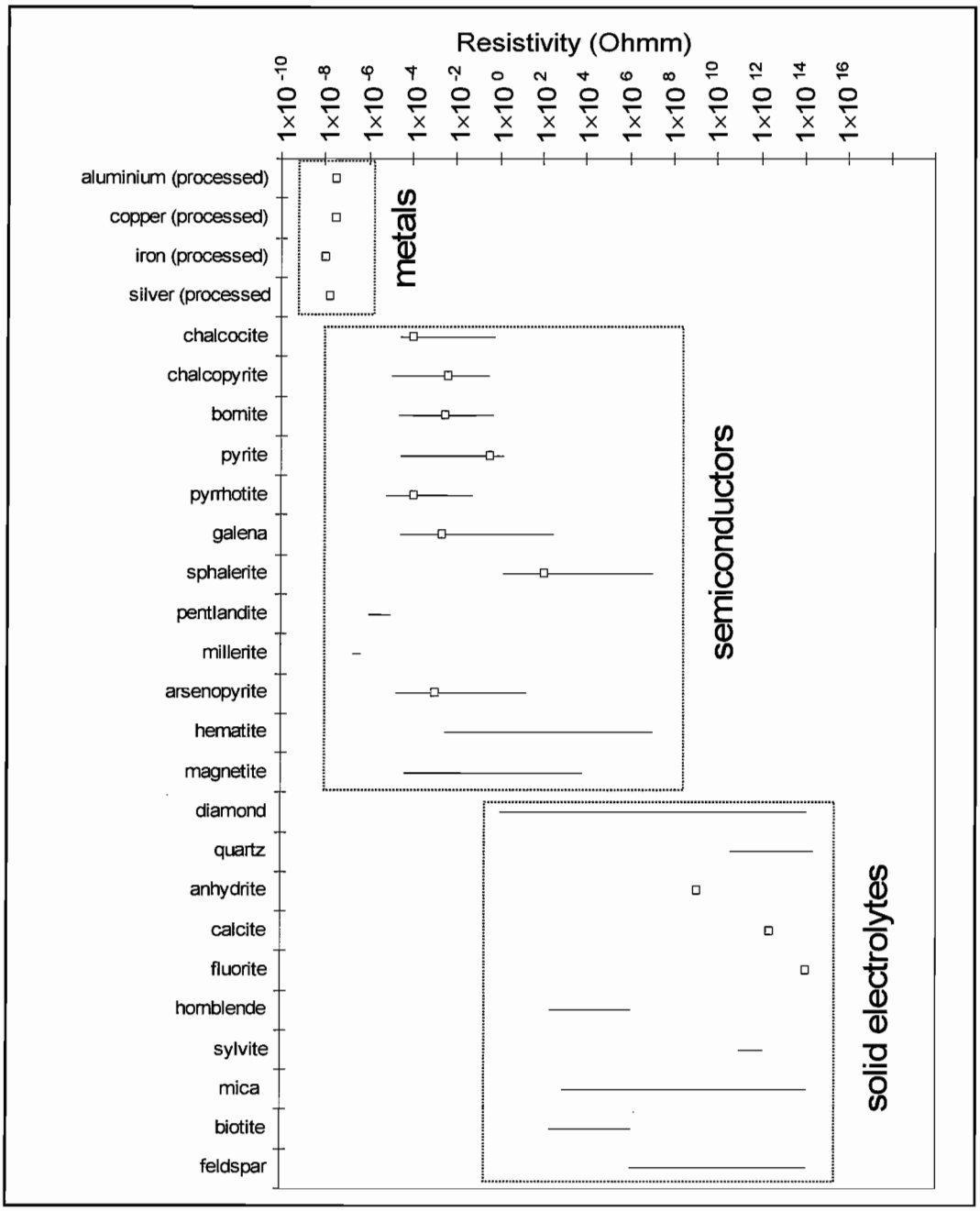

Figure 2.1. Electrical resistivity for a variety of minerals. White boxes indicate average values, where listed. Source: Keller (1966); Telford et al. (1990).

There are some interesting features of Figure 2.1 that should be highlighted. The most conductive sulphide minerals are pyrrhotite and chalcocite, followed by galena, arsenopyrite, chalcopyrite and bornite. The electrical

resistivity of hematite and magnetite (oxides) can greatly vary and are typically more resistive than sulphides. Sphalerite is one the most resistive sulphide minerals and is commonly considered an insulator. Electrical semi-conduction in sphalerite is controlled by holes and not electrons (Keys et al., 1967). The highly resistive nature of quartz (~10^{12} Ωm) is also noteworthy, as it is one of the most commonly occurring rock-forming mineral. Feldspars are the most important group of rock-forming minerals, occurring in many igneous and metamorphic rocks; their resistivity ranges from 10^{6}-10^{14} Ωm.

2.2.2. Electrical resistivity of rocks

Rocks are not composed of minerals alone, but contain a porous network that is partially or fully saturated with a pore-fluid. Pore-fluids are electrolytes, whose resistivity is determined by the mobility and number of ions in solution (Keller, 1988). These ions are produced by the disassociation of salts dissolving in ground waters. Most crustal rocks are comprised of silicate minerals whose electrical resistivities are in the order of 10^{6} to 10^{14} Ωm, whilst their pore fluids have much lower electrical resistivities ranging from less than 10 to 10^{2} Ωm (DaRocha and Habashy, 1997). Thus, conduction in most rocks is largely electrolytic, occurring through interstitial pore-fluid effectively bypassing resistive mineral grains (Ward and Fraser, 1967; Keller and Frischknecht, 1966; Keller, 1989). Only where a rock contains an abundance of conductive minerals (e.g., metallic or clay minerals) does conduction through the rock matrix become appreciable. The bulk electrical resistivity of a rock, therefore, largely depends on; the mineral constituents forming the matrix, the distribution of these minerals (texture), the presence and distribution of conductive minerals, porosity, the degree of pore connectivity, and pore-fluid characteristics (degree of saturation, composition, concentration, etc).

The electrical resistivity of a variety of earth materials is shown in Figure 2.2. The electrical resistivity of rocks varies over eight orders of magnitude, from less than 10^{-1} Ωm in massive sulphides, to as high as 10^{5} Ωm for fresh crystalline rocks. Near surface rocks can be classified into two broad groups dependent upon their mineralogy. The first group consists of most crustal rocks, which are composed of resistive minerals. The second group consists of rocks that contain an abundance of conductive minerals. This group includes the sulphide and some oxide ore minerals.

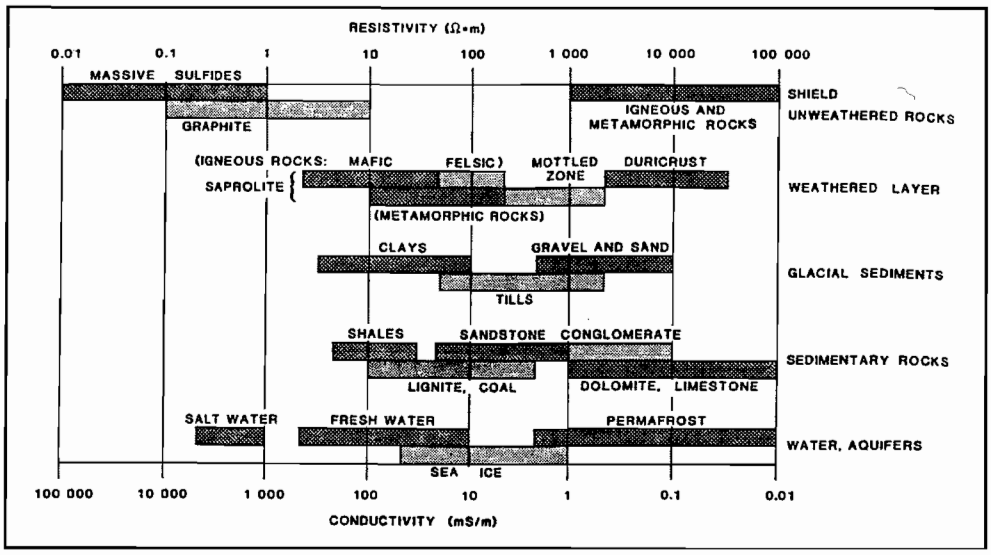

Figure 2.2. Electrical resistivity for common earth materials, from Palacky (1988), shows a wide variation, over eight orders of magnitude.

2.2.2.1. Rocks containing resistive minerals

Most crustal rocks are composed of rock-forming minerals in which conduction occurs through interstitial fluids, which are considerably less resistive less than the minerals forming the rock matrix. The ratio of rock resistivity (ρ_0) to electrolyte resistivity (ρ_w) is termed the formation factor:

$$F = \frac{\rho_0}{\rho_w} \qquad (2.2)$$

As the majority of crustal rocks are composed mostly of silicate minerals, their resistivities would all be extremely high, if they did not contain a pore-fluid. All crustal rocks are porous to some extent and contain a variable fluid quantity. There are three main types of porosity that occur in rocks; (1) intergranular, (2) fractures and jointing, and (3) vuggy or large, poorly interconnected pores. Most sedimentary rocks mainly exhibit intergranular porosity. Crystalline rocks mainly exhibit fractures, jointing and micro crack porosity and vuggy porosity is characteristic of volcanic rocks and limestone.

The resistivity of water-bearing rocks is largely determined by their porosity type, distribution of pores, pore connectivity, pore-fluid composition and degree of saturation. The variation in resistivities between different rock types shown in Figure 2.2 (excluding massive sulphides) can be largely attributed to differences in these parameters. Unweathered crystalline rocks (i.e. igneous and metamorphic) have the highest resistivities. These rocks typically have very low intergranular porosities, but exhibit fracture/jointing porosities, and may have resistivities of less than 10^3 Ωm. Weathering of crystalline rocks typically lowers their resistivities, due to an increase in porosity and the addition of clay (conductive) minerals. Sediments and sedimentary rocks exhibit low to moderate resistivities, due to high intergranular porosity and increased pore connectivity. Some shales are relatively conductive due to the presence of graphite or sulphides.

The parameters influencing the electrical resistivity of water-bearing porous rocks have been well researched (Parkhomenko, 1967; Keller and Frischknecht 1966). The majority of this work has been conducted on saturated sedimentary rocks, whose physical properties are important for oil and gas reservoir rocks. Studies into the effects rock fabric and water saturation have on crystalline rocks have been conducted by Olhoeft, 1981 and Siegesmund et al., 1991.

The most significant relationship developed for water-bearing rocks, known as Archie's Law, expresses the bulk electrical resistivity of a porous rock as a function of its resistivity, volume and distribution of pore-spaces and the amount of water present:

$$\rho_b = \rho_f a \phi^{-m} \qquad (2.3)$$

where ρ_b is bulk resistivity (Ωm), ρ_f is pore-fluid resistivity (Ωm), ϕ is the volume fraction porosity and a and m are coefficients that characterise the porosity structure. Although this relationship was originally derived for sandstones, the expression is applicable to other rock types, by varying the coefficients a and m accordingly. Examples of these coefficients for different rock are shown in Table 2.1.

Rock	ϕ	a	m
weakly cemented, detrital sedimentary rocks	25 to 45 %	0.88	1.37
moderately-well cemented sedimentary rocks	22 to 35%	0.62	1.72
well cemented sedimentary rocks	5 to 25%	0.62	1.95
Highly porous volcanic rocks	<5%	1.4	1.6
Dense, igneous, metamorphic rocks	2 to 8%	3.5	1.4

Table 2.1. Parameters for Archie's Law for different lithologies (modified from Keller 1988).

Recent methodologies for calculating the electrical resistivity of water-bearing porous rocks incorporate fractals to model the geometrical distribution of pore spaces (eg: Katz and Thompson, 1985; Ruffet et al., 1991; Clennell, 1997; DaRocha and Habashy 1997). These models can be used to predict the porosity of materials from electrical measurements, commonly applied in geophysical borehole investigations. Other complex relationships have been developed by Sen (1981), Sen (1984), De Lima and Sharma, (1990), and Katz and Thompson (1985). These later models include parameters to simulate small proportions of disseminated conductive minerals, such as clay or sulphide minerals. Chelidze et al. (1999) provides a review of theoretical models, which adequately describe electrical spectroscopy (i.e. complex resistivity and dielectric response) of water-bearing porous rocks.

2.2.2.2. Rocks containing conductive minerals (sulphide and oxide ore minerals)

"There is far less information available on the bulk resistivity of rocks containing highly conductive minerals than on rocks containing electrolytic conductors" Keller (1988). Although there are a number of conductive minerals, there are only a few that occur in quantities sufficient to influence the bulk resistivity of the rock matrix. These include some sulphide ore minerals, which are of economic importance (eg: chalcopyrite, chalcocite, galena and bornite). Other conductive minerals that occur in substantial quantities include pyrite pyrrhotite, magnetite, specular hematite, and graphite (Parkhomenko, 1967). The electrical conduction through the electrolyte is still significant in most sulphide-bearing rocks. However, Alvarez (1973) demonstrated the effect of water saturation for conductive samples is negligible for samples containing 50% pyrite and samples containing 75% galena.

The electrical resistivity of rocks containing sulphide minerals is largely controlled by their composition and distribution. These two factors vary widely for different deposit types. For example, zones within volcanogenic massive sulphide deposits can be composed almost entirely of sulphide minerals, whereas porphyry deposits are characterized by low concentrations of sulphides, typically disseminated in a resistive host. Although texture has a significant effect on the electrical properties of rocks, detailed studies on its effects are limited in the literature (Parkhomenko, 1967; Keller 1989).

The resistivity of a sulphide rock not only depends on sulphide content, but also on the distribution of the conducting minerals. As little as 1% pyrrhotite can make a rock conductive, as it may form a 3-dimensional anastomosing network, that is electrically continuous, whereas disseminated mineralisation

may contain up to 15 to 19 percent of an ore mineral without a significant effect on the bulk resistivity (Parkhomenko, 1967). Some vein-type deposits can be resistive if ore minerals grow individually and become surrounded by gangue minerals (Keller and Frishchenckt, 1966). This can occur in some pyrite ores, whereby the pyrite forms blobs that can be insulated by gangue minerals, thus increasing the bulk resistivity of the ore (Keller, 1989). This is observed at the Chester mine, Tasmania, which is non-conductive to electrical exploration techniques. Hand-specimens appear to consist of massive pyrite, but microscopic analysis reveals that the pyrite grains are coated by a thin siliceous layer, hence making the deposit non-conductive (Keller, 1989). Examples of other non-conducting massive sulphide deposits are discussed by Gunn and Chisholm (1984). Studies have demonstrated that small proportions of impurities may form an insulating monomolecular film around a mineral grain (Parkhomenko, 1967).

Resistivity studies of sulphide-bearing rocks have included theoretical modeling and laboratory measurements of artificial samples. Theoretical studies have largely involved the use of mathematical expressions to calculate the bulk resistivity of multi-component mixtures. These models have been developed to accommodate a variety of textures using simple geometrical models, from dispersed conductive spheres to interconnecting rods, hosted in a resistive matrix. A more detailed discussion of mixing theories can be found in chapter 8. Such models have been successful fitted to resistivity measurements conducted on artificial samples representative of disseminated mineralisation (eg: Mandel et al., 1957; Scott and West, 1969; Mahan, et al., 1986).

Compilations of electrical resistivity measurements from a variety of sulphide deposits are reported in the literature (eg: Parasnis, 1957; Parkhomenko, 1967; Keller, 1989; Vanhala and Peltoniemi, 1992; Bishop and Emerson, 1999). Parasnis (1957) conducted electrical resistivity measurement for a large number of sulphide ores from various European ore deposits. His method involved taking multiple measurements on a single sample, using a small four point electrode system. He concluded that the electrical resistivity of a single sample may vary "locally" by up to factors of 10 to 100, but are generally within 30% of each other. The resistivity of similar samples from the same locality may vary by even greater amounts (factors of 10^2 to 10^4). Although the electrical resistivity of sulphide ores may be highly complex, insitu and laboratory studies have typically shown a negative correlation between resistivity and sulphide content (Figure 2.3., from Keller, 1988).

2.2.3. Non-linearity

It is usually assumed that a rock's electrical resistivity will obey Ohm's law, which states the resistivity of a material is proportional to the electrical field strength and inversely proportional to current density. Generally this is valid, but only at low current densities. At higher current densities resistivity becomes non-linear, particularly in semiconductors (i.e. sulphide minerals) and at mineral-electrolyte interfaces where oxidation-reduction reactions are occurring.

Studies into non-linear conduction in sulphide rocks are reported by Katsube et al. (1973); Olhoeft (1977, 1982); Shaub (1965); Shaub (1969); and Petrov and Fedorov (1988). These studies have demonstrated that non-linear properties may be used to discriminate between sulphide and clay

responses. The electrical non-linearity of sulphides generally occurs at higher frequencies and current densities than the equivalent response of clays (Olhoeft, 1977). The non-linear phenomena is strongly dependent upon mineral type and chemistry (salinity, eH, pH) of the saturating electrolyte (Olhoeft, 1977). White (1974) suggests that the non-linear properties of sulphides are due to non-ohmic contacts of differently doped materials (i.e. a semiconductor p-n junction).

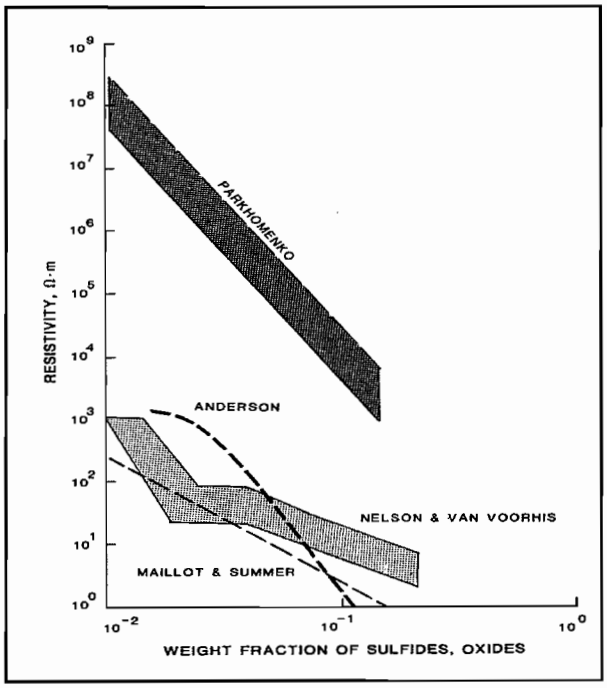

Figure 2.3. Inverse relationship between resistivity and the weight fraction of sulphides. Parkhomenko's (1967, 1982) laboratory measurements were conducted for pyritic rocks. Anderson's (1960) laboratory measurements were done on wet samples of mineralised gabbro. The other two data sets (Maillot and Sumner, 1966; Nelson and Van Voorhis, 1983) are from insitu measurements of porphyry copper ores. (From Keller, 1988).

2.2.4. Anisotropy

The resistivity of a mineral or rock is not always isotropic. In fact, electrical anisotropy is common in many rocks and minerals. Electrical anisotropy can be described using a 3 x 3 matrix, typically referred to as a conductivity tensor (Clark et al., 1988). Few detailed laboratory studies investigating electrical anisotropy have been conducted. Hill (1972) defined conductivity tensors for metamorphic rocks and showed how the electrical properties were influenced by the petrofabric. A similar study was conducted by Siegesmund et al. (1991) for mylonites. Parkhomenko (1967) commented on the highly anisotropic nature of graphite. Clark et al. (1988) conducted a study of sulphide ores from the Mt Lyell region, western Tasmania, and showed saturated layered rock to be characterised by large anisotropies, whose conductivity tensor was reflective of the petro-fabric.

Electrical anisotropy can have a significant impact on survey design, data modelling and interpretation, but its effects are often ignored. The effects of anisotropy on resistivity field measurements are described by Bhattacharya and Sen (1981) and Matias and Habberjam (1986). More recently, resistivity inversion techniques, which incorporate anisotropy, have been developed by Christensen (2000) and Yin (2000). These methods have been shown to improve data resolution in anisotropic environments.

2.3. Induced Polarisation

The previous definition of resistivity (Eqn 2.1) assumes that the electrical properties of earth materials are independent of frequency. However, the electrical resistivity of a rock is often observed to decrease as the frequency of the applied current is increased. This effect, known as induced polarisation (IP), is typically accentuated by the presence of clay and metallic minerals. In time domain measurements this effect is observed as a slow decaying residual voltage, when the applied current is abruptly switched off.

2.3.1. Explanation of the IP effect

The IP effect has been subject of extensive research and the reader is referred to; Keller, 1959; Madden and Cantwell (1967); Ward and Fraser (1967); and Keller and Frischknecht (1966) for detailed summaries. Monographs on the subject are provided by Wait (1959) and Sumner (1976). The following provides a brief summary of the induced polarisation phenomena.

Studies by Marshall and Madden (1959) and Mayper (1959) showed that the principal mechanism for the IP effect is the storage of chemical energy. This storage of energy can take place due to the various motilities of ions throughout the rock. When a current passes through a rock, excesses or deficiencies of ions occur at boundaries between zones of different motilities. The concentration of ions at the boundaries opposes the current flow and causes a polarising effect. The induced polarisation effect can be produced by two mechanisms: membrane polarisation and electrode polarisation.

Most minerals when in contact with a pore fluid develop a net negative surface charge, whose resulting potential attracts positive ions close to the surface and repels negative ions. This zone (diffuse layer) of unequal ionic charge extends into the solution to a distance of around $1x10^{-8}$ metres. If the pore space is restricted enough that the current can only be transported by the smaller positive ions, the mobility of the larger negative ions is decreased (Madden and Cantwell, 1967). When a current is applied, the positive ions are displaced, and on switching the current off the charges redistribute themselves back into equilibrium. This phenomenon is called membrane polarisation, or may be referred to as the "background effect" (Wait, 1959). The effect is pronounced when clay particles are present, resulting in little or no flow of negative ions through the system when a current is applied (Figure 2.4).

A similar effect occurs in rocks containing minerals that conduct electronically. Figure 2.5 displays a metallic mineral blocking a pore path in a saturated rock. At the electrolyte-electronic conductor interface, a potential barrier is produced which inhibits current flow. When a current is applied, ionic charges build up along the interface, with positive ions along one face and negative ions on the opposing face. The opposing charges result in a potential gradient that opposes the flow of current across the interface, thus "polarising" the mineral. If the current is switched off, a residual voltage continues across the mineral due to bound ionic charges that decreases as the ions slowly diffuse back into their original equilibrium (Parasnis, 1997). Studies by Klein et al. (1984) indicate the induced polarisation phenomenon of most sulphide minerals is due to surface diffusion (i.e. conduction within the grain), as opposed to diffusion of

aqueous species (i.e. conduction within the electrolyte). The intensity of the polarisation is dependent on the content and distribution of the conducting minerals. Olhoeft (1985) examined the electrical polarisation of a number of minerals; arranged in order of decreasing polarisability, these minerals include graphite, cobalite, magnetite, niccolite, pyrite, chalcocite, pyrrhotite, proustite, hematite and goethite.

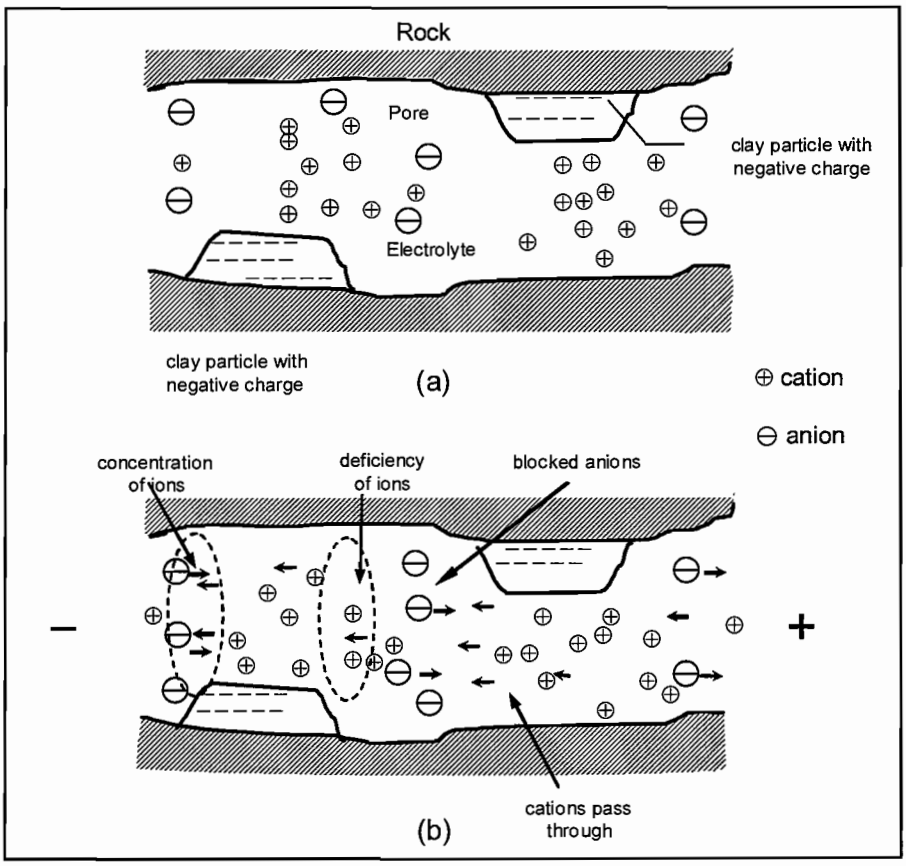

Figure 2.4. Membrane polarisation effect in porous sandstone containing clay particles (a) normal distribution of ions prior application of an electrical potential, (b) polarised distribution of ions after application of an electrical potential (after Ward and Fraser, 1967).

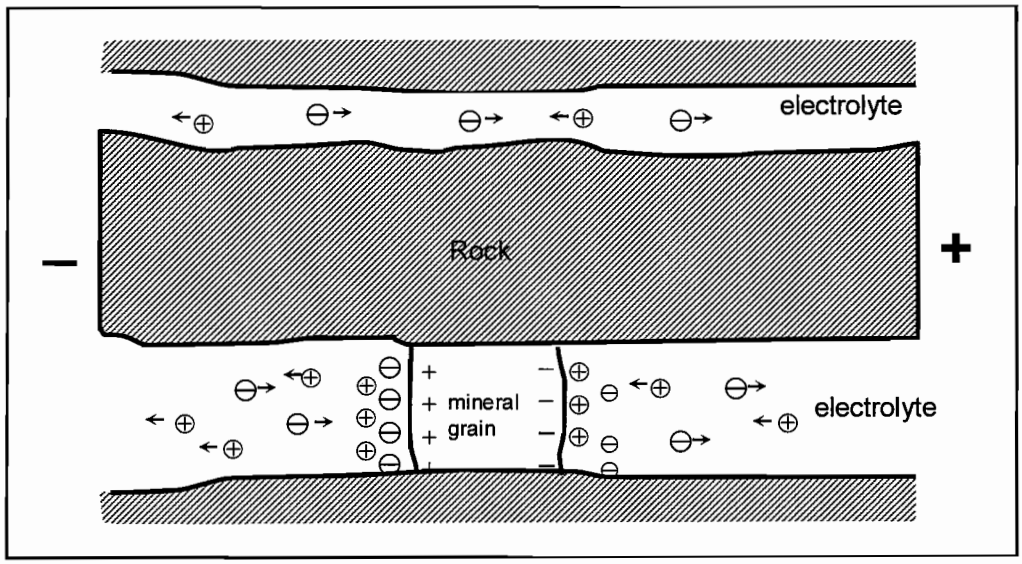

Figure 2.5. An application of an electrical potential causes electrolytic flow in the upper pore, whilst electrode polarisation occurs in the lower pore due to the presence of a mineral grain (after Telford *et al.*, 1990).

The IP effect is marked by a decrease in resistivity with increasing frequency using an alternating current (AC). This is called electrode polarisation, as the effect is analogous to electrolysis along the surface of a metal electrode immersed in an electrolyte (Bleil, 1953). This phenomenon may be referred to as the "overvoltage effect", a term given to the extra potential gradient required to drive a current from an electrolyte into a metallic conductor (Wait, 1959). Other authors (Ovchinnikov *et al.*, 1968; Angoran and Madden, 1977; Olhoeft, 1985) have described the induced polarisation effect of metallic ores in terms of oxidation-reduction reactions occurring at the ore mineral-electrolyte surface. Studies into the electrochemical nature of IP phenomenon have been conducted by Angoran and Madden (1977); Guptasarma (1983); Klein et al. (1984); Wyller et al. (1992); and Appararo (1994).

The IP effect doesn't occur for all sulphides minerals. Markushin et al. (1973) and Olhoeft (1985) conducted IP measurements of a variety of minerals. Markushin et al. (1973) state sphalerite and cinnabar are not polarisable minerals. However a recent study by Hawk and Brooker (2001) gives examples of high-grade sphalerite ores with chargeable properties. However the exact source of the IP effect in this study could not be identified.

2.3.2. Induced polarisation measurements and parameters

The induced polarisation effect can be observed in both the time and frequency domains. Time domain measurements involve sending an interrupted direct current into the ground and observing the decaying residual voltage between a pair of potential electrodes, after the current is switched off. Frequency domain measurements involve measuring the variation of apparent resistivity of the ground at different frequencies typically up to several hundred Hz.

The simplest method of measuring the IP effect in the time domain is to compare a residual voltage at a certain time after the current cut-off with the potential during steady-state current flow. Chargeability measured in this way is expressed as millivolts per volt, or may be expressed as a percentage.

An alternative method commonly employed in commercial time-domain instruments measures the potential integrated over a time interval of the transient decay (Figure 2.6). Chargeability *(m)* is defined as the integral of polarisability (residual voltage (V)) over a time interval from t_1 to t_2 after the shut-off an infinitely long transmitted current pulse (Seigel, 1959) expressed as:

$$m = \frac{1}{\Delta V} \int_{t_1}^{t_2} \Delta V(t) dt \qquad (2.4)$$

Frequency domain measurements involve measuring the resistivity at varying frequencies. The *frequency effect(FE)* parameter is defined as:

$$F.E. = \frac{\rho_{dc} - \rho_{ac}}{\rho_{ac}} \qquad (2.5)$$

where ρ_{dc} is the resistivity of the rock at near DC (i.e. low frequency, typically (~0.1)) and ρ_{ac} is the resistivity of the rock at high frequency (typically 100 to 1000 Hz).

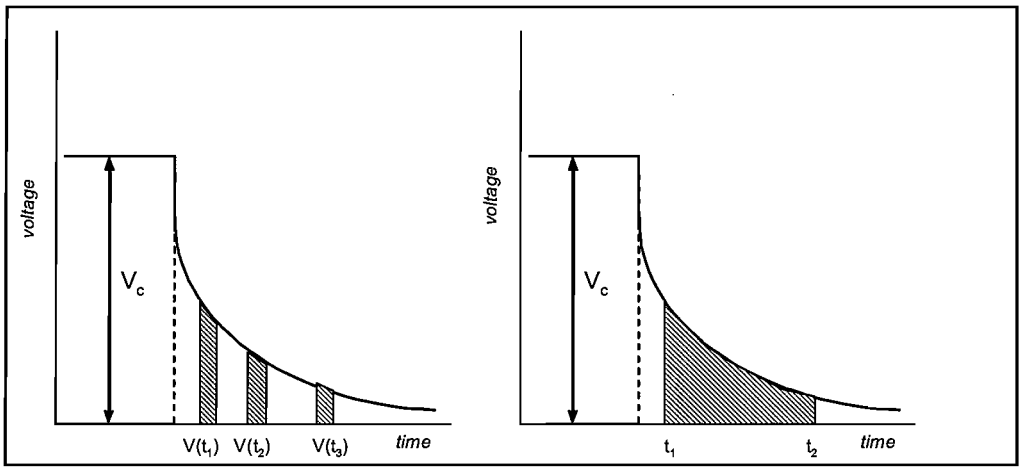

Figure 2.6. Time integral measurement of IP (a) showing recorded channels (b) complete integral (*after* Telford *et al.*, 1990).

The IP effect is influenced by the effective resistivity of the electrolyte in the rock and consequently by the type of electrolyte and temperature. Marshall and Madden (1959) devised a parameter called the *metal factor (MF)*, which attempts to remove this effect and is defined as:

$$M.F. = \frac{\rho_{dc} - \rho_{ac}}{\rho_{dc}\rho_{ac}} \times 2\pi \times 10^5 \qquad (2.6)$$

The metal factor attempts to highlight responses attributed to metallic polarisable targets rather than clays.

Standard measurements of induced polarisation provide a measure of the magnitude of the induced polarisation. A more comprehensive method commonly referred to as spectral IP or complex resistivity was developed to measure both amplitude and phase components of resistivity over a broad range of frequencies. Early Investigations by Shaub and Ivanov (1971); and Zonge (1972), indicate that different minerals may show different phase shift patterns in spectral IP measurements. It is common for the real (amplitude) and imaginary (phase) components to be plotted versus frequency, and theoretical models calculated by curve fitting or inversion (Song and Vozoff, 1985). Zonge and Wynn (1975) state that the main benefits of spectral IP include removal of electromagnetic coupling effects, host rock response identification and mineral discrimination.

2.3.3. Equivalent circuits (Cole-Cole model)

Equivalent circuits are often used as analogue models for the conduction mechanism in rocks. Figure 2.7 shows an example of a circuit representing the mechanism of conduction of a porous rock, with or without a polarisation zone. Figure 2.7 shows a parallel circuit where R_0 and R_1 are the effective pore-fluid resistances and Z_m is the impedance in the solution due to a mineral or clay particle. The branch containing R_0 represents an unblocked alternate zone whose resistance is controlled by electrolytic conduction.

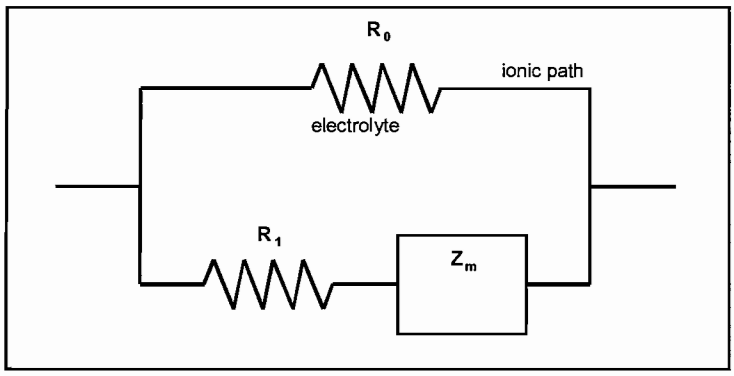

Figure 2.7. An equivalent circuit representing the mechanism of conduction in a porous rock, with or without a polarisation zone (*after* Telford *et al.*, 1990). R_0 and R_1 are the effective pore-fluid resistances and Z_m is the impedance in the solution due to a mineral or clay particle.

Keller and Frischknecht (1966) use an equivalent circuit to qualitatively discuss the effect of certain factors to the overall resistivity of the rock. From their circuit they describe several factors that affect the magnitude of induced polarisation:

1. The greater number of pores blocked by the conducting grains (sulphide content), the larger the polarisation effect.
2. Grain size affects the magnitude of polarisation, as polarisation is a function of the amount of grain surface exposed. Polarisation is optimal for intermediate sized grains.
3. Polarisation decreases with increasing porosity, as more current flows in the unimpeded paths (R_0) (Figure 2.7).
4. The amount of water infilling these pores also effects polarisation with maximum polarisation occurring when the rock is 75% saturated.

Early models (Ward and Fraser, 1967) defined Z_m as the *Warburg* impedance, which varies inversely to the square root of frequency. The Warburg impedance provides an overly simplistic representation of frequency dependence and a more realistic representation known as the Cole-Cole model (Pelton et al., 1978) commonly used to describe the complex resistivity spectrum of rocks is expressed as:

$$\rho(\omega) = \rho_0\left\{1 - m\left[1 - \frac{1}{1+(i\omega\tau)^c}\right]\right\} \qquad (2.7)$$

where; $\rho(\omega)$ = complex resistivity, ρ_0 = direct-current resistivity, m = chargeability, c = frequency dependence, τ = time constant, ω = angular frequency and $i^2 = -1$.

Although spectral IP is originally defined as a frequency method, Lee (1981), Johnson (1984), Lewis (1985) and Yuval and Oldenburg (1997) provide numerical techniques to derive Cole-Cole parameters from time-domain data. Duckworth and Calvert (1995) compare Cole-Cole parameters derived from both time domain and frequency domain measurements.

The Cole-Cole model is the most widely accepted method for parameterising the resistivity spectrum of rocks (Vanhala, 1997). Parameters m, c, τ, and ρ_0 are obtained from fitting the model to the complex data. The

chargeability (m) describes the magnitude of polarisation, the time constant (τ) is related to the relaxation time (indicative of maximum phase response) and the exponent (c) controls the curvature of the decay curve (in log-log space). Seigel et al. (1997) provides some characteristic values of τ for a variety of IP sources (Table 2.2). The use of Cole-Cole parameters for characterising IP responses is often referred to as spectral IP (Seigel et al., 1997).

IP Source	τ- seconds				
	10^{-2}	10^{-1}	1	10	100
Background (non-metallic)	✓	✓			
Gold deposits with disseminated sulphides or arsenides	✓	✓			
Bedded lead-zinc (MVT)	✓	✓	✓		
Porphyry copper deposits	✓	✓	✓		
Massive pyritic deposits			✓	✓	✓
Pyrrhotite related deposits				✓	✓
Magnetite-related deposits			✓	✓	✓
Cultural sources (pipelines, powerlines, etc.				✓	✓

Table 2.2. Tau properties of various IP sources, after Seigel et al. (1997).

DaRocha and Habashy (1997) proposed a new model incorporating elements from Dias (1972) and Pelton *et al.* (1978). Their model simulates the effects of the fractal pore interfaces between the electrolyte and metallic grains by using an impedance of $Z_m = K(i\omega)^{\eta}$, where K = diffusivity of charge and η is related to the fractal geometry of the medium. Dias (2000) provides a summary of the various analogue circuits used to model the electrical conduction mechanism of rocks. He presents a refined model which incorporates two additional parameters, an electrochemical parameter and pore length fraction dimension.

2.3.4. Nonlinearity

In common with resistivity measurements, induced polarisation measurements are dependent on current density, although for low current densities, chargeability remains consistent. Petrov and Fedorov (1988) estimated nonlinear behaviour of time-domain IP data. They showed considerable deviation from linear dependence occurred at current densities equal or greater than 10^{-3} to 10^{-2} A/m^2.

Scott and West (1969) measured the IP responses of several sulphide ore samples. Chargeability was observed to be independent of current density when operating at current densities less than 10^{-3}A/m^2, but was non-linear for higher values.

2.3.5. Qualitative analysis of IP

The factors that influence the induced polarisation response of a rock have been studied using theoretical, laboratory and insitu techniques. Studies into the induced polarization effects of sulphide bearing rocks have largely focused on correlating spectral parameters (Cole-Cole) with ore content, grain size and distribution (texture), and mineral discrimination.

2.3.5.1. Effect of ore texture and mineral grain size

The induced polarisation effect is a surface controlled process. Thus the effects of grain size and texture have a profound influence on the induced polarisation properties of a rock. Disseminated deposits are typically more polarisable than massive sulphide deposits, as they contain a number of isolated conductive particles that are in contact with an electrolyte. If the same quantity of conductive minerals were concentrated to form a vein, the surface area of grains-electrolyte interfaces would be substantially reduced, thus lowering the polarisability of the material. Some massive sulphides have a chargeable response as conductive grains may be isolated by resistive matrix (Pelton et al., 1978).

Pelton et al. (1978) demonstrated that Cole-Cole parameters could be used to determine the ore texture and grain size of disseminated sulphide deposits (Figure 2.8). Similar conclusions were derived for spectral IP measurements of synthetic cores (Mahan et al., 1986). Spectral IP measurements showed that the time constant (τ) increased with an increase in sulphide grain size for artificial samples of disseminate chalcopyrite (Mahan et al., 1986). These experimental results support the theoretical model of Wong (1979) and de Witt (1979). These models also suggest that for elongated mineralisation (eg: ellipsoidal grains), the phase amplitude and critical frequency are dependent on grain orientation with respect to the electric field (Wong and Stangway, 1981). Vanhala and Peltoniemi (1992) showed the time constant varies almost as the square of the average grain size for *insitu* spectral measurements.

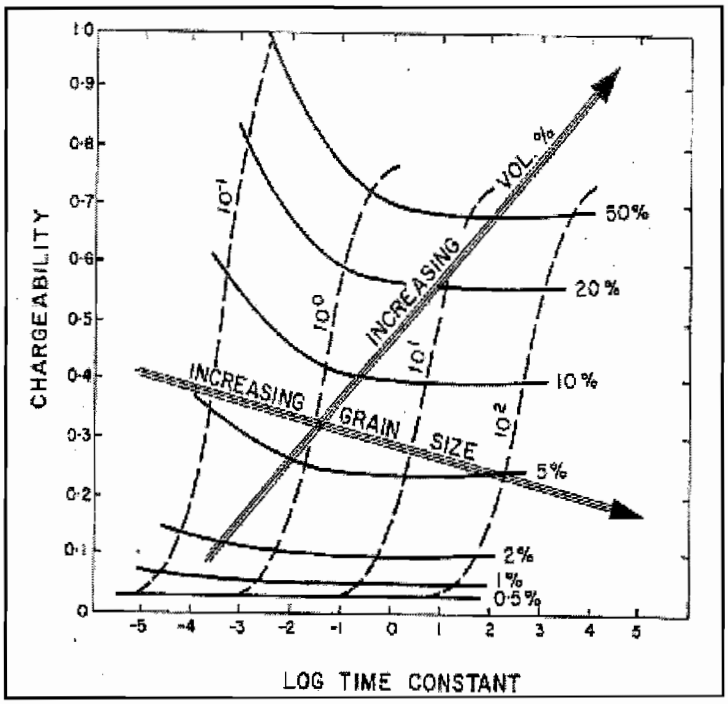

Figure 2.8. Chargeability-time constant plot for artificial samples containing pyrite, arrows indicate increasing sulphide concentration and grain size (after Pelton *et al.*1978).

Spectral IP studies of a number of Finnish ore deposits by Vanhala (1997) showed that the time constants for disseminated mineralisation and net-textured mineralisation differ only slightly. Vanhala (1997) showed grain-size estimates based on Cole-Cole parameters was the most effective technique in distinguishing different ore textures for homogeneous disseminated

sulphides. Homogenous grain size distributions (i.e. grains all have the same diameter) were found to have a tight phase spectrum (Vanhala, 1997), with a c value of 0.5. Broader distributions of grain sizes were indicated by a flat spectrum with lower c values.

Asymmetric phase spectra derived from spectral IP measurements have been used to describe roughness of grains even in intergranular texture (Saloheimo, 1990). Vanhala (1997) states the asymmetry can also be caused by grain size distribution, with the phase peak of the IP spectra (i.e. frequency at which the phase shift reaches a maximum) shifting towards lower frequencies within increasing grain size. A generalised Cole-Cole model incorporates an additional constant to model this asymmetry (Dias, 2000).

2.3.5.2. Ore-grade

The relationship between sulphide content and polarisability is largely controlled by the distribution of the conducting minerals. Numerous studies (McEuen et al., 1959; Scott and West, 1969; Mahan et al., 1986) have demonstrated disseminated deposits typically show a positive correlation between magnitude of polarisation and sulphide content (Figure 2.8).

Nelson and Van Voorhis (1983) examined the insitu spectral IP response of a copper porphyry deposit in an attempt to estimate sulphide content. They showed there is a general trend of resistivity decreasing and phase lag increasing, as sulphide content increases. The ratio of phase to resistivity can be used to estimate *sulphide* content. By multiplying this ratio by a suitable conversion factor it becomes equivalent to the quadrature component of electrical conductivity and metal conduction factor.

2.3.5.3. Mineral discrimination

Pelton et al. (1978) demonstrated the Cole-Cole parameter Tau (τ) derived from insitu measurements could be used to discriminate between (1) massive sulphides and graphite, (2) magnetite and nickeliferous sulphide mineralisation. These differences are largely accounted by variation in texture.

Lewis and Bishop (1988) illustrate the value of mineral discrimination using Cole-Cole parameters derived from *insitu* measurements collected from sulphide deposits of western Tasmania. The Cole-Cole parameters were derived from inversion of time-domain IP data and a chargeability-time-constant (m-τ) plot of the measurements clearly distinguishes the various lithologies investigated (Figure 2.9).

Seigel et al. (1997) provides a case study on the spectral IP properties of a number of different deposits. The use of Cole-Cole parameters appears to discriminate different sources of IP responses. Although spectral IP can be used to characterise certain types of minerals or mineral assemblages Seigel et al. (1997) warns that universal rules for IP source discrimination cannot be generally applied and discrimination is typically site specific. Spectral IP responses may be complicated if multiple IP sources, bimodal grain distribution, and/or electromagnetic induction effects occurs. Telford et al. (1990) show the spectra for porphyry mineralisation is similar to that of

volcanogenic massive sulphide deposits. Vanhala (1997) showed that the phase spectra varied for different areas of alteration. However in complicated areas, ore zones may not be clearly identified.

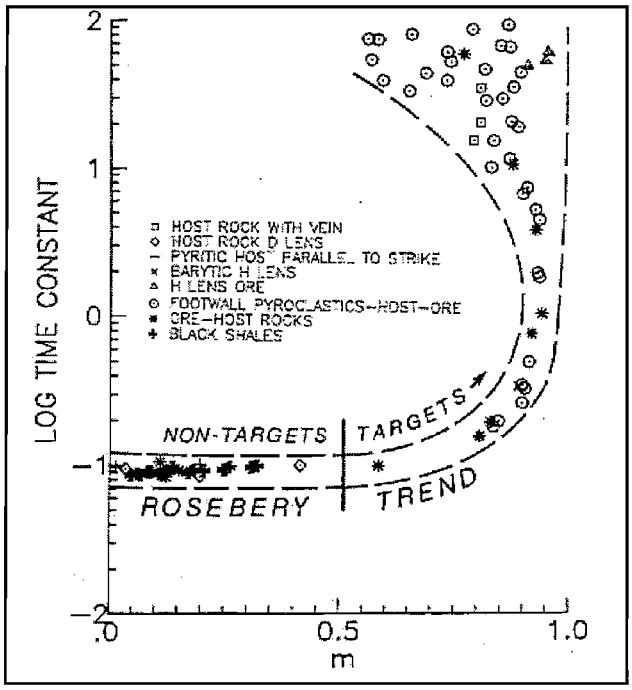

Figure 2.9. Chargeability-time-constant (m-τ) plot of spectral IP measurements conducted in western Tasmania, discriminating various lithologies (from Lewis and Bishop, 1988).

2.3.5.4. Other properties

Studies into the effects of primary voltage, amount of electrolyte, type of electrolyte, concentration of electrolyte, and temperature for induced polarisation have been conducted using standard samples (Collett, 1959;, Mahan et al., 1986). Electrolyte activity effects are discussed by Keevil and Ward (1962) and Fraser et al. (1964). General findings show pressure and temperature has little effect on IP, but a change in electrolyte activity (concentration) does. Increase in electrolyte activity decreases IP responses of clays or disseminated mineralisation, but increases the response for vein-style mineralisation. Emerson and Smith (1969) showed that sulphide polarisation increases with pore water conductivity, as suggested by the theoretical model of Bhattacharya and Morrison (1963). This is in contrast with the laboratory measurements conducted by Fraser et al. (1964).

2.4. Summary

Exploration for sulphide minerals is typically conducted using zero or low frequency electrical techniques. Low frequency properties include resistivity and induced polarisation.

The electrical conduction in most rocks primarily occurs through interstitial pore fluids whose resistivity is far less than the resistivity of the minerals constituting the rock matrix. Only where a rock matrix contains an abundance of conducting minerals, does conduction through the rock matrix becomes appreciable, reducing the overall resistivity. The electrical resistivity of rocks containing sulphide minerals is largely controlled by their

composition and distribution. The resistivity of sulphide bearing rocks is typically in the range of 0.01 to 1 Ωm.
The induced polarisation effect caused by sulphide minerals involves oxidation-reduction reactions occurring at the mineral-electrolyte interfaces in the presence of an external electric field. These effects can be measured using time and frequency domain methods. The Cole-Cole model described by Pelton *et al.* (1978) is the most widely used model to describe the details of the induced polarisation phenomena. The Cole-Cole parameters (*m*, *c*, τ, and ρ_0), although designed to express the resistivity spectrum of a rock can also be derived from time-domain data. These parameters are useful in characterising textural characteristics of disseminated sulphides and for mineral discrimination.

Chargeability (m) is roughly proportional to sulphide content (volume percent), and decreases with increasing grain size for disseminated sulphides. For massive sulphides, conductive paths, result and induced polarisation effects (hence chargeability) are reduced. The time constant (τ) represents the rate of decay of the residual voltage, and is proportional to the average grain size of the sulphide minerals. τ values range from milliseconds up to thousands of seconds. The shape of the decay curve is controlled by the exponent (c), and reflects mineral grain size distribution.

Chapter 3

Methodology: Resistivity and induced polarisation techniques for insitu and laboratory measurements

3.1. Introduction

The electrical characterisation of the three sulphide deposits described in this thesis (Scuddles, McArthur River and North Parkes) was conducted using resistivity and induced polarisation methods at insitu and laboratory scales. Such techniques are well established and routinely applied in electrical geophysical prospecting for sulphide ore-bodies.

Electrical galvanic measurements are suitable for scale-variation studies as the distance between electrodes primarily controls the scale of investigation. Electrode arrays can be dimensioned to accommodate a wide range of scales from micro-scale measurements of individual minerals to several hundred metres for large field surveys. Inductive methods have some operational advantages over galvanic techniques. However, as the majority of the insitu electrical studies were completed in underground workings the use of inductive methods was considered inappropriate, due to the close proximity of underground mining services and infrastructure (electrical/plumbing, ground support, etc). Low frequency galvanic methods are less affected by electromagnetic noise and also allow induced polarisation properties to be measured.

This chapter is divided into two main sections discussing the methodology applied at each scale of investigation; insitu measurements and laboratory measurements.

3.2. Insitu measurements

3.2.1. Site Selection

The aim of the insitu investigations was to measure the scale variation and bulk electrical response of the various geological zones at each deposit. Site selection was a critical component of this study, as it is a major factor that influences the applicability of the results.

Sites were selected:

- in consultation with the mine geologists,
- to characterise the range of different ore and alteration types,
- in areas of "homogeneous" geology,
- with as little as possible mining-induced fracturing,
- free from ground support and shotcrete,
- with smooth flat surfaces, thus surface can be considered planar for geometric calculations,
- 3-12 metres in extent.

Most sites were selected along vertical faces, with the exception at North Parkes (E27 open-pit), where some measurements were collected along solid

sections of the pit floor. Site exposures were typically six metres long, although this varied accordingly to accommodate site heterogeneity, site geometry, geological and ground support factors.

3.2.2. Equipment

All insitu electrical measurements were conducted using a Scintrex IPC-9 250W battery powered time-domain induced polarisation transmitter and a Scintrex IPR-12 induced polarisation receiver. All measurements were collected using a four-second on-cycle time to enable direct comparisons between the electrical responses of each deposit. Precise transmitter current was controlled by a resistor shunt box and determined by measuring the potential difference across a 1kΩ resistor in series with the rock using a digital voltmeter (±1% accuracy). The shunt box was mainly used to reduce current density to levels comparable to surface surveys. The IPR12 receiver automatically stacked measurements collected for five cycles (80 seconds). Induced polarisation measurements were collected using the standard time slices of the IPR12 (Appendix-A). A single chargeability window was defined from 340 to 520 milliseconds to provide a simple comparative value for all chargeability measurements.

Induced polarisation data from insitu measurements were often affected by noise and low signal levels. This problem was most pronounced in highly conductive areas (<1 Ωm; see Chapter 5). As a result, transient decay curves in these environments were often irregular and noisy. The criteria adopted for the acceptance of valid decay curves required a smooth monotonic decrease in voltage and no negative voltages at early or late times. The majority of insitu decay curves for both the North Parkes and McArthur River deposits were accepted as valid (95%), whereas a large proportion of decay curves for Scuddles (40%) were rejected.

The field procedure adopted was similar at all sites, but with minor improvements in data acquisition and resolution being systematically developed throughout the study. Three types of measurement were conducted at each site to characterise the insitu electrical properties:

- **Vertical electrical soundings**: this was the primary method of characterising the electrical scale variation at each site.
- **Lateral electrical mapping**: using small electrode spacings to provide an indication of the electrical heterogeneity of the site.
- **Anisotropy mapping**: measurement of the angular variations in apparent resistivity and chargeability and their relationship to ore fabric and texture.

3.2.3. Vertical electrical sounding

The vertical electrical soundings were conducted using a spreading Wenner array, with potential electrode spacing ("a") ranging from 0.11 metres to a maximum of four metres (Table 3.1). At least one sounding was completed at each site, although for many sites additional soundings were collected to examine data variability.

Point electrical contacts with the rock face for large electrode spacings were made using 6.5 mm nickel-coated masonry anchors (dynabolts) inserted in holes drilled to a depth of approximately 25 mm. The electrical

contact between the dynabolts and the face was achieved by filling each hole with conductive medical ECG gel (MES Gel) prior to insertion of the dynabolt. Tests conducted during preliminary investigations showed the gel to have no measurable IP response. Standard electrode spacings listed in Table 3.1 were employed at all sites and were selected in part to minimise the number of dynabolts required.

"a" spacing (m)	Maximum spread (m)
0.11	0.33
0.22	0.66
0.33	1.0
0.5	1.5
0.66	2.0
1.0	3.0
2.0	6.0
4.0	12.0

Table 3.1. Wenner 'a' electrode spacings for insitu measurements, and maximum array length (3 x 'a').

The measurements were conducted in order from large spaced measurements to small spaced measurements. Thus the electrodes are used as potentials first, then as current electrodes later to avoid any spurious effects. Measurements for small electrode spacings (0.33, 0.22, 0.11 metres) were conducted using the mobile electrode array (see following section 3.2.4).

3.2.4. Lateral variations

Lateral mapping was conducted at most sites using a fixed mobile electrode array (MEA). Measurements were collected along traverses or grids across the site. The MEA consists of spring-loaded sponge electrodes with fixed separation. Initial testing at Mt Lyell, Tasmania showed that resistivity and IP measurements using dynabolt electrodes were effectively the same as results achieved using sponge electrodes saturated in a saline solution and held firmly on to the rock face. The dynabolts were preferred over the sponge electrodes as they enable "hands-free" operation and provided a more repeatable and convenient method of measurement, particularly for largely spaced electrodes and in inaccessible locations. However for lateral and anisotropic measurements, the use of dynabolts was time consuming and the mobile electrode array (MEA) was developed to allow a large number of measurements to be collected quickly and easily.

The MEA array (Figure 3.1) can be freely rotated and moved for anisotropy and lateral electrical mapping. The MEA consists of a number of electrode "rods" whose spacing is fixed within a wooden frame. Each electrode is spring-loaded to provide an opposing force to the operator to ensure good contact with the rock-face (even if the face exposure is irregular). The MEA electrodes were arranged in a Wenner configuration to be consistent with the sounding data, although the array could easily be modified for dipole-dipole measurements if required.

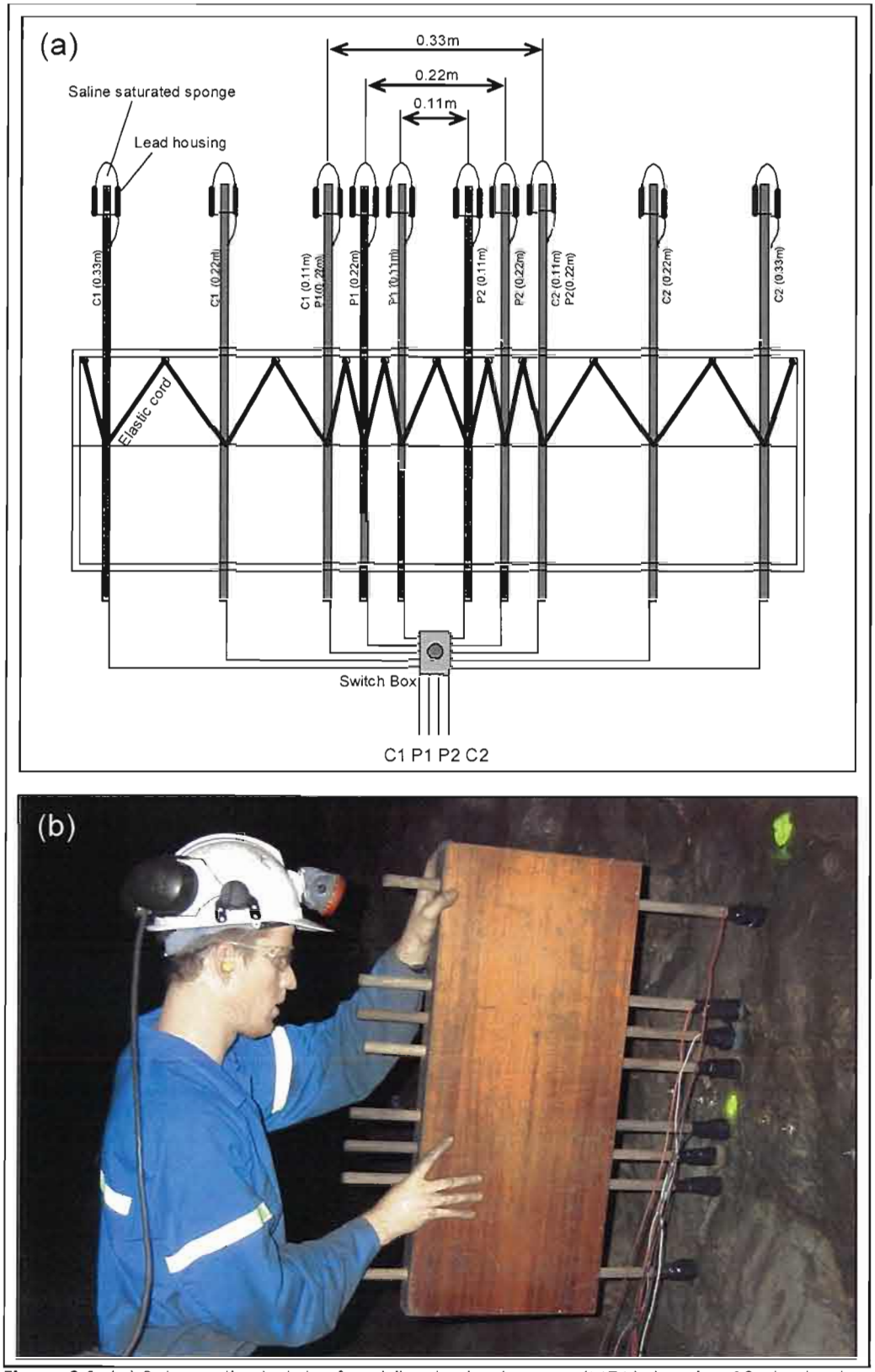

Figure 3.1. (a) Schematic sketch of mobile electrode array (MEA) showing 10 electrodes, arranged in Wenner configuration with a=0.11, 0.22 and 0.33 metres. (b) Photograph of an eight electrode MEA in use at Scuddles (0.11 and 0.22m).

The MEA was originally developed with 0.22 m electrode spacings, however two stages of modifications involved the addition of 0.11 m and subsequently 0.33 m spaced electrodes. The additional electrodes provide a measurement of lateral and anisotropic electrical variability at three scales. The electrode spacing was selected using a switch box.

Resistivity and chargeability data from the lateral measurements are presented as gridded images (maps of resistivity or chargeability) or as profiles along traverses.

3.2.5. Anisotropy

Insitu anisotropy measurements were conducted by rotating the MEA in 30 degree intervals around a central mid-point. This provides a two-dimensional anisotropy map defined by 6 measurements (12 points due to the symmetry of the Wenner array). Anisotropy measurements conducted using this methodology are "apparent anisotropy" since they only provide an indication of electrical variability in a single plane. However, in many cases where exposures were orientated perpendicular to the strike of the geology the recorded resistivities probably represent absolute maximum and minimum values.

Resistivity and chargeability data are presented as 2-D radar plots, which clearly indicate the degree and direction of anisotropy. Examples of MEA anisotropy resistivity and chargeability maps collected at McArthur River are shown in Figure 3.2. The ore in this case consists of finely laminated sphalerite-galena bands interbedded with siliceous sediments and pyrite. The chargeability anisotropy map is relatively isotropic, obviously not influenced by the strong textural anisotropy (laminations). The resistivity map shows marked anisotropy, with the maximum resistivity being recorded parallel to bedding and the minimum resistivity recorded in the transverse direction.

Interpretation of anisotropy data is complicated by the "paradox of anisotropy' that states in an anisotropic medium, the apparent resistivity measured by an array orientated transverse to the bedding is equivalent to the longitudinal resistivity. For an array parallel to the bedding the apparent resistivity recorded is a function of both the transverse and longitudinal components. This effect is described mathematically by Keller and Frischcnecht (1966) and Parasnis (1997) as:

$$\rho_{aT} = \rho_{\parallel}$$

$$\rho_{aL} = (\rho_{\perp}\, \rho_{\parallel})^{1/2} \qquad (3.1)$$

ρ_{aT} = transverse apparent resistivity (perpendicular to bedding)
ρ_{aL} = longitudinal apparent resistivity (parallel to bedding)
$\rho_{\parallel}$ = apparent resistivity measured from horizontal array (parallel to bedding)
$\rho_{\perp}$ = apparent resistivity measured from vertical array (perpendicular to bedding)

A qualitative understanding of the paradox of anisotropy can be obtained by comparing the electrical potential distribution created by current electrodes in isotropic and anisotropic media (Figure 3.3). For a homogeneous medium the generated equipotentials are symmetric, thus resistivity derived from two orthogonal arrays are equivalent. In an anisotropic medium, distortions are created in the equipotentials, and the actual measured apparent resistivity for measurements parallel to layering is equivalent to the transverse resistivity. For measurements perpendicular to the layering the measured resistivity is equivalent to the longitudinal resistivity. The parallel measurements reflect a function of transverse and longitudinal components.

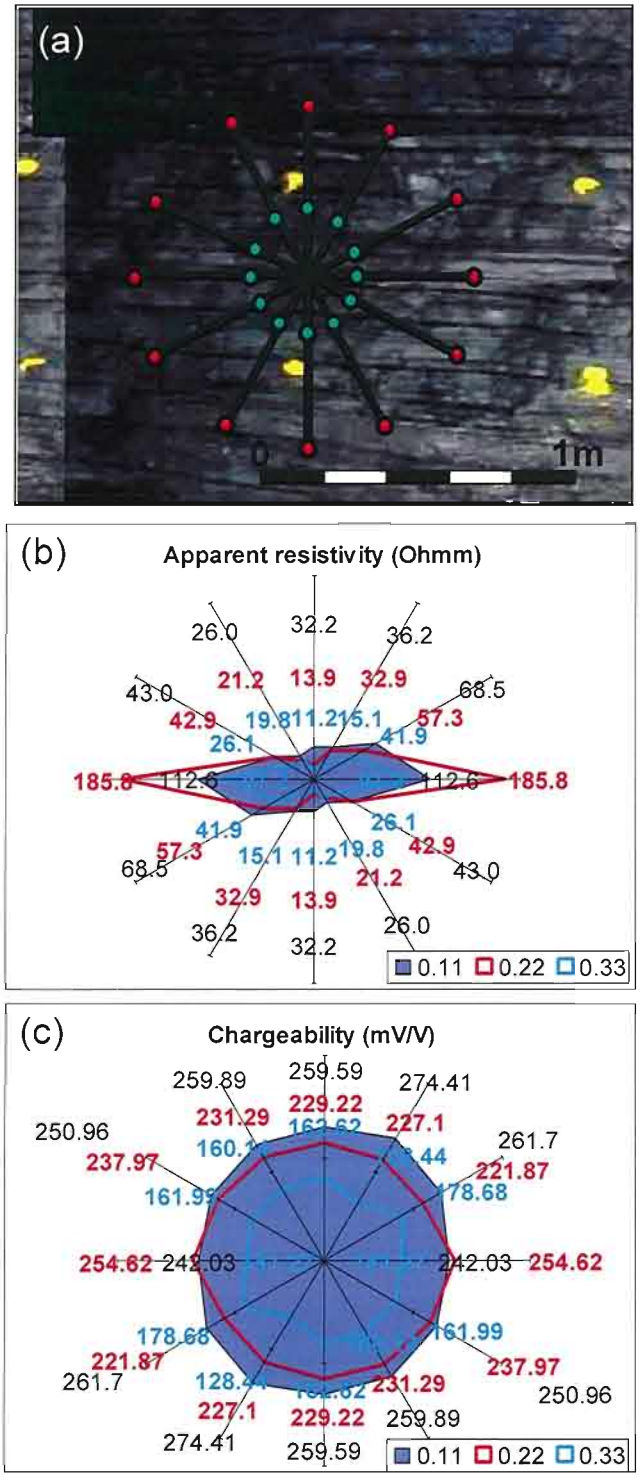

Figure 3.2. Example of anisotropy measurements from McArthur River. (a) photograph of measurement location, showing the laminated nature of the massive Zn-Pb ore. Red dots indicate current electrode positions. Green dots indicate potential electrode positions for 0.33m electrode array. (b) resistivity maps shows marked anisotropy. (c) chargeability map is isotropic.

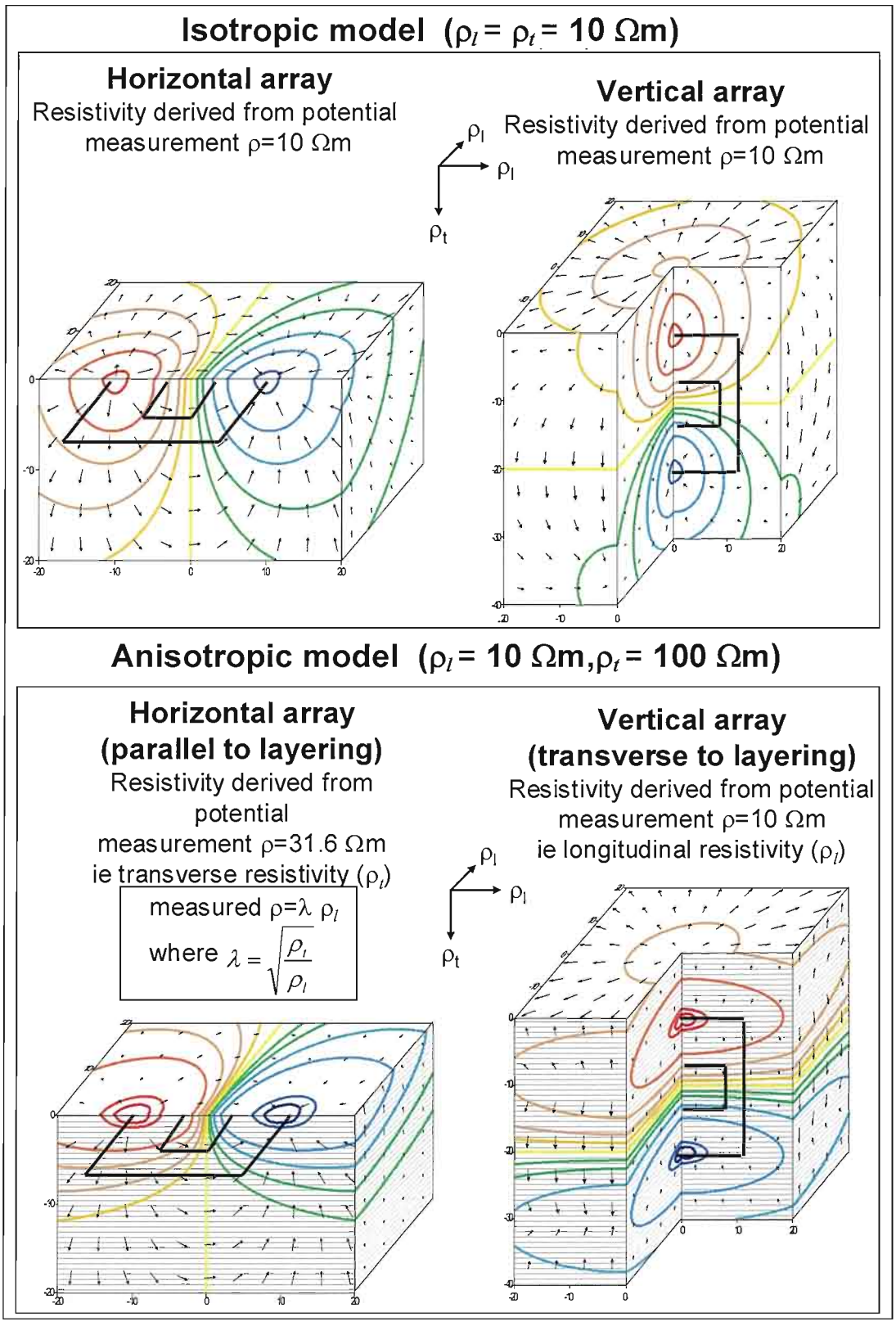

Figure 3.3. Paradox of anisotropy: in the isotropic model, the potential measured between the current electrodes remains constant for both horizontal and vertical arrays. In the anisotropic model, the increase in transverse resistivity distorts the equipotentials. For an array lying parallel to the layering, a larger potential difference is measured, which is a product of the coefficient of resistivity (λ). For an array lying perpendicular to the layering, a function of the longitudinal resistivity is measured (not the transverse resistivity). The derivation of equipotential surfaces is listed in Appendix-B.1.

3.2.6. Current density

The electrical behaviour of rocks, particularly those abundant in sulphides, becomes non-linear at high current densities, thus producing erroneous measurements of resistivity and chargeability. The current density at which non-linearity effects becomes prominent is typically dependent on rock mineralogy and electrolyte composition, but generally lies between 10^{-4} and 10^{-3} A/m^2 (Petrov and Fedorov, 1988). Electrical measurements were conducted at low current densities (typically <10^{-3} A/m^2) in order to be equivalent to those exhibited in exploration surveys. In general the lowest density that yielded a reasonable signal to noise ratio was used.

At each deposit, initial measurements were collected at different currents (typically over three orders of magnitude) to check the consistency of resistivity and chargeability measurements. Although non-linearity was not investigated in detail in this study, a series of measurements were conducted at the McArthur River deposit to illustrate the effect.

The variations of resistivity and chargeability as a function of current density are shown in Figure 3.4. Measurements were collected at different currents, at the largest electrode spacing for several insitu sites. The apparent resistivity shows little variation with increasing current density; however chargeability decreases rapidly for values greater than 1.5 x 10^{-3} mA/m^2. Although the resistivity results are effectively constant within the range of the currents tested (the transmitter output of the IPC-9 is limited to 1.5 A- 300W and affected by open-loop protection) non-linear behaviour may occur at greater currents.

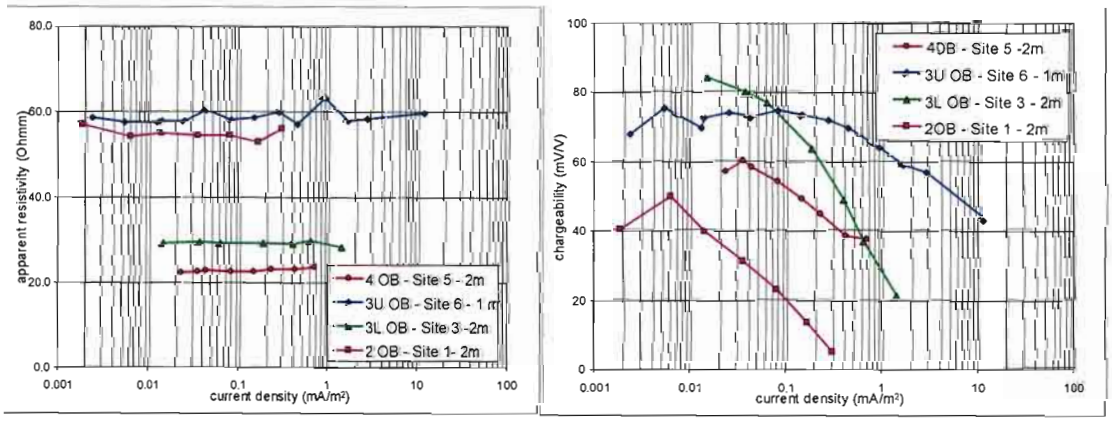

(a) (b)

Figure 3.4. Resistivity (a) and chargeability (b) as a function of current density at several sites from the McArthur River Pb-Zn deposit. Resistivity is effectively constant over the applied current densities. Chargeability shows markedly non-linear behaviour for current densities greater than 0.01 mA/m^2. Current density (maximum) is calculated from field measurements according to the equation listed in Appendix-B.2

Although operating currents were typically kept to a minimum, the highly conductive nature of several sites at the Scuddles deposit necessitated the use of much higher currents in order to provide a measurable signal (an increase of up to two orders of magnitude). The IPR12 although able to record signals as low as 50 μV generally failed to synchronise with the transmitter in this environment for signals less than 0.5 mV. Lower values were recorded using a digital voltmeter. In these environments, conduction through the highly conductive sulphides is primarily galvanic, and the non-

linearity effect commonly associated with electrolyte-mineral interactions is likely to be less significant (White, 1974).

3.2.7. Range of measurements

The resistivity and chargeability recorded at the three different deposits span a large range of values (Figure 3.5; Table 6.2). The large range of electrical measurements for the Scuddles deposit reflects the heterogeneity of the ore-body's mineralisation. In contrast, the electrical distribution for the McArthur River and North Parkes deposits are more tightly grouped, reflecting the more homogenous nature of these deposits.

Deposit	Deposit type	Mineralisation	Site selection	Median Resistivity	Median Chargeability
Scuddles	Volcanic-hosted massive sulphide	Heterogeneous -distinct zones within the massive sulphide Pb-Zn-Cu-Au	Sites were located in the various ore zones and host sequence.	Low 0.5 Ωm	84 mV/V
McArthur River	Sediment -hosted massive sulphide	Homogeneous Laminated Pb-Zn ore	Measurements were confined to the ore zone	Medium 46 Ωm	147 mV/V
North Parkes (E27)	Porphyry	Homogeneous 0.5-3% Cu-Au Porphyry	Measurements located in ore and host sequence	High 900 Ωm	46 mV/V

Table 3.2. Summary of the characteristics and electrical properties of the three deposits in the study (refer to Figure 3.6 for histograms of insitu resistivity and chargeability).

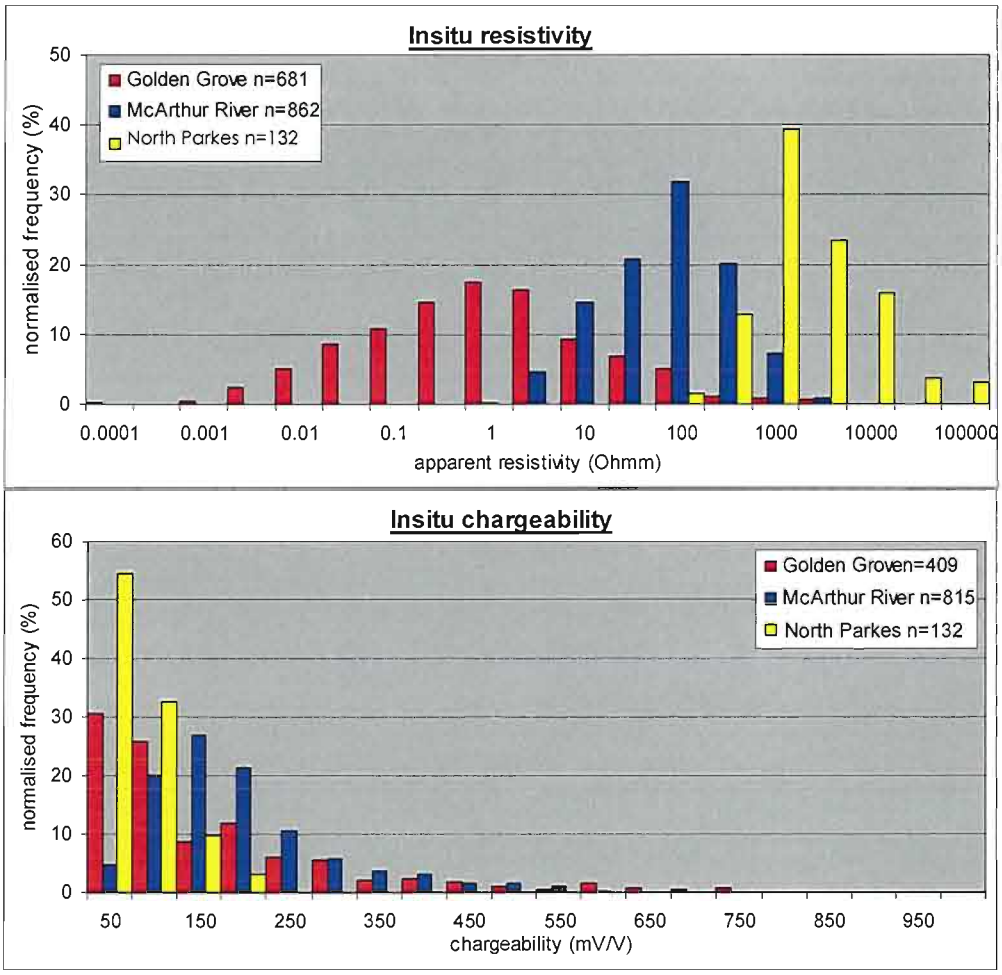

Figure 3.5. Normalised insitu resistivity and chargeability distributions for the three deposits; Scuddles, McArthur River and North Parkes.

For the majority of the field investigations, measurements were acquired readily using the IPR-12 and IPC-9 equipment. However, in highly conductive sites, such as the massive pyrite-chalcopyrite sulphide ore found at the Scuddles deposit, the lowest resistivity determined from the equipment was limited to 0.002 Ωm. This was primarily controlled by the maximum power output of the transmitter through the resistance shunt box and inability of the IPR12 to synchronise on the signal at these low signal levels.

3.2.8. Additional techniques and sampling

In addition to the electrical measurements, magnetic susceptibility mapping was conducted at most sites using an Exploranium KT-5 handheld meter. Magnetic susceptibility measurements were typically collected over the same grid or traverse as the electrical measurements, to allow direct comparisons between the two properties. Geological variation was recorded by visual inspections and sites were photographed for later comparisons with the geophysical measurements.

Large samples were collected from each site for laboratory testing. The original aim was to collect a sample from the centre of each expanding array. Unfortunately in most cases survey sites were located to record the electrical properties of the competent un-fractured rock and this usually precluded collection of a sample from the centre of the array. Typically two to three samples representative of the mineralogical and textural variability at each site were collected. Sample collection was often completed prior to electrical measurements when the exposure was scaled to remove loose material. Samples were orientated where possible prior to removal. The location of the sample in relation to the measurement grid was recorded.

3.3. Laboratory measurements

Samples from each site were cut into prisms for petrophysical measurements. Where possible, blocks were cut so that one face of the block was parallel to bedding or the foliation. Ideally, samples were cut to ensure a minimum block volume of 1000 cm^3. In some cases this was difficult or impossible due to the irregular geometry of the sample. Representative off-cuts generated during preparation of each prism were used for major and trace element geochemical analysis.

3.3.1. Resistivity measurements of hand specimens

To enable direct comparison to insitu data, laboratory measurements were conducted using galvanic resistivity techniques. These techniques are commonly used in petrophysical investigations and are well documented (eg: Mayper 1959; Keevil and Ward, 1962; Emerson, 1969; Katsube et al., 1973). Laboratory techniques for measuring the resistivities of rock samples/cores using inductive techniques are less common, typically less accurate, complicated by the presence of magnetite, and nominally only suitable for highly conductive samples (Emerson, 1969). Recent studies of the electrical conductivity of synthetic disseminated sulphide cores using inductive techniques are described by Yang and Emerson (1997).

Galvanic measurements of resistivity can be conducted using two or four electrode systems. Four electrode arrays are commonly used for laboratory galvanic measurements of rocks (Parkhomenko, 1967; Emerson, 1969) as this

configuration eliminates the effects of electrode electro-chemical polarisation (Collett and Katsube, 1973).

An electrode-electrolyte system was designed and constructed to enable measurement of the resistivity and IP properties of the prismatic samples. The electrode design (Figure 3.6) allowed a uniform contact of electrolyte over the entire end area of each sample using rubber o-rings. The current electrode was located within the end of the electrode housing and the potential electrode consisted of a wire loop that was positioned within the electrolyte close to the specimen surface. The current and potential electrodes were made of platinum to reduce electrode polarisation effects (Emerson, 1969; Collett and Katsube, 1973). A number of electrodes were constructed to accommodate the various sized faces of the samples. The electrolyte consisted of tap water (Hobart, Tasmania) with added NaCl (typically 3g/L).

Laboratory resistivity and induced polarisation measurements were conducted using the Scintrex IPC-9 transmitter and Scintrex IPR-12 receiver to enable direct comparisons between insitu and laboratory data. A cycle time of 4 seconds and the standard Scintrex time gates were used for all measurements (Appendix-A). The current through the sample was reduced to a low value (0.1 mA to 100 μA) using a low resistance parallel shunt and additional series resistors. This was to simulate current densities similar to those encountered in typical field surveys.

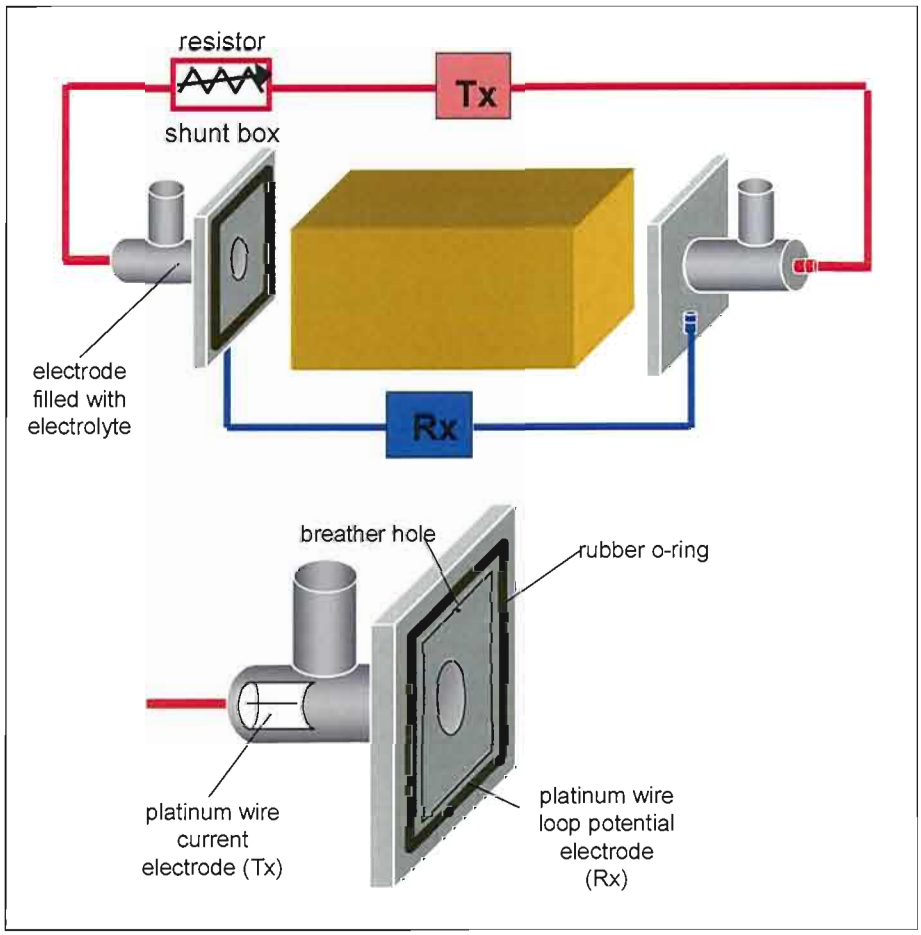

Figure 3.6. Four-electrode-electrolyte system, designed for prismatic samples of various sizes.

The prismatic petrophysical samples were hydrated for a minimum of 48 hours prior to measurement. The conductivity of the water used to hydrate the samples was adjusted to match the conductivity of the ground water as measured in the field by the addition of sodium chloride (NaCl). Various authors (Mandel et al., 1957; Scott and West, 1969; Alvarez, 1973; Mahan et al. 1986) have discussed the variation of resistivity measurements with electrolyte concentration, but these effects typically predominate in rocks with high porosities and low sulphide content. Alvarez (1973) showed that the electrical resistivity of sulphide samples containing more than 50% pyrite or 75% galena has no dependence on water saturation. This largely reflects the fact that conduction in high grade sulphide ores is predominantly controlled by ohmic processes, rather than electrolytic processes.

The procedure for the laboratory measurements involved the following steps.

- The saturated sample was surface dried, to eliminate surface conduction effects and clamped between the electrodes.
- The electrodes were filled with saline electrolyte (tap water with added NaCl (typically 3g/L).
- The transmitter applied a four-second half-period square waveform. The resistance of the shunt box was adjusted until the desired current was obtained through the sample. Current was determined by measuring the potential difference across a 1000 Ω resistor built into the current-shunt box. The potential difference was measured with a digital voltmeter.
- The IPR12 receiver measures the potential difference as a function of time, using a series of gates after current turn off. The resistivity and IP measurements were recorded and stacked for five durations of a complete cycle.
- Repeat measurements were conducted at three currents (typically 0.1, 0.01 and 0.001 mA). These currents equate to current densities ranging from 0.0001 to 0.01 A/m^2 depending on the current and cross sectional area of the sample.
- Measurements were collected for the three orthogonal sample orientations.
- Dimensions of samples were measured to the nearest millimetre and the resistivity of each sample was calculated using the following formula.

$$\rho = \frac{V}{I}k \qquad \text{where} \qquad k = \frac{A}{l}$$

ρ = resistivity (Ωm)	V = potential difference (V)
I = current (A)	K = geometric factor
l = sample length (m) (i.e. electrode separation)	A= cross-section area of sample (m^2)

- Chargeability data was scrutinised in a similar manner to the insitu data (Section 3.2.2) to remove erroneous data.
- Transmitter current and measured potential signals were routinely monitored using an oscilloscope (using either a Hewlett Packard 141B 100 MHz Oscilloscope or Fluke 99 50 MHz Scopemeter) for quality control.

3.3.2. Rocks with low resistivities

The four-electrode system was suitable for measurements of samples with resistivities typically greater than 1 Ωm, however for measurements of rocks with lower resistivities the technique proved inaccurate. This limit was determined by comparing galvanic measurements and inductive measurements using a hand-held conductivity meter (Geoinstruments GCM-2) for a range of samples. The problem became apparent when sample resistivity measurements appeared to reach a minimum of ~0.2 Ωm, irrespective of the nature of the sample. In the case of the four-electrode laboratory measurements, electrical contact to the sample is via an electrolyte-electrode. For samples with high resistivity, the additional resistance of a thin layer of electrolyte makes little difference to the measured potential. However for a highly conductive sample, this resistance can be quite large when compared to the sample resistance. Thus, the measured potential may be significantly higher than the real potential developed across the sample, resulting in an erroneously high value for resistivity.

A two-electrode system was developed in order to measure low resistivity samples of less than 1 Ωm (i.e. predominantly samples of massive pyrite-chalcopyrite ore collected from Scuddles). Each sample face was sanded with wet and dry sandpaper (400-800 Grit) to remove surface oxide accumulation and hence reduce the contact resistance.

Initial testing of a two electrode system involved painting electrodes across the sample faces with conductive silver paint. Using this method it was possible to measure extremely low values of resistivity (as low as 10^{-4} Ωm). Subsequent work led a more efficient technique; using burnished lead sheet electrodes clamped tightly to opposite faces of the sample (Figure 3.7) insulated by thick blocks of PVC. Resistivity recorded using the silver paint and lead electrodes were comparable to one another.

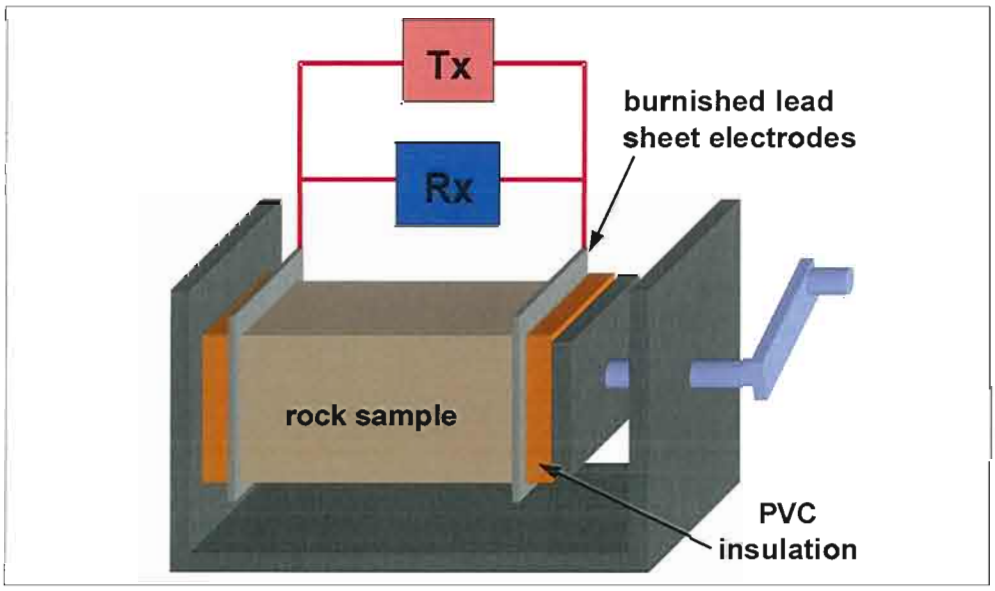

Figure 3.7. Two-electrode measuring system for highly conductive samples, utilising burnished lead sheet electrodes.

3.3.3. Highly resistive rocks

Difficulties were also encountered using the standard four-electrode system for extremely resistive samples (predominantly those collected from the North Parkes deposit). This problem occurs when the resistance of the sample approaches or exceeds the input resistance of the Scintrex IPR-12 (16 MΩ when inactive, ~1MΩ when sampling).

For these problematic samples, resistivity and chargeability were measured using a National Instruments DAQ1200 12 bit PC data acquisition card with time series data recorded using PC software *Labview*. The DAQ1200 has an input impedance of 2GΩ and did not affect current flow for the most resistive samples. The recorded time-series data was stacked and binned into the standard IPR12 windows for comparison with other IPR-12 data.

The DAQ card and PC system were also affected by electrical interference and a Faraday cage was used to attenuate electrical noise around samples. Time series data were sampled at 1000 samples/second and then smoothed using a running average filter prior to binning.

3.3.4. Anisotropy

The geometry of the prismatic samples allowed electrical measurements (resistivity and IP) to be conducted in three orthogonal dimensions, to provide an indication of electrical anisotropy. Hill (1972) and Clark et al. (1988) define electrical anisotropy using a conductivity tensor, which requires measuring a minimum of six differently orientated samples (typically drill core). As the faces of the sample were cut parallel and perpendicular to any planar fabric in the rock (bedding/cleavage/layering), in this case it is assumed the three orthogonal measurements of the sample approximate the three principal axes of resistivity (Figure 3.8).

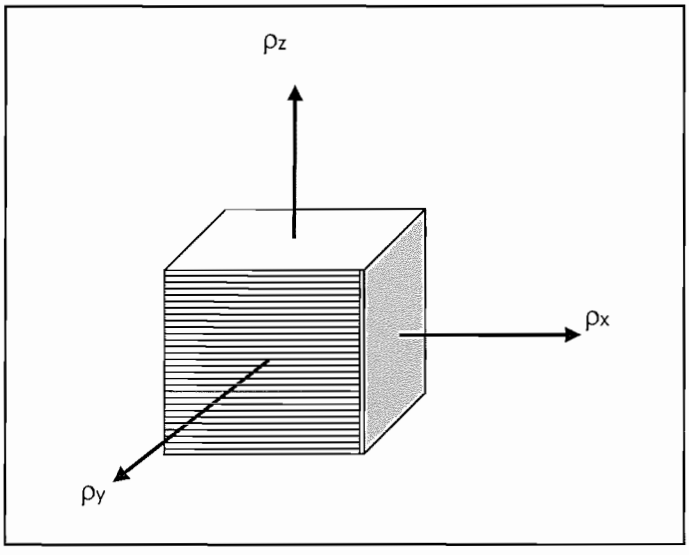

Figure 3.8. Prismatic sample, showing the three different dimensions which anisotropy can be measured. As the sample is cut parallel and perpendicular to planar features, it is assumed the three orthogonal axes approximate the three principal axes of resistivity (ρ_x, ρ_y, and ρ_z).

3.3.5. Current density and non-linearity

Laboratory measurements were conducted at low current densities in order to be equivalent to those used for insitu measurements. A detailed series of measurements were initially conducted on several samples from the Mt Lyell disseminated Cu-Au deposit in western Tasmania, to assess the dependence of resistivity and chargeability on current density. There is significant non-linearity in both the resistivity and chargeability at high currents. Figure 3.9 shows plots of resistivity and chargeability as a function of current density for three orthogonal directions of a Mount Lyell ore sample. For low current densities the sample behaves as an Ohmic conductor and resistivity is generally constant, however above a current density of 0.01mA/m^2 the electrical behaviour becomes non-linear. The chargeability shows minor fluctuations at low currents, but becomes more significantly more variable at higher values (greater than 0.1 mA/m^2).

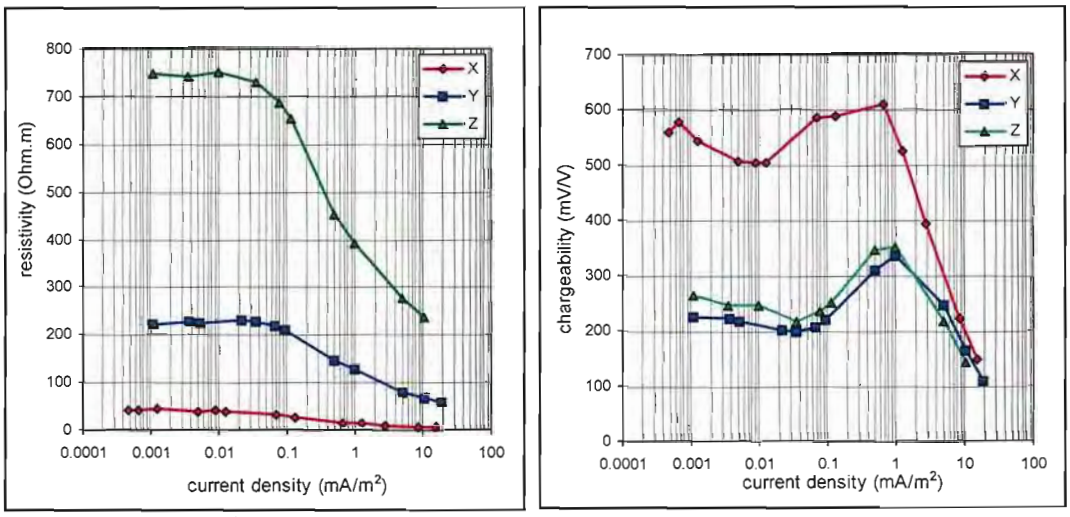

Figure 3.9. (a) Resistivity as a function of current density for a Mount Lyell ore sample (ML32), recorded in three orthogonal directions. Resistivity becomes non-linear for values exceeding 0.01 mA/m^2. (b) Chargeability as a function of current density for a Mt Lyell ore sample (ML32), in three orthogonal directions. Chargeability variations are more irregular, but show a marked decrease above a current density of 0.1 mA/m^2.

Measurements of samples from all deposits were conducted at three low current densities (covering three orders of magnitude) to assess the consistency of resistivity and chargeability measurements. High currents were only necessary for very low resistivity samples. For very low resistivity samples recorded using the two-electrode system chargeability was not recorded, nor possible to detect using the higher currents necessary to provide a measurable signal across the potential electrodes.

Repeatability of measurements was tested for several samples. Data repeatability was within 2% for resistivity and 5-10% for chargeability measurements over several days, but began deteriorating over longer periods, likely due oxidation of the specimens, which generally increases after hydration of the specimen. Galvanic measurements were generally completed soon after specimen preparation (i.e. cutting), to reduce the effects of long-term surface oxidation.

3.3.6. Summary of laboratory techniques

The experimental conditions used for the laboratory measurements are summarised in Table 3.3. Emerson (1969) extensively describes the influence of each of these factors in detail for laboratory electrical measurements.

Factors	Experimental conditions
Electrodes	4 electrode – electrolyte (wet) 1+ Ωm 2 lead electrode system <1 Ωm
Sample Preparation	cut into prism prior to measurement
Measurement errors	Current ±0.1% (accuracy of current meter) Absolute accuracy of Scintrex IPR 12 receiver 1%
Temporal current variations	Monitored current waveform with multimeter and oscilloscope
Current density	Low current densities (nonlinear tests performed) Typically less than 0.1 mA/m^2
Frequency	0.0625 Hz (Tx signal) (4 second on, 4 second off)
Electrolyte composition	Similar to groundwater salinity of deposit (3g/L NaCl added to tap water if unknown)
Electrolyte saturation	48 hours saturation
Pressure	Atmospheric
Temperature	Atmospheric

Table 3.3. Experimental conditions for laboratory electrical measurements of samples. Emerson (1969) discusses the effects of each of these factors in detail.

Chapter 4

Continuity and Current Mapping: New laboratory electrical techniques

4.1. Introduction

The laboratory techniques described in chapter 3 are commonly applied in electrical petrophysical investigations of hand samples and drill-core; however techniques to assess electrical heterogeneity of samples are quite limited. Rauen and Soffel (1995) developed a four electrode technique to measure the electrical resistivity of drill core. The system rotated and ran along the length of the drill-core to provide a measurement of anisotropy and heterogeneity. A non-contact resistivity imaging method for drill-core is described by Jackson et al. (1997) but was only applied to synthetic samples. The resolution of the method was in the order of 5-10 mm.

The methods described in this chapter are refinements of those originally developed by Roach et al. (1997) and Roach and Fitzpatrick (1999) to investigate the relationship between ore textures and electrical parameters. The continuity and current mapping methods assess the local continuity of sulphide and oxide phases and map the distribution of current flow in thin prismatic samples. Both techniques produce images that can be directly related to mesoscopic textural and mineralogical variations of samples. The examples of these techniques provided in this section are for samples from the Peak Cu-Au deposit in New South Wales, and the Mount Lyell Cu deposit in western Tasmania. Continuity and current mapping data of samples from the Scuddles and McArthur River study sites can be found in the respective case study chapters (Chapters 5 and 6). The samples from North Parkes were not suitable for these techniques due to their low total sulphide content (<2%) and random distribution of sulphide grains.

4.2. Continuity Mapping

The continuity mapping system (Figure 4.1) was designed to assess the electrical continuity of individual sulphide phases in a mesoscopic prismatic sample. It can be applied to both resistive disseminated mineralised samples and to conductive samples to identify relative low or high resistance zones.

A schematic diagram is shown in Figure 4.2. A flatbed A3 plotter was modified to hold rock slabs 5 mm to 30 mm thick and up to 270 mm x 160mm. Fixed electrodes are painted along two opposing sides of the slab using silver conductive paint and wires are fixed to the painted electrodes with solder. The plotter mechanism is used to move a weighted or spring-loaded stainless steel or copper electrode in a regular grid across the surface of the sample.

The measured potential across a 1 kΩ resistor in series with the mobile electrode is used to calculate the current flowing through the circuit, the potential between the fixed and moving electrodes, and the resistance between electrodes. The movement of the mobile electrode is controlled by

instructions from the computer (HPGL). A 12-bit analogue to digital converter (ADC) (range 0 to 4.095V) is used to record the potential with a resolution of 1 mV. The voltage recorded is inversely proportional to the sample resistance between the fixed and mobile electrodes. A real-time colour continuity image is provided on the computer, with an ASCII text file generated as an output. These files are simply converted to BIL(band-interleaved-line) images using a simple basic routine. Image processing to enhance features of the continuity image is conducted using *ERMapper*.

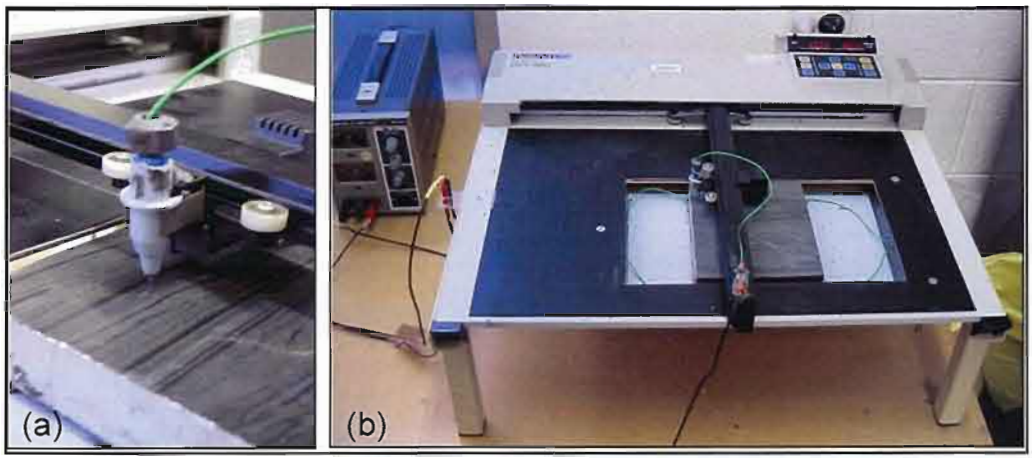

Figure 4.1. Photograph of continuity mapping system (a) electrode; spring-loaded stainless steel pin (b) plotter with sample; the power supply can be seen in the top left of the image.

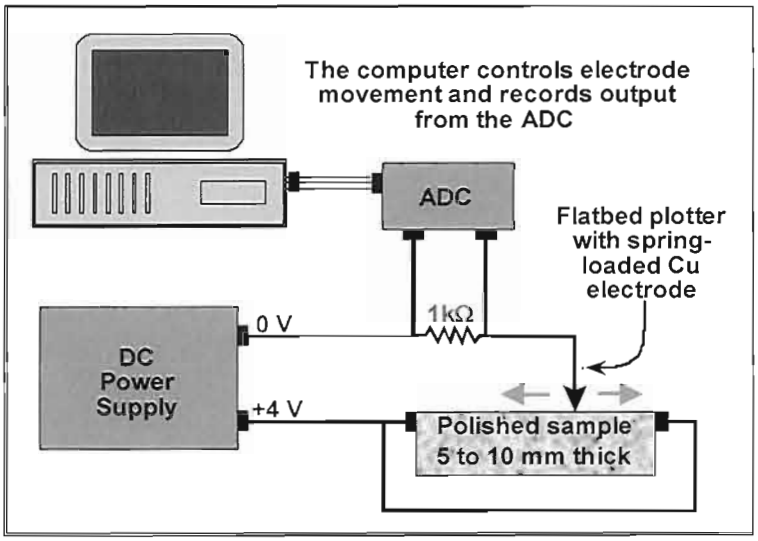

Figure 4.2. Schematic diagram of the continuity mapping system. ADC: Analogue to Digital Converter.

The instrument takes approximately two hours to map a sample of dimensions 150 x 100 mm with a resolution of 0.25 mm. Repeat measurements are effectively identical suggesting that the influence of variable contact resistance between the mobile electrode and rock surface is not significant.

Continuity data are typically presented as pseudocolour images that can be qualitatively and quantitatively compared with mineralogical and textural variations in the ore sample. The values from the analogue to digital converter are typically normalised by the maximum voltage (4.095 V) to present continuity data in percentage units.

A number of electrode configurations can be adopted with this apparatus (Figure 4.3). Most measurements have been completed with a DC potential of +4V applied to fixed electrodes located on opposing edges of the sample. Samples are usually orientated so any structures or fabric in the sample are aligned perpendicular to the fixed electrodes.

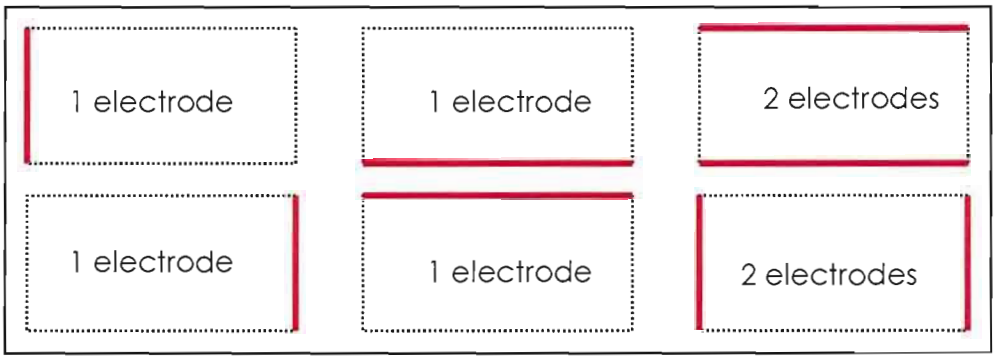

Figure 4.3. A number of different electrode configurations can be used for continuity mapping system (red line). The 2 electrode configuration (bottom right) was used throughout the study.

Continuity maps with different electrode configurations for a sulphide sample from the Mt Lyell disseminated Cu-Au deposit in western Tasmania is shown in Figure 4.4. The sample consists of irregular disseminated pyrite and chalcopyrite in an altered volcanic matrix (Figure 4.4a). The optical image of the sample was classified using an image processing system to clearly illustrate the distribution of sulphide grains (38% from the classified image), although it was not possible to differentiate between pyrite and chalcopyrite (Figure 4.4b). The three continuity images (each with different electrode positions; Figure 4.4 c, d, & e) illustrate the potential measured across the series resistor with red indicating a high potential hence, low sample resistance. Black zones (nulls) in the image indicate areas of silicate and feldspar minerals with extremely high sample resistance (>4 MΩ). The intensity of the continuity image reflects variable sample resistance. The continuity images clearly show that a proportion of the sulphide grains are electrically connected to the corresponding electrodes. The two single electrode images illustrate the electrical continuity of the sulphides extends for only two to three centimetres from the fixed electrodes, despite the sulphides being dispersed throughout the entire sample.

A continuity map for a high-grade chalcopyrite-galena sulphide ore from the Peak Pb-Zn-Cu-Au deposit, New South Wales is shown in Figure 4.5. The sample consists of chalcopyrite, pyrrhotite and galena within a matrix of sheared metasediments. The optical image of the sample (Figure 4.5a) was classified to illustrate the distribution of sulphides (Figure 4.5b).The following classes were generated: chalcopyrite, pyrrhotite, galena, and metasediments. The continuity image for this sample is shown in Figure 4.5c with a linear colour distribution applied to the image. A histogram equalised colour distribution has been applied to the image in Figure 4.5d. The continuity image (Figure 4.5d) shows the sample is well connected, but different sulphide phases and textures are reflected by differences in the measured potential. The least resistive zones, shown in red predominantly reflect the pyrrhotite, moderate zones (yellow-blue) reflect the chalcopyrite (and the large galena aggregate located within the centre of the specimen). Black zones in the image indicate areas of metasediments, with extremely high sample resistance (>4 MΩ).

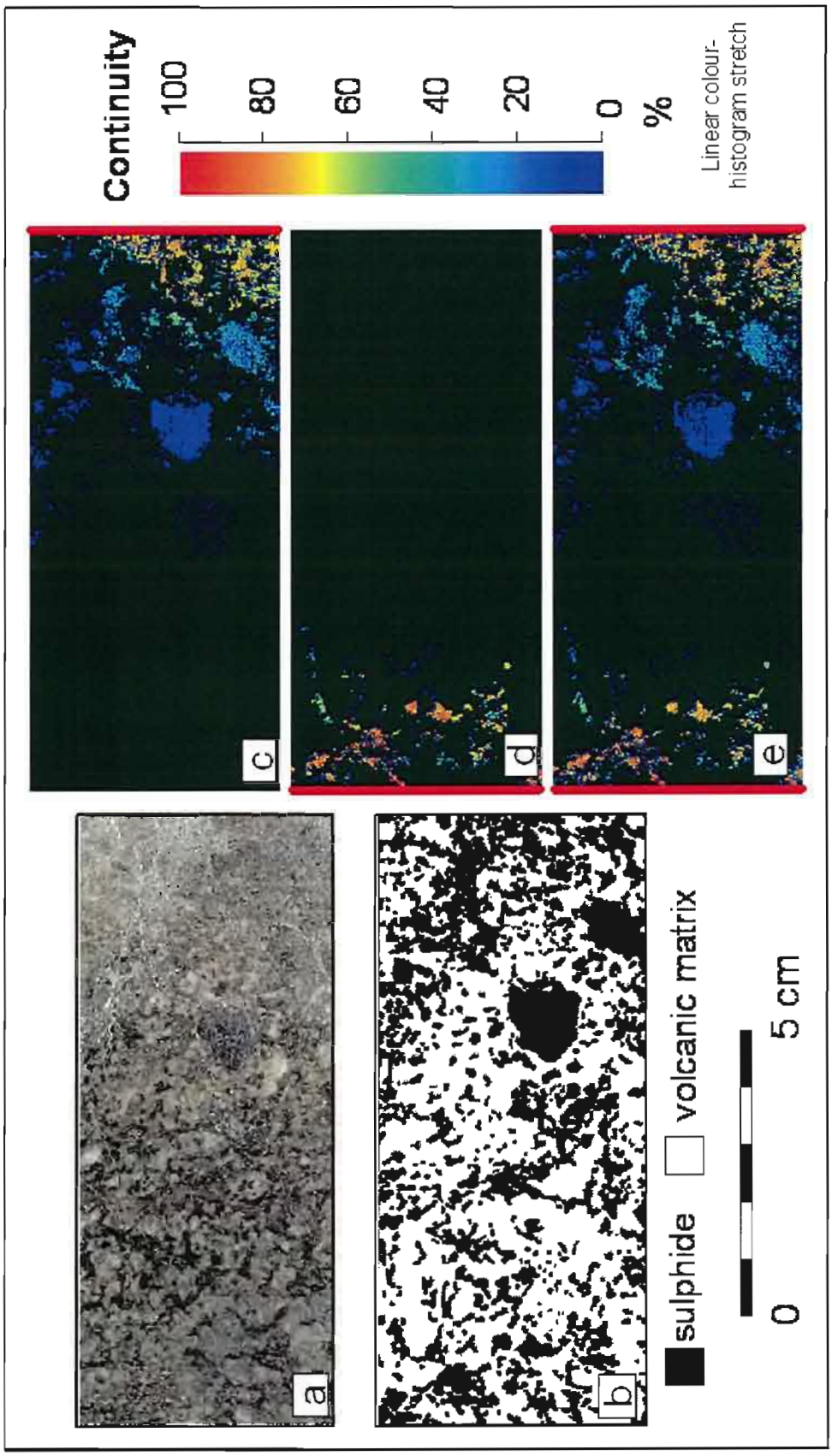

Figure 4.4. Continuity mapping results for a disseminated pyrite-chalcopyrite ore sample from the Mt Lyell deposit, western Tasmania. (a) Optical image of ore sample. (b) Classified optical image illustrating distribution of sulphide minerals within the volcanic host. (c, d, e) Continuity images of sample, with different electrode positions (marked with red lines). Electrical continuity of the sulphides only extends 3 to 4 cm from the fixed electrodes. Continuity images are displayed with a linear histogram colour stretch.

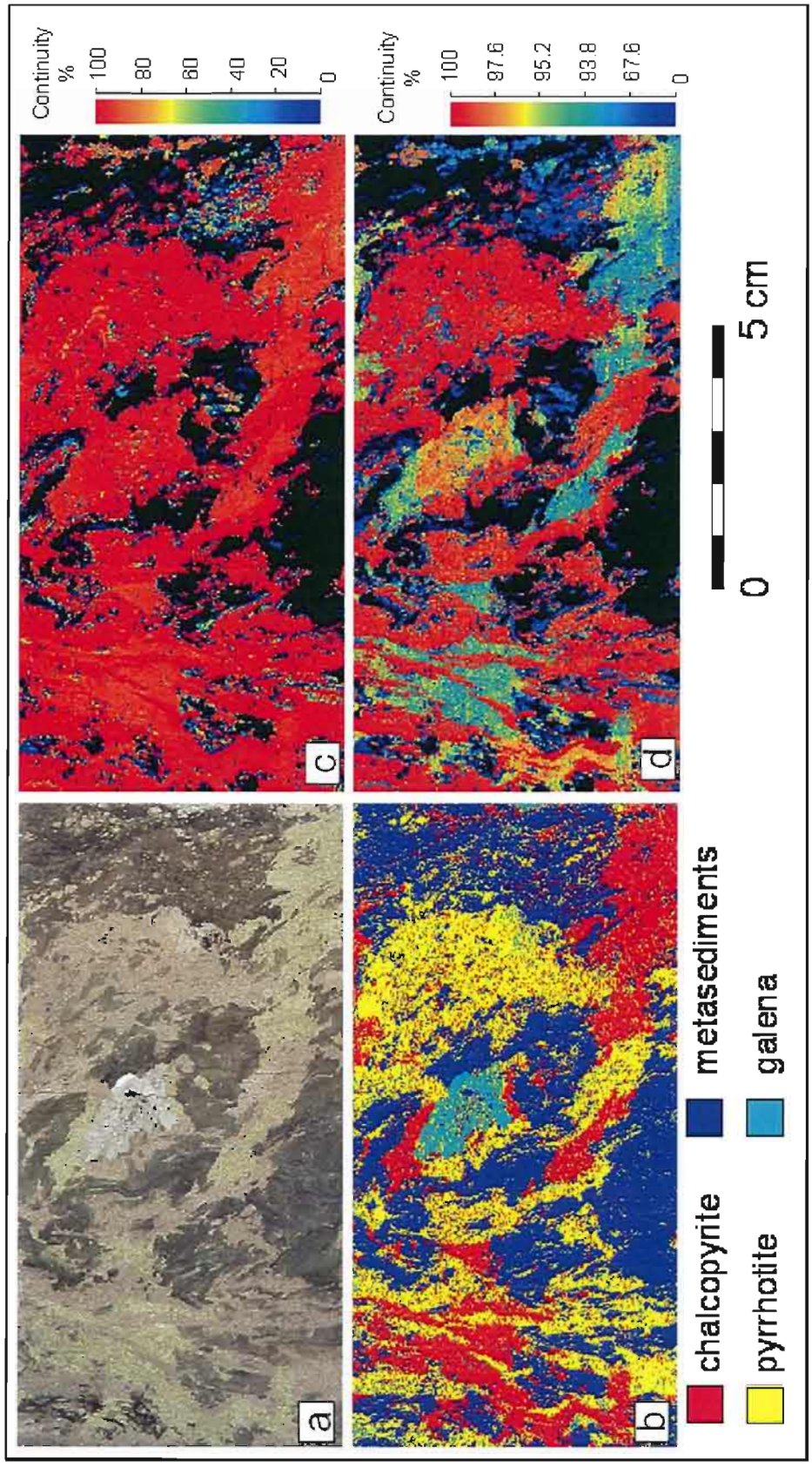

Figure 4.5. Continuity mapping results for a sample (PK10) of massive base metal ore sample from the Peak deposit, New South Wales. (a) Optical image of the sample illustrating various sulphides. (b) Classified image of photograph showing different minerals. (c) Continuity map for the sample shown in 'a', with a linear colour scale, between 0 and 100% output. Image appears mostly red reflecting the highly conductive nature of sample; black areas (nulls) indicate areas of quartz. (d) Continuity map, with histogram equalized colour distribution applied. Non conductive zones appear black. The relative variations in the continuity map correlate to the different sulphide phases, shown in (b).

Continuity images such as Figure 4.4 and Figure 4.5 provide a clear visual representation of the degree of continuity of sulphides within a sample, but to be able to compare continuity images to other conventional petrophysical, textural or chemical criteria it is first necessary to derive quantitative statistics from each image. The simplistic statistic that can be defined for each sample is the "sample continuity" which is defined as:

$$\text{sample continuity} = \frac{\text{mean of all image pixels (mV)}}{\text{maximum possible value (4000 mV)}} \times 100 \qquad (4.1)$$

The sample continuity will vary due to both the proportions of sulphide minerals in the sample and the degree to which the sulphide minerals are connected. A better statistic, which largely removes the dependence on the volume percentage of sulphide material present, is to calculate the mineral continuity. This implements the formula above only for the pixels in the image which are classified as sulphide or alternatively for each individual sulphide mineral present.

The process involves acquiring a photographic image of the sample, which is then classified to differentiate the different minerals/assemblages where possible. A supervised maximum likelihood classification is typically used to generate the classified image. The optical classification is only effective where there are clear differences in colour and reflectivity between minerals and for this reason it is not always possible to uniquely classify individual minerals.

From the classified image, a series of binary masks are generated to represent a single mineral component. Multiplication of each binary mask by the raw continuity image produces an output image where all non-null values belong to the same image class and hence to the same mineral in the sample.

The mineral continuity is then calculated from the mean of all the non-null pixels in the image. The output will be percentage continuity where 100% indicates that all grains of a particular mineral are very well connected. A value of 0% implies no grains are connected. The mineral continuity is defined as:

$$\text{mineral continuity} = \frac{\text{mean of single component (mV)}}{\text{maximum possible value for single component area (4000 mV)}} \times 100 \qquad (4.2)$$

An example of mineral continuity images is shown in Figure 4.6 using the same Peak sample presented in Figure 4.5. The mineral continuity for the entire sample and each mineral phase is listed in Table 4.1. In the example illustrated, the pyrrhotite is almost maximally connected. The image in Figure 4.6f, shows the continuity image for the area classified as volcaniclastic sediments. Although these should be completely null, zones of continuity indicate magnetite, which was not classified separately from the original optical image, and was included in the volcaniclastic class.

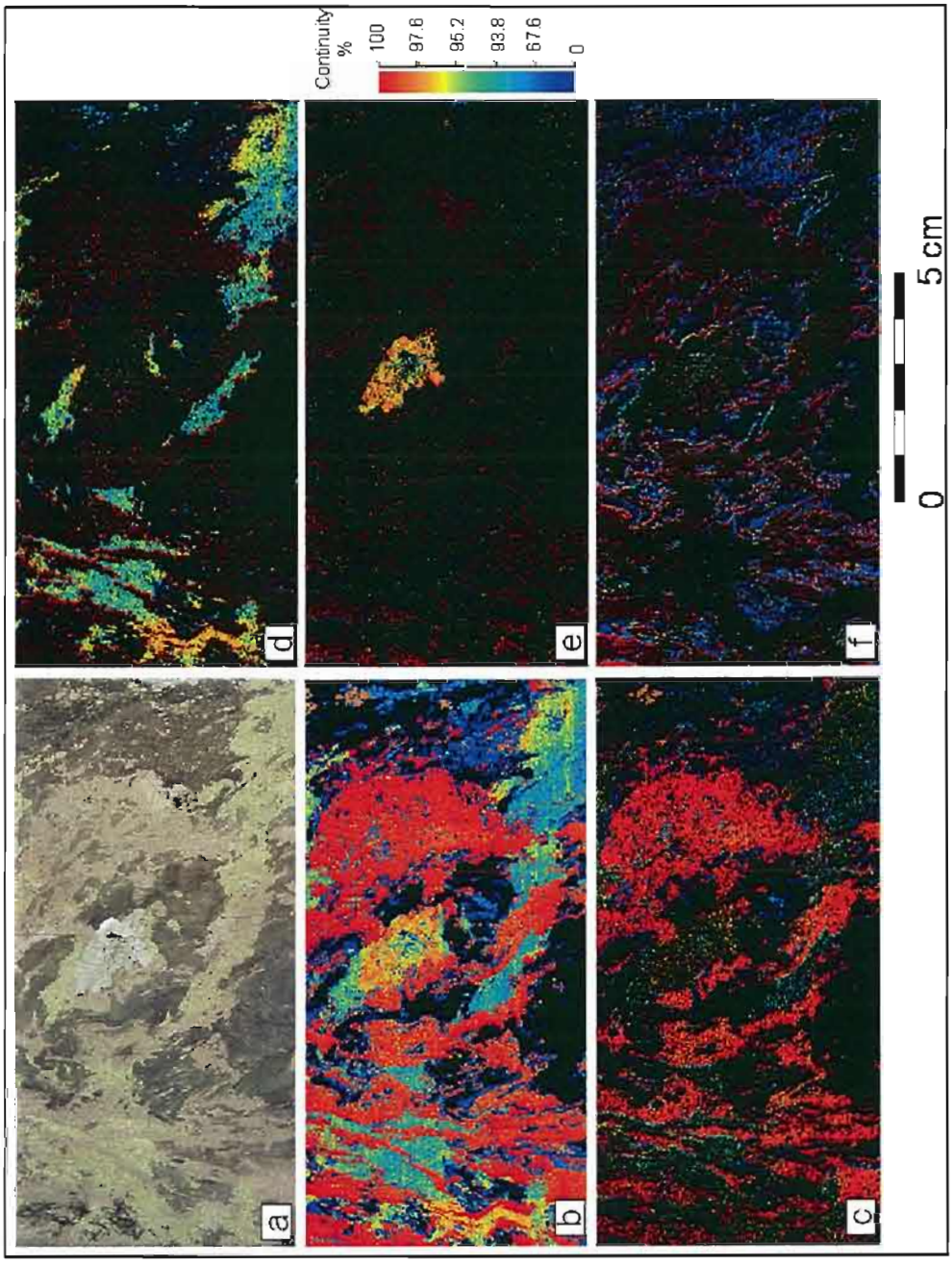

Figure 4.6. Continuity mapping results for a sample and classified mineral phases for the massive base metal ore sample (PK10) from the Peak deposit, New South Wales. (a) optical image. (b) continuity image of entire sample. Continuity results for (c) pyrrhotite; (d) chalcopyrite; (e) galena; and (f) metasediments and magnetite (classified as one unit). Continuity images all shown with the same equalised histogram colour-stretch.

Sample/Mineral	Mineral continuity (%)
Entire sample	79.5
Chalcopyrite	86.9
Pyrrhotite	89.3
Galena	88.5
Volcaniclastics/magnetite	55.3

Table 4.1. Mineral continuity for Peak sulphide sample presented in Figure 4.5.

4.3. Current Mapping

Current mapping is a small-scale application of the magnetometric resistivity (MMR) technique utilising a small receiver coil to sense the magnetic fields generated by the primary current flow through the sample. It can be applied to moderate to highly conductive samples to assess the path of current through the sample and its relationship to mineral constituents.

A schematic diagram for the mesoscopic current mapping system is shown in Figure 4.7. The same plotter used for continuity mapping is utilised for current mapping. A small (3mm) ferrite-cored coil receiver is placed in the plotter mechanism positioned approximately 1mm above the sample surface (Figure 4.8). A 10 kHz sine wave signal is passed directly through the sample via fixed silver paint electrodes. The primary magnetic field generated by current flow through the sample induces a sinusoidal potential in the receiver coil. An absolute value rectifier (AVR) converts this signal to direct-current prior to digitisation. The output from the coil sensor depends on the magnitude and direction of current flow within the sample and on the orientation of the coil.

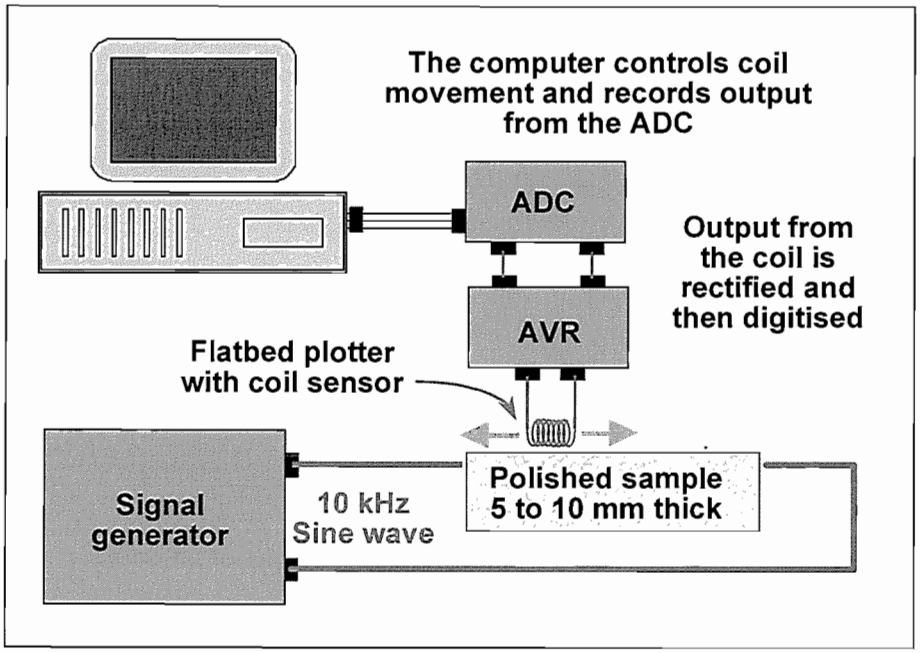

Figure 4.7. Schematic diagram of mesoscopic current mapping apparatus. The moving coil sensor has a cylindrical tip with diameter of 3mm. ADC: Analogue to Digital Converter; AVR: Absolute Value Rectifier.

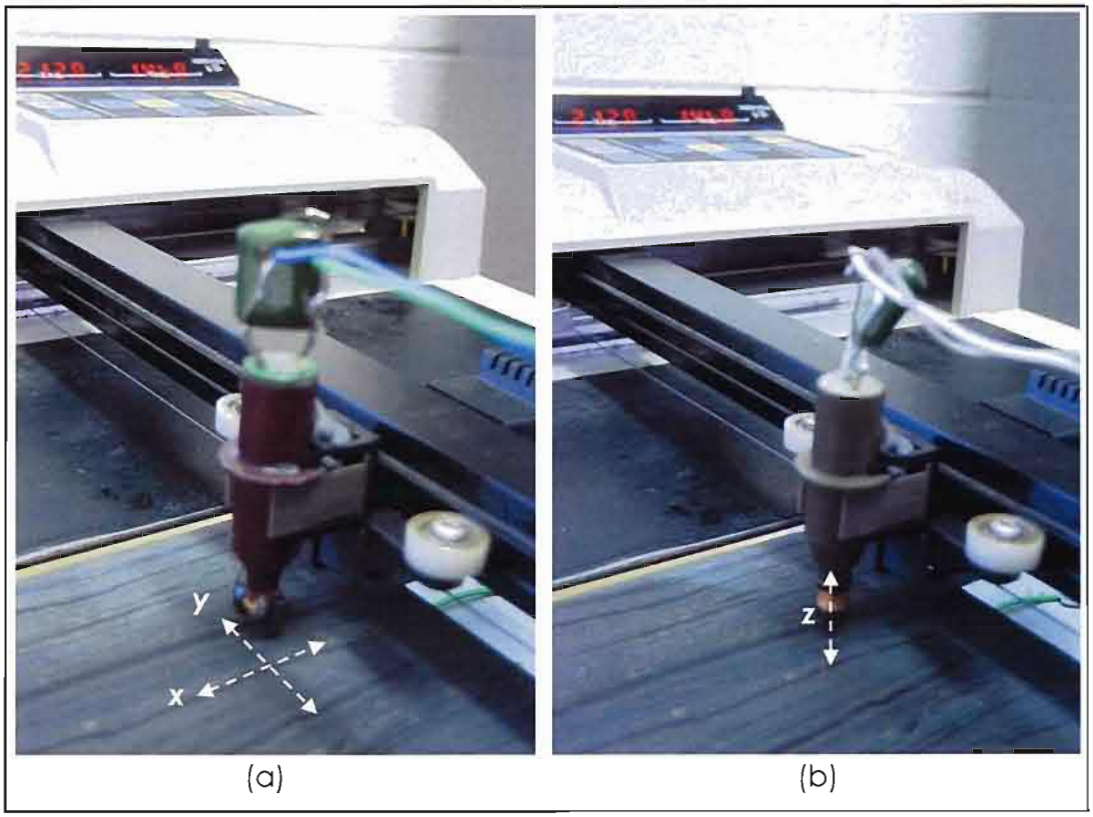

Figure 4.8. Receiver coil in current mapping system; (a) y component shown, rotated 90 degrees for x direction; (b) z component.

Prior to collection of a current map, an oscilloscope is used to monitor and measure the amplitude of the transmitter waveform from the signal generator. Measurements are completed across the sample and the amplitude of the waveform is adjusted appropriately to provide an optimal signal from the receiver coil; within the 0 to 4 volt input range of the analogue to digital converter. The measured peak to peak voltage from the signal generator is entered and recorded into the acquisition program.

The response recorded by the ADC depends on the electromagnetic coupling of the system which is determined by the direction of the current flow and the orientation of the sensor coil.

The sensor coil can be orientated to collect one of the three components of the primary field (Figure 4.8). For current flow through the sample in the x direction, little or no signal will be recorded for the x axis coil, maximum signal will be recorded immediately over the conductor for the y axis coil and a minimum with flanking highs will be apparent for the z coil. The y and z components maps are commonly used in identify the prominent current pathways.

Current mapping data for each coil orientation are typically presented as pseudocolour images that can be visually compared with mineralogical and textural variations in the ore sample, and with the electrical continuity data. The images are typically presented with an auto-clipped linear histogram stretch, to highlight only the relative variations within the data recorded.

While it would be possible to invert these three component magnetic field images to produce a "true" quantitative maps of current or resistivity, this has not been attempted, as in almost all cases the main paths of current flow are

usually readily apparent from the component images. The emphasis of this work has been on the qualitative interpretation of the relationship between ore textures and current flow and the magnetic component images are sufficient for this purpose.

The current path through the sample is also affected to some extent by the connections to the fixed electrodes (Figure 4.9); hence wires were connected to the bottom corners of the sample to reduce their bias and to be systematic (Figure 4.9b). A range of electrode configurations can be applied, and the two opposing electrode configuration was adopted for all measurements within this study.

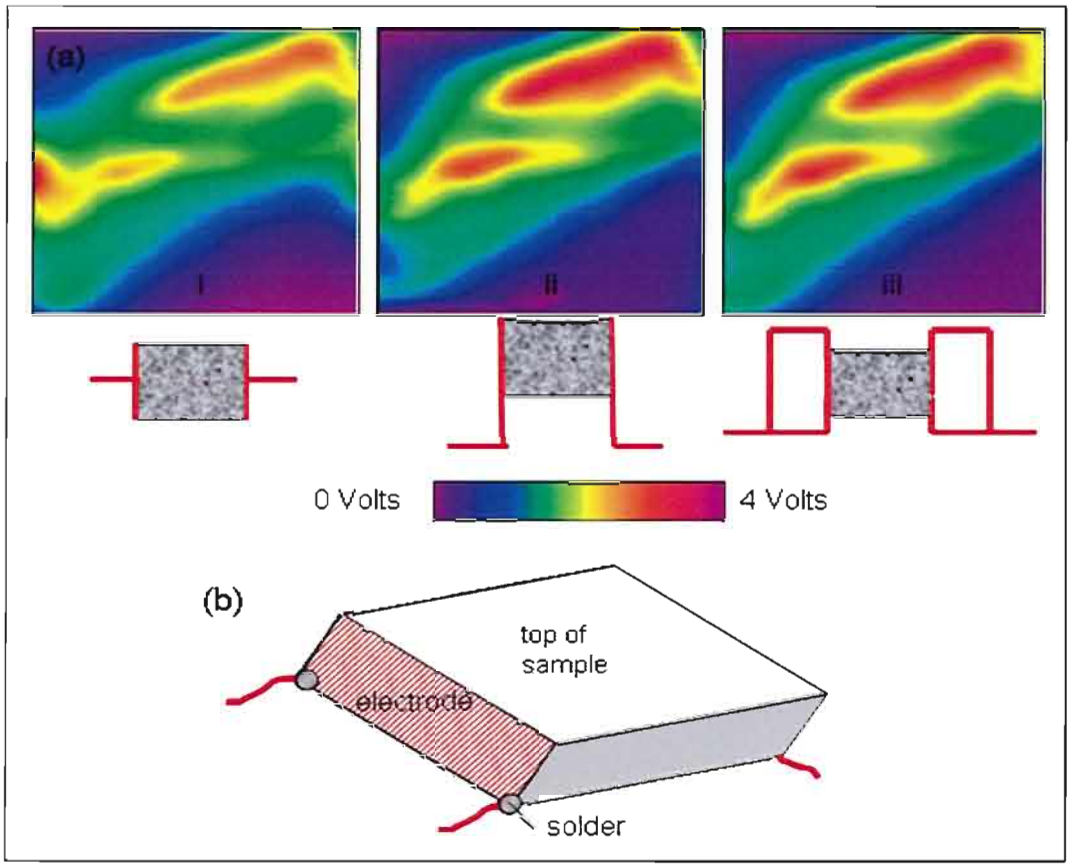

Figure 4.9. (a) The current mapping system was sensitive to where the wires were connected to the fixed electrodes. Configuration 'iii" was used for all measurements. (b) Wires were connected to the bottom corners of the sample to minimise their influence.

An example of current mapping of the Peak ore sample used to illustrate continuity mapping (Section 4.2) is shown in Figure 4.10. The current images show a complex current pathway through the sample. The current images show a well-defined coincident 'y' component maximum and 'z' component null extending horizontally though the sample.

Although these anomalies correspond to the distribution of the massive pyrrhotite and chalcopyrite veins within the resistive metasediments, the current equally flows through the disseminated sulphides located on the right side of the sample, extending 2 cm from the fixed electrode. The x component image which is primarily sensitive to current flow in the y direction shows an unusual distribution, reflecting the complex nature of sulphide veining.

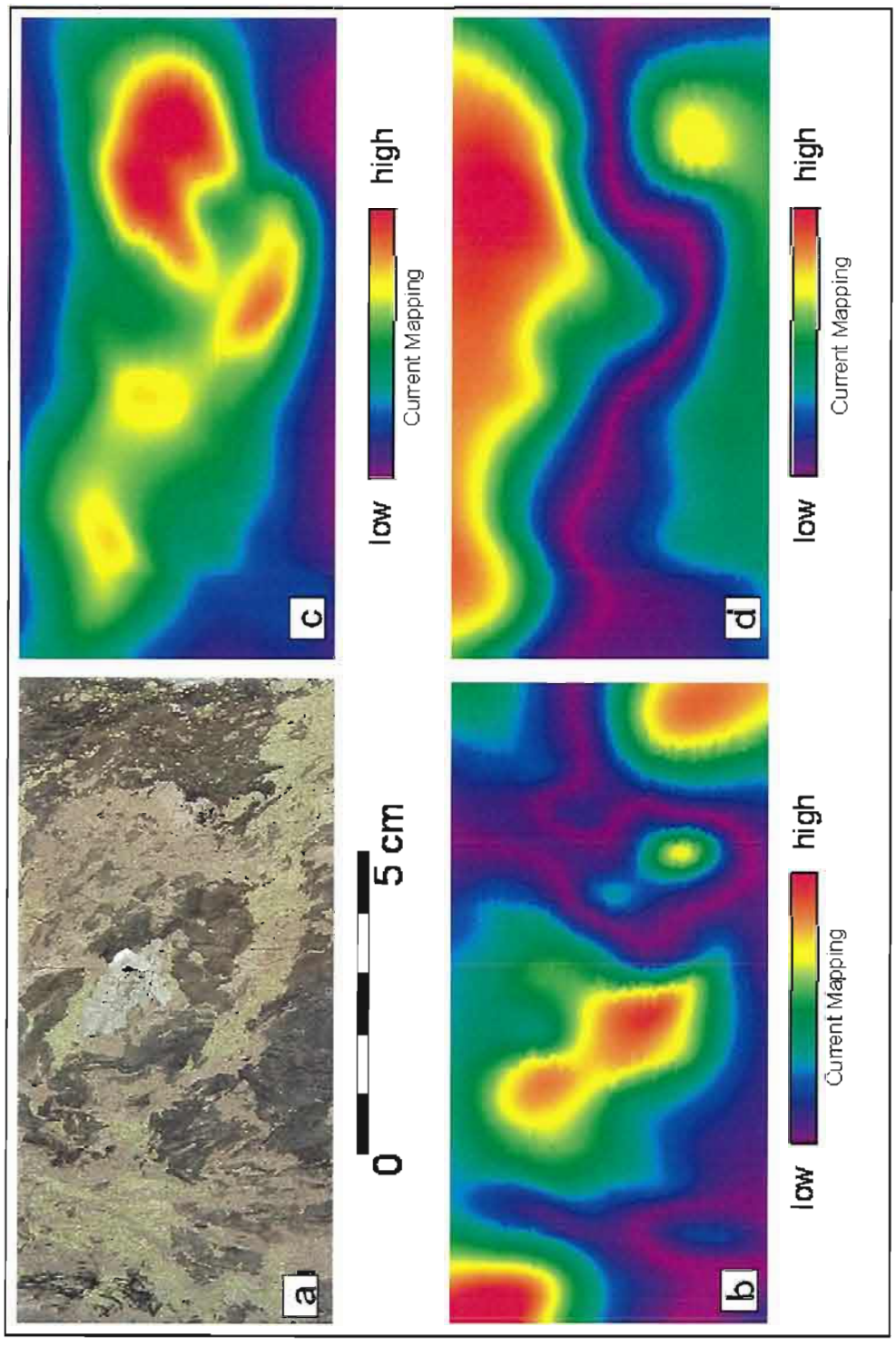

Figure 4.10. Current mapping results for a sample of massive base metal ore sample (PK10) from the Peak deposit, New South Wales (from Figure 4.5, 4.6). (a) optical image. Current mapping images for (b) X, (c) y and (d) z receiver coil orientations. The 'y' maximum and 'z' minimum in current maps (c and d respectively) best illustrate the current flow-path through the sample. Current maps are shown with a linear colour stretch clipped to 99% of the input data (for each image).

The following discussion provides several more examples of using continuity and current mapping on sulphide ore samples;

Continuity and current mapping results for a chalcopyrite ore sample from the Mt Lyell deposit, western Tasmania are shown in Figure 4.11. The sample consists of foliated quartz chlorite schist with white carbonate segregations sub-parallel to foliation. Sulphides (pyrite and chalcopyrite) are abundant in elongate domains, parallel to foliation. The optical image of the sample (Figure 4.11a) was classified to illustrate the distribution of the sulphides (Figure 4.11b). A simple binary classification was generated: sulphides (chalcopyrite and pyrite) and non-sulphides (quartz and chlorite schist), as the image classification was unreliable in identifying chalcopyrite from pyrite. The continuity map (Figure 4.11c) clearly identifies the distribution of sulphides veins within the quartz-chlorite material. The red zones correspond to chalcopyrite rich material, the yellow-blue colours reflect the distribution of pyrite, and black zones (nulls) reflect the quartz and chlorite sediments. The current images show a well-defined coincident 'y' component maximum (Figure 4.10e) and 'z' component minimum (Figure 4.10f) corresponding to the main chalcopyrite veins running through the sample, as expected.

Continuity and current mapping results for a chalcopyrite-sphalerite ore sample from Peak Au deposit, New South Wales, consisting of quartz, sphalerite, chalcopyrite and pyrrhotite in a matrix of sheared metasediments are shown in Figure 4.12. The optical image of the sample (Figure 4.12a) was classified to illustrate the distribution of sulphides (Figure 4.12b).The following classes were generated: chalcopyrite, sphalerite, magnetite and metasediments. The continuity map (Figure 4.12c) clearly identifies the distribution of different sulphide minerals within the samples. Red values indicate pyrrhotite, yellow areas correspond to chalcopyrite, blue areas correspond to magnetite and black zones reflect the resistive metasediments. The current mapping images (Figure 4.12 d, e and f) show a well-defined coincident 'y' component maximum and 'z' component minimum (null) corresponding to a combination of a connected pyrrhotite-chalcopyrite vein located in the lower end of the sample. In addition, a smaller current path is detected running in a pyrrhotite vein located in the top section of the sample.

4.4. Summary

The continuity and current mapping techniques supplement the existing range of laboratory electrical petrophysical techniques. Both methods provide graphic illustration of the influence of ore textures on the electrical properties of sulphide ore samples.

Continuity mapping can be used to assess the local continuity of sulphide phases, while current mapping can directly map the distribution of current flow within thin prismatic samples. The results can be directly compared to optical images of the samples to provide a better understanding of the factors that influence the electrical properties of sulphides ore bodies.

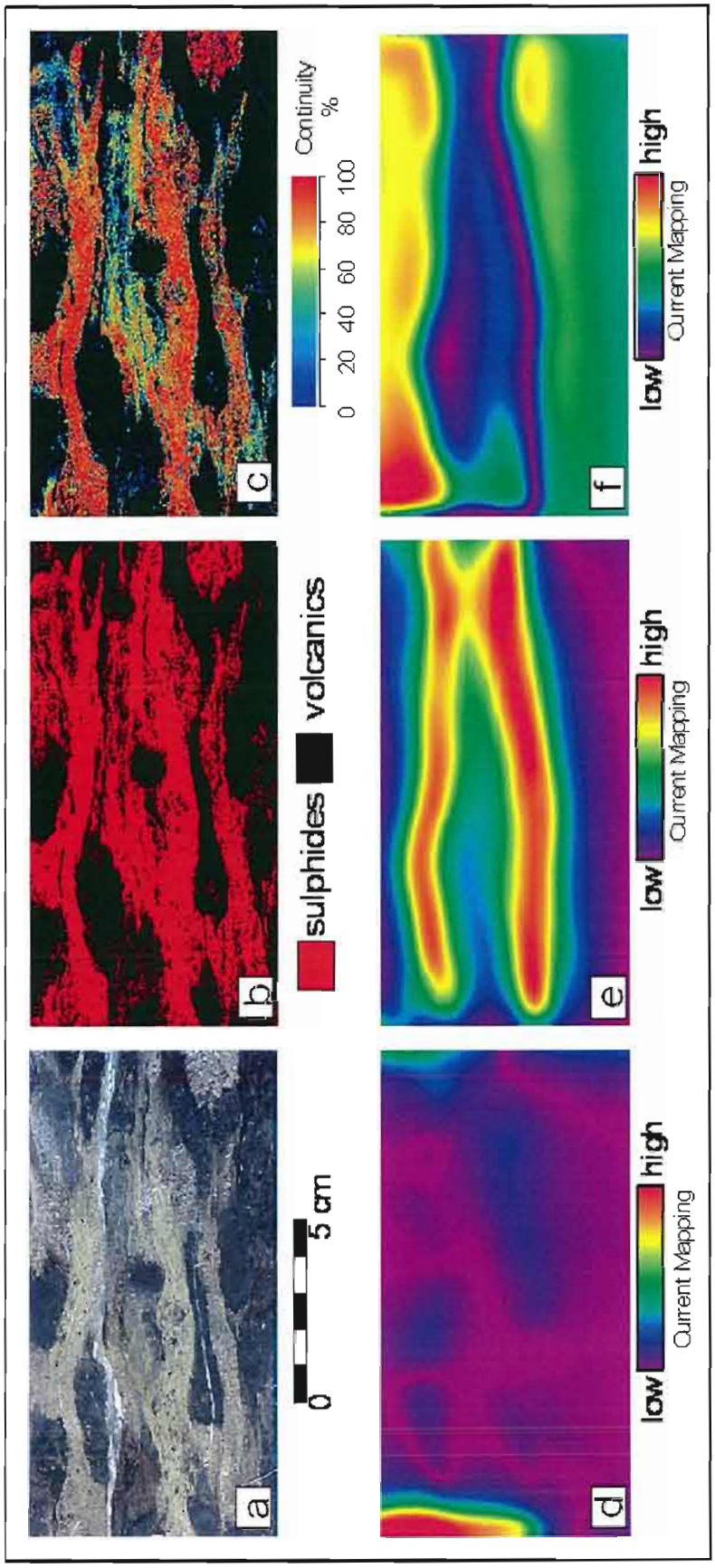

Figure 4.11. Continuity and current mapping results for a sample of massive sulphide ore from the Mt Lyell Copper deposit, western Tasmania. (a) Optical image. (b) Classified optical image illustrating distribution of sulphide minerals within the volcanic host. (c) Continuity image (linear colour stretch). (d) Current mapping images of sample for X (d), Y (e) and Z (f) receiver coil orientations. The 'y' maximum and 'z' minimum in current maps (e and f respectively) best illustrate the current flow-path through the sample. Current maps are shown with a linear colour stretch clipped to 99% of the input data (for each image).

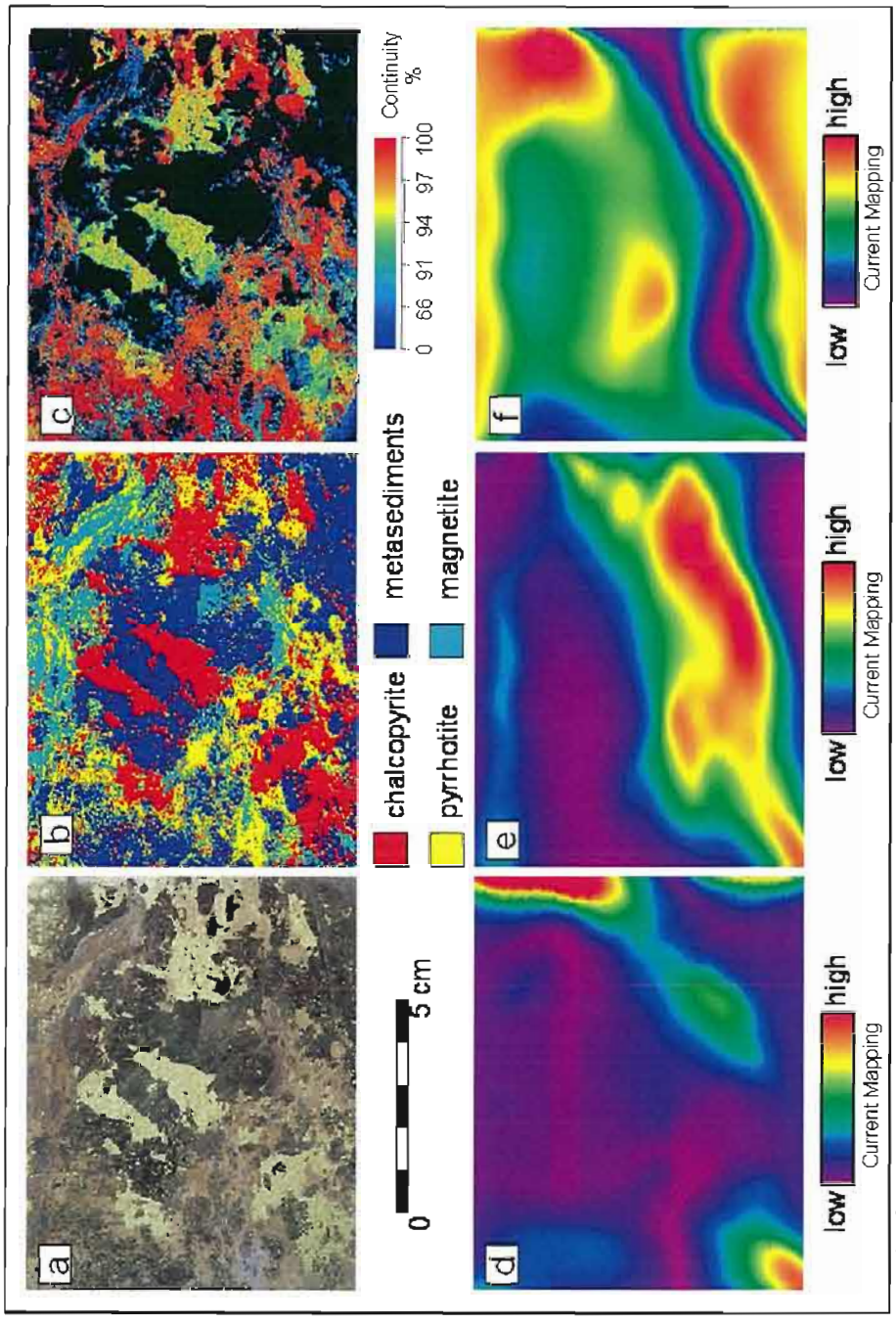

Figure 4.12. Continuity and current mapping results for a sample of massive sulphide ore from the massive base metal ore sample (PK22) from the Peak deposit. (a) Optical image. (b) Classified optical image illustrating distribution of sulphide minerals within the volcanic host. (c) Continuity histogram equalized image. (d) Current mapping images of sample for X (d), Y (e) and Z (f) receiver coil orientations. The 'y' maximum and 'z' minimum in current maps (e and f respectively) best illustrate the current flow-path through the sample. Current maps are shown with a linear colour stretched clipped to 99% of the input data (for each image).

Chapter 5

An electrical study of the Scuddles massive sulphide ore system

5.1. Introduction

This chapter describes the electrical characteristics of the Golden Grove-Scuddles copper-zinc-lead deposit and its host sequence. The Scuddles ore body provided an excellent example of a classic volcanic-hosted massive sulphide (VHMS) deposit (Lydon, 1988; Humphreys et al., 1991) consisting of an extensive mineralised stringer zone, overlain by iron-rich and copper rich massive sulphides and an upper zinc-rich zone. The mine's underground production facilitated easy access to the wide variety of ore types and textures exhibited by the Scuddles deposit. Sites and samples investigated include the volcanic host sequence, chalcopyrite stringer zones, barren pyrite zones, massive chalcopyrite-pyrite mineralisation, and massive pyrite-sphalerite mineralisation.

Insitu electrical and laboratory measurements were conducted at Scuddles to examine the effect of scale of investigation and their implications for the exploration of such targets using electrical geophysical techniques. The field methodology and laboratory techniques are described in Chapter 3. Geochemical and petrographic analyses of the hand specimens provide additional quantitative and qualitative data for a comparative discussion of the results. Magnetic susceptibility measurements collected insitu and on hand specimens supplement the petrophysical database of the deposit.

5.2. Geological Setting

The Golden Grove ore deposits are located approximately 370 kilometres north-north-east of Perth, Western Australia (Figure 5.1) and are situated in the Achaean Warriedar greenstone belt of the Yilgarn Craton.

The Warriedar greenstone belt is a tectonic unit of supracrustal rocks bounded by intrusive granitoid batholiths (Mill et al., 1990) (Figure 5.2). The unit consists of a mix of metamorphosed felsic and volcanic rocks, volcaniclastic and pelitic sedimentary rocks and banded iron formations (Boyd and Frankcombe, 1994). Several generations of rhyolitic and dolerite dykes crosscut this sequence, which is further disrupted by a series of NNE to NE trending faults.

The Golden Grove ore deposits lie on the northeast flank of the Warriedar Fold-belt on the eastern limb of a major syncline, with stratigraphy dipping steeply to the west. The Golden Grove domain has been metamorphosed to biotite grade greenshisct facies (Sharpe, 1999) with original textures preserved in some of the volcanic and sedimentary rocks (Mill et al., 1990).

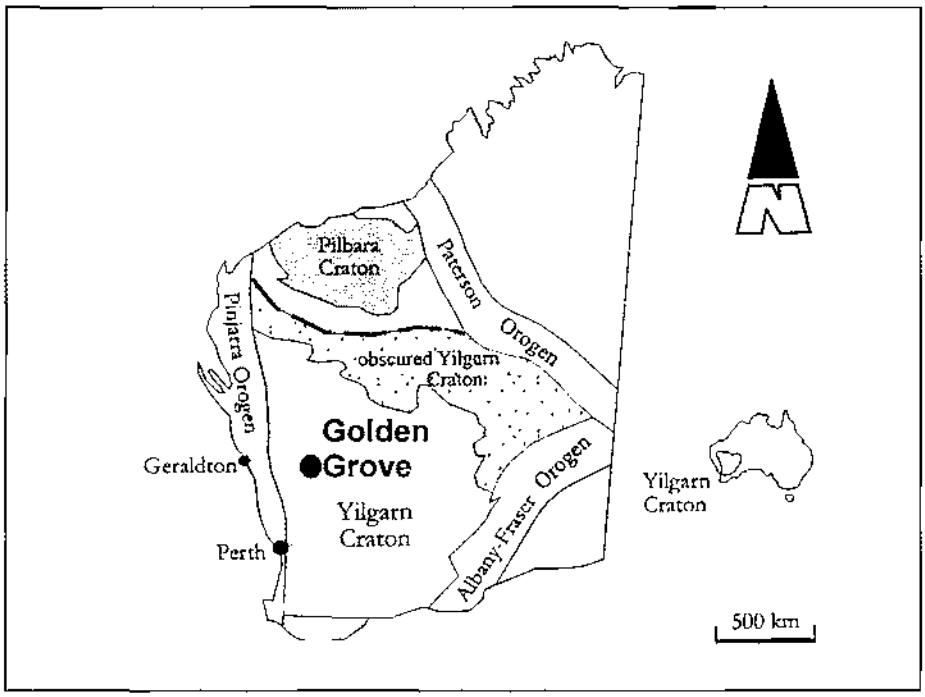

Figure 5.1. Golden Grove (Scuddles) location map (modified from Sharpe, 1999).

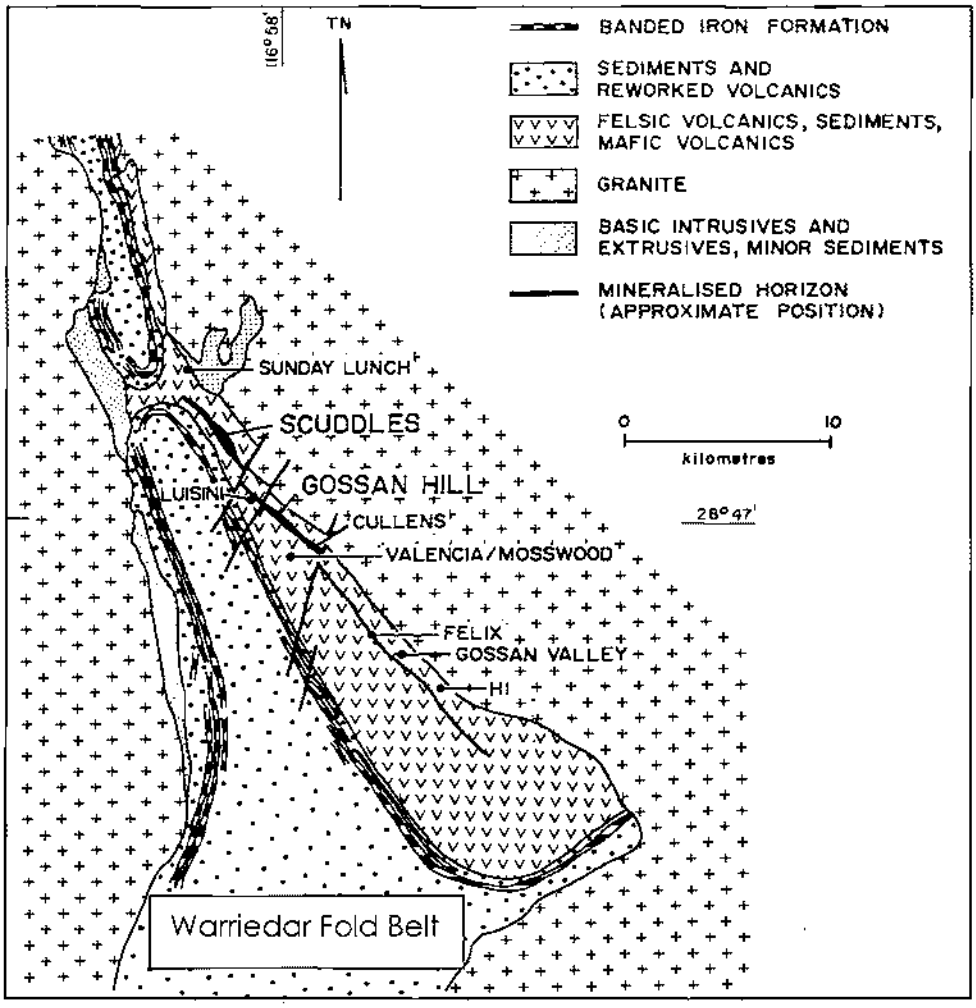

Figure 5.2. Regional geology of the Warriedar Fold Belt (from Mill et al., 1990). The Golden Grove ore deposits; Scuddles and Gossan Hill lie on the flank of the Warriedar greenstone belt on the eastern limb of a major syncline. Stratigraphy dips steeply to the west.

Detailed stratigraphy (Figure 5.3) of the Golden Grove locality is described by Clifford (1992) and Sharpe (1999). Mineralisation occurs within the Golden Grove Formation of the Gossan Hill Group within a sequence of felsic and intermediate volcaniclastic rocks and minor epiclastic units. The thickness of the Golden Grove formation varies from 175 to 800 metres.

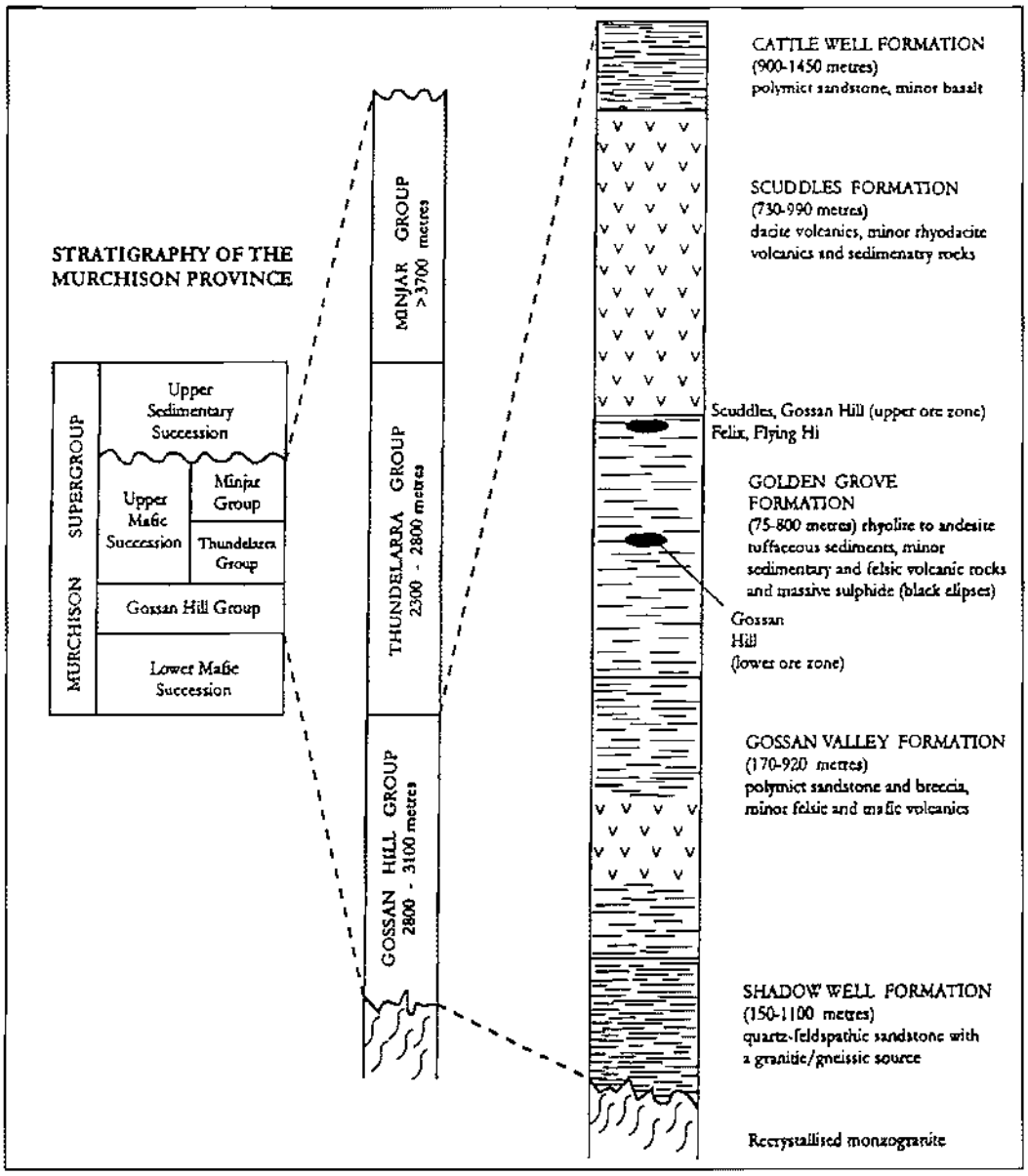

Figure 5.3. Generalised stratigraphic column for the Golden Grove area, showing locations of Scuddles and Gossan Hill mineralisation (from Normandy, 1999).

Two economic deposits are located at Golden Grove (Figure 5.4); Scuddles and Gossan Hill separated by four kilometres. The Gossan Hill deposit consists of two discrete sub-vertical ore zones, and outcrops as a prominent gossan. The top of the economic mineralisation of the Scuddles ore body lies 140 metres below the surface in an area of little or no topographic relief. Gossan Hill was discovered in 1971 (Humphreys et al., 1991) during regional exploration and Scuddles in 1979 as result of a combined geophysical and geochemical exploration campaign (Boyd and Frankcombe, 1994). The deposit was originally identified as an aeromagnetic anomaly and subsequently tested using down-hole EM. The Scuddles mine commenced production in 1990 and Gossan Hill became operational in 1998.

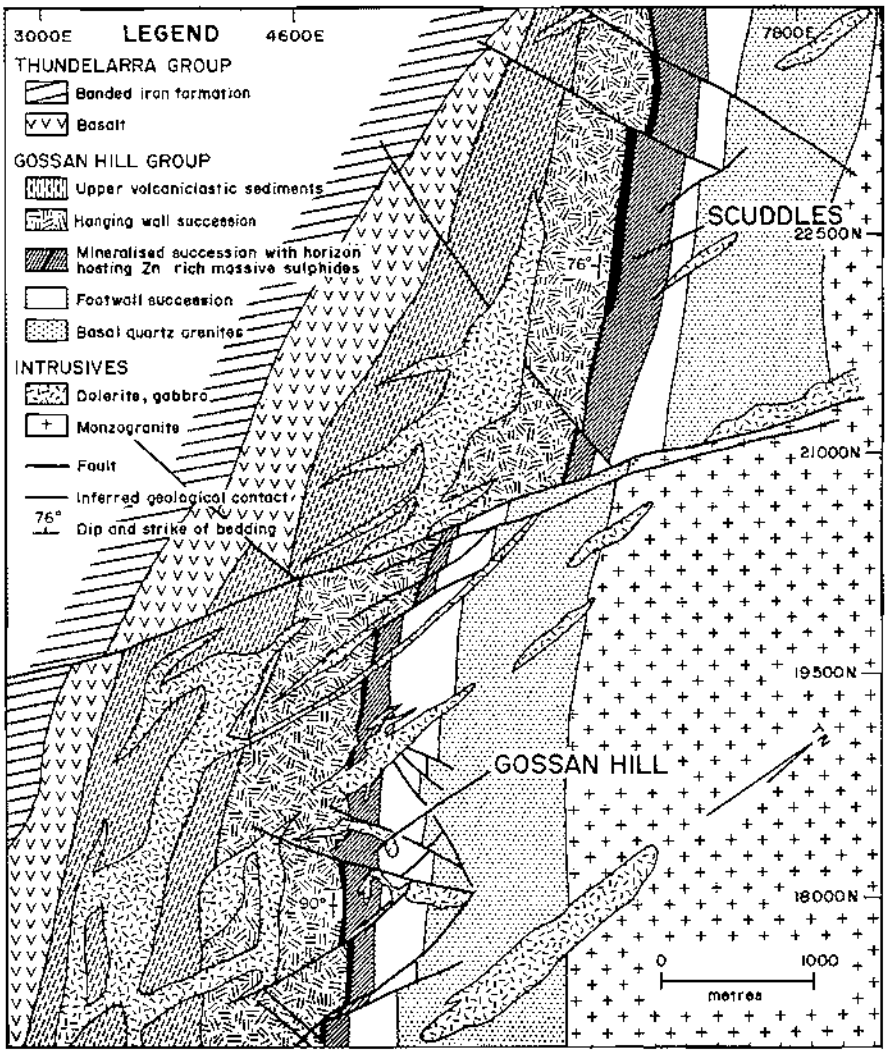

Figure 5.4. Simplified local geology of the Golden Grove area showing the location of the Scuddles and Gossan Hill deposits (from Mill et al., 1990)

Stratabound mineralisation at both sites occurs at a single stratigraphic interval near the top of the Golden Grove Formation and exhibits many features characteristic of classic volcanic-hosted massive sulphide (VHMS) mineralisation including an upper zinc-rich zone underlain by iron-rich and copper-rich massive sulphides. An extensive stringer-stockwork zone underlies the massive sulphide mineralisation.

Cross-cutting copper-rich mineralisation occurs at a lower stratigraphic level within the Golden Grove Formation at Gossan Hill, where it is closely associated with lenses of massive and disseminated magnetite (Sharpe, 1999). At Scuddles, epigenetic copper mineralisation crosscuts the stratabound mineralisation in a number of zones. Additional supergene copper and oxide gold resources are also located in the near surface above the Gossan Hill deposit.

Pre-mining resources for the two deposits are shown in Table 5.1.

	Mt	Zn %	Cu %	Ag ppm	Au ppm
Scuddles	10.5	11.7	1.2	89	1.1
Gossan Hill Zn	2.2	11.3		102	1.5
Gossan Hill Cu	7.0		3.4		

Table 5.1. Pre-mining resources for the Golden Grove deposits (from Normandy, 1999).

5.2.1. Scuddles Geology

Mineralisation at Scuddles lies at the top of Member 6 of the Golden Grove Formation (GG6) and is overlain in most areas by a thin layer of sediments followed by rhyodacitic and dacitic rocks of the Scuddles Formation (Figure 5.3) The deposit occurs as a near vertical irregular sheet-like body that extends over 500 metres along strike and is up to 50 metres thick, with mineralisation occurring as two distinct lenses of massive sulphides (Main and Central lenses) separated by 150 metres of un-mineralised section.

The deposit as defined by mine geologists is categorised into eight rock types consisting of different massive sulphide ore types and the volcanic host sequence (Table 5.2). At the base of the deposit lies the footwall zone (FW), which contains a small number of thin sulphide stringers within silicious metasediments. Commonly, lying at the top of the footwall lies a well developed zone of semi-massive and stringer mineralisation (SSC) consisting of pyrite and chalcopyrite veins distributed within the footwall sequence. The local volume percentage of sulphide minerals in the stringer zone is highly variable ranging from <5-30%. The stockwork is best developed beneath the thickest accumulations of the overlying massive sulphides. Stratigraphically above the stringer zones is a zone of massive pyrite which is differentiated into three units; sub-massive pyrite breccia (BSC), massive pyrite with chalcopyrite content grater than 5% (MSC), and massive pyrite (MSP). The sub-massive pyrite breccia (BSC) occurs as irregular zones commonly underlying the massive pyrite chalcopyrite ore (MSC). The massive pyrite chalcopyrite unit (MSC) is differentiated from the massive pyrite (MSP) when chalcopyrite content is greater than 5%. Overlying these pyrite rich zones is a zone of massive sphalerite-pyrite ore which is subdivided into two categories based upon sphalerite grade: MSO – 10-30% sphalerite and MSS >30% sphalerite. The hanging-wall volcanic sediments (HW) overlays this blanket of sphalerite and is unmineralised.

Unit	Rock Type
FW	footwall with sulphide stringer
SSC	stringer zone
BSC	massive pyrite breccia
MSC	massive pyrite with chalcopyrite mineralisation
MSP	massive pyrite
MSO	massive sulphide ore(sphalerite)
MSS	massive sulphide ore (sphalerite)
HW	hanging wall volcanic sediments

Table 5.2. The Scuddles deposit is divided into eight categories according to mine production.

In the main ore lenses a later phase of epigenetic copper rich mineralisation crosscuts the zinc ore. Ore minerals have been re-crystallised during metamorphism and deformation. Primary and secondary ore textures are observed at Scuddles and are summarised by Mill et al. (1990). Sphalerite ore is typically coarse-grained (2-3 mm). Magnetite is a common accessory mineral both within the massive sulphide and footwall rocks. Minor accessory minerals include galena, which typically occurs within the sphalerite mineralisation and pyrrhotite, which occurs throughout the deposit, but typically concentrated in the massive pyrite and chalcopyrite ore. The ore textures vary throughout the deposit. Examples of samples collected for six of the eight units are shown in Figure 5.5 (a, b & c).

Footwall

SiO_2	Fe_2O_3	S	Cu	Pb	Zn
76.75	12.35	7.57	0.68	0.00	0.04

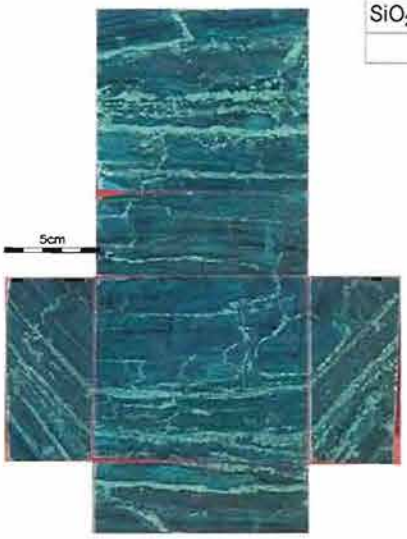

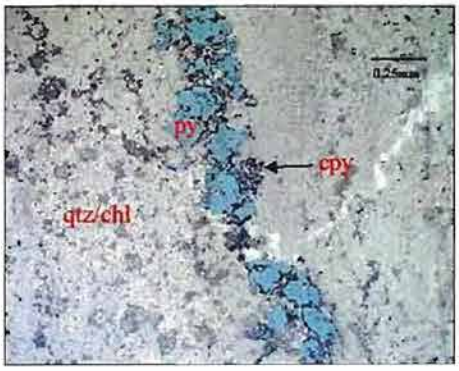

Sample GG35 chloritic quartzite,

A dark grey, massive quartzite cut by sulphide (pyrite) veins (<1-8 mm) that are parallel to bedding planes. The rock framework comprises microcrystalline quartz and chlorite with minor ilmenite, carbonate and white mica. The specimen is cut by subparallel quartz-chlorite-sulphide veins (<0.1-4 mm). These contain anhedral quartz, pyrite and chlorite with chalcopyrite, sphalerite and pyrrhotite filling remaining space. Chalcopyrite, sphalerite and pyrrhotite occur as anhedral intergrowths

MSC

SiO_2	Fe_2O_3	S	Cu	Pb	Zn
1.04	51.12	33.78	7.31	0.02	0.33

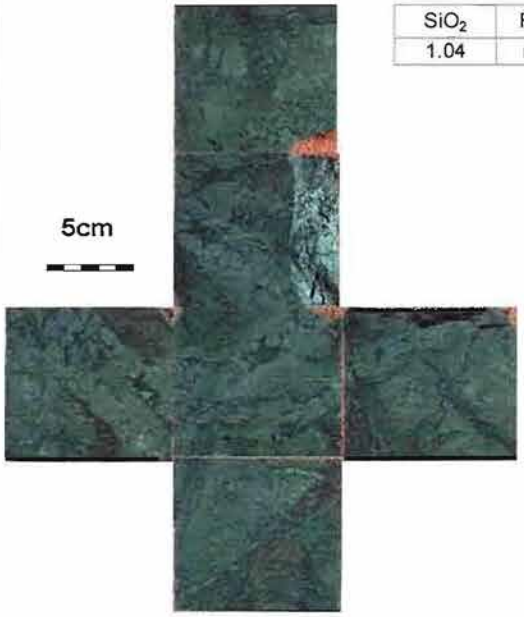

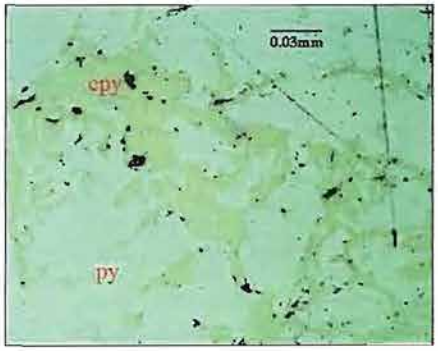

Sample GG24 Massive sulphide (pyrite-chalcopyrite)

Massive sulphide dominated by pyrite which occurs in coarse irregular aggregates overgrown by chalcopyrite. White quartz-carbonate veins (<10 cm) cut sulphide aggregates and fill some areas interstitial to pyrite. Sulphides enclose magnetite grains. Coarse pyrite grains (2-5 mm) are fragmented, with fine fractures filled by chalcopyrite. Pyrrhotite, chalcopyrite, fine grained pyrite and rare sphalerite are intergrown and form a networked aggregate enclosing granular magnetite, carbonate, K-feldspar, white mica and chlorite.

Figure 5.5. (a) Representative samples from different stratigraphic intervals from the Scuddles deposit (FW, and MSC). py: pyrite, cpy: chalcopyrite, qtz: quartz, chl: chlorite. Ore grade (%). The photographs of the samples show an "exploded" view displaying all six sides of the prismatic sample. Reflected light microphotographs illustrate micro-textures.

MSP

SiO_2	Fe_2O_3	S	Cu	Pb	Zn
0.26	59.74	50.86	0.54	0.03	0.04

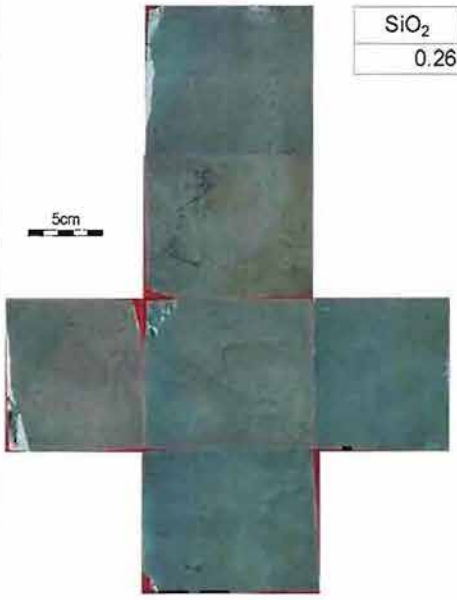

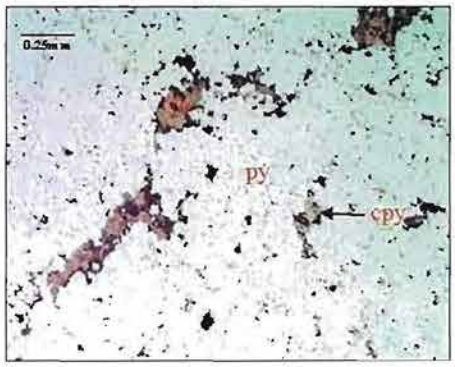

Sample GG30 Massive sulphide (pyrite)

Massive pyrite with sparse and fine grained areas (<2mm) filled with dark grey carbonate. Pyrite makes up approximately 97% of the specimen as a massive aggregate. Chalcopyrite occurs filling pyrite interstices with rare pyrrhotite and sphalerite. Remaining cavity space is filled with carbonate, chlorite and rare quartz. Tourmaline is enclosed in pyrite.

MSO

SiO_2	Fe_2O_3	S	Cu	Pb	Zn
18.48	22.84	18.16	0.26	6.07	27.36

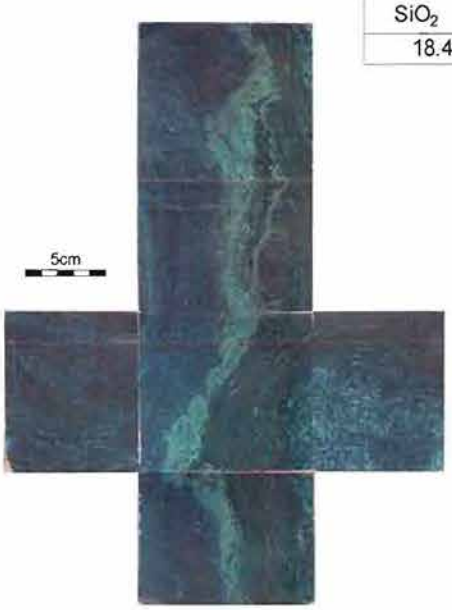

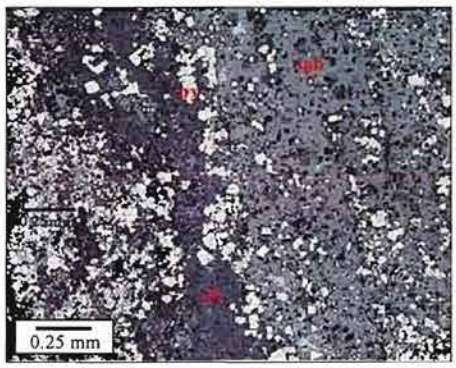

Sample GG13 Massive sulphide (sph-pyrite) in quartz-chlorite schist

A schistose rock with a domain of semi-massive sphalerite. Foliation is defined by quartz- and chlorite-rich bands (<2 mm). Bands of anhedral, mosaic quartz alternate with subparallel chlorite flakes. Pyrite-rich domains are comprised of loosely interlocking euhedral grains enclosed by sphalerite. In the semi-massive sulphide sphalerite encloses chlorite and anhedral quartz. Galena fills cavities, with minor pyrrhotite.

Figure 5.5. (b) Representative samples from different stratigraphic intervals from the Scuddles deposit (MSP, MSC). py: pyrite, cb: carbonate, sph: sphalerite. Ore grade (%).The photographs of the samples show an "exploded" view displaying all six sides of the prismatic sample. Reflected light microphotographs illustrate micro-textures.

MSS

SiO_2	Fe_2O_3	S	Cu	Pb	Zn
1.95	4.04	25.23	0.12	9.23	56.35

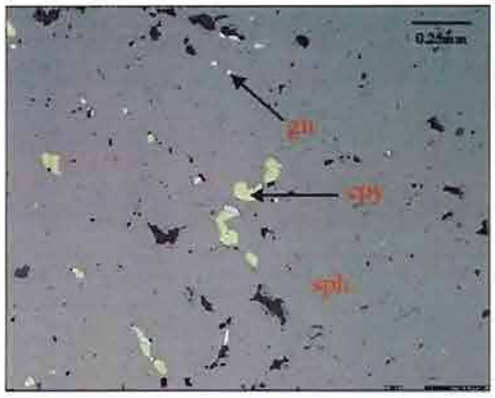

Sample GG17 Massive sphalerite

Massive sphalerite with white quartz and carbonate occurring as fine, sparse inclusions. Gangue minerals, quartz, carbonate and rare chlorite occur as anhedral grains enclosed by sphalerite. Other sulphides make up less than a few percent of the rock. Euhedral arsenopyrite rhombs are enclosed by sphalerite. Chalcopyrite and galena are present as anhedral grains

HW

SiO_2	Fe_2O_3	S	Cu	Pb	Zn
71.24	5.33	0.97	0.01	0.00	0.10

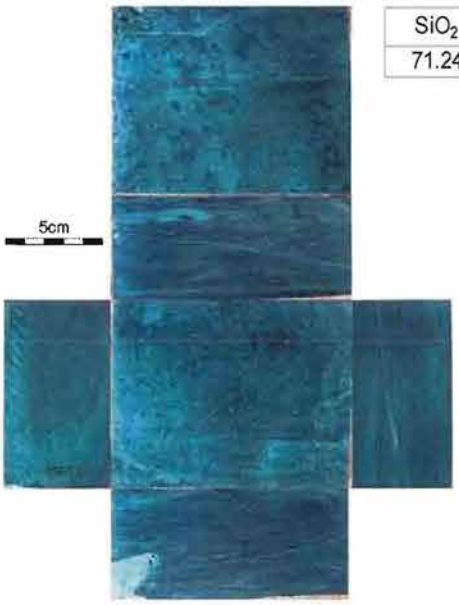

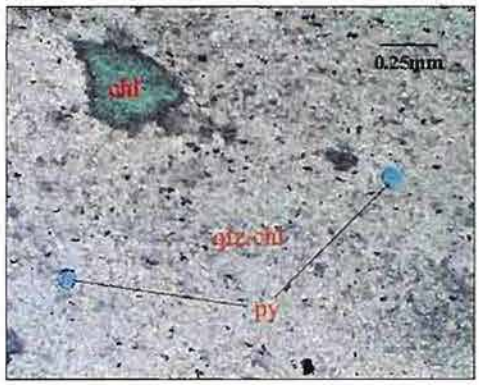

Sample GG05 Quartz-chlorite schist

A fine grained, weakly schistose rock with a framework comprised of fine grained quartz and chlorite. Fine flakes of white mica highlight schistosity. Anhedral quartz porphyroblasts (<0.6mm) are present (<1%). Prismatic crystals of tourmaline and ilmenite are sparsely disseminated, along with accessory leucoxene and epidote (clinozoisite). Sulphides make up no more than 0.5% of the rock. Fine disseminated grains are evenly distributed throughout.

Figure 5.5. (c) Representative samples from different stratigraphic intervals from the Scuddles deposit (MSS and HW). (py: pyrite, qtz: quartz, chl: chlorite, sph: sphalerite, gn: galena). The photographs of the samples show an "exploded" view displaying all six sides of the prismatic sample. Reflected light microphotographs illustrate micro-textures.

5.3. Methodology

5.3.1. Field Measurements

Fourteen underground sites on the 437 level of the Scuddles ore body were selected for insitu electrical studies. This level provides type examples of most of the characteristic features exhibited by the Scuddles deposit. Most major rock units have been sampled at two or more sites, with the exception of the barren pyrite unit (MSP) and the hanging-wall volcanic-sediment host. The fourteen sites (Figure 5.6) can be categorised into six of the eight main ore types (Table 5.3). The geological boundaries shown in Figure 5.6 were provided by the mine geologists and were drawn from backs mapping[1]. Grade control at Scuddles is conducted on the basis of visual estimation of sulphide proportions. Routine grade samples are not collected during development, thus it is not possible to directly ascribe bulk assay values to each site.

Rock Type	Grade	Ore Grade	Sites
Stringer Zone footwall sediments **FW and SSC**	Low grade	>10% Cu	11,12,13
Massive Pyrite with Chalcopyrite mineralisation **MSC**	Low-moderate grade	>5%Cu	7, 8, 9
Massive Pyrite **MSP**	Barren	Nil	10
Massive Sulphide ore(sphalerite) **MSO**	moderate grade	10-30% Zn	1,3,4 6
Massive Sulphide ore (sphalerite) **MSS**	High grade	30+% Zn	5, 14
Hanging wall volcanic sediments **HW**	Nil	Nil	2

Table 5.3. Ore types and associated insitu survey sites located on the 437 level of the Scuddles ore body. Grade grades are based upon visual estimation of sulphide proportions.

Ideally, homogenous exposures were selected for site investigation to allow independent assessment free from the effects of local mineralogy heterogeneities. However, insitu electrical measurements collected across many sites showed significant variations in electrical resistivity that weren't expected based on the macroscopic visual observations. Site selection was also limited by access and sources of electrical interference, such as mining infrastructure.

Insitu measurements of apparent resistivity and chargeability were completed using an expanding Wenner electrode array. The electrode 'a' spacing (potential-potential electrodes) ranged from 0.11 metres to 2 metres for most sites, but for some sites with problematic geometry, geological or ground support factors the maximum current electrode spacing was reduced to 1 metre.

The electrical heterogeneity of each site was resolved through lateral traversing with a fixed mobile electrode array (MEA). The mobile electrode array is described in detail in chapter 3 and permits measurements at 0.11 metre and 0.22 metre electrode spacings. The MEA measurements were collected at 0.5 metre intervals along site traverses. For some sites (those showing greatest variability) measurements were collected over a grid to map both lateral and vertical variations.

[1] Backs mapping refers to mapping the roof of an underground mine drive.

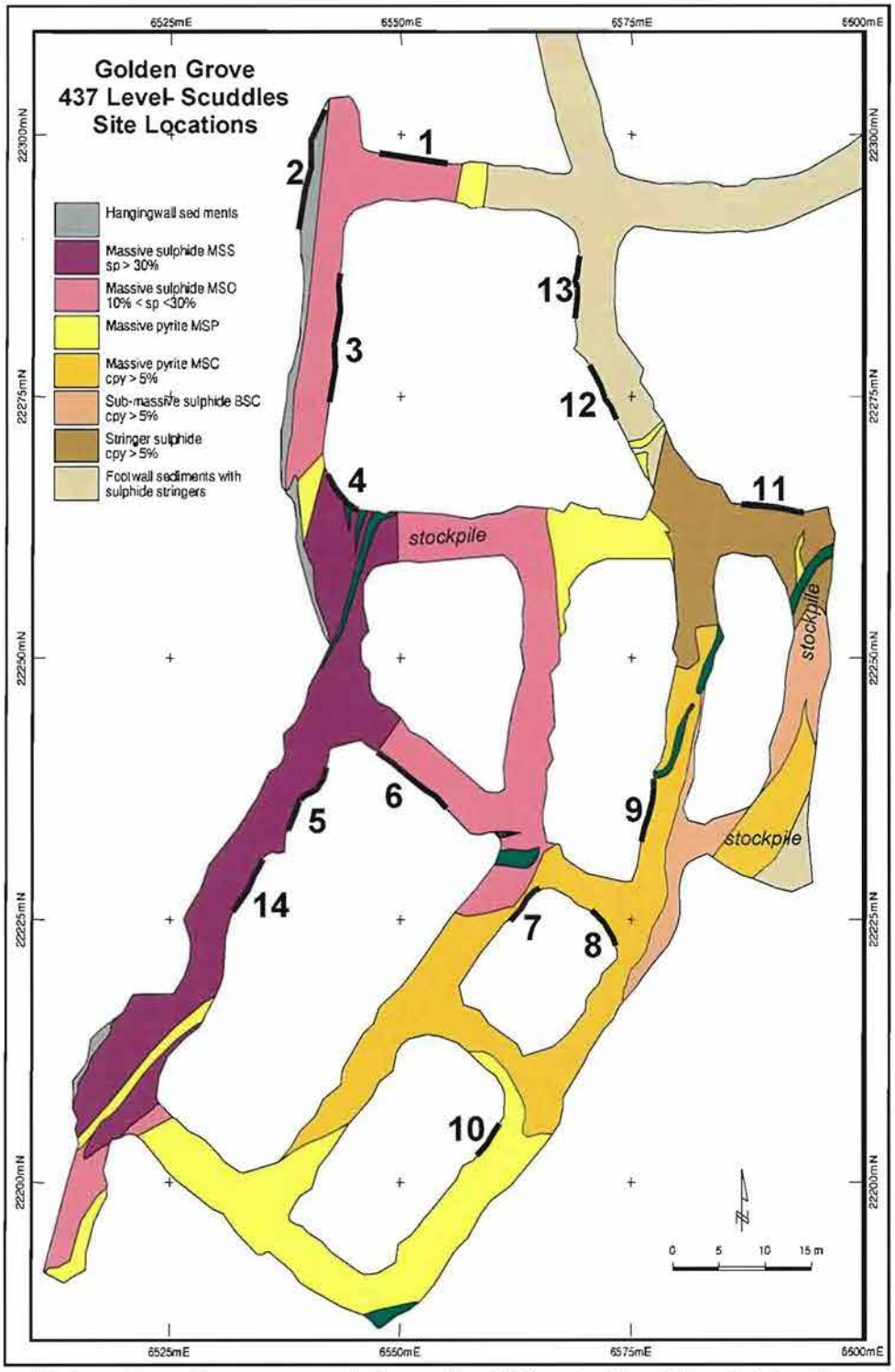

Figure 5.6. Locations of measurement sites on the 437 level at Scuddles, Golden Grove. Insitu measurement sites are numbered (13 in total) and marked with a thick black line. Ore boundaries are derived from backs-mapping.

All measurements were collected using a Scintrex IPR12 receiver and IPC9 transmitter. Where practical, transmitter currents were kept to a minimum using a resistance shunt box in an attempt to simulate current densities similar to those generated during surface exploration (Section 3.2.1). However, the conductive nature of a majority of the massive sulphide ore at Scuddles (10^{-4} – 10^{-1} Ωm) generally necessitated the use of higher current densities to ensure instrument synchronisation. A four second square pulse cycle was utilised for all insitu measurements. Chargeability was recorded in mV/V over the time interval 340-520ms after the current turn-off. Resistivity measurements as low

as 0.001 Ωm could be recorded using this equipment, but chargeability decay curves were often irregular or very noisy for measurements with apparent resistivities of less than 0.5 Ωm. Chargeability data was scrutinised and only those curves that showed a smooth monotonic decrease in voltage and contained no negative voltages at early or late times were accepted. These criteria led to the rejection of over 40% of the chargeability data.

In addition to galvanic electrical measurements magnetic susceptibility data were acquired at several sites using an Exploranium KT-6 magnetic susceptibility meter. Susceptibility measurements were recorded at 0.25 metre intervals. Digital photographs of each site were also taken to record variations of mineralogy, texture and structure and for qualitative comparison to the geophysical data.

5.3.2. Laboratory measurements

A suite of thirty-eight large, mostly oriented, rock samples was collected from the fourteen insitu sites for laboratory-scale testing. Samples were generally collected during the initial preparation of each site, which involved the removal of loose or broken material to ensure electrical measurements were conducted on solid surfaces.

Galvanic electrical measurements of apparent resistivity were conducted for all samples (detailed procedures were described in Chapter 3). The highly conductive nature of the Golden Grove samples created significant problems with laboratory galvanic resistivity measurements and led to the utilisation of the dry 2-electrode system for measuring galvanic properties of highly conductive samples (<~5Ωm) (See section 3.3.2 for a detailed explanation). Electrical measurements of samples were taken in three orthogonal directions to quantify anisotropy. Multiple measurements were collected at three different current densities to assess linearity in resistivity data.

All samples were assayed for major and trace elements. Density and magnetic susceptibility measurements were also completed. A number of suitable samples were selected for mesoscopic continuity and current mapping techniques (refer Chapter 4). These techniques assess the electrical variation within individual samples.

5.4. Results

The discussion of the results has been subdivided on the basis of the six different ore types shown in Table 5.3 (with results of MSC and MSP combined), presented in stratigraphic order. A "type example" site is presented for each ore type prior to a summary of the data for all sites.

A standard approach has been adopted to describe the field and laboratory data from each site and as follows;

1. Describe the insitu expanding array measurements.
2. Compare insitu results to laboratory measurements of samples.
3. Describe local insitu variability data.
4. Observe and discuss reasons for variability, using other techniques, i.e. petrography, geochemical assays, continuity and current mapping of samples.

For qualitative analysis, insitu apparent resistivity data is plotted as a function of electrode spacing, together with laboratory measurements. Multiple data points for each sample show the range for a series of measurements conducted on different faces of a prismatic sample, and at varying current densities.

No valid time domain chargeability data were recorded in laboratory measurements for the majority of samples, due to the high sample conductivity (typically less than 1 Ωm). In these highly conductive samples, current flows directly through the conductive sulphide veins uninhibited, and very low chargeability is observed. Due to the limited insitu and near total absence of laboratory chargeability data, chargeability will be described only in the summary of all sites.

Histograms of apparent resistivity for insitu and sample measurements have been produced to indicate the variability in the data. The histograms of the insitu resistivity data are predominantly biased towards smaller spaced measurements as the majority of the insitu measurement were collected using the mobile-electrode array (i.e. at 0.11 and 0.22 metre spacings). Therefore, the distribution observed in insitu measurements is at a scale which is directly comparable to the scale of resistivity measurements collected for samples. The bulk insitu resistivity at each site (i.e. insitu measurement collected at the largest electrode spacing) has also been superimposed onto each histogram.

Measurements of insitu anisotropy are also compared to values obtained from laboratory samples. The insitu measurements only record anisotropy in two dimensions, whereas sample measurements allow anisotropy to be recorded in three dimensions. Thus, anisotropies derived from the insitu data, may be less than those derived from the laboratory sample data.

5.4.1. Footwall stringer zone

The footwall stringer zone was comprised of strongly silicified sediments, cut by numerous pyrite-chalcopyrite veins up to 0.3 metres in thickness. The footwall stockwork stringer zone was examined at three locations; Sites 11, 12 and 13 (Figure 5.6). Valid resistivity and chargeability data was not obtained at Site 11, with no signal recordable for electrode greater than 0.33 m. The results of site 12 will be discussed in detail. The rock mass of Site 12 is relatively heterogeneous with the concentration and distribution of sulphides veins highly variable (Figure 5.7). The spacing of the stockwork veins varies from millimetres to decimetres.

Figure 5.7. Site photograph of Site 12 located within the footwall-stringer zone. The distribution and scale of stockwork veining is obvious. The high conductive nature of the unit resulted in a limited number of measurements to be collected across all sites. Location of sample, GG34 is shown.

The variation in apparent resistivity as a function of electrode spacing for Site 12 is shown in Figure 5.8. There is an overall slight decrease in resistivity with increasing electrode spacing, but there is a degree of local variability, presumably a function of the geometry and scale of the conductive stockwork. The apparent resistivity values range slightly over one order of magnitude. The expanding array was centred on a pyrite rich vein, which likely attributed to the low resistivity recorded at small scale measurements. No insitu chargeability was recorded with the expanding array, due to the highly conductive nature of the site.

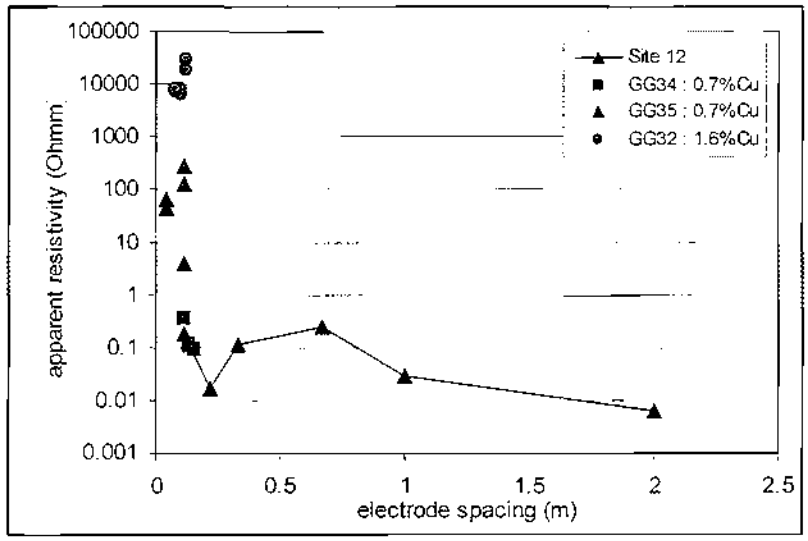

Figure 5.8. Apparent resistivity versus electrode spacing for Site 12 located in the footwall-stockwork zone. Galvanic laboratory resistivity measurements of sample are also plotted.

The distribution and scale of stockwork within footwall sites created difficulties in sampling, with the siliceous rock mass commonly fracturing along pyrite veins during removal. The large thickness and distribution of sulphide veins resulted in samples either consisting of predominantly pyrite vein material or mostly volcanic sediment. As a result only three suitably sized samples were collected from all Footwall sites. As only one sample was collected from Site 12, resistivity measurements of all Footwall samples are plotted on to Figure 5.8, to provide an indication of the variability. Sample GG34 was collected from Site 12, GG35 from Site 13 and GG32 from Site 11. The resistivity for Footwall samples range over five orders of magnitude (Figure 5.8), from 10-1 to 10^4 Ωm. The lowest sample resistivity (0.1 Ωm) produced from GG34 is equivalent to the small scale insitu measurements. GG34 contains a large proportion (20-30%) of sulphide stockwork. The high resistivity of GG32 (>10^4 Ωm) is due to the absence of sulphides in a sample comprising entirely of quartz-volcanic metasediment.

A resistivity and magnetic susceptibility traverse was conducted at site 12 (Figure 5.9). As expected there is an extremely irregular variation in apparent resistivity with values ranging from 0.01 to 20 Ωm due to the varying distribution and scale of stockwork veining. The variation in the resistivity traverse correlates to mesoscale mineralogical and textural differences, with lower values associated with more pyrite-rich sections, and higher values with volcanic sediments. There is no correlation between magnetic susceptibility and apparent resistivity signals.

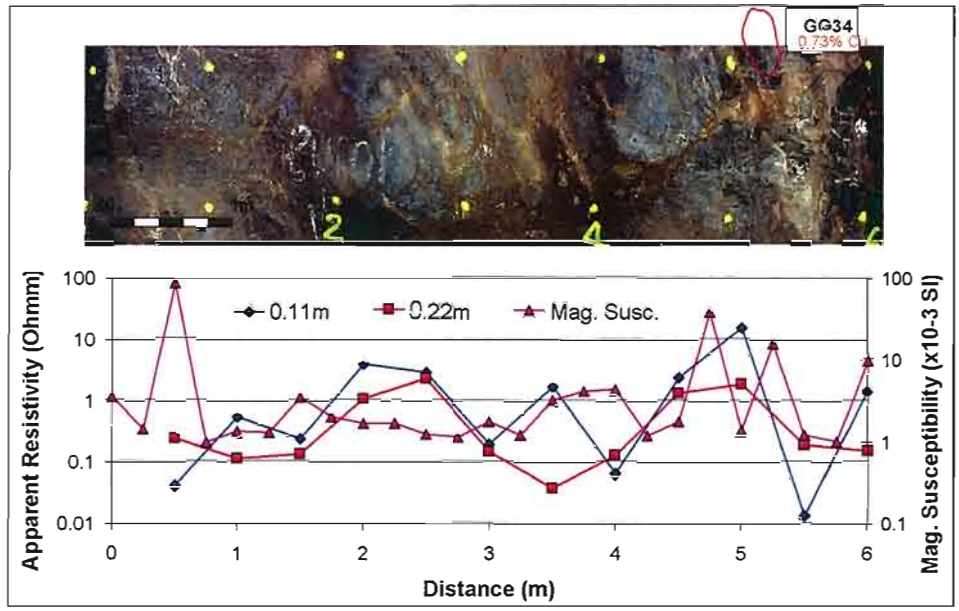

Figure 5.9. Traverse of resistivity and magnetic susceptibility measurement across Site 12 centred in the middle of the site photograph. Variations in apparent resistivity (red and blue lines) reflect the heterogeneity of the stockwork veining, with pyrite rich areas reflecting low values, and volcanic sediments reflecting higher values.

Histograms were generated for insitu resistivity measurements from Site 12 and all Footwall samples, as shown in Figure 5.10. The insitu measurements show three modal peaks equally separated by one order of magnitude. This distribution reflects the variability in stockwork veining across the site; thick vein-rich domains contribute to the conductive modal peak (~0.03 Ωm), vein-rich poor domains contribute to the resistive modal peak (~2 Ωm) and the main modal peak occurring at 0.3 Ωm lies between the two end member distributions. Despite the three modal peaks, the overall range of insitu resistivity values is fairly low, indicating that the pyrite bands (even in low proportions) significantly reduces the resistivity within the footwall, effectively bypassing the resistive silicious sediments. The sample resistivity distribution is bimodal, and shows a much greater range of values, clearly indicating conductive and end members; the conductive modal peak is coincident with the main insitu modal peak. The mean sample resistivity (10-100 Ωm) would overestimate the bulk insitu resistivity (~0.01 Ωm) by two orders of magnitude.

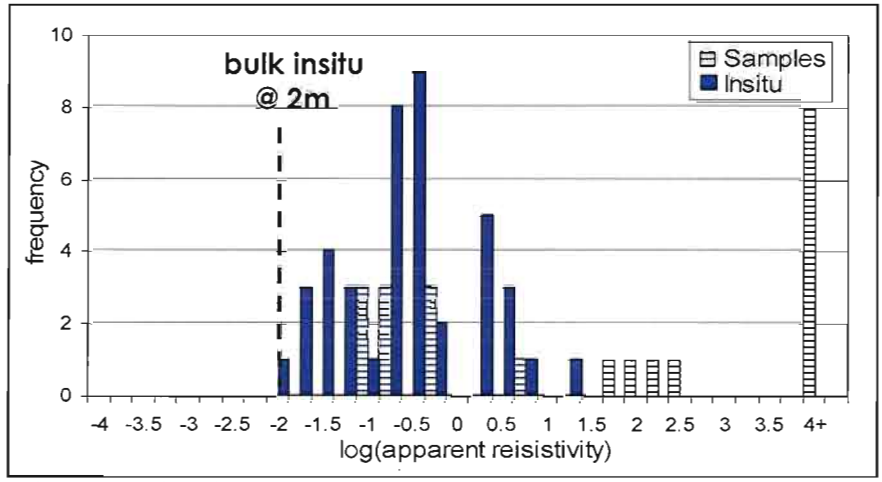

Figure 5.10. Histogram of log(apparent resistivity) shows the distribution of insitu resistivity measurements for Site 12 located in the footwall-stockwork zone. Galvanic laboratory resistivity measurements and the bulk insitu apparent resistivity are also plotted.

The influence of the stockwork veining on electrical properties was furthered examined using continuity and current mapping methods. The continuity and current mapping results for sample GG34 (Figure 5.11) collected from Site 12, clearly shows electrical conduction to be primarily controlled by the mineralised stockwork. The continuity image clearly shows high levels of connectivity associated with pyrite-chalcopyrite veining occurring within the null response attributed to the siliceous sediments. The current maps show current to preferentially flow through mineralised veins as expected, correlating directly to visual observations.

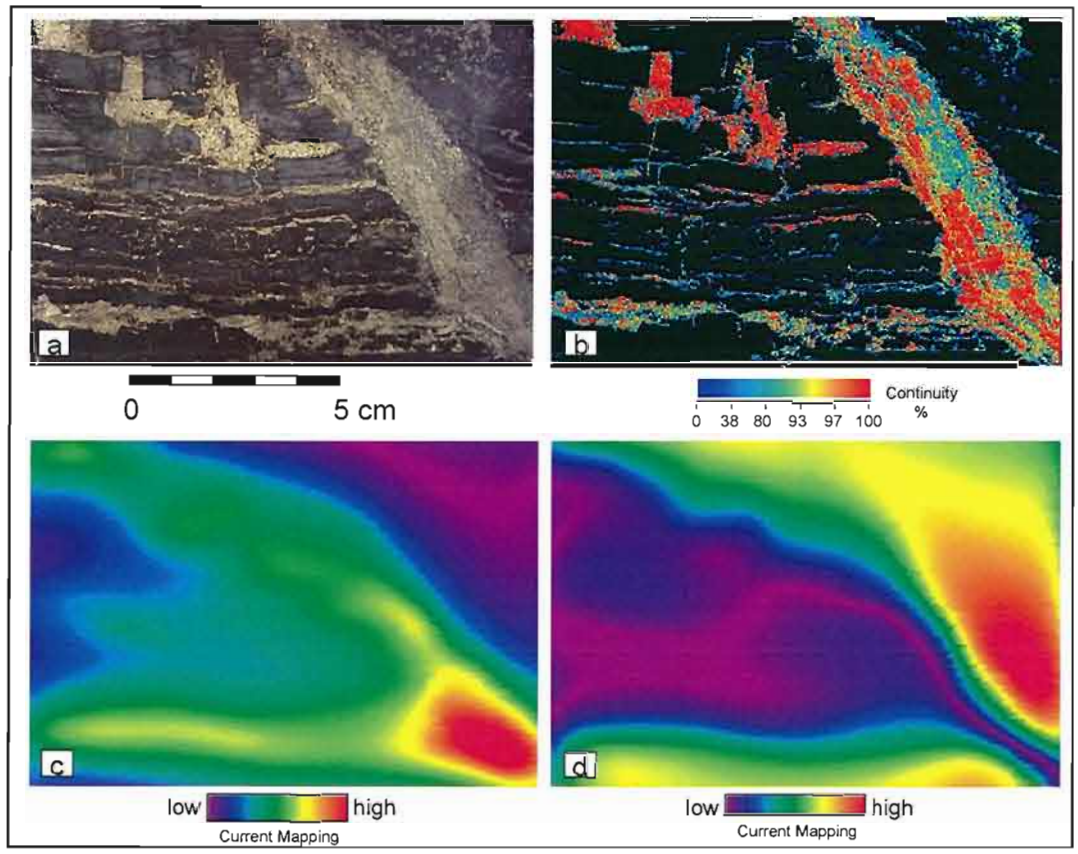

Figure 5.11. Continuity and current mapping results for Sample GG34 collected from Site 12 (FW). (a) Optical image. (b) Continuity image (histogram-equalised colour distribution). (c) Y component current map. (d) Z component current map. The mineralized pyrite-chalcopyrite veins are clearly indicated by the coloured zones in the continuity image (b). The current preferentially flows through the most prominent veins, as indicated by the Y (maximum) and Z (minimum) current maps.

5.4.2. MSP Massive pyrite (without chalcopyrite mineralisation)

The massive pyrite ore unit (MSP) was examined at one location, site 10, which is observed to be composed entirely of massive sulphide (Figure 5.12). Despite the site being classified as non-mineralised according to the mine plan (Figure 5.6), sample assays and visual inspection reveals some minor chalcopyrite mineralisation.

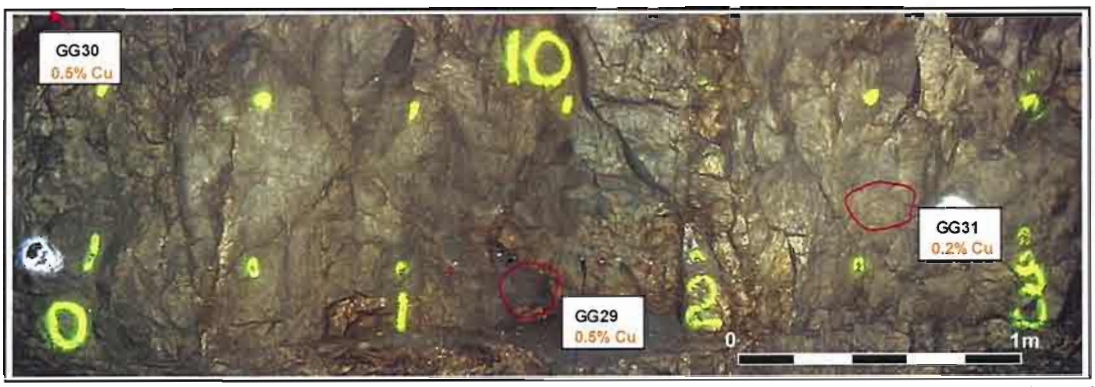

Figure 5.12. Site photograph of Site 10 located within the massive pyrite unit (MSP). Location of samples, GG29, 30 and 31 are shown.

The insitu expanding electrode measurements for site 10 (Figure 5.13) show little scale variation for all measurements. Insitu resistivity is quite low varying from 0.04 Ωm to 0.009 Ωm. The lack of variation suggests no predominant current pathways are apparent at this scale of investigation, which reflects the relatively homogeneous nature of the massive pyrite observed at this site.

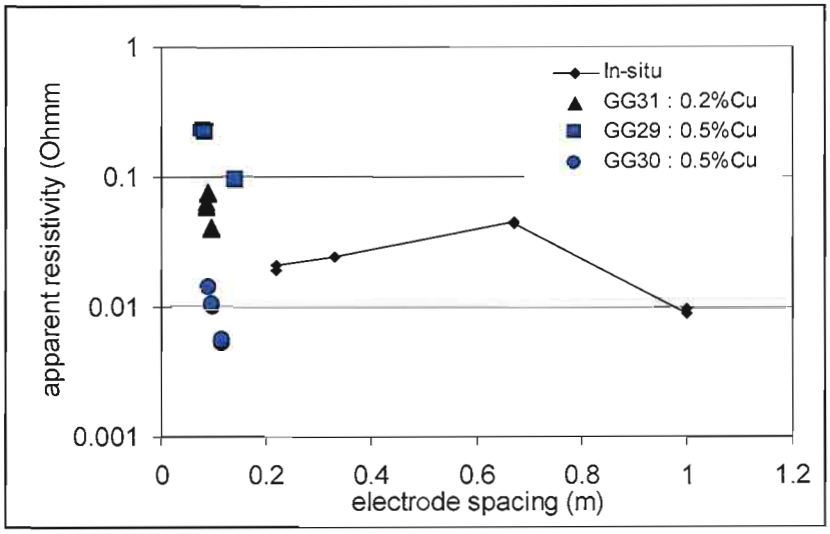

Figure 5.13. Apparent resistivity versus electrode spacing for Site 10 located in the massive pyrite zone (MSP). Galvanic laboratory resistivity measurements of samples are also plotted.

The laboratory resistivity of samples collected from Site 10, range over one order of magnitude (<0.01 to >0.1 Ωm). The three orthogonal measurements of each sample are tightly grouped indicating their isotropic nature. Samples from Site 10, consist of homogeneous massive pyrite with sparse and fine grained areas (<2mm) filled with dark grey carbonate, showing no prominent features which would preferentially conduct or impede conduction through the massive sulphide (Figure 5.14).

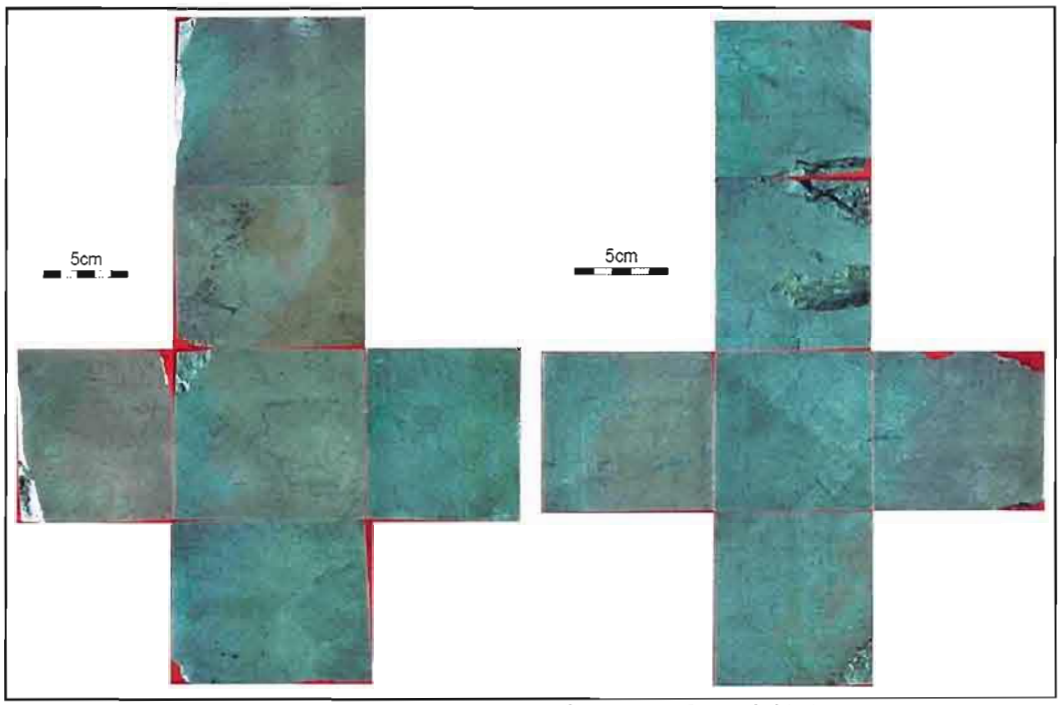

Figure 5.14. Samples GG30 and GG31 collected from Site 10 are fairly homogeneous consisting primarily of massive pyrite (95+%). The photographs of the samples show an "exploded" view displaying all six sides of the prismatic sample.

Histograms of insitu and laboratory resistivity measurements are shown in Figure 5.15. There is a good correlation between insitu and laboratory resistivity measurements. A noteworthy observation from the results of Site 10 is the lack of scale variation observed in insitu measurements and the similarity between laboratory and insitu measurements. This observation is believed to reflect the electrical homogeneity of the ore, thus laboratory derived sample resistivity of the massive pyrite is equivalent to insitu measurements at all scales.

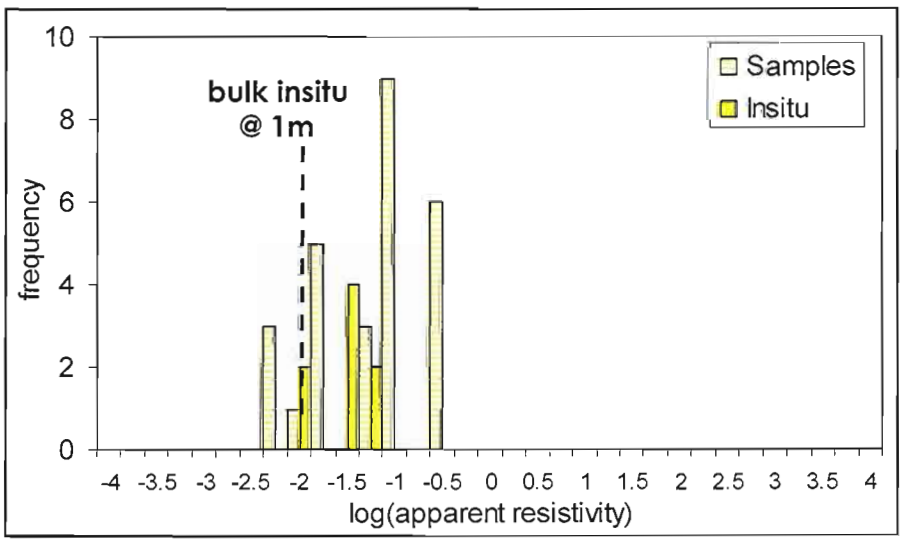

Figure 5.15. Histogram of log(apparent resistivity) shows the distribution of insitu and laboratory resistivity measurements for Site 10 located in the massive pyrite zone (MSP). The bulk insitu apparent resistivity is also plotted.

5.4.3. MSC Massive pyrite-chalcopyrite

The massive pyrite-chalcopyrite ore unit (MSC) was examined at three locations, sites 7, 8 and 9. The materials across the MSC zone were extremely conductive resulting in collection of a limited number of measurements. Signal levels measured by the IPR12 receiver were extremely low resulting in receiver synchronisation problems. At site 8 no signal could be recorded for any electrode spacing even for extremely large transmitter currents; an insitu apparent resistivity of <0.0002 Ωm is implied. Very little chargeability data was recorded for these sites. The results from site 9 will be discussed in detail.

Site 9 consists primarily of massive pyrite-chalcopyrite ore with magnetite veining (Figure 5.16). The site is of high grade (10-20% Cu) with samples assaying between 14 and 18% copper.

Figure 5.16. Site photograph of Site 9 located within the massive pyrite-chalcopyrite unit (MSC). Dark areas in the middle of the section depict large magnetite veins. Location of samples, GG27 and GG28 are shown.

Site 9 was the only site within the MSC ore that provided a significant number of successful insitu measurements, although for many measurements signal levels were very small and signal quality poor. The expanding electrode measurements at site 9 (Figure 5.17) shows scale variation, with apparent resistivity decreasing gradually from 0.01 Ωm to 0.002 Ωm with increasing electrode spacing. The scale variation is expected to continue, as an insitu apparent resistivity of less than 0.001 was inferred by the inability to record a measurement, due to low signal strength, for the 2 metre electrode spaced measurement.

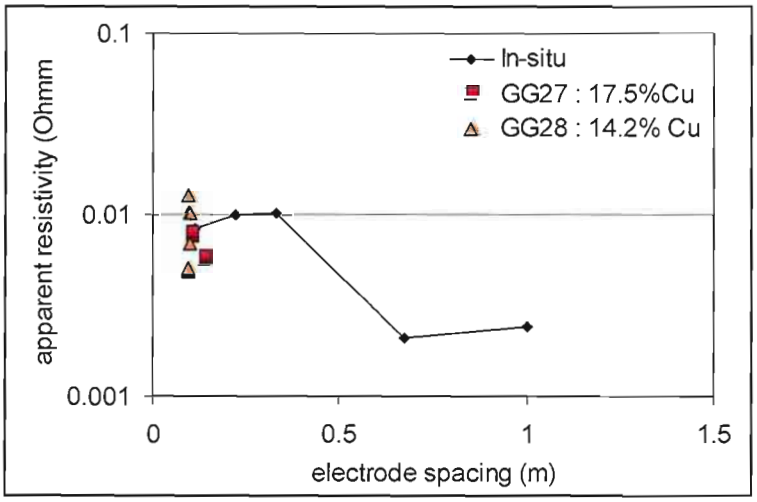

Figure 5.17. Apparent resistivity versus electrode spacing for Site 9 located in the massive pyrite-chalcopyrite zone (MSC). Galvanic laboratory resistivity measurements of samples are also plotted.

Galvanic resistivity measurements on samples from this site are tightly grouped around the insitu value at the smallest electrode spacing and range from 0.005 Ωm to 0.013 Ωm. Samples are comprised mainly of pyrite and chalcopyrite, with weak foliation defined by sub-parallel veinlets filled with chlorite.

Although the sample resistivities are tightly grouped, an insitu resistivity traverse conducted across site 9 (Figure 5.18) reveals an anomalous resistive zone located at the right-hand end of the traverse. The resistive anomaly doesn't appear to correlate to any obvious mesoscale mineralogical textures. Apparent resistivity values collected along the traverse range from 0.001 to 1 Ωm. The magnetic susceptibility measurements have no clear correlation with electrical measurements.

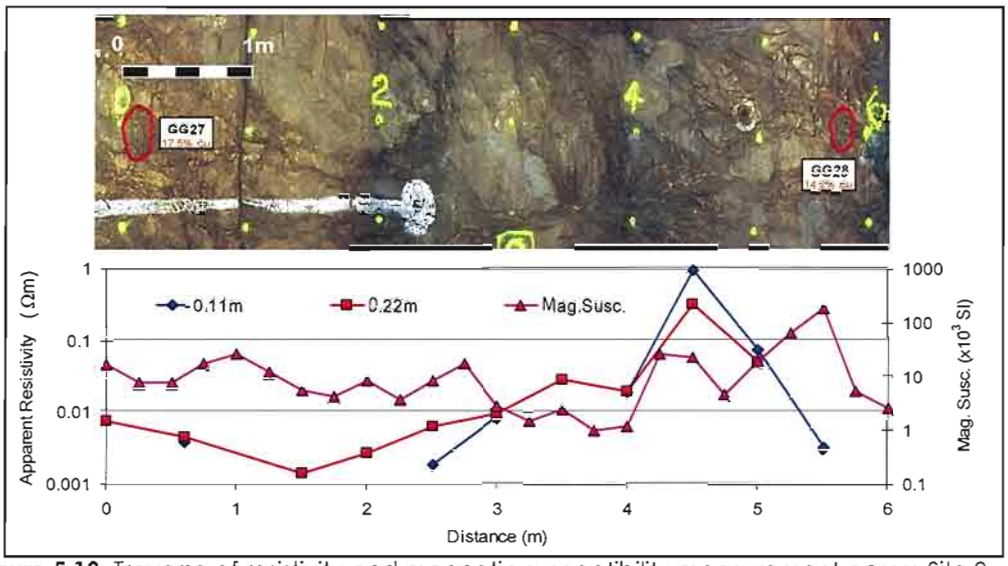

Figure 5.18. Traverse of resistivity and magnetic susceptibility measurement across Site 9 centred in the middle of the site photograph. Variations in apparent resistivity and magnetic susceptibility do not correlate to obvious mineralogical textures.

The distribution of insitu and sample resistivity measurements is shown in Figure 5.19. Both display log-normal distributions, sharing a common modal peak at 0.01 Ωm. The bulk resistivity value occurs by less than one order of magnitude towards more conductive values.

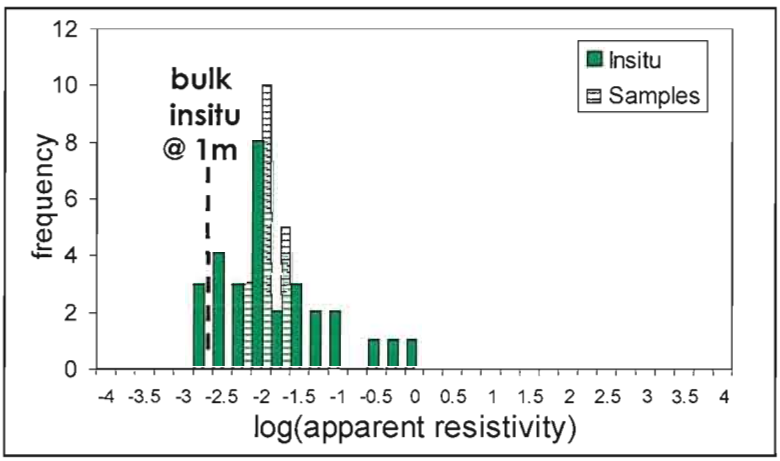

Figure 5.19. Histogram of log(apparent resistivity) shows the distribution of insitu and laboratory resistivity measurements for Site 9 located in the massive pyrite-chalcopyrite zone (MSC). The bulk insitu apparent resistivity is also plotted. Both sets of measurements show a log-normal distribution.

Continuity and current mapping was completed on sample GG27 collected from Site 9 (Figure 5.20). The sample comprises of a semi-massive sulphide with broad, irregular areas (>4 cm across) of chalcopyrite and pyrite separated by, and intergrown with grey quartz veins (>2 cm). The mapping results show the massive pyrite-chalcopyrite zones to be well connected, and provide prominent current pathways through the sample. Petrographic analysis of these zones reveals subhedral pyrite grains which are commonly fragmented and enclosed by chalcopyrite (Figure 5.21). Chalcopyrite encloses gangue minerals and is intergrown with pyrrhotite and sphalerite.

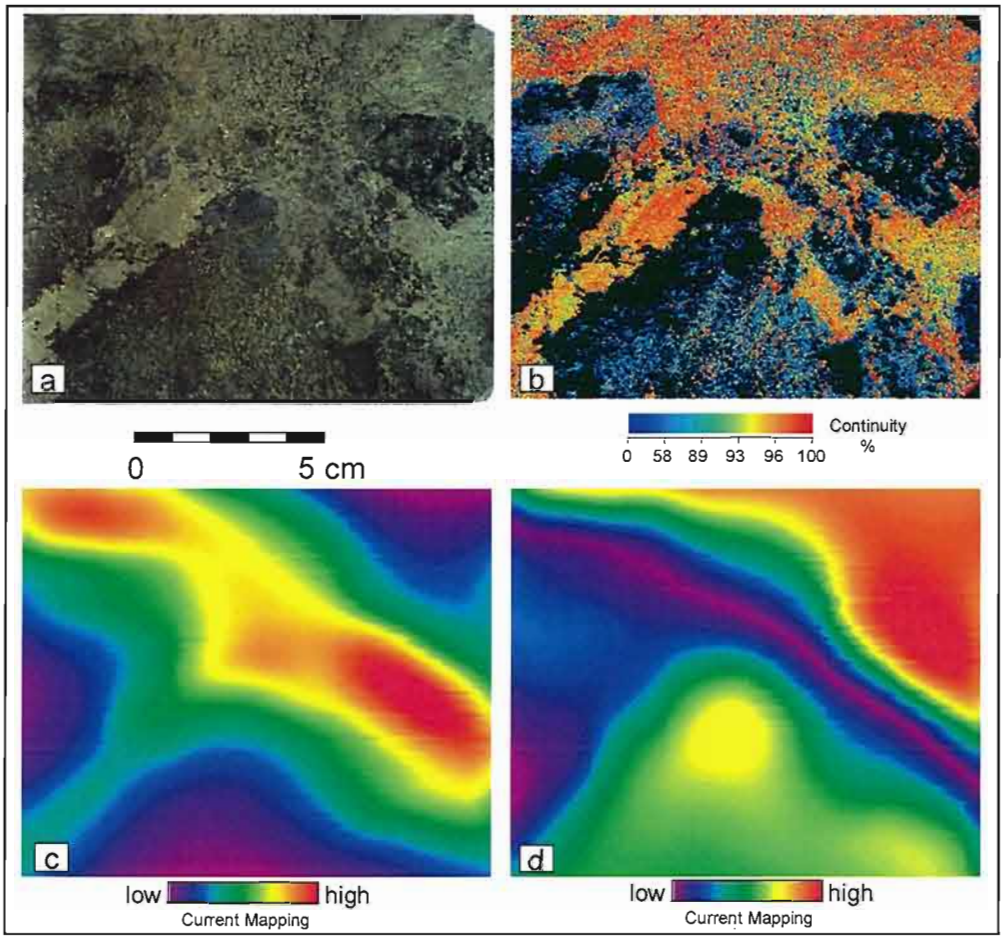

Figure 5.20. Continuity and current mapping results for sample GG27 collected from Site 9 (MSC). (a) Optical image. (b) Continuity image (histogram-equalised colour distribution). (c) Y component current map. (d) Z component current map. The mineralized pyrite-chalcopyrite veins are clearly indicated by the coloured zones in the continuity image (b). The chalcopyrite-pyrite zones are well connected, and provide pathways for conduction, as indicated by the Y (maximum) and Z (minimum) current maps.

As previously stated, measurements in other MSC sites were problematic, due to the highly conductive nature of the ore. For all measurements at Site 8 and for larger scale measurements at Site 7, no measurements were recorded, implying resistivity to be less than 0.001 Ωm. The high conductivity of these sites was further investigated using mesoscale electrical techniques (continuity and current mapping) on samples collected from the MSC sites.

Of particular interest are the continuity and current mapping results for sample GG24 collected from Site 7(Figure 5.22). The classified image of the sample photograph (Figure 5.22b) clearly shows the massive pyrite to be intersected by a dark vein of material consisting of magnetite, silicates and

minor disseminated pyrite. The class labelled as magnetite actually contains fine grained carbonate, pyrrhotite and pyrite in addition to magnetite

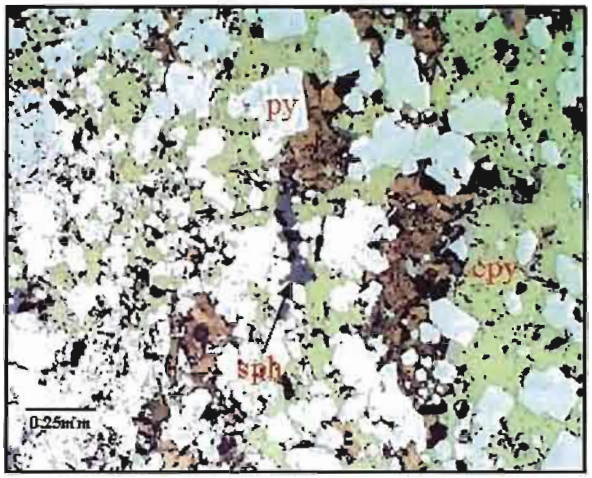

Figure 5.21. Reflected light microphotograph of sample GG27, showing the fragmented subhedral pyrite (py) enclosed by chalcopyrite (cpy) forming a highly conductive medium. Chalcopyrite also encloses gangue minerals. Sph: sphalerite.

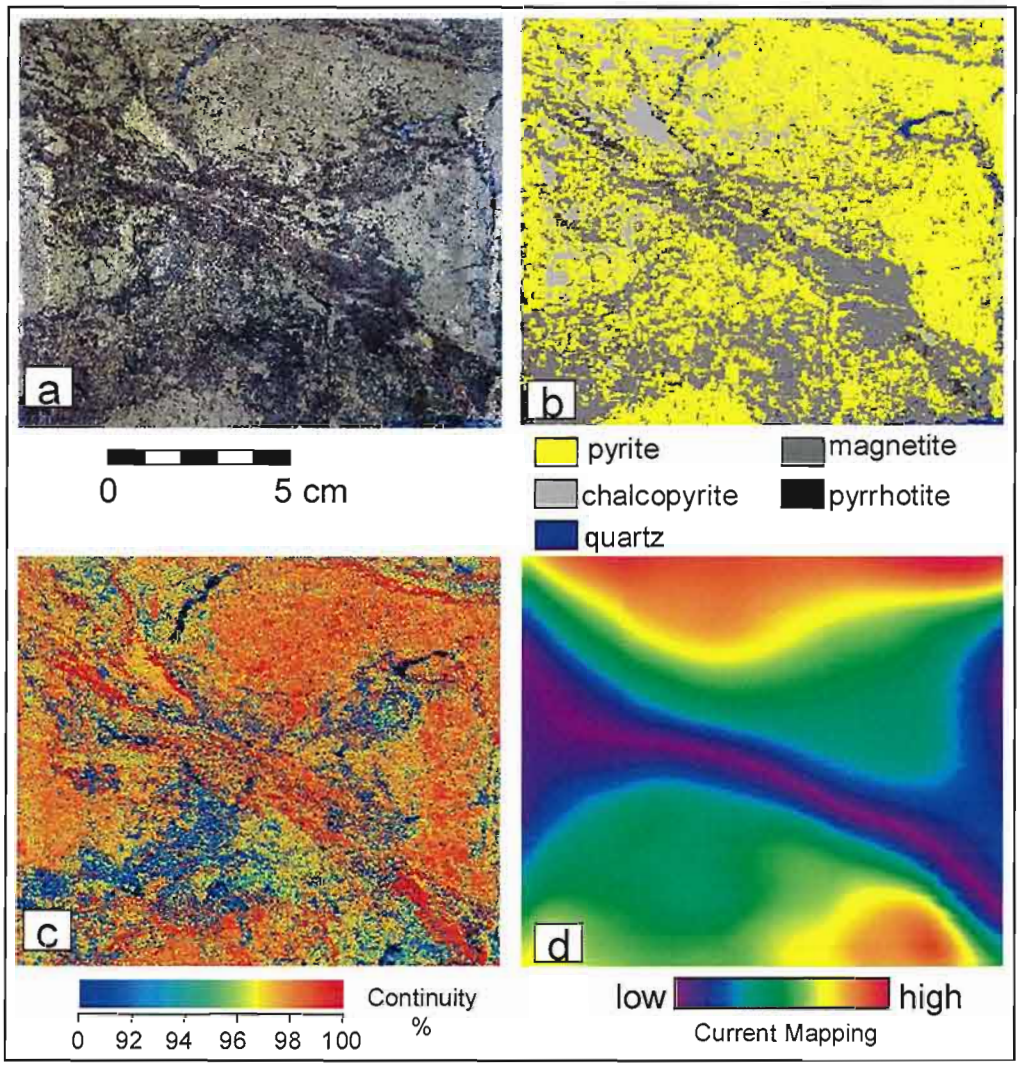

Figure 5.22. Continuity and current mapping results for sample GG24 collected from Site 7 (MSC). (a) Optical image. (b) Classification of optical image (Classes; pyrite, chalcopyrite, magnetite, pyrrhotite and quartz. (c) Continuity image (histogram-equalised colour distribution). (d) Z component current map. Maximum current flow (minimum Z value) is observed in the dark magnetite-carbonate band rather than through the pyrite and chalcopyrite.

The continuity map (Figure 5.22c) shows the pyrite and chalcopyrite correspond to moderate-high continuity (yellow-orange-red), the magnetite-carbonate in the lower part of the sample shows low continuity (blue), quartz appears as a null (black), and very high continuity is associated with small proportions within the diagonal magnetite-carbonate vein (red). The current map of the sample (Figure 5.22d) is particularly interesting as it indicates that almost all of the current flows diagonally through this dark vein, rather than the much more abundant pyrite and chalcopyrite. This result is quite unusual since pyrite and chalcopyrite are much more conductive than magnetite and carbonate. These results are highlighted in the continuity images of each mineral class (see Section 4.2 for description of method) shown in Figure 5.23. The small zones of pyrrhotite are almost maximally connected (98%), while the class labelled as magnetite has a continuity of only 84%.

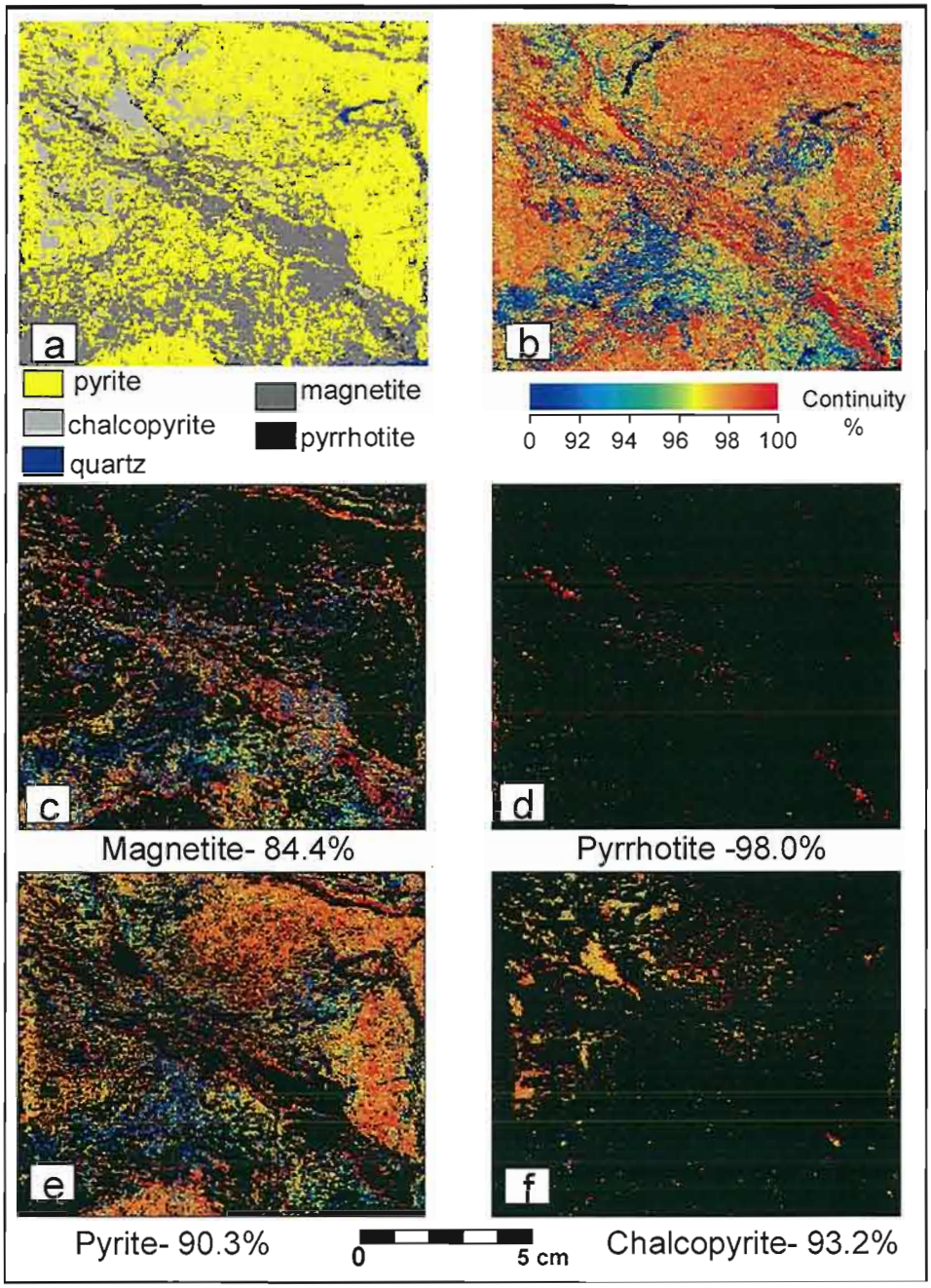

Figure 5.23. (a) Classification of optical image. (b) Continuity image of entire sample (90.1%). (c) continuity image of magnetite-carbonate (84.4%). (d) Continuity image of pyrrhotite (98.0%). (e) Continuity image of pyrite (90.3%) (f) Continuity image of chalcopyrite (93.2%). Percentages indicate mean continuity across sample for each phase for non-null cell values.

Microscopic examination of this dark zone in GG24 (Figure 5.24) revealed the presence of a fine connected network of pyrrhotite interstitial to equant magnetite and carbonate grains. The presence of pyrrhotite in this sample was not originally identified from visual investigation of hand specimens. Although the average grain-size of pyrrhotite is less than 0.08 mm it forms an anastomosing network interstitial to the carbonate plebs and is probably electrically continuous in three dimensions. The high levels in continuity response (i.e. low resistance) of GG24 (Figure 5.22c; Figure 5.23d) are coincident with the accumulations of pyrrhotite. The pyrrhotite is believed to dramatically reduce the overall resistivity within the massive pyrite unit. Similar results were observed in komatiite ores by Emerson, 2001.

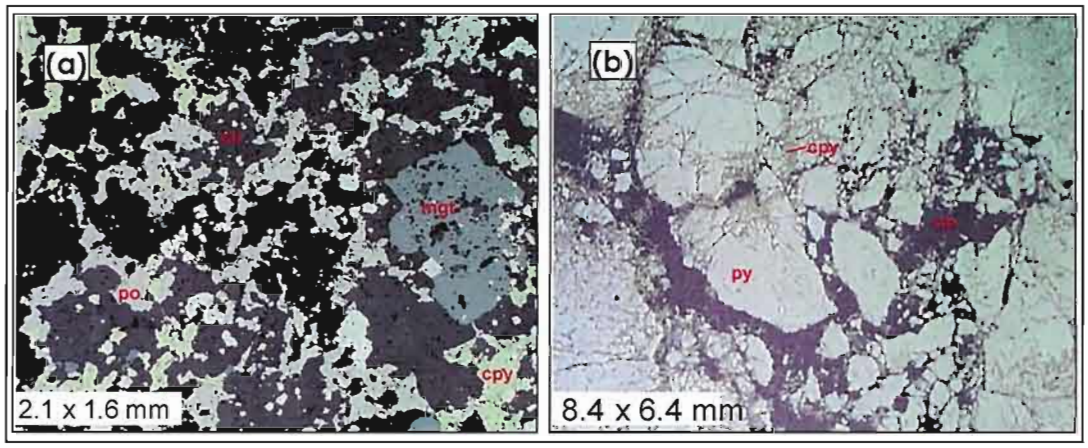

Figure 5.24. Reflected light microphotographs of; (a) typical ore texture within the dark band in sample GG24 (po- pyrrhotite, py-pyrite, mgt-magnetite, cpy- chalcopyrite and cb-carbonate); (b) typical ore texture of pyrite-chalcopyrite zone in sample GG24 (py-pyrite, cpy-chalcopyrite and cb-carbonate).

A photomicrograph of the massive pyrite in GG24 (Figure 5.24b) shows the pyrite to be highly brecciated with fractures in some cases filled by chalcopyrite but more commonly by resistive carbonate. The combination of a fine network of conductive pyrrhotite and the reduction in conductivity of the pyrite zone, due to brecciation, act together to determine the least resistive path through the sample, which in this case is through the gangue material rather than the economically important sulphide minerals. It is likely that small proportions of the highly conductive interstitial pyrrhotite observed in GG24 is distributed throughout sites 7 and 8, resulting in the extreme insitu conductivities inferred at both sites.

5.4.4. Electrical properties of MSO – 10-30%Zn

Four sites, 1, 3, 4 and 6, examined the electrical variability of the massive sphalerite pyrite ore of intermediate zinc grade (10-30%). The MSO sites are primarily composed of massive pyrite and sphalerite with secondary chalcopyrite and galena. Accessory minerals include magnetite, carbonate, quartz and minor pyrrhotite. Compositional layering was poorly developed at sites 1 and 3, but was more pronounced at sites 4 and 6. The results of Site 6 and Site 4 are explained in detail, as both are particularly interesting in showing significant scale variation.

5.4.4.1. Site 6

Site 6 was located in the sphalerite-pyrite ore as shown in Figure 5.25, together with photographs and descriptions of collected hand specimens.

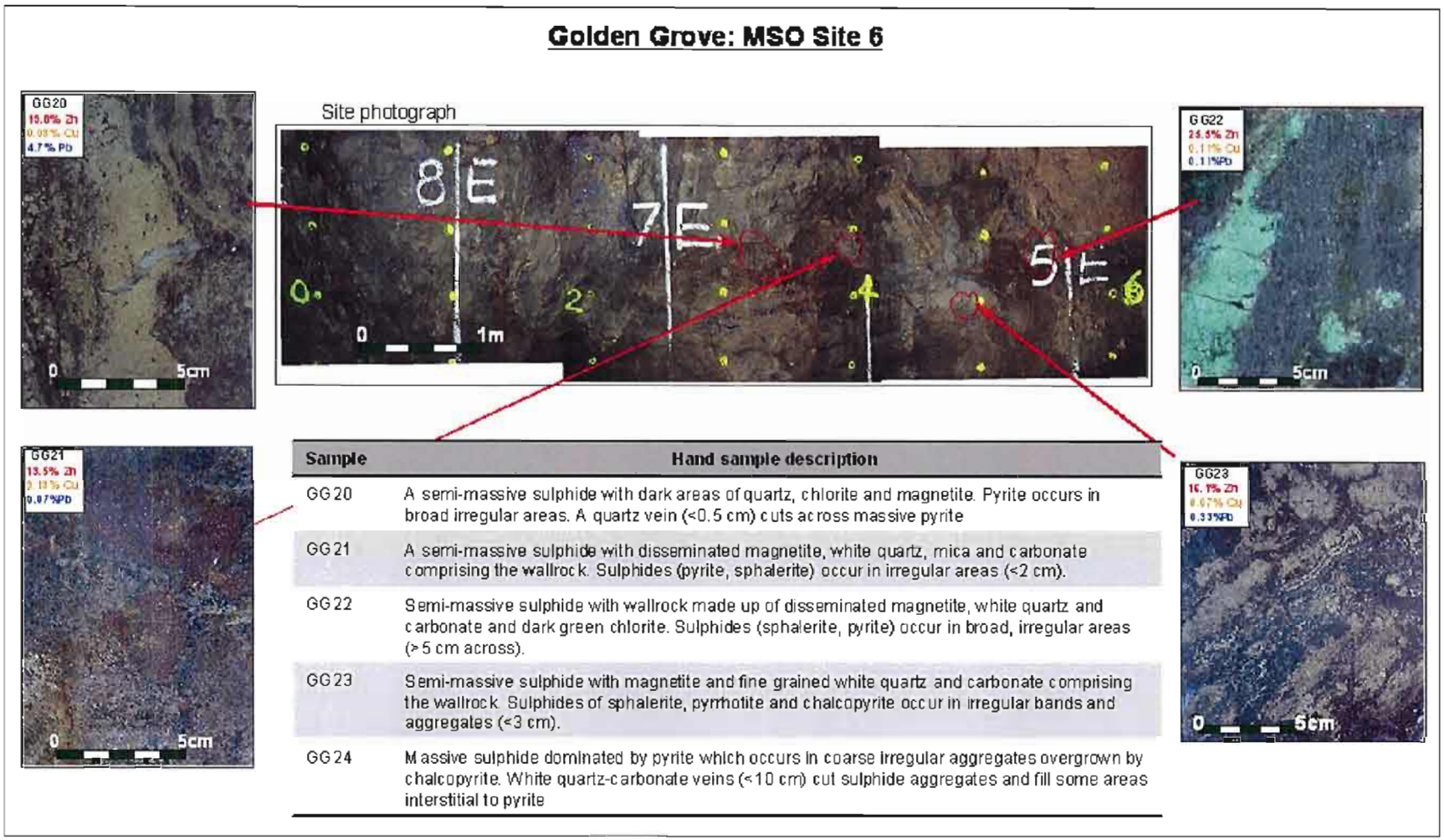

Sample	Hand sample description
GG20	A semi-massive sulphide with dark areas of quartz, chlorite and magnetite. Pyrite occurs in broad irregular areas. A quartz vein (<0.5 cm) cuts across massive pyrite
GG21	A semi-massive sulphide with disseminated magnetite, white quartz, mica and carbonate comprising the wallrock. Sulphides (pyrite, sphalerite) occur in irregular areas (<2 cm).
GG22	Semi-massive sulphide with wallrock made up of disseminated magnetite, white quartz and carbonate and dark green chlorite. Sulphides (sphalerite, pyrite) occur in broad, irregular areas (>5 cm across).
GG23	Semi-massive sulphide with magnetite and fine grained white quartz and carbonate comprising the wallrock. Sulphides of sphalerite, pyrrhotite and chalcopyrite occur in irregular bands and aggregates (<3 cm).
GG24	Massive sulphide dominated by pyrite which occurs in coarse irregular aggregates overgrown by chalcopyrite. White quartz-carbonate veins (<10 cm) cut sulphide aggregates and fill some areas interstitial to pyrite

Figure 5.25. Geology of MSO:Site 6. Site consists primarily of sphalerite-pyrite ore. The complexity of mineral textures is reflected in the various samples collected.

A total of four expanding array measurements were collected at this site (Figure 5.26). These are designated by the position with respect to 'y' (vertical) coordinate. All arrays show a significant decrease in resistivity with increasing electrode spacing. Although the curves diverge at small electrode spacing due to local effects, they all converge at larger electrode spacings. The bulk resistivity for this site is quite low (0.002 Ωm) despite the reasonably high sphalerite content (15-25% Zn).

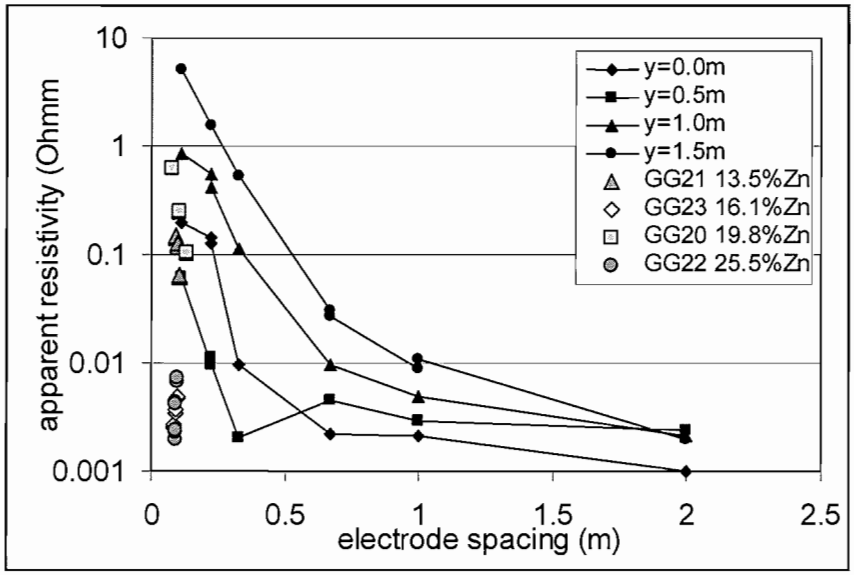

Figure 5.26. Apparent resistivity versus electrode spacing for Site 6 located in the massive sphalerite zone (MSO). Galvanic laboratory resistivity measurements of samples are also plotted.

The laboratory galvanic resistivity measurements of samples from Site 6 span a large range of values (0.002 to 0.6 Ωm), but lie within the range recorded insitu (Figure 5.26). The four samples all have similar chemistry (Table 5.4) and macroscopic mineralogy (Figure 5.24) but varying resistivity. The relatively more resistive samples GG20 and GG21 were collected from the centre of the site where small-scale insitu measurements were completed. The laboratory resistivity for these samples lies within the range defined by the small-scale insitu measurements. The relatively more conductive samples GG22 and GG23 have laboratory resistivity values that correspond more closely to the insitu values collected at larger spaced measurements.

Sample	Zn%	Cu%	Pb%	Fe_2O_3	SiO_2
GG20	19.8	0.08	4.7	35.8	3.5
GG21	13.5	0.13	0.07	47.2	5.8
GG22	25.5	0.11	0.11	37.6	4.5
GG23	16.1	0.07	0.33	46.6	5.1

Table 5.4. Geochemical assays for GG20, GG21, GG22 and GG23, showing fairly similar composition.

Maps of apparent resistivity were generated for site 6 on a grid extending from x=0 to x=6m and y=0 to 1.5m at 0.5 m intervals with the MEA orientated horizontally (Figure 5.27). The apparent resistivity map spans a wide range of values from 0.001 Ωm to 6.6 Ωm. As expected the 0.11 metre apparent resistivity map displays a wider range of values than the 0.22 metre apparent resistivity map. The apparent resistivity map shows a complex pattern, and only a general correlation with mesoscopic ore mineralogy and textures. The zone of high resistivity between 1.5 and 3.5 m corresponds to a zone of high grade coarsely crystalline sphalerite ore, which is clearly visible in the photographic image. However there are other zones that do not have a high apparent resistivity which appear to have a similar mineralogy (such as near (x,y)=3.2, 0.5; Figure 5.27). Macroscopic mineralogical variations across the site do not explain the patterns shown in the resistivity images, in particularly the more conductive zone near the base of the exposure and between 4 and 5 metres in the X direction.

Magnetic susceptibility was also recorded across the site on a 0.25 metre grid (Figure 5.27). The magnetic susceptibility and apparent resistivity maps clearly show an inverse relationship with areas of high magnetic susceptibility corresponding to low resistivity and low magnetic susceptibility to high resistivity. A scatter plot of magnetic susceptibility versus apparent resistivity is shown in Figure 5.28. The graph shows a wide scatter, but a very general negative correlation. The correlation coefficient between log(magnetic susceptibility) and log(apparent resistivity) is –0.65 for the 0.11m electrode and –0.57 for the 0.22m electrodes. Apart from the obvious zone of high grade sphalerite between 1.5 and 4 metres, which displays low susceptibility, there is no obvious correlation between macroscopic features and the magnetic susceptibility map.

The magnetic susceptibility recorded at many locations exceeds 0.5 SI units. Detailed investigation of the exposure with a hand lens indicated the presence of significant proportions of magnetite with a grain size of <1mm both within sphalerite-rich and pyritic ores. This led to the initial speculation that high concentrations of magnetite may have been responsible for the low apparent resistivities observed in these areas. However, subsequent petrographic analysis, continuity and current mapping of samples identified fine grained pyrrhotite, which formed a highly-conductive anastomosing system through the sample

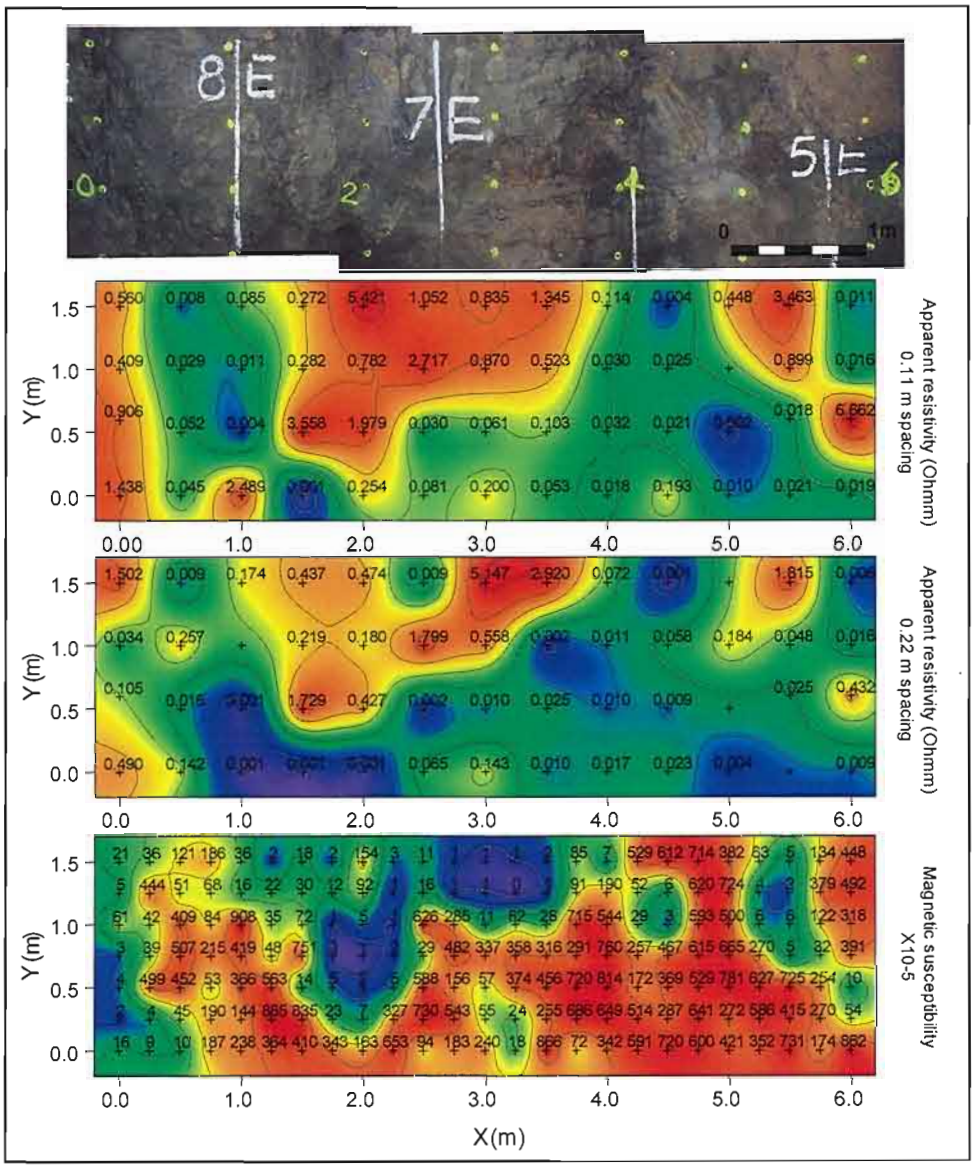

Figure 5.27. MSO-Site 6 apparent resistivity (0.11m and 0.22m) and magnetic susceptibility maps. The MEA was orientated horizontal, perpendicular to the compositional layering. Variations of resistivity do not correlate to mesoscopic or macroscopic compositional and textural features. The magnetic susceptibility map has an inverse correlation to the resistivity map.

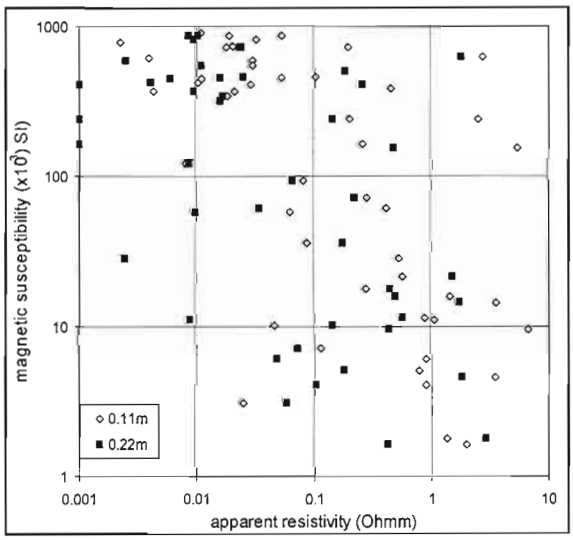

Figure 5.28. Scatter plot of magnetic susceptibility versus apparent resistivity at MSO: site 6 derived from lateral measurements. A poorly defined negative correlation is apparent; correlation coefficients –0.65 for 0.11m and –0.57 for 0.22m electrodes.

The distribution of insitu and sample resistivity measurements is shown as histograms in Figure 5.29. Both datasets show a similar bimodal logarithmic distribution, consisting of (relatively) resistive and conductive end members. The insitu measurements clearly show that the bulk response lies at the extreme end of the conductive population, indicating that on a large scale the conductive zones are well connected. In this case the most conductive sample measurement would approximate the bulk insitu resistivity response.

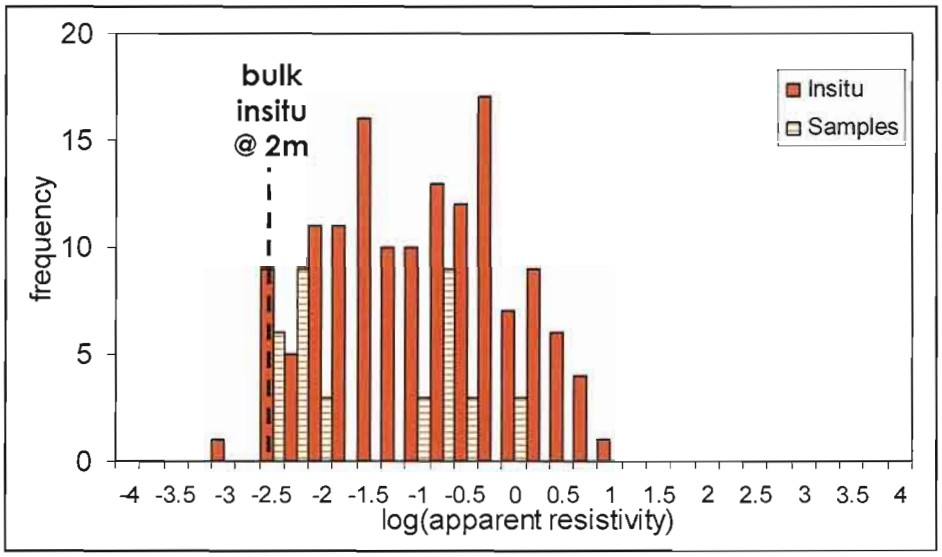

Figure 5.29. Histogram of log(apparent resistivity) shows the distribution of insitu and laboratory resistivity measurements for Site 6 located in the massive sphalerite ore (MSO). The bulk insitu apparent resistivity is also plotted.

The cause of the bimodal distribution in resistivity was further investigating by comparing the electrical properties between the conductive samples (GG22 and GG23) and the resistive samples (GG20 and GG21) using continuity and current mapping techniques.

The most resistive sample GG20 (Figure 5.30) contains bands of sphalerite and magnetite distributed through the massive pyrite, and cross-cut by a quartz vein. The continuity map (Figure 5.30c) shows high continuity occurring within bands of pyrite, whereas low continuity corresponds to areas of magnetite and sphalerite. The current images show that maximum current does not flow through the obvious continuous pyrite vein, but flows through both the pyrite and magnetite-sphalerite material (Figure 5.30c and d).

The conductive sample GG23 (Figure 5.31) has a similar composition (Table 5.4) and texture to resistive sample GG20. The continuity image of GG23 (Figure 5.31b) shows high continuity within pyrite bands. However, the current map (Figure 5.31c) shows that current flow occurs predominantly through dark sphalerite-magnetite zones, rather than the pyrite. This abnormality was further investigated by petrographic analysis.

Photomicrographs of typical micro-textures from the magnetite-sphalerite bands in both samples (GG20 and GG23) are shown in Figure 5.32. In sample GG20 magnetite, sphalerite and pyrite are in roughly equal proportions.

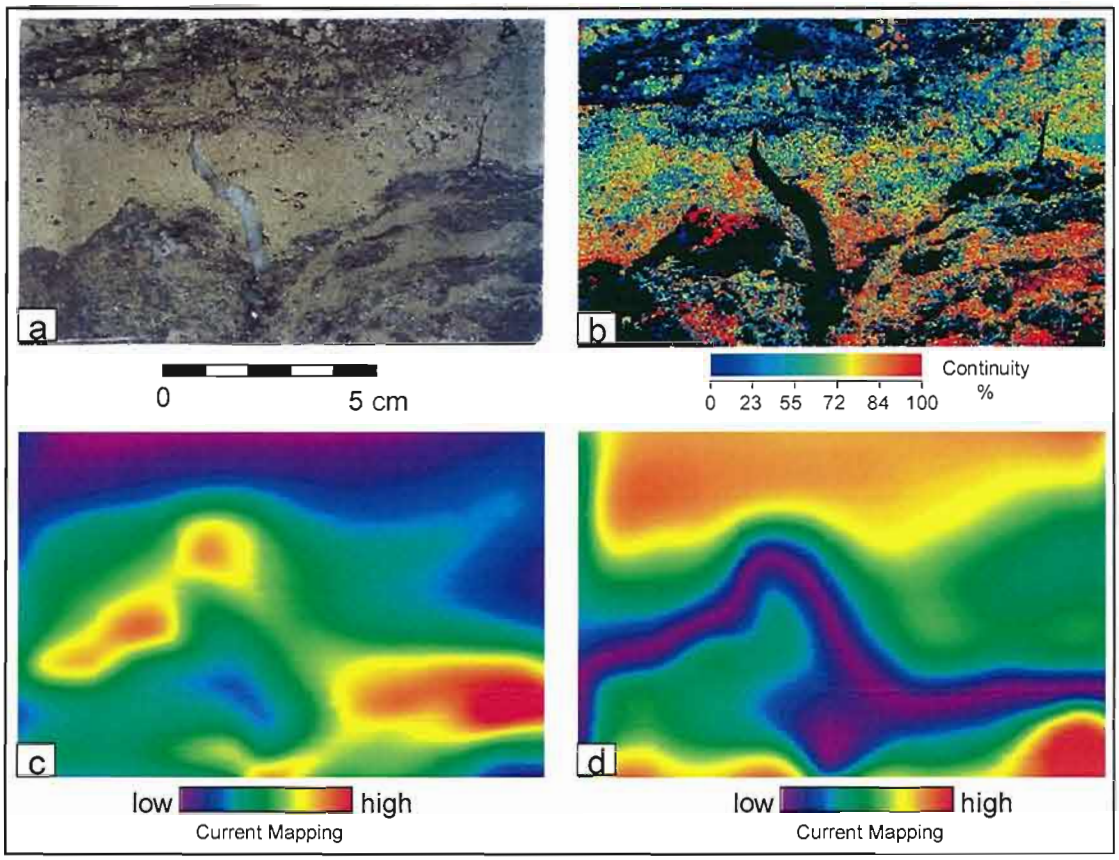

Figure 5.30. Continuity and current mapping results for sample GG20 collected from Site 6 (MSO). (a) Optical image. (c) Continuity image (histogram-equalised colour distribution). (c) Y component current map. (d) Z component current map. Maximum current flow (Y-max, Z-min).

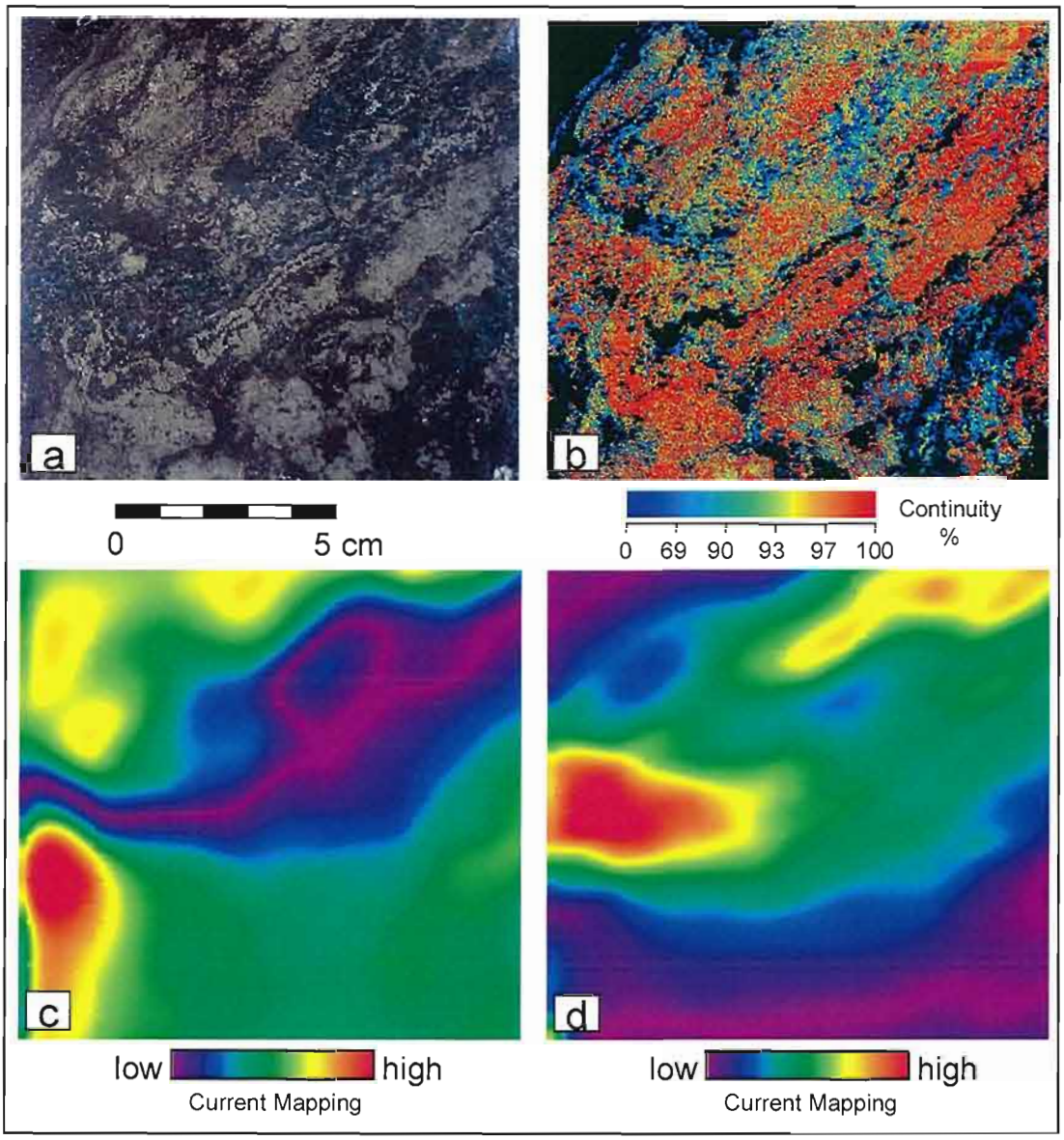

Figure 5.31. Continuity and current mapping results for sample GG23 collected from Site 6 (MSO). (a) Optical image. (c) Continuity image (histogram-equalised colour distribution). (c) Y component current map. (d) Z component current map. Maximum current flow is observed in the sphalerite-magnetite bands and indicated by Y-maximum and Z-minimum.

Magnetite and pyrite crystals are generally euhedral and seldom form large connected aggregates. Quartz, chlorite, white mica and carbonate are interstitial to the magnetite and pyrite. In sample GG23 (Figure 5.32b), magnetite is more abundant and forms an aggregate in the groundmass together with sphalerite, carbonate and quartz. However, the most significant difference when compared to GG20 is the presence of pyrrhotite veins that form a connected network and provide an obvious preferential pathway for electrical conduction. The distribution of the pyrrhotite micro-veining within the sample correlates to the distribution of maximum current flow in the GG23 current map (Figure 5.31).

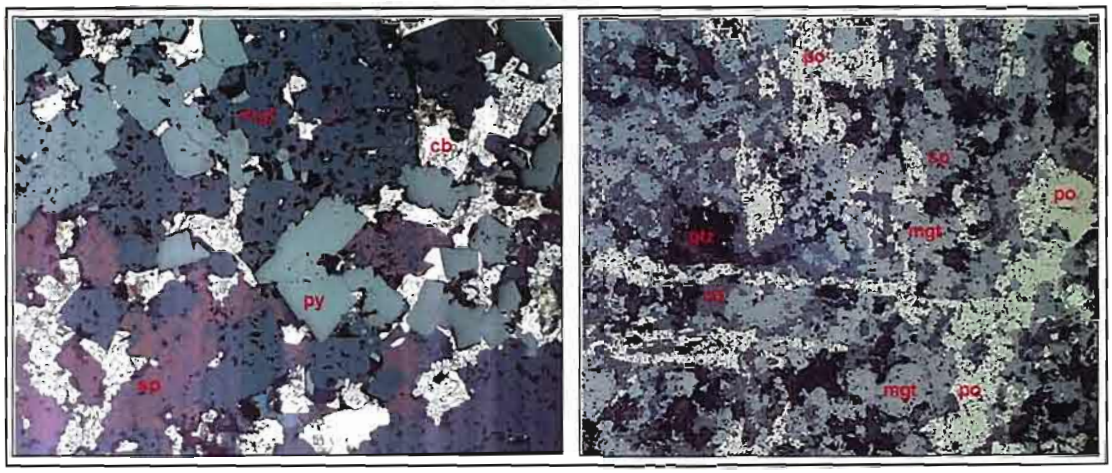

Figure 5.32. Reflected light microphotographs of; (a) typical ore texture from sample GG20, composite reflected and transmitted light; (b) typical ore texture from sample GG23. The main difference between the two samples is the presence of a continuos network of pyrrhotite in GG23. (py-pyrite, mgt-magnetite, sp-sphalerite, cb-carbonate, po- pyrrhotite, and qtz-quartz).

Petrographic inspection of the other samples from Site 6, GG21 and GG22 showed similar micro-textural associations with pyrrhotite present in GG22, but not in GG21. Thus, the high conductivities recorded for samples GG22 and GG23 are attributed to the presence of a very small proportion of highly conductive pyrrhotite forming an anatomising network interstitial to the sphalerite-magnetite. The more resistive samples, GG20 and GG21, do not contain connected networks of pyrrhotite and current predominantly flows through the relatively more resistive pyrite bands. It is interesting to note that although pyrrhotite appears to be the most important conductive mineral, it occurs in small proportions and its disproportionate electrical influence is attributed to its microscopic texture. The presence of pyrrhotite also explains the negative correlation previously observed between apparent resistivity and the magnetic susceptibility measurements (Figure 5.26), the conductive pyrrhotite not only is magnetic itself, but is commonly associated with the distribution of magnetite. Thus, high magnetic susceptibility and low resistivity observed insitu correlate to zones of magnetite-pyrrhotite.

The presence of pyrrhotite, forming a conductive network within the pyrite-sphalerite ore (also conductive, but to lesser an extent) can adequately explain the scale variations in apparent resistivity observed insitu. The bimodal distribution observed insitu and in laboratory resistivity data, can be considered a mixture of two distinct end members. The conductive end member has been identified to contain pyrrhotite, whereas its absence is noted in the resistive end member. The decrease of insitu apparent resistivity within increasing scale of investigation, reflects a greater connectivity of both pyrrhotite and pyrite conductive networks at larger scales at this site. This result is significant in that even in a pyrite-pyrrhotite dominant system, the contrast in resistivity between these two "conductive" minerals can result in scale variation in resistivity of several orders of magnitude.

5.4.4.2. Site 4

Site 4 is an extremely heterogeneous example of the MSO ore type, exhibiting a wide variety of different ore textures and mineral associations as shown in Figure 5.33.

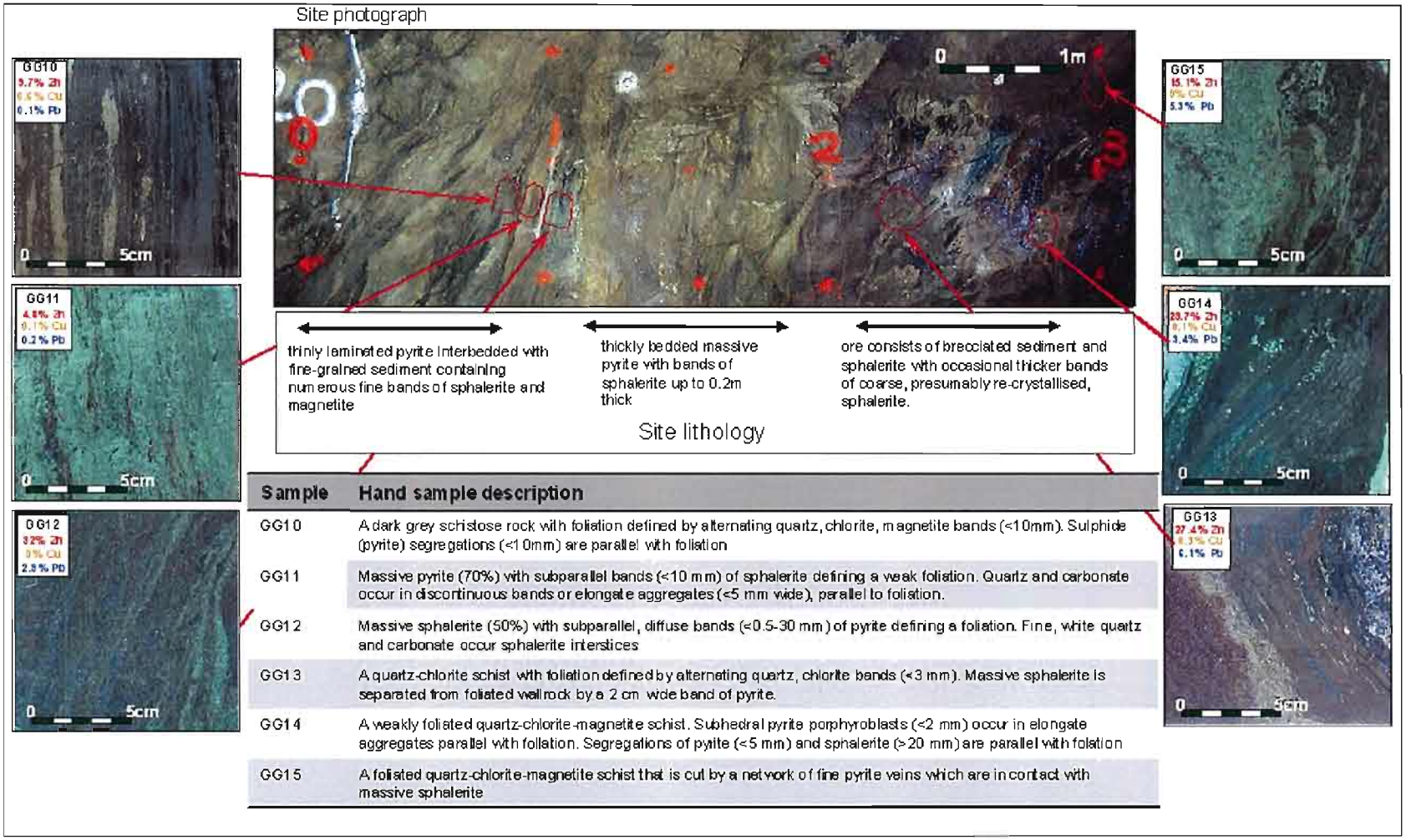

Sample	Hand sample description
GG10	A dark grey schistose rock with foliation defined by alternating quartz, chlorite, magnetite bands (<10mm). Sulphide (pyrite) segregations (<10mm) are parallel with foliation
GG11	Massive pyrite (70%) with subparallel bands (<10 mm) of sphalerite defining a weak foliation. Quartz and carbonate occur in discontinuous bands or elongate aggregates (<5 mm wide), parallel to foliation.
GG12	Massive sphalerite (50%) with subparallel, diffuse bands (<0.5-30 mm) of pyrite defining a foliation. Fine, white quartz and carbonate occur sphalerite interstices
GG13	A quartz-chlorite schist with foliation defined by alternating quartz, chlorite bands (<3 mm). Massive sphalerite is separated from foliated wallrock by a 2 cm wide band of pyrite.
GG14	A weakly foliated quartz-chlorite-magnetite schist. Subhedral pyrite porphyroblasts (<2 mm) occur in elongate aggregates parallel with foliation. Segregations of pyrite (<5 mm) and sphalerite (>20 mm) are parallel with foliation
GG15	A foliated quartz-chlorite-magnetite schist that is cut by a network of fine pyrite veins which are in contact with massive sphalerite

Figure 5.33. Geology of MSO:Site 4. Site is extremely heterogeneous with a large variety of different ore textures and mineral associations. The heterogeneity is reflected in the various samples collected.

At the left-hand end of the exposure (between 0 and 1metres) the ore is thinly bedded to laminated and consists of pyrite and fine-grained sediment with numerous thin bands of sphalerite and magnetite (Figure 5.33). Between 1 and 2 metres, the ore is more thickly bedded with bands of pyrite and sphalerite up to 0.2 metres thick. From 2 to 3 metres the ore consists of brecciated sediment and sphalerite with occasional thicker bands of coarse, presumably re-crystallised, sphalerite. Measurements were performed both perpendicular and parallel to the compositional layering at this site. The heterogeneity of the site is reflected in the mesocopic variations observed in collected samples, especially the differences between GG10, GG11 and GG12 which were collected from adjacent locations.

The expanding array measurements at site 4 (Figure 5.34) shows a significant decrease in apparent resistivity with increasing electrode spacing (6.2 Ωm to 0.05 Ωm). Galvanic measurements of samples from this site show an even greater range of apparent resistivity from 0.006 to 141 Ωm. The median of laboratory sample data (1.6 Ωm) is close to the resistive limit of the insitu data (i.e. insitu resistivity derived from small electrode spacing).

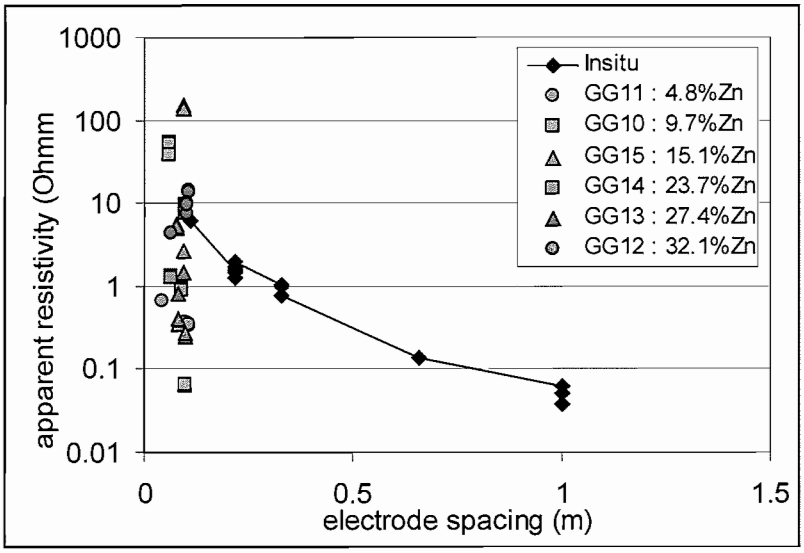

Figure 5.34. Apparent resistivity versus electrode spacing for Site 4 located in the massive sphalerite zone (MSO). Galvanic laboratory resistivity measurements of samples are also plotted.

A map of apparent resistivity on a grid extending from x=0 to x=3m (Figure 5.35) was generated with the MEA orientated perpendicular to layering. The variations observed in the apparent resistivity are similar for both 0.11 m and 0.22 m maps. Marked variations in the apparent resistivity images correspond to the obvious variations in the ore texture. The finely layered ore from 0 to 1 metres is most conductive, the more massive ore centred in the grid (1-2 metres) is relatively more resistive, whilst the sphalerite-schist section (2-3 metres) displays the highest resistivity.

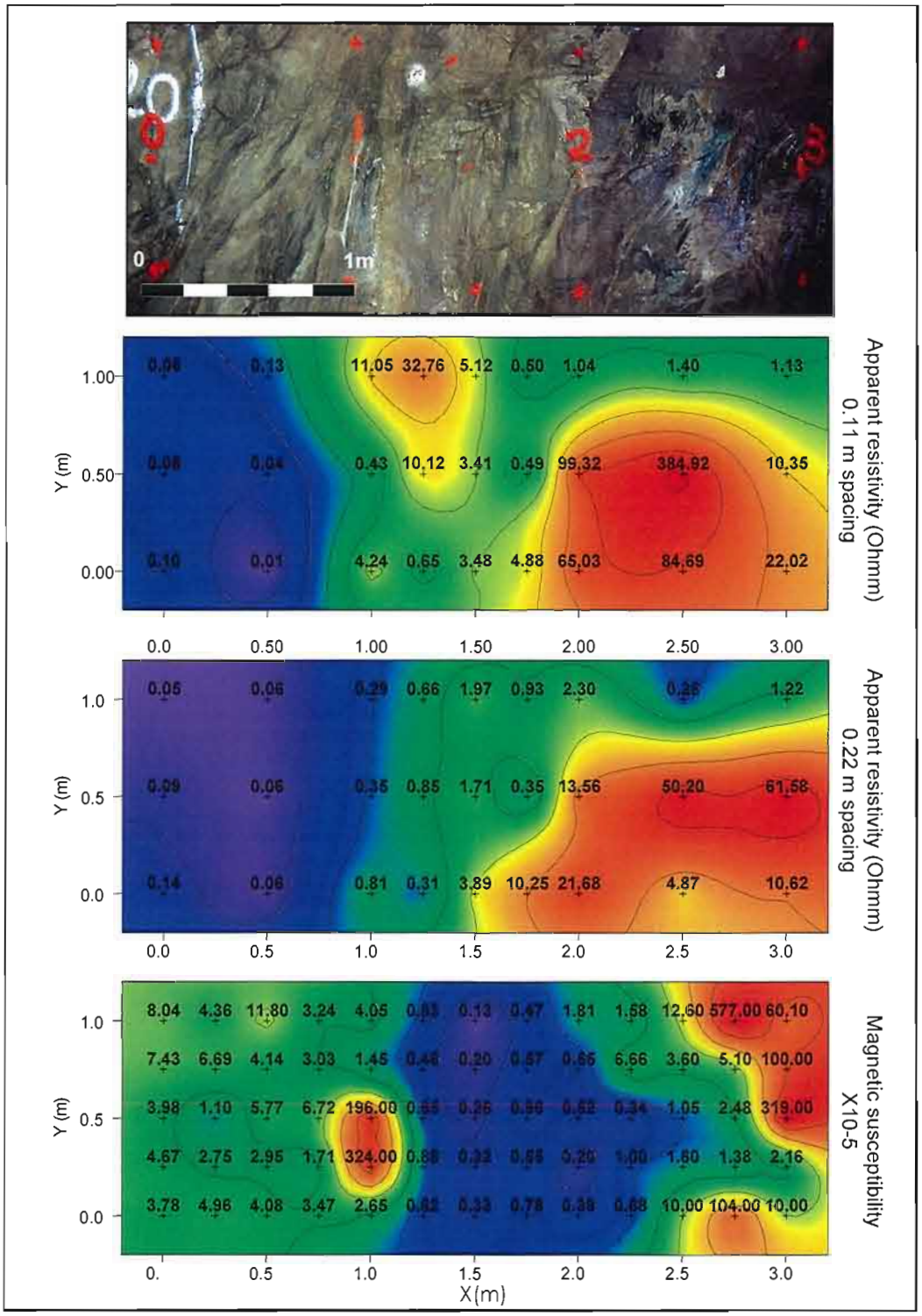

Figure 5.35 MSO-Site 4 apparent resistivity and magnetic susceptibility maps. The MEA was orientated perpendicular to the compositional layering. Variations of resistivity correlate to obvious compositional and textural features. The magnetic susceptibility map has an inverse correlation to the resistivity map.

Magnetic susceptibility measurements were also conducted across the grid (Figure 5.35). The ore textural boundaries are clearly apparent in this image. Of particular note are the zones of extremely high magnetic susceptibility within the sphalerite-breccia ore, which presumably mark accumulations of magnetite. Magnetic susceptibility is plotted as a function of apparent resistivity for Site 4 in Figure 5.36 Despite the general correlation of both parameters with ore texture and mineralogy there is no clear overall correlation between magnetic susceptibility and apparent resistivity.

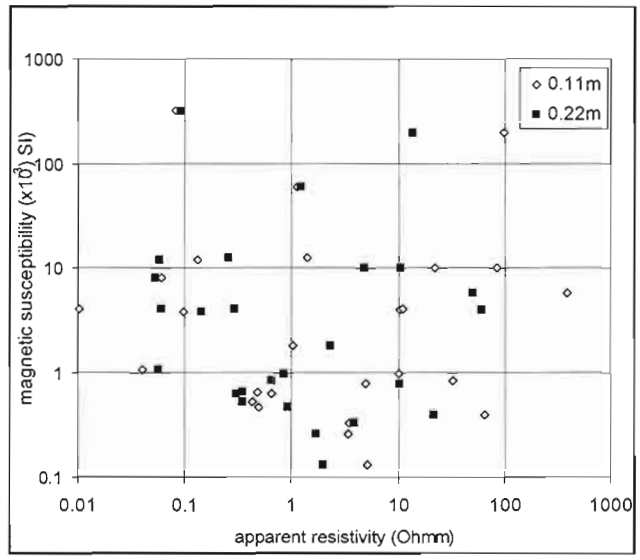

Figure 5.36. Scatter plot of magnetic susceptibility versus apparent resistivity at MSO: site 4 derived from lateral measurements. No clear correlation between the two parameters is evident.

The histogram of insitu and laboratory measurements (Figure 5.37) for Site 4 shows a variable distribution reflecting the heterogeneity of the site. Despite the heterogeneity, the bulk resistivity lies towards more extreme conductivity values. As observed at Site 6, the most conductive sample measurement would provide a better estimate of the bulk insitu response rather than the mean or median.

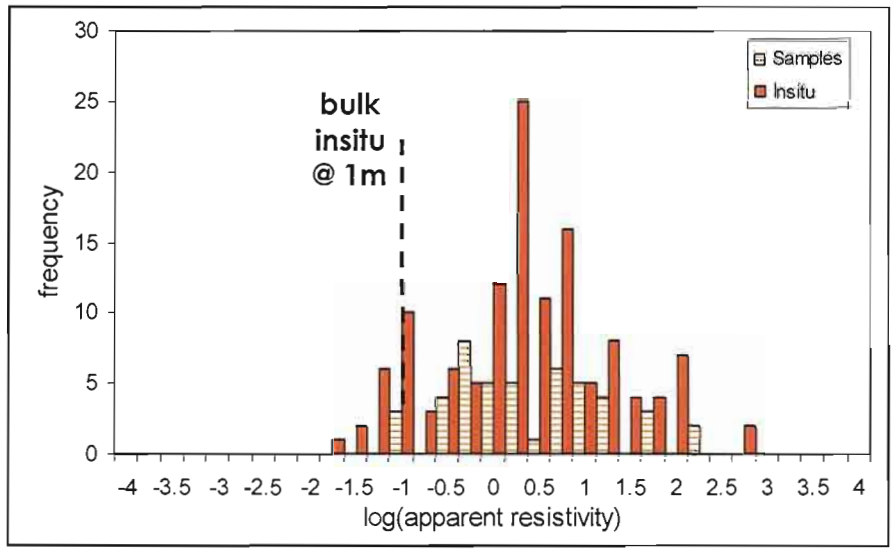

Figure 5.37 Histogram of log(apparent resistivity) shows the distribution of insitu and laboratory resistivity measurements for Site 4 located in the massive sphalerite zone (MSO). The bulk insitu apparent resistivity is also plotted. Both sets of measurements show a log-normal distribution.

The variation observed in the resistivity was further investigated by detailed laboratory analysis of samples. Out of all the samples, GG10 is the most interesting, in that it exhibits extreme anisotropy and the resistivity of the sample (0.06 to 52 Ωm) spans nearly the entire range observed for insitu measurements. The sample was collected from the most conductive zone measured insitu within the finely layered sediments. GG10 is a dark grey schistose rock with foliation defined by alternating quartz, chlorite, magnetite bands (<10mm). Sulphide (pyrite) segregations (<10mm) are parallel with

foliation (Figure 5.33). Sample assays indicate 9.7% zinc, 0.6% copper and 0.1% lead.

Galvanic laboratory measurements of sample GG10 conducted parallel to the banding produced the lowest resistivity (~0.05 Ωm), whereas perpendicular measurements produced the highest values (~50 Ωm). Continuity mapping clearly identifies a number of pyrite rich veins associated with high values (low resistance) (Figure 5.38). Sphalerite and chlorite-quartz bands are indicated by null values. Despite the large number of connected pyritic veins, current mapping shows current to preferential flow within the thickest continuous band (Figure 5.38 c and d).

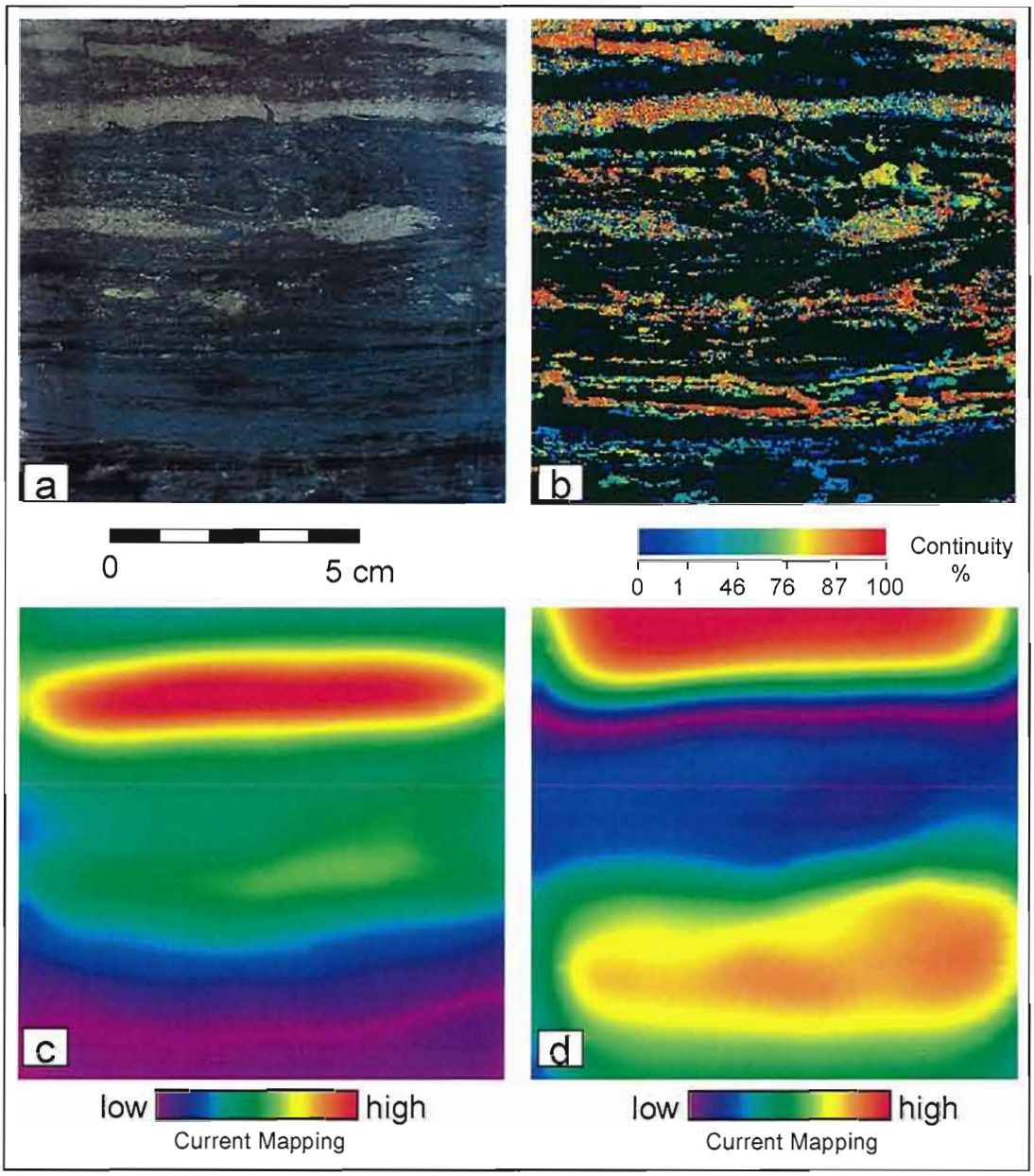

Figure 5.38. Continuity and current mapping results for sample GG10 collected from Site 4 (MSO). (a) Optical image. (b) Continuity image (histogram-equalised colour distribution). (c) Y component current map. (d) Z component current map. Maximum current flow is observed in the pyrite bands and indicated by Y-maximum and Z-minimum.

Petrographic analysis (Figure 5.39) of the sample show the pyrite bands (<4 mm) to consist of loosely interlocking pyrite euhedra. Sphalerite is present as elongate anhedral grains aligned parallel with foliation. It is commonly

intergrown with magnetite and chalcopyrite. Pyrrhotite is present in only minor amounts, with chalcopyrite and sphalerite.

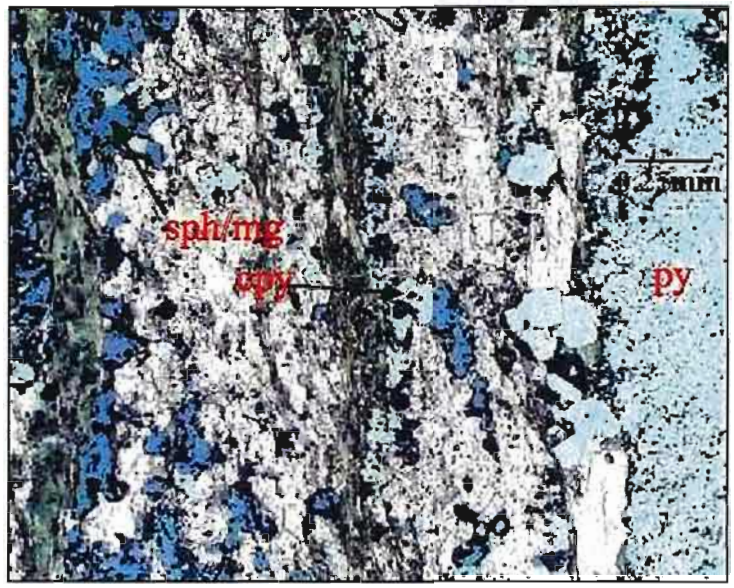

Figure 5.39. Reflect light photomicrograph of GG10 showing the massive pyrite aggregate and sphalerite-magnetite foliations. sph: sphalerite, mg: magnetite, cpy: chalcopyrite, py: pyrite.

The layered texture of GG10 explains the sample's extreme resistivity anisotropy. The continuous pyrite layers provide pathways for preferential current flow in measurements conducted parallel to layering, and hence low sample resistivity. Whereas, in the orthogonal direction current is impeded by resistive sphalerite and magnetite bands, and hence significantly increases the sample resistivity. These pyrite veins occur in all samples (Figure 5.32), although in varying quantities in each. The variability in continuous veins in each sample is likely to account for the wide range of sample resistivity (Figure 5.34; Figure 5.37). As these conductive veins become better connected at larger scales, as measured insitu, the bulk apparent resistivity will decrease.

5.4.5. Electrical properties of MSS – 30+%Zn

Two sites, 5 and 14, examined the electrical variability of the massive sphalerite pyrite ore of high zinc grade (30-50+%) (MSS). The MSS sites are primarily composed of massive sphalerite and pyrite with secondary galena. Accessory minerals include chalcopyrite, magnetite, carbonate, quartz and minor pyrrhotite. Compositional layering was poorly developed at site 5 and well defined at site 14. The results of Site 14 will be discussed in detail.

Site 14 was located in high-grade sphalerite-pyrite ore in the hanging-wall drive. The rockmass at this site is characterised by decimetre scale irregular compositional banding (Figure 5.40). Changes in ore composition are reflected by variations in colour and texture with darker zones marking zones of sphalerite-rich ore, whilst lighter tones indicate areas of higher pyrite concentration.

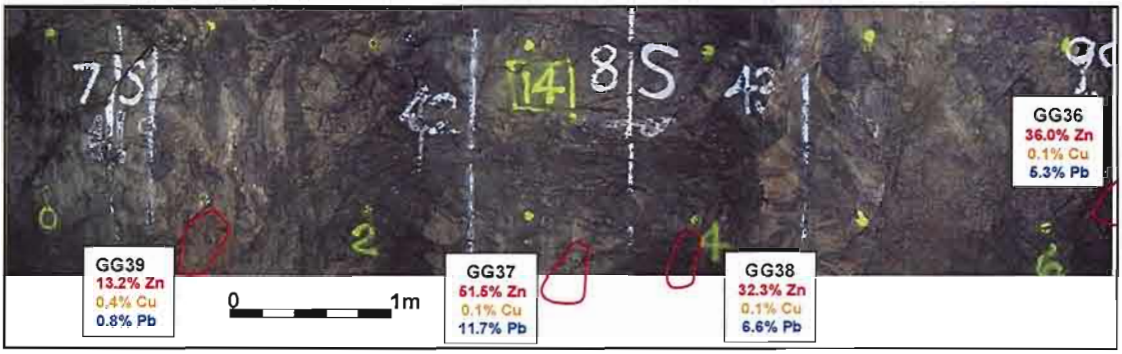

Figure 5.40. Site photograph and sample locations for Site 14 located in the MSS ore. Dark areas distinguish sphalerite rich zones, lighter areas distinguish pyritic rich zones.

The expanding array measurements at site 14 (Figure 5.41), show a steady decrease in apparent resistivity (10 to 0.2 Ωm) with increasing electrode spacing. It important to note that despite the material from this site having an excess of 30% zinc content, the bulk resistivity is less than 1 Ωm. Galvanic resistivity measurements of samples from site 14 (Figure 5.41) range across three orders of magnitude from 0.2 Ωm (GG36) to 44 Ωm (GG37) and are consistent with values recorded during insitu mapping. The samples only differ by minor compositional and textural variations.

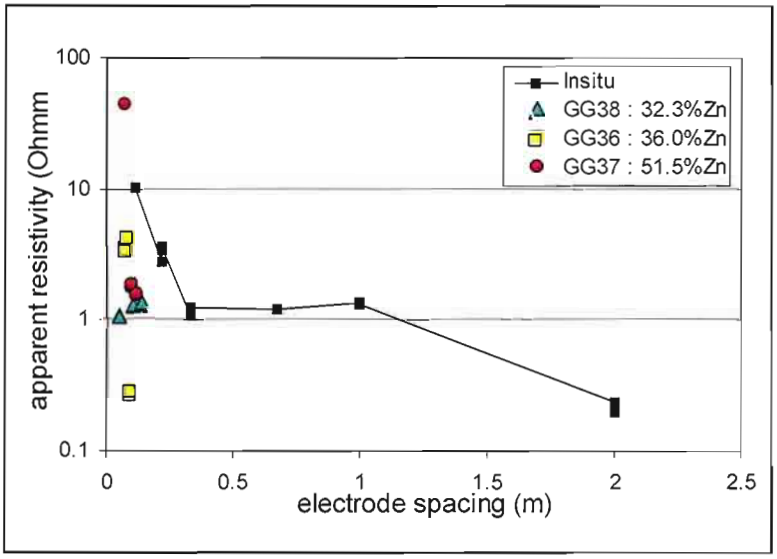

Figure 5.41. Apparent resistivity versus electrode spacing for Site 14 located in the massive sphalerite zone (MSS). Galvanic laboratory resistivity measurements of samples are also plotted.

A grid of apparent resistivity and chargeability measurements was recorded at this site using the MEA (Figure 5.42). The apparent resistivity maps for 0.11m and 0.22 metre electrode spacings are very similar and show a central zone of high resistivity (up to 125 Ωm) flanked by more conductive regions (as low as 0.01 Ωm). The resistive zone correlates to very high grade sphalerite ore, whilst the conductive flanks correlate to areas enriched in pyrite.

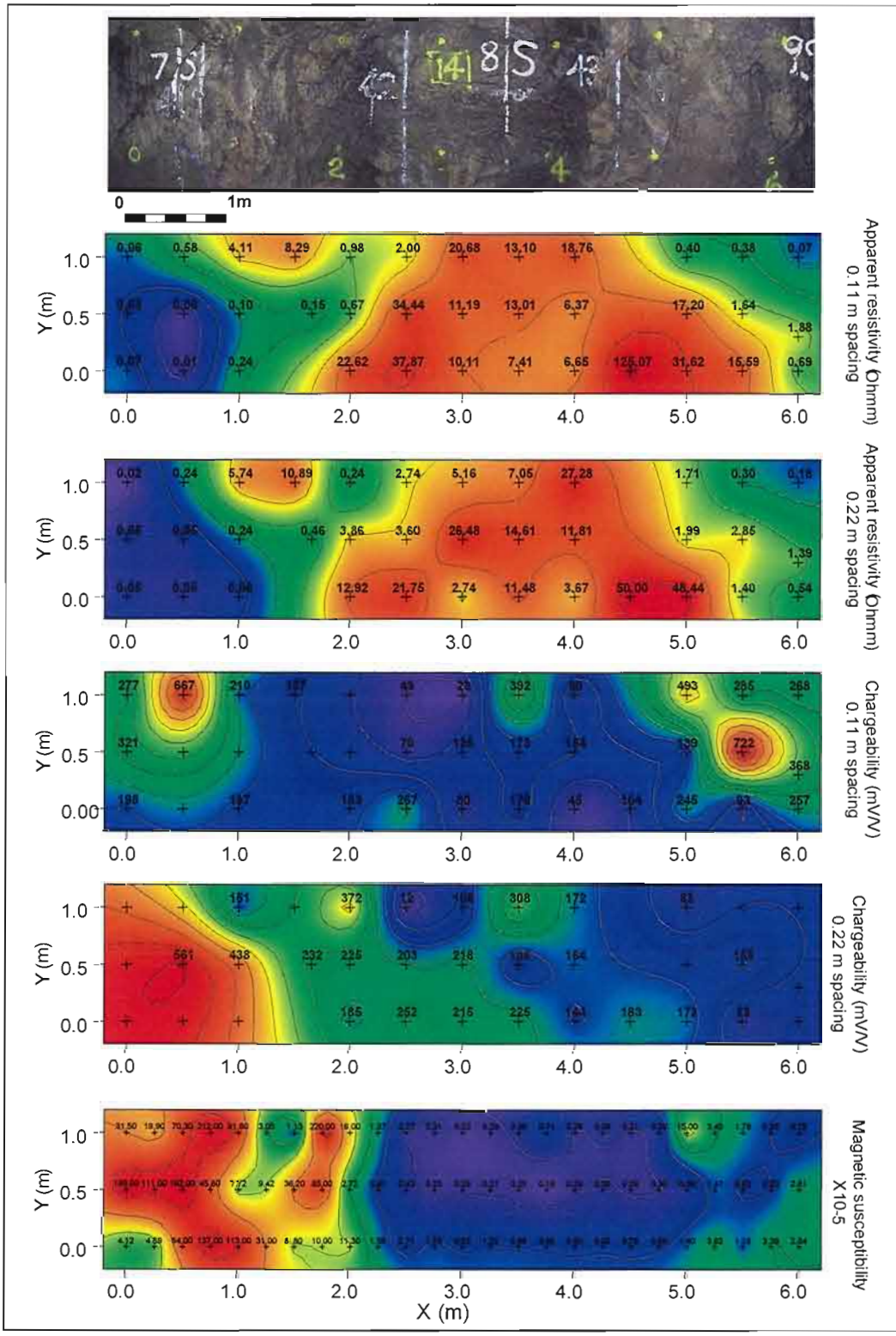

Figure 5.42. Apparent resistivity, chargeability and magnetic susceptibility maps for Site 14 (MSS). The MEA was orientated perpendicular to the compositional layering. Variations of resistivity do not appear to correlate to mesoscopic or macroscopic compositional and textural features. Chargeability images have numerous values missing and as a result differ significantly, although generally high chargeability values are associated within pyritic-enriched zones. The magnetic susceptibility map has an inverse correlation to the resistivity map.

Chargeability maps (Figure 5.42) have numerous missing values and significant local variability. Higher chargeability values are generally associated with the pyrite-enriched areas (up to 722mV/V) with lower values recorded within the massive sphalerite.

Magnetic susceptibility mapping was conducted over the same grid at 0.25 metre intervals (Figure 5.42). The magnetic susceptibility image generally shows a negative correlation with the apparent resistivity image (Figure 5.42). This correlation is also illustrated by the cross plot of magnetic susceptibility against apparent resistivity (Figure 5.43). The cross-plot clearly shows a broad negative correlation, with correlation coefficients of -0.5 and –0.48 for respective measurements at 0.11 metre and 0.22 metre spacings.

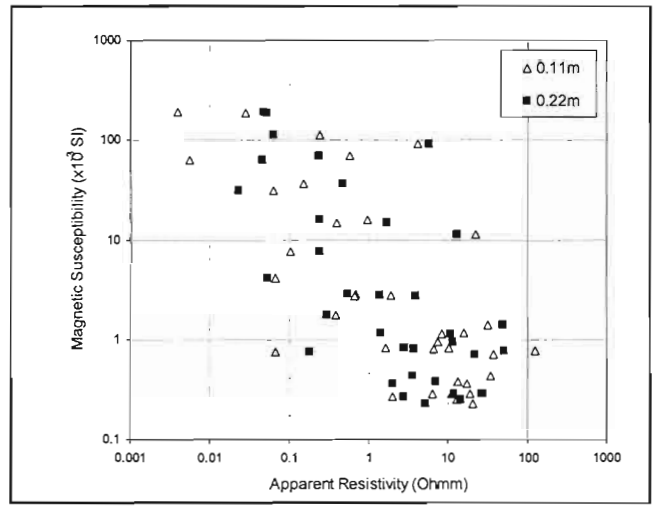

Figure 5.43. Scatter plot of magnetic susceptibility versus apparent resistivity at MSS: site 14 derived from lateral measurements. There is a moderate negative correlation between resistivity and magnetic susceptibility. Correlation coefficients for 0.11m: -0.5 and 0.22m: –0.48.

The histogram of insitu and laboratory measurements (Figure 5.44) for Site 14, show a variable distribution and a wide range of values. The bulk resistivity lies towards more extreme conductivity values. Again, the most conductive sample measurement would best approximate the bulk insitu response.

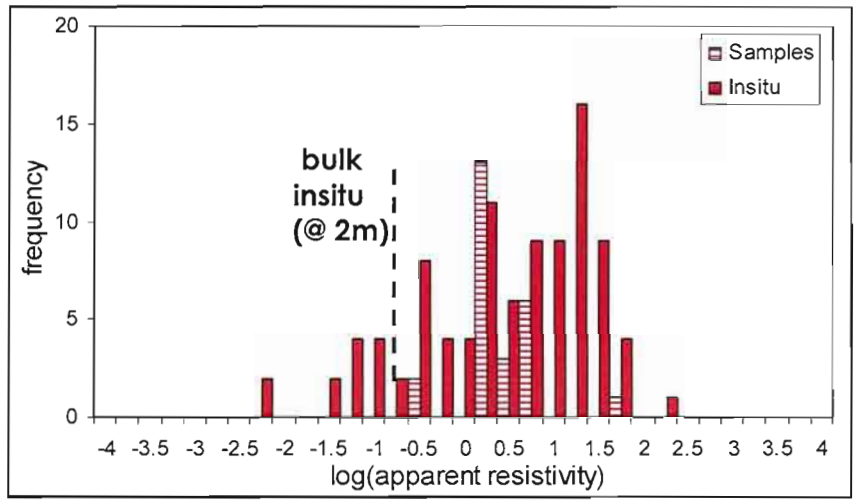

Figure 5.44. Histogram of log(apparent resistivity) shows the distribution of insitu and laboratory resistivity measurements for Site 14 located in the massive sphalerite zone (MSS). The bulk insitu apparent resistivity is also plotted. Both sets of measurements show a log-normal distribution.

The samples collected from site 14 consist of massive sulphide with areas of sphalerite cut by sub-parallel bands of pyrite (3-30 mm) (Figure 5.45). Continuity and current mapping of samples from Site 14 show current to preferentially flow through within these pyrite veins, similar to the MSO sites. Thus, despite the high sphalerite content, galvanic resistivity measurements of

samples are quite low (0.2-6 Ωm) as conduction is unimpeded through the pyrite.

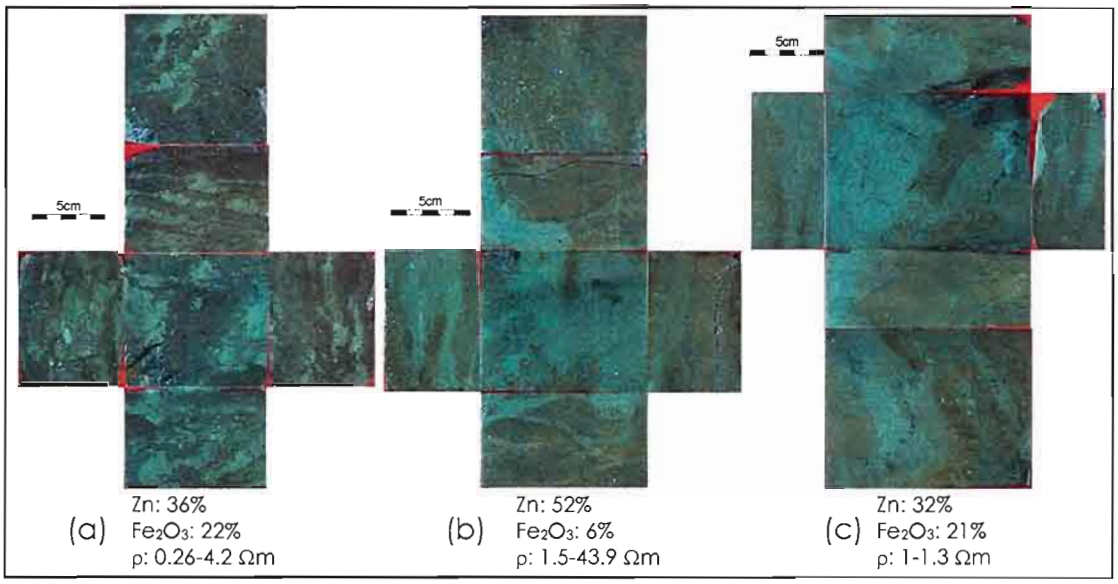

Figure 5.45. Samples from MSS ore, Site 5. (a) GG36: Massive sphalerite enclosing irregular, elongate, sub-parallel aggregates (<2-30 mm) of pyrite, (b) GGG37 and (c) GG38: Massive sulphide with areas of sphalerite cut by sub-parallel bands of pyrite (3-30 mm). Areas of fine grained white quartz and carbonate in sphalerite are sub-parallel to bands of pyrite.

In contrast, several samples collected from MSS Site 5, contained less pyritic material and had higher resistivity, up to several thousand Ωm. Sphalerite-rich samples GG16, GG17 and GG18 are shown in Figure 5.46. The continuity and current mapping on the massive sphalerite sample GG17 yielded null results, indicating no conducting pathways within the sample. For one of the MSS samples collected from Site 5, GG16, continuity and current mapping (Figure 5.47) identified conduction to occur through the sphalerite rich ores, via pyrite veins. Petrographic analysis (Figure 5.48) shows the galena occurs in sphalerite interstices and enclosing pyrite crystals.

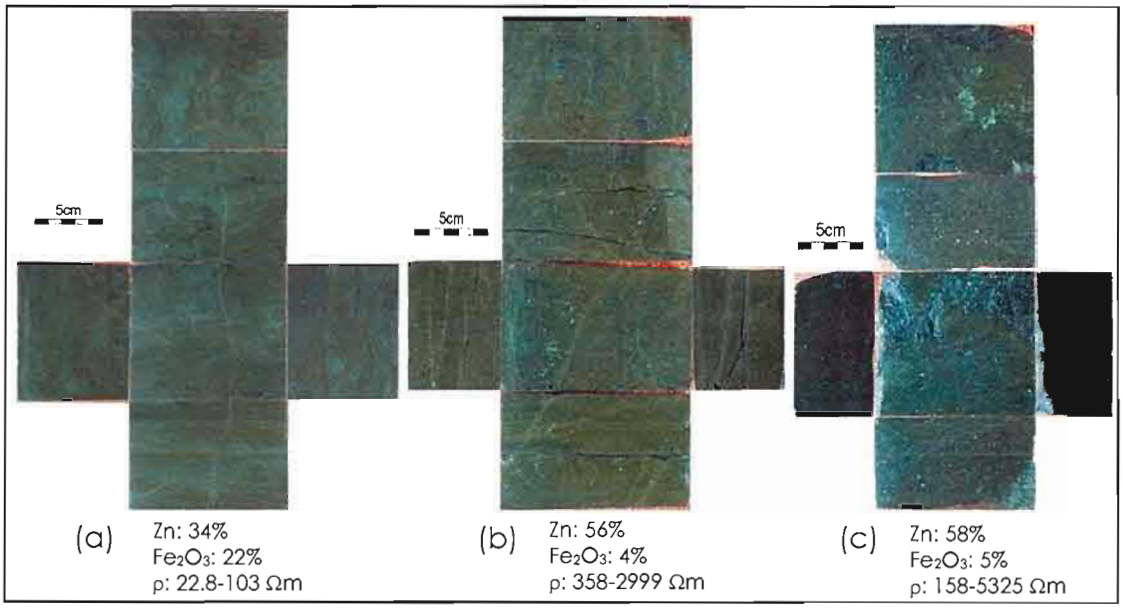

Figure 5.46. Samples from MSS ore, Site 14 (a) GG16: Massive sulphide with sub-parallel and discontinuous bands (<0.5-2 cm) of euhedral pyrite enclosed in sphalerite, (b) GG17: Massive sphalerite with white quartz and carbonate occurring as fine, sparse inclusions, (c) GG18: Massive sphalerite with irregular patches (<0.5 cm) of dark green chlorite.

The samples from Site 5 tabulated in Table 5.5 show the wide variation in resistivity is primarily controlled by composition, with resistivity being proportional to both increasing zinc grade and decreasing pyrite content. In samples GG17 and GG18, the pyrite does not form continuous veinlets. The electrical anisotropy of the samples is influenced by the sulphide texture.

Sample	Zinc grade (Vol %)	Approx. pyrite content (Vol%)	Apparent resistivity (Ωm)	Anisotropy ratio
GG19	16.2	38.4	1.7-5.8	3.4
GG16	33.7	23.9	22.8-103	4.5
GG17	56.4	4.0	358-2999	8.4
GG18	58.8	4.9	158-5325	33

Table 5.5. Samples in order of increasing zinc grade. Pyrite content is approximated from Fe_2O_3 assay with these samples containing little/no magnetite. The combined effect of increasing zinc grade and decreasing pyrite content correlates to increasing resistivity of the samples. Arrows indicate trends.

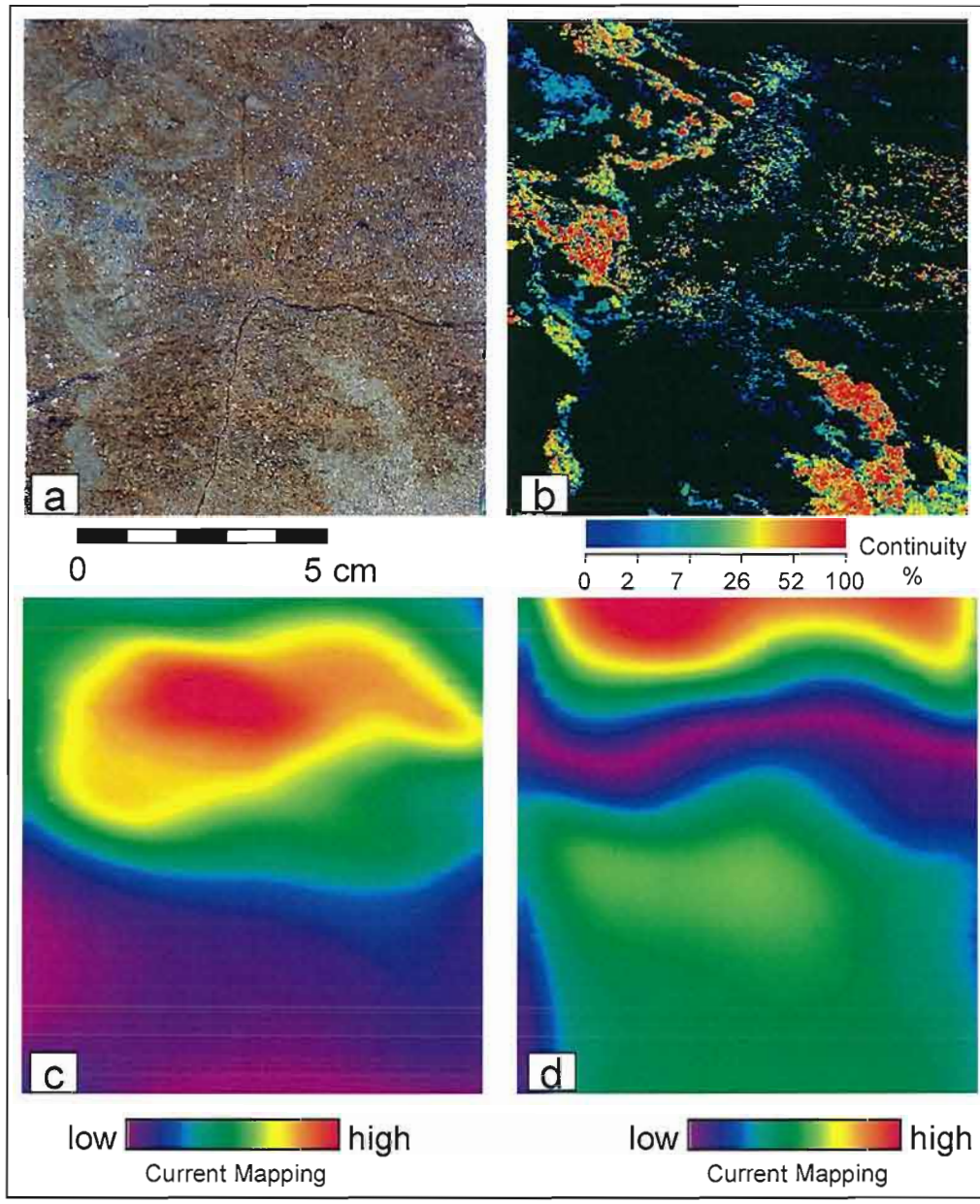

Figure 5.47. (a) Photograph, (b) continuity and (c) current mapping images of sample GG16 collected from Site 5 (MSS). Continuity highlights the presence of pyrite and galena veins occurring within the resistive sphalerite.

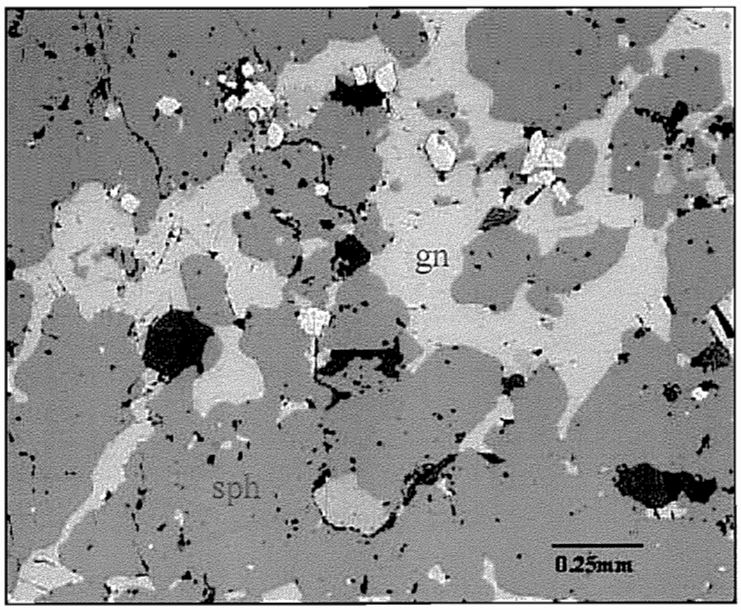

Figure 5.48. Reflected light photomicrograph of GG16, collected from Site 5 (MSS), showing galena occurring in sphalerite interstices and enclosing pyrite crystals. Py: pyrite, gn: galena, sph: sphalerite.

The insitu scale variation in resistivity observed at MSS sites is attributed to an increase in connectivity of preferential pathways, predominantly due to local accumulations of pyrite and in some cases galena within the resistive sphalerite. This results in the decrease in insitu apparent resistivity for larger scale measurements.

5.4.6. Hanging-wall host volcanics

The hanging-wall host-volcanic unit was examined at one location (Site 2). Site 2 (Figure 5.49) was located in hard fine-grained foliated metasediments in the hanging-wall of the deposit. Insitu measurements were conducted at this site parallel to bedding. In the sediments immediately overlying the ore body, thin layers of pyrite are common parallel to bedding planes (Figure 5.48a).

Insitu apparent resistivity as a function of electrode spacing is shown in Figure 5.50. A steady decrease in apparent resistivity from 2290 Ωm to 22 Ωm occurs as electrode spacing increases from 0.11 to 4 metres. Galvanic measurements of samples are consistent with insitu measurements at small spacings. The low resistivities recorded for larger electrode spacings may indicate the cumulative effects of the thin pyrite layers.

The two samples collected from the site, GG05 and GG06 (Figure 5.5c) are both quartz-chloritic schists containing sparse quartz-sulphide veins parallel to the foliation. Sample GG06 also contains disseminated and randomly oriented pyrrhotite needles (<2 mm long). Both samples contain less than 1% sulphides which are sparsely distributed. The high resistivity of the samples and very low sulphide content negated the use of continuity and current mapping methods.

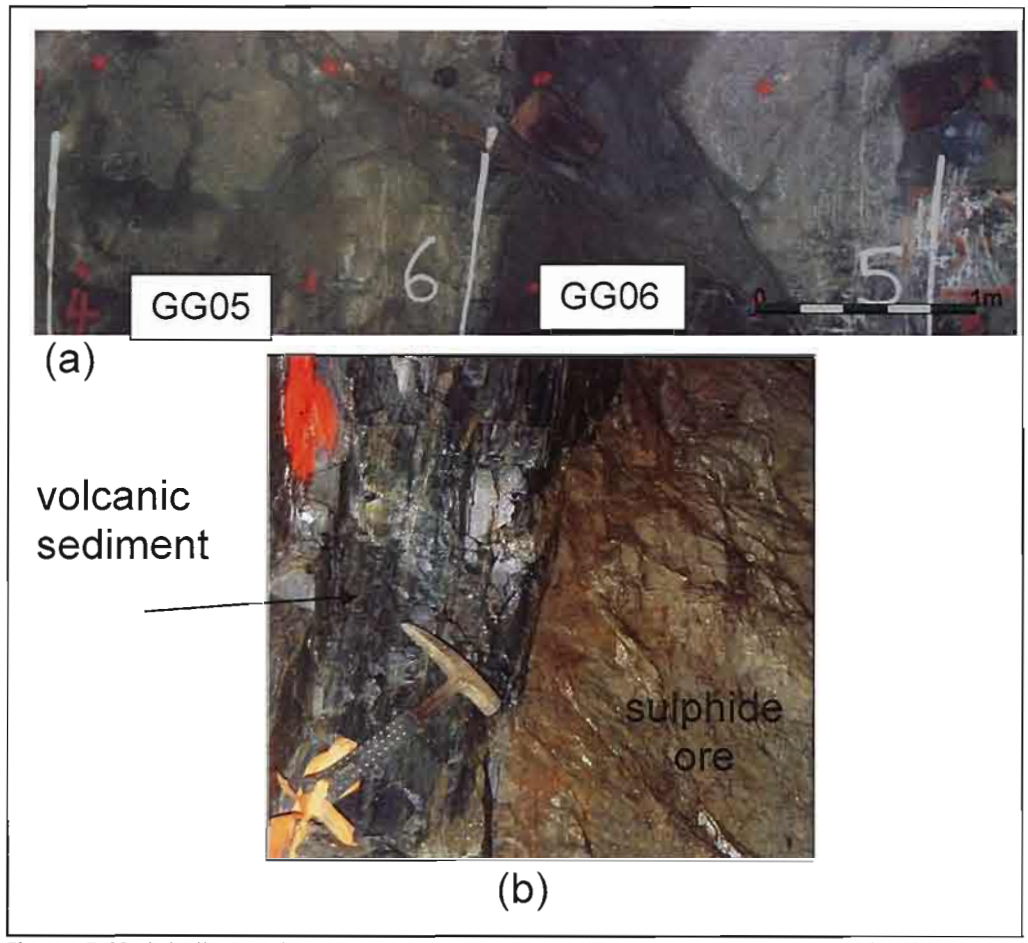

Figure 5.49. (a) Site photograph and sample locations for Site 2 located in the hanging-wall. (b) The hanging-wall contact of the Scuddles orebody exposed near Site 2. Note the extremely sharp contact and the presence of thin pyrite layers and veins within the hanging-wall sediments (LHS).

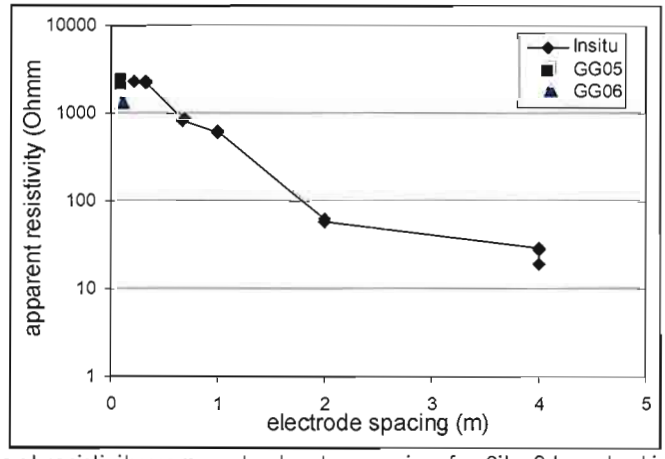

Figure 5.50. Apparent resistivity versus electrode spacing for Site 3 located in the hanging-wall volcanic host unit (HW). Galvanic laboratory resistivity measurements of samples are also plotted.

From the limited data collected at Site 2, it appears the scale variation is likely attributed to the increased connectivity of widely spaced thin-sulphide veins occurring through the highly resistive silicious host material. The high resistivity at small scale insitu measurements, clearly indicate the resistive end member.

5.4.7. Summary of Scale variation

The Scuddles orebody exhibits large variability in apparent resistivity across the deposit and within individual ore types. The variation in insitu apparent resistivity as a function of electrode spacing for all sites is shown in Figure 5.51 and 5.52. There is a clear general trend of decreasing resistivity with increasing electrode spacing for the majority of the sites, typically 1-2 orders of magnitude from 0.1 to 2 metres.

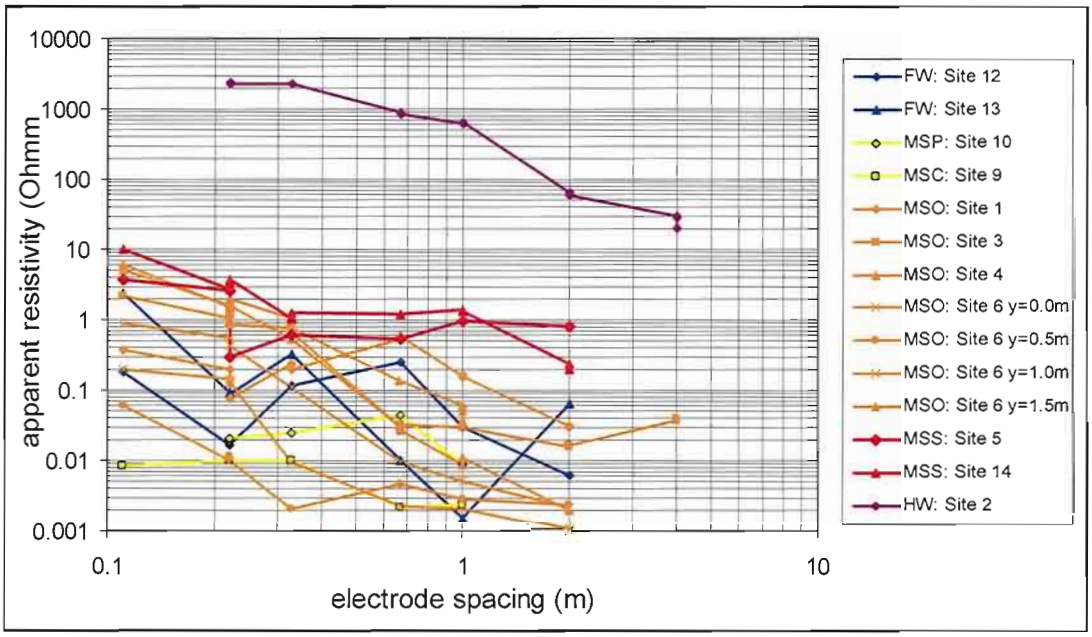

Figure 5.51. Apparent resistivity versus potential electrode spacing for all sites at Scuddles (log-log plot). Sites are numbers are located in the legend and are colour coded according to ore type.

In most cases the rockmass can be considered simply as a heterogeneous material consisting of conductive and resistive phases (Table 5.6). The bulk apparent resistivity is controlled by the proportions and distribution of these phases, but in most cases the effects of the conductive phase predominates at larger scales.

Ore	Conductive phases	Resistive phases
Footwall (FW)	pyrite-chalcopyrite	volcaniclastic sediments
Massive Pyrite (MSP)	Pyrite	quartz
Massive Pyrite-chalcopyrite (MSC)	pyrite-chalcopyrite Pyrrhotite	magnetite, quartz
Massive sphalerite –sulphide ore (MSO)	pyrite ,chalcopyrite Pyrrhotite	magnetite, sphalerite, quartz
Massive sphalerite-sulphide ore (MSS)	pyrite, chalcopyrite pyrrhotite	magnetite, sphalerite, quartz
Hanging-wall (HW)	Pyrite	volcaniclastic sediments

Table 5.6. Conductive and resistive mineral phases with each ore type examined at Scuddles.

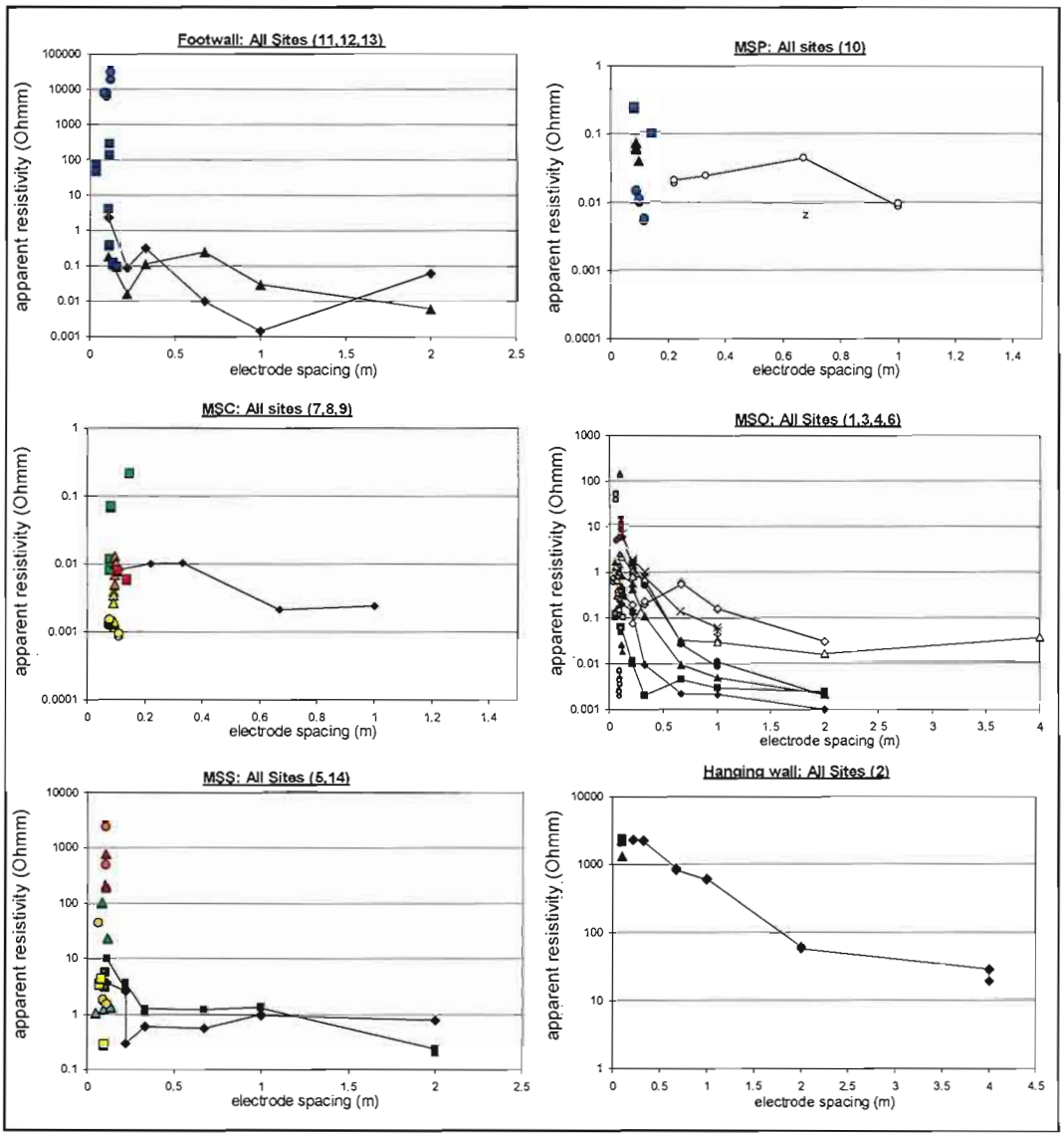

Figure 5.52. Apparent resistivity versus potential electrode spacing for each major ore type examined at Scuddles (Footwall: FW, Massive Pyrite: MSP, Massive pyrite-chalcopyrite: MSC, Massive Sphalerite-sulphide Ore (moderate grade): MSO, Massive Sphalerite-sulphide Ore (high grade): MSS, Hanging-wall: HW). Laboratory resistivity of samples in three orthogonal directions is also plotted for each ore type.

In all sites, the properties of the resistive mineralogical end members appear to dominate the electrical response at small measurement scales, while the conductive minerals dictate the bulk insitu response, even if they are present in relatively low proportions. This is illustrated by the near identical bulk resistivities of the massive sphalerite-pyrite ore (MSO: 0.03Ωm) and footwall pyrite-chalcopyrite stockwork (FW: 0.025 Ωm) ore zones, whose compositions are vastly different, but whose bulk resistivity is dominated by the conductive phase (pyrite-chalcopyrite), rather than the combined effects of all minerals. These observations illustrate the relationship between connectivity and scale of measurement. At small scales, measurements are highly variable, indicative of both resistive and conductive end members. This is reflected in the wide spread in insitu apparent resistivity and laboratory measurements of samples for each ore type (Figure 5.52). At larger scales the conductive components appear to be well connected, thus a greater number of conductive paths are generated and reduce the overall site resistivity.

The scale effects are most pronounced for Site 2 and Site 6 (3 to 4 orders of magnitude). These sites have vastly different lithologies; Site 2 is located in the unmineralised hanging-wall volcanics, and Site 6 is located in the massive sphalerite sulphide (MSS) ore. The large decrease in apparent resistivity measured insitu in both sites is attributed to an increase in the electrical connectivity of conductive sulphide bands occurring within a resistive unit. In the case of Site 2, thin conductive pyrite veins (<1mm) are distributed sub-parallel through the resistive volcaniclastic sediments. At Site 6, thick pyrite-chalcopyrite-galena bands from conductive networks through resistive sphalerite and magnetite assemblages.

Scale effects are observed in the majority of the other sites. The pyrite-chalcopyrite stockwork veining in the footwall sequence (Sites 11, 12 and 13) clearly provides pathways for conduction through the highly resistive silicious host material. The variability observed in insitu electrical soundings for footwall sites reflects the scale of the conducting stockwork network. Even in highly conductive sites, such as the massive sulphide- chalcopyrite (MSC) sulphide ores, the well-connected distribution of a small proportion of highly conductive pyrrhotite veins in relatively less conductive massive pyrite, can significantly reduce the resistivity of the ore.

The minimum scale variation in resistivity is observed in the massive pyrite unit (MSP). Field and laboratory observations show the MSP ore to consist almost entirely of massive pyrite and with randomly <1% distributed gangue minerals. The minor amount and random distribution of resistive minerals does not impede conduction through the massive pyrite, and as such, insitu resistivity measurements at Site 10 are generally consistent at all scales. In this case, the MSP ore is considered to consist of a homogeneous electrical media, for the range of measurements collected.

Laboratory resistivity measurements commonly range over several orders of magnitude (Figure 5.52), for each ore type. Some of the laboratory data typically correlates well with insitu measurements at small electrode spacings, while other samples are more conductive and have resistivities close to the bulk value implied by insitu measurements at the large electrode spacings. This relationship suggests that the rockmass at each site is typically characterised by both resistive and conductive mineral assemblages. For the majority of the ore types examined at Scuddles, the bulk insitu resistivity of each ore type could be approximated from the minimum resistivity measurement obtained from laboratory samples, representative of the conductive end member.

Histograms of apparent resistivity of the ore types at Scuddles subdivided into insitu and sample measurements are shown in Figure 5.53. The overall distribution (insitu and samples) appears close to normal in log-transformed space (Skewness 0.12) and hence the overall variation in apparent resistivity approximates a lognormal distribution. The insitu values include measurements at all electrode spacings, but since the measurements using the MEA (0.11 and 0.22m) predominate, the insitu histograms largely show the variation observed at relatively small electrode spacings. Thus the distribution of insitu data generally correlates well with galvanic measurements of samples.

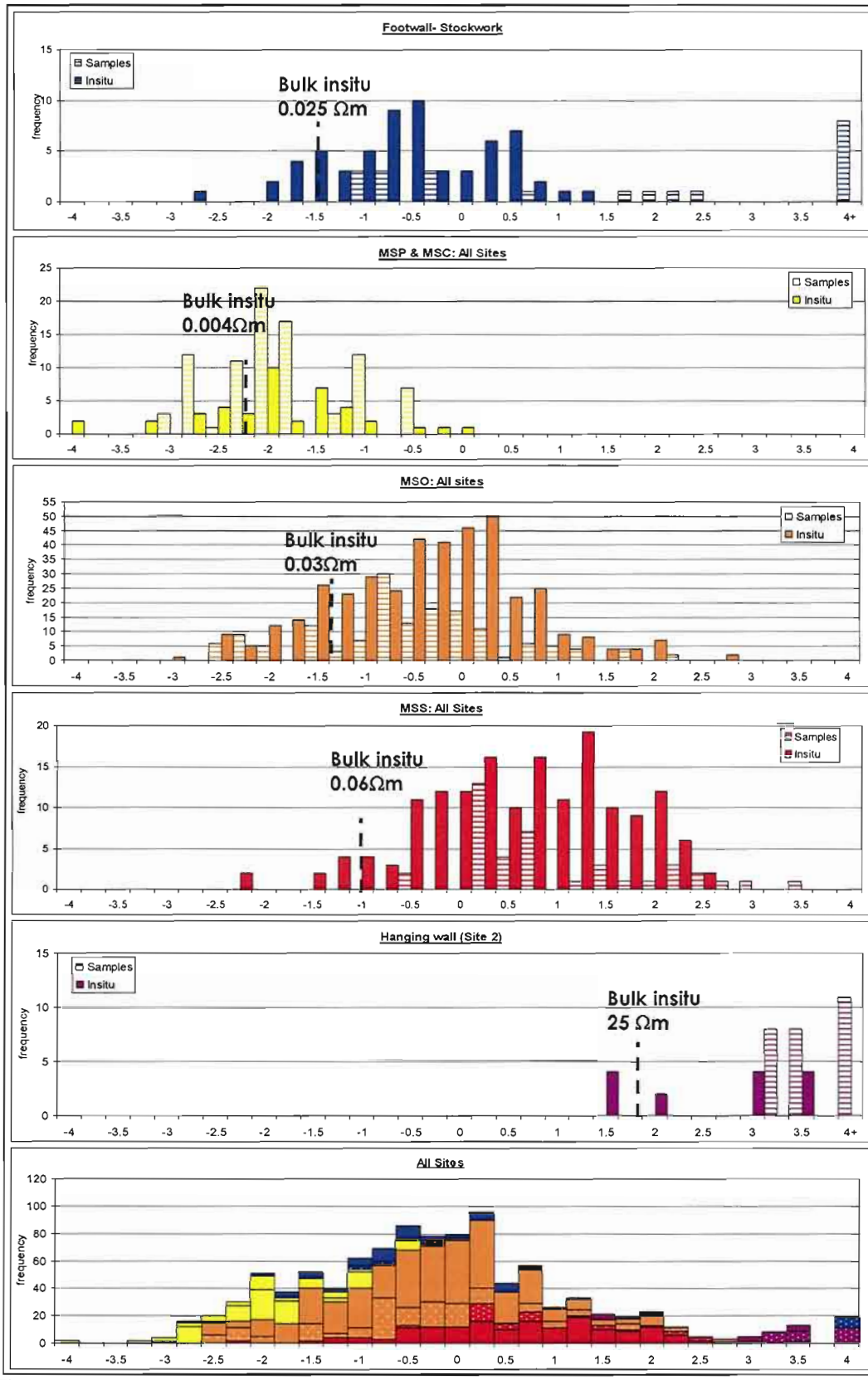

Figure 5.53. Histograms of log(apparent resistivity) for insitu and laboratory measurements collected for the various Scuddles ore types. Bulk insitu apparent resistivity measurement is marked for each site by the dotted line.

The mean insitu bulk resistivity of each ore type (inferred from measurements at largest electrode spacing) is indicated on each histogram. The bulk insitu resistivity is consistently displaced from the median position of insitu and sample data towards more conductive values. This displacement is typically

approximately one standard deviation, with the exception of the hanging-wall site (2 standard deviations). To statically estimate the bulk scale insitu response from sample measurements, the sample population must include representative members of the conductive population. In most cases, the minimum laboratory resistivity is the simplest statistic that best estimates the bulk insitu response, rather than the geometric mean or median.

Valid insitu chargeability data was collected at a number of sites. Chargeability as a function of electrode spacing is shown in Figure 5.54. The massive pyrite (MSP) and massive pyrite-chalcopyrite (MSC) ores are absent as, no valid chargeability data was recorded for many measurements, due to low signal levels, attributed to its highly conductive nature. The hanging-wall shows the strongest scale variation with an increase in chargeability with increasing scale, likely reflecting a greater number of disseminated pyrite grains being detected. The other more conductive ore types (FW, MSO, MSS) show a general, but poorly defined decrease in chargeability at larger electrode spacings.

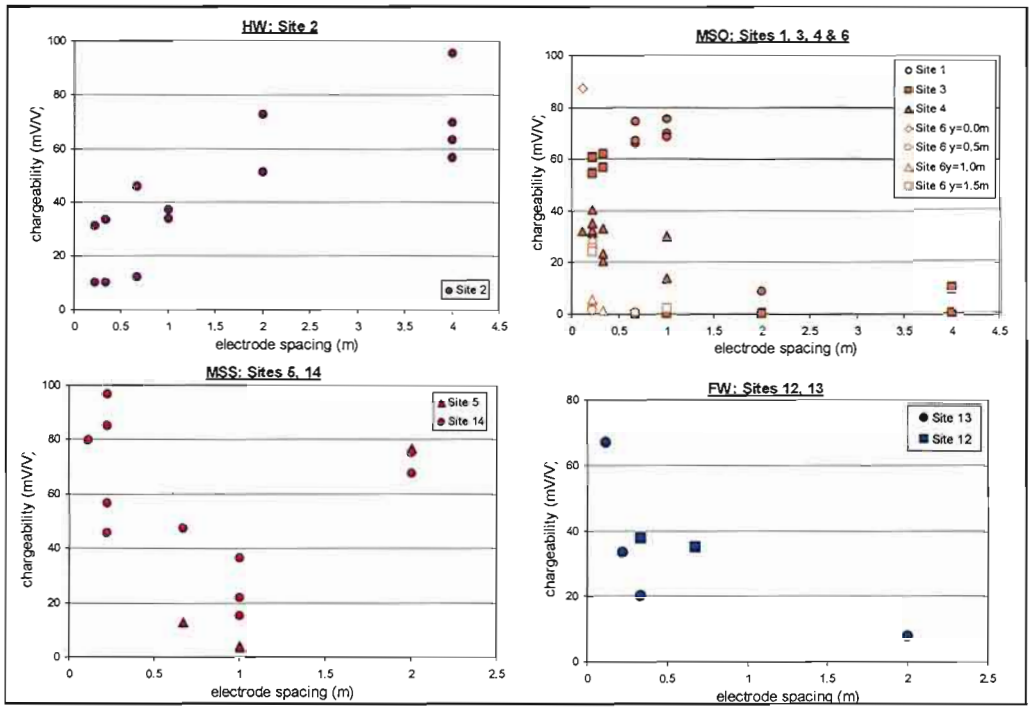

Figure 5.54. Chargeability versus potential electrode spacing for ore types examined at Scuddles (Footwall: FW, Massive Sphalerite-sulphide Ore (moderate grade): MSO, Massive Sphalerite-sulphide Ore (high grade): MSS, Hanging-wall: HW). No valid chargeability measurements were recorded for large scale measurements for Massive pyrite-chalcopyrite: MSC and Massive pyrite ores: MSP. Chargeability: 340-520 ms.

The chargeability histogram of all observations (Figure 5.55) has a large positive skew and a sub-population centred at a chargeability of approximately 200 mV/V. This more chargeable subpopulation corresponds to the sphalerite rich ore; MSS and MSO. The zinc rich proportion of the ore-body should respond as an induced polarisation target whilst the all the ore types would contribute to an electromagnetic response. In the MSO ore unit areas enriched in sphalerite correlated to higher chargeability and lower values corresponded to pyrite-rich areas. In contrast in the higher grade MSS unit, the opposite trend occurs with high chargeability recorded in pyrite-enriched zones, and low values recorded in the sphalerite. In the rich sphalerite ores of the MSS, the pyrrhotite is generally well connected and thus

the ore is less chargeable. The high chargeability observed in pyrite-rich zones in MSS ore maybe due to brecciation of the pyrite, which is typically infilled by resistive carbonate. The isolation of the pyrite within the resistive network produces a highly chargeable source.

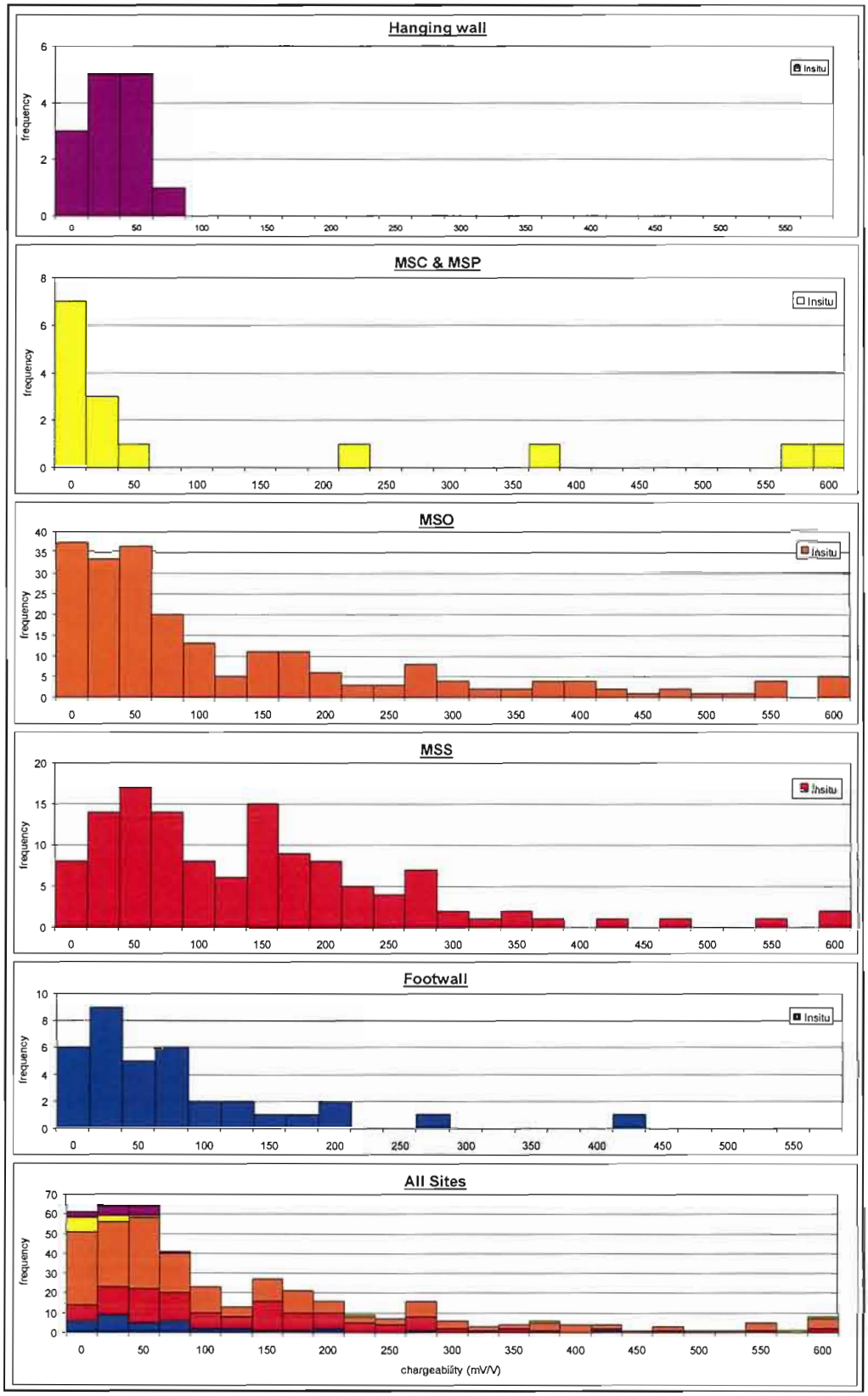

Figure 5.55. Histograms of insitu chargeability for each ore type examined at the Scuddles orebody.

Despite the large variability shown in the histograms there is marked difference in the range and distributions of resistivity data collected for each ore type. The relationship between apparent resistivity, chargeability and ore type is illustrated in Figure 5.56. The sphalerite rich units (MSO and MSS) are more resistive and chargeable, than pyrite rich units (MSC, MSP and FW.

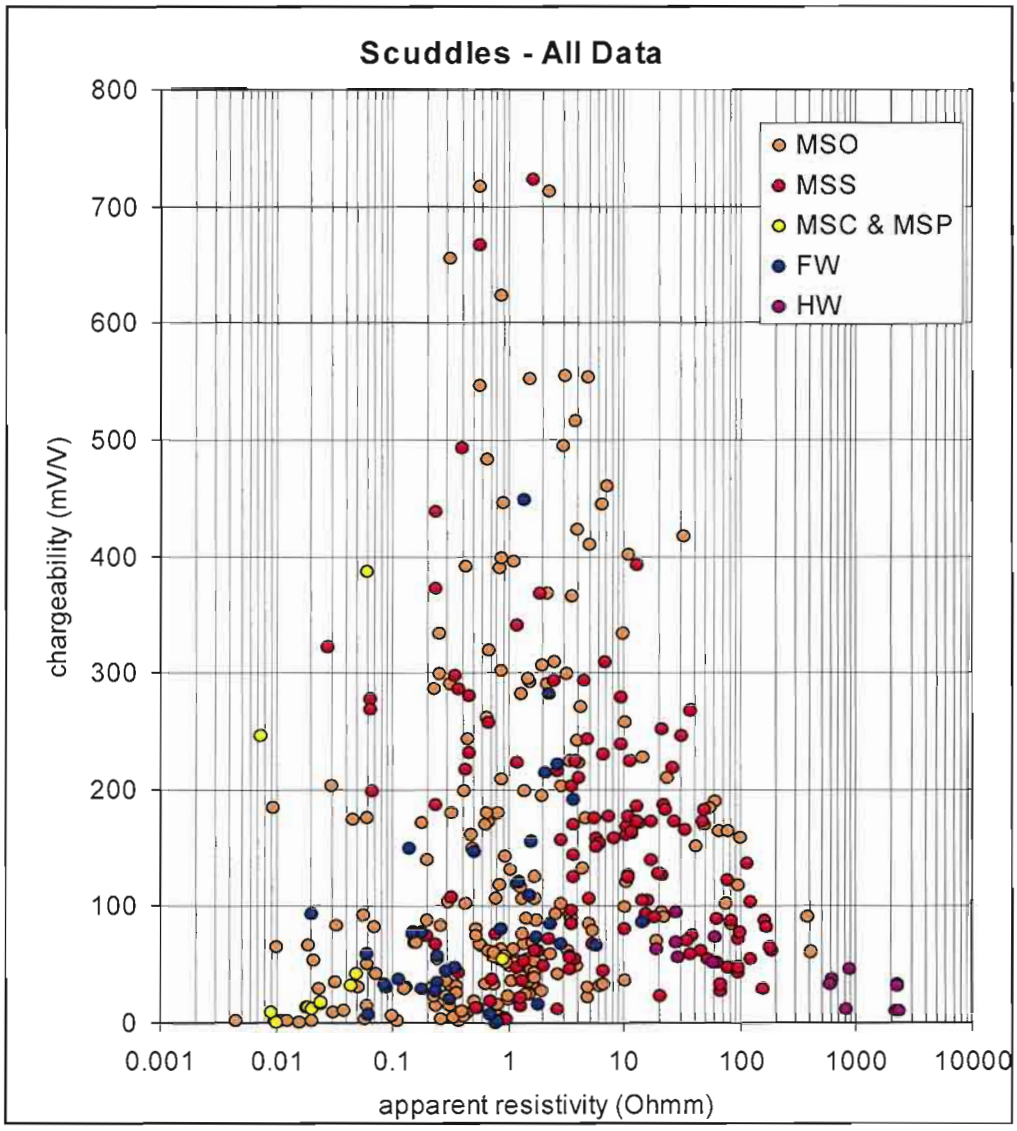

Figure 5.56. Chargeability versus apparent resistivity for all measurements at Scuddles. Measurements are categorised according to ore type.

The following provides a summary of the electrical properties and scale variation exhibited by each ore type. As expected, the massive pyrite-chalcopyrite ore (MSC) and barren massive pyrite (MSP) units are the most conductive ore types with a median insitu apparent resistivity of 0.009 Ωm. The relatively low number of measurements in this class reflects the difficulty of conducting measurements in extremely conductive materials. Few readings were recorded at site 7 and 8, implying resistivities closer to 0.0001 Ωm. Petrographic analysis and current mapping of samples collected from these sites show highly connected pyrrhotite is the cause of the extremely low resistivity. The median resistivity from this class would be even lower if data could have been acquired from these sites. The bimodal distribution observed in the resistivity histogram reflects the difference between the massive-pyrite-chalcopyrite ore (MSC) and the barren pyrite unit (MSP).

Although both units are extremely conductive, the presence of small proportions of pyrrhotite forming a conductive network reduces the median resistivity of the MSC unit at least an order of magnitude lower than the MSP unit. The pyrrhotite occurrence is commonly associated with chalcopyrite mineralisation.

The footwall stockwork zone was surprisingly conductive with a median resistivity (0.18 Ωm) lower than the median recorded for either sphalerite rich ore types (MSO- 0.43 Ωm or MSS- 3.6 Ωm). The connectivity of the sulphide stockwork increases with increasing measurement scale thus reducing the overall resistivity (i.e. at larger electrode spaces, a larger number of veins are connected). As in other ore types, large scale measurements are indicative of the conductive end member, in this case the pyrite-chalcopyrite veins, whereas the maximum resistivity value collected from samples are representative of the quartz-chloritic groundmass of the footwall unit.

The massive sphalerite ore sites (MSO and MSS) show the widest range of apparent resistivities (<0.01 Ωm >100 Ωm). The high-grade MSS unit is more resistive than the lower grade MSO ore, and shows the least scale variation. Several sub-populations observed in the MSO and MSS histograms correspond to different mineral associations and reflect heterogeneities in these units. In these units connected networks of pyrrhotite in the sphalerite result in these units to be very conductive and almost certainly contribute to the bulk response of the ore system, despite their high zinc content.

The hanging-wall zone, comprised of quartz-chloritic schist, exhibits the highest resistivity, although insitu measurements show a significant decrease from 2340 to 20 Ωm with increasing electrode spacing. This trend is likely indicating increased connectivity of thin sulphide veining occurring within the massive siliceous sediments. Hand-specimens are considerably more resistive ranging from 1309-24000 Ωm.

5.4.8. Relationship between resistivity and chemical trends

The effects of chemical variations on the electrical properties of the Scuddles ore samples were assessed using laboratory scale data. Scatter plots of laboratory resistivity data as a function of Fe_2O_3, S, Cu, Zn and Pb for all ore types are shown in Figure 5.57. In each case data points have been colour-coded based on ore type. The graphs include measurements conducted at all current densities for the three directions in each sample. The following provides a summary of the electrical properties exhibited by each mineral phase.

At Golden Grove iron occurs within pyrite, sphalerite, chalcopyrite, pyrrhotite and minor silicates. The presence of both pyrite and pyrrhotite in the samples makes calculation of mineral modal percentages from the chemical data difficult and imprecise. However petrographic estimates suggest that the gross variation in Fe_2O_3 % (0->60%) is due primarily to changes in pyrite content. There is a clear general trend of decreasing apparent resistivity with increasing iron content (Figure 5.57a) although a scatter of two or more orders of magnitude is apparent for any given iron content. This scatter is presumably due to variations in the proportions of sulphide minerals and to the effects of anisotropy due to variations in texture.

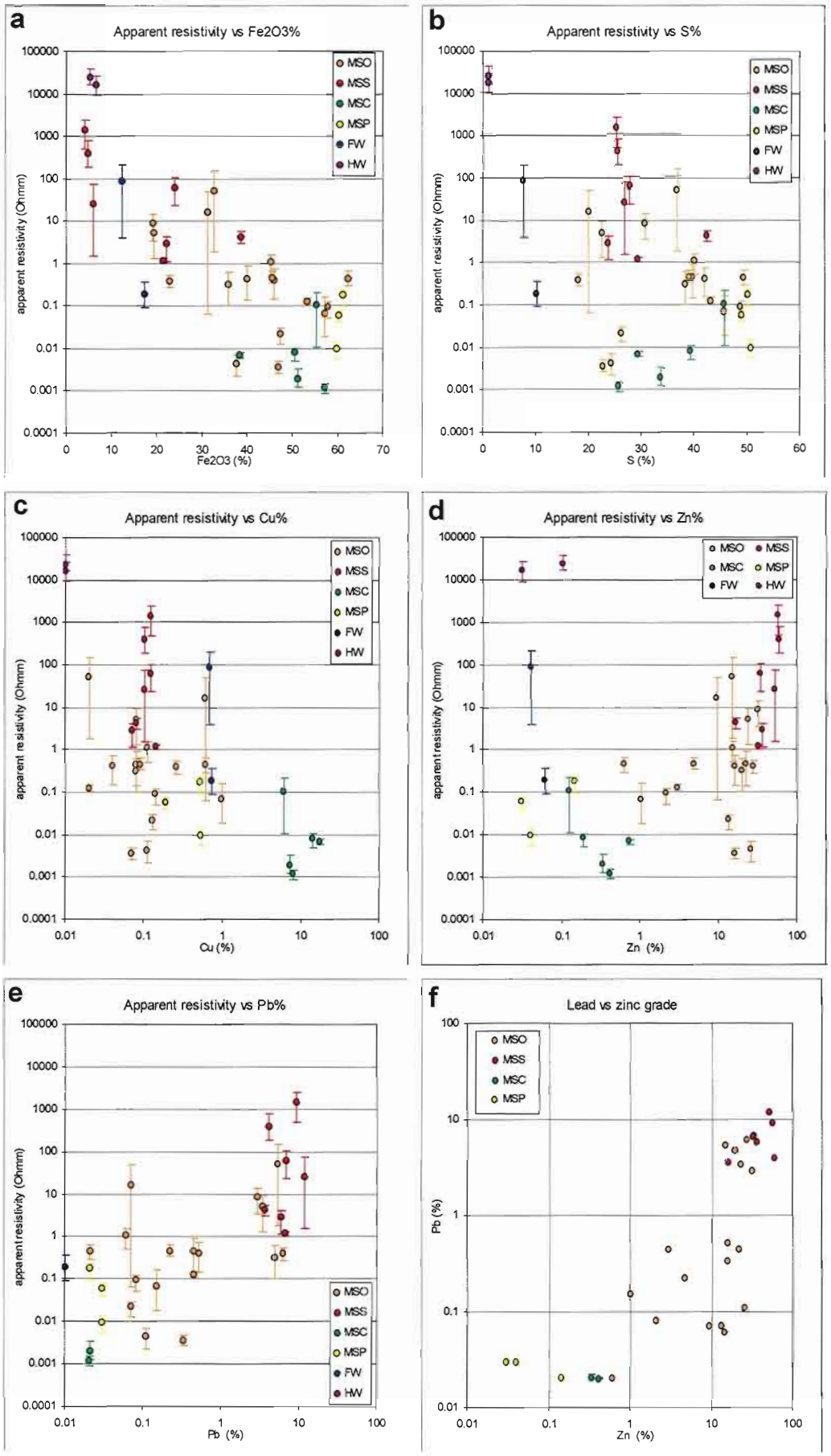

Figure 5.57. Scatter plots of resistivity as a function of (a) Fe_2O_3% (b) S% (c) Cu% and (d) Zn% (e) Pb% (f) lead versus zinc cross-plot. All laboratory measurements including different directions and current densities are included in these diagrams. The mean value is plotted along with the minimum and maximum values as indicated by the error bars.

Sulphur provides a measure of the total proportion of sulphides (Figure 5.57b). There is only a very poor correlation between apparent resistivity and S% since sulphur increases either with increasing resistive sphalerite or conductive pyrrhotite, chalcopyrite and pyrite.

Chalcopyrite as indicated by Cu% (Figure 5.57c) has little effect on the resistivity at low concentration (<1%Cu). Samples of high grade pyrite-chalcopyrite ore have very low resistivities, but this trend is complicated by the presence of pyrrhotite in these samples.

There is a clear increase in resistivity with increasing zinc content above 1% Zn. (Figure 5.57d) However, some high-grade zinc samples (15-25% Zn) are also highly conductive due to the presence of small amounts of pyrrhotite. This occurs in samples GG22, and GG23.

A similar trend occurs for resistivity plotted against lead grade (Figure 5.57e), which seems unusual as galena is typically conductive. However, the cross-plot of lead versus zinc (Figure 5.57f) shows lead content to be proportional to zinc content, showing the close association of the two minerals. Thus the resistivity-lead cross-plot is more likely indicating the variation of zinc rather than lead composition and is largely misleading.

Examination of all the cross-plots shows the complexity in trends between chemical composition and apparent resistivity. The poly-metallic nature of the ores causes difficulty in correlating chemical properties directly to apparent resistivity. This is predominantly due to the conflict between the different sulphide phases, with sphalerite (zinc) being resistive and other sulphides exhibiting varying degrees of conductivity. The combined effects of composition and texture of the all mineral phases contribute to the overall resistivity.

A better correlation would be achieved by incorporating the major components into a single parameter, which could be compared to resistivity. Additionally this may lead to the ability to estimate/predict the resistivity of a sulphide specimen based upon chemical composition.

A simple approach was applied to the MSC/MSP, MSO and MSS range of samples. The electrical resistivity of these samples is largely controlled by two components: resistive sphalerite and conductive pyrite, which constitute to the majority of their composition. The assays of Zn and Fe_2O_3 primarily reflect the composition of these two minerals. The scatter plot of resistivity versus Zn (Figure 5.58a) shows a positive trend with a correlation of 0.56. The scatter plot of resistivity versus Fe_2O_3 (Figure 5.58b) shows a negative trend with a correlation of –0.49. Using the ratio of the two assays Zn/Fe_2O_3 incorporates the effects of both resistive and conductive phases (Figure 5.58c). The scatter plot of resistivity versus Zn/Fe_2O_3 provides a stronger correlation of 0.8. The two outliers in Figure 5.58c (samples GG22 and GG23) are sphalerite rich and contain a network of conductive pyrrhotite, thus reducing their resistivity. Unfortunately pyrrhotite and pyrite are both incorporated into the assay of Fe_2O_3.

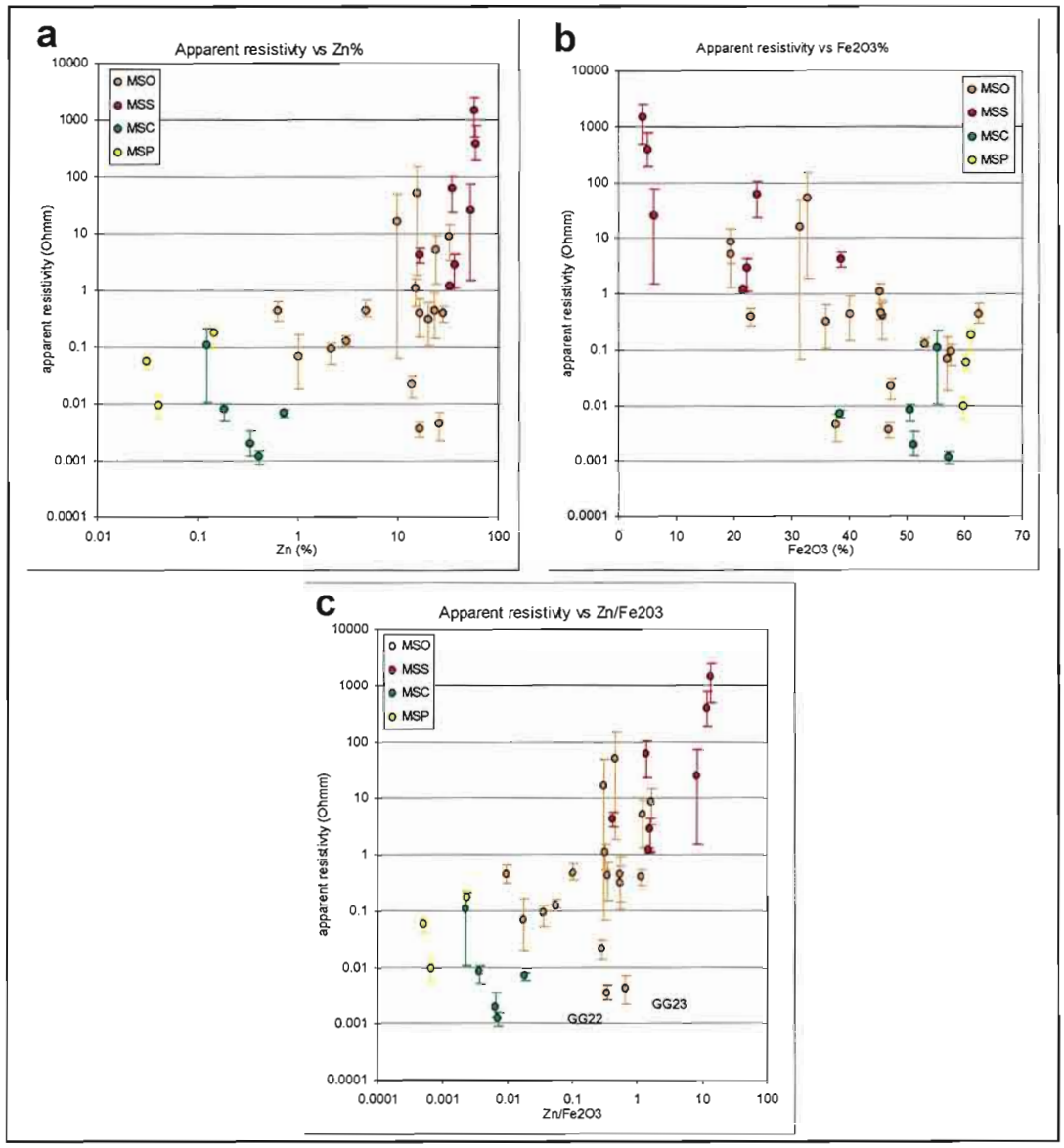

Figure 5.58. Scatter plots of laboratory measurements for MSO, MSS, MSC and MSP samples. The correlation coefficient for (a) resistivity versus zinc is 0.56 (b) resistivity versus Fe203 is –0.49. (c) The scatter-plot of resistivity versus the ratio of Zn/Fe0203 improves the correlation to 0.8. The mean value is plotted along with the minimum and maximum values as indicated by the error bars in all plots. The sample outliers GG22 and GG23 indicated contain interstitial pyrrhotite, which reduces their overall resistivity.

A more complicated ratio termed the resistive-conductive element (RCE) ratio was applied to the entire sample data (i.e. all units) from the Scuddles orebody. The ratio divided the main conductive and resistive mineral assemblages to counteract their opposing effects. In this case the ratio (equation 5.1) utilised the major components assayed, constituting at least 60% of the sample.

$$\text{RCE ratio} = \frac{\text{resistive elements}}{\text{conductive elements}} \cong \frac{\text{Zn} + \text{Si}}{\text{Fe}_2\text{O}_3 + \text{Cu} + \text{Pb}} \qquad (5.1)$$

The cross-plot of resistivity versus the resistive/conductive mineral ratio is presented in Figure 5.59 and shows a positive trend with a strong correlation of 0.86. The use of the RCE ratio shows that the resistivity of a sample can reasonably be predicted from the knowledge of the bulk rock chemistry. The scatter in the data is largely due to the texture controlling the distribution of mineral phases in each sample.

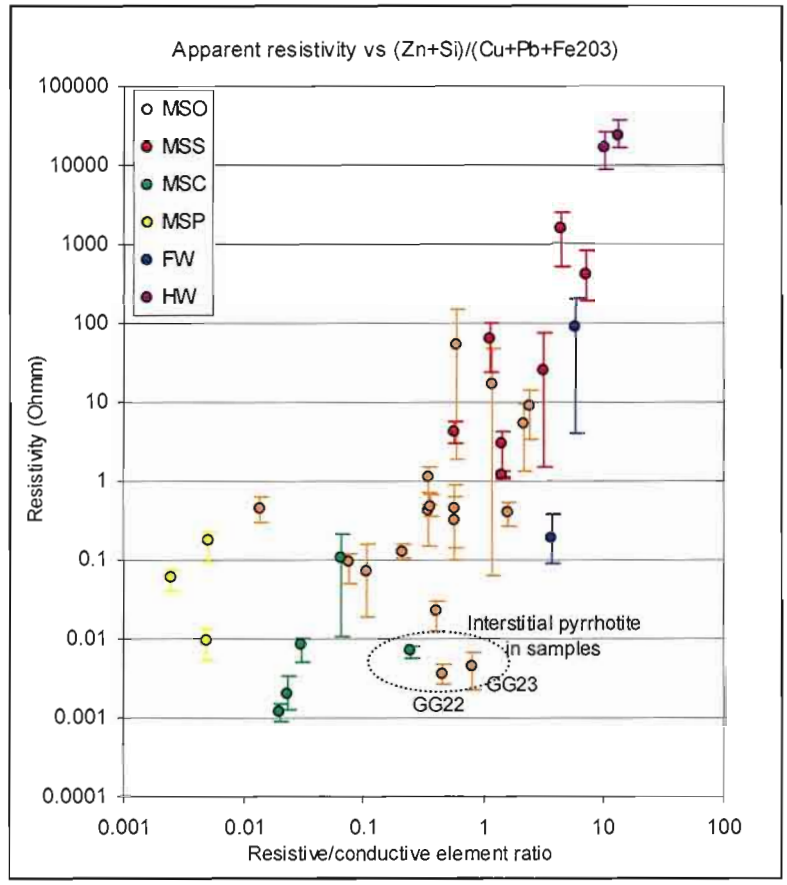

Figure 5.59. Scatter plots of resistivity as a function of (Zn+Si)/(Fe_2O_3+Cu+Pb). This ratio provides a parameter which incorporates the major resistive and conductive phases. The scatter plot shows a clear positive trend with a correlation of 0.86. The sample outliers indicated contain interstitial pyrrhotite, which reduces their overall resistivity.

5.5. Conclusions

Scuddles was selected as a study site as an example of a massive sulphide deposit, which contained a wide variety of ore types and textures. The electrical measurements from Scuddles clearly demonstrate a systematic trend of scale variation involving decreasing apparent resistivity with increasing electrode spacing. For many sites at Scuddles marked scale variation of apparent resistivity of in excess of two orders of magnitude was observed between measurements acquired at electrode spacings of 0.11 and 2 metres. The degree of scale variation differs from site to site associated with variations in ore composition, texture and mineralogy. Laboratory resistivity measurements on samples show a wide distribution but typically fall within the range of the small scale insitu measurements.

For some sites laboratory and small-scale insitu resistivity data displayed a distinctly bimodal distribution with the more resistive end members having values that were close to the insitu apparent resistivity at small electrode spacings, while the more conductive samples approximate the bulk insitu resistivity. This is an important empirical observation with implications for estimating the bulk rock properties from limited small-scale sampling. For the majority of sites the most conductive sample measurement would provide the best estimate of the bulk insitu response rather than the geometric mean or median. Such a predictor would also require a large sample population to ensure adequate sampling of the conductive end members.

The presence of small proportions of highly conductive minerals was also found to have a profound influence on reducing the resistivity of the rockmass. In particular the presence of minor pyrrhotite forming highly connected pathways in massive pyrite samples greatly reduced the overall sample resistivity, in compared to samples absent of pyrrhotite. Similarly sphalerite rich portions of the deposit were unexpectedly found to display dramatic scale variation and to be quite conductive at large scales due to minor pyrrhotite occurrence. This observation highlights the significant influence small proportions of well-connected highly-conductive phases make to the overall electrical resistivity.

Chapter 6
An electrical study of the McArthur River Lead-Zinc ore deposit

6.1. Preamble

This chapter describes the electrical characteristics of the McArthur River Lead-Zinc deposit. The site variability is in contrast to the Scuddles ore body, where by all sites are near identical in mineralogy and texture and only differ by minor variations in composition. A brief description of the geology, site selection and methodology is provided. Due to the similarity between sites, the electrical scale dependence for one site at McArthur River is presented in detail, followed by a general discussion of the results from all sites. The final section compares geochemical properties with laboratory electrical measurements of samples.

A significant electrical property of the McArthur River Deposit is its highly anisotropic nature, due to the fine layers within the ore. Thus a series of measurements were collected with arrays orientated both parallel and perpendicular to the laminated ore, to capture this variability. Although these measurements adequately provide indication of insitu scale variability, they cannot be directly related to sample measurements, without consideration of the "paradox of anisotropy". This paradox (see section 3.2.5) states that the true "longitudinal" electrical resistivity (parallel to bedding) is directly measured by an array orientated perpendicular to bedding. Whereas, the "transverse" electrical resistivity (perpendicular to bedding) is related to a function of both the parallel and perpendicular measurements orientated with respect to bedding. The "transverse" resistivity is required to be calculated in order to compare with transverse laboratory measurements of samples.

In this chapter, the terms "parallel" and "perpendicular" describe the orientation of the measuring array with respect to the sub-parallel layering of the ore. Whereas, "longitudinal" and "transverse" describe the orientation of the components of resistivity, that are calculated from the parallel and perpendicular measurements.

6.2. Introduction

The McArthur River (HYC) orebody is a stratiform sediment-hosted lead-zinc deposit, which contains 8 ore horizons. The underground development of the deposit is mainly restricted to 2 Orebody, although access to other portions of the stratigraphy was possible. There is little lateral variability within each ore horizon and sites were selected to primarily provide data from a range of stratigraphic levels.

Electrical insitu and laboratory measurements have been conducted to examine the effect of scale of investigation and their implications for the exploration of such targets using electrical geophysical techniques. The field methodology and laboratory techniques are described in Chapter 3.

Geochemical and petrographic analyses of the hand specimens provide additional quantitative and qualitative data for a comparative discussion of the results.

6.3. Geological Setting

The McArthur River (referred to as HYC, "*Here's Your Chance*") orebody is a Proterozoic stratiform sediment-hosted lead-zinc deposit located within the McArthur River area, Northern Territory (Figure 6.1) (Murray, 1975). The orebody occurs within the HYC pyritic shale member of the McArthur Group, an interbedded sequence of dolomite, sandstone, shale, breccia and tuff (Figure 6.2). McArthur Group sediments accumulated in a north-south trending basin bounded in the east by the major Emu Fault system which lies 1-2 km east of the HYC orebody. The origin of the deposit is the subject of continuing debate with models ranging from sedimentary exhalative to syndiagenetic replacement (Large, 1998).

Figure 6.1. The McArthur River (HYC) deposit is the largest of the sediment-hosted Zn-Pb-Ag deposits in the North Australian Proterozoic Zinc Belt.

The McArthur River orebody is the largest known example of a sediment-hosted zinc-lead deposit with a geological resource of 237 Mt at 9.2% Zn and 4.1% Pb including an underground mining resource of 103.7 Mt at 14.1% Zn and 6.4% Pb (Large et al. 1998). Mineralisation covers an area of approximately 2 km^2 and has an average thickness of about 55 m (Logan et al., 1990). The mineralised interval contains eight orebodies separated by relatively barren breccia and siltstone units (Figure 6.2). Current mining activity is concentrated in 2 Orebody.

Mineralisation is very fine grained and consists of thin laminations (<1 – 5mm) of sulphides, siltstone and carbonates (Figure 6.3). Thin siltstone, carbonate and silica bands (1-10 cm) are also common within the ore as are small

normally graded beds of sandstone to siltstone. Bands of breccia are also common.

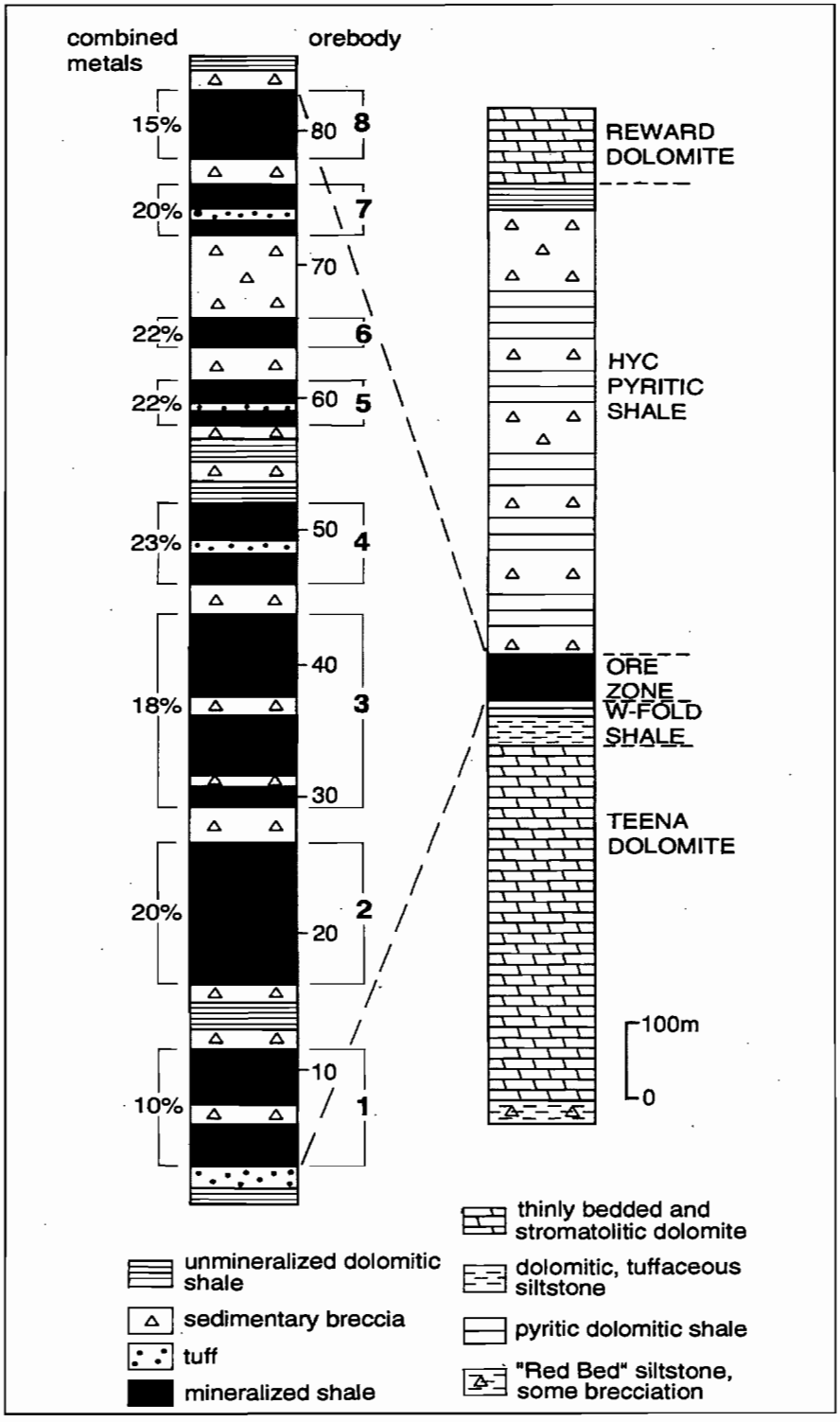

Figure 6.2. McArthur River deposit (HYC), regional and local stratigraphy. The orebody occurs within the HYC pyritic shale member of the McArthur Group. The 8 ore horizons are clearly marked. From Large et al (1998).

The major sulphide minerals are pyrite, sphalerite and galena with minor chalcopyrite and arsenopyrite. Two generations of pyrite are recognised and are here referred to as type-1 and type-2 pyrite. Type-1 pyrite occurs finely disseminated within the sulphide lamina as euhedral to rounded grains up to 20 μm in diameter but typically less than 5 μm. Type-2 pyrite is recrystallised and usually occurs as aggregates (up to 1 mm in diameter) of euhedral to

irregular grains concentrated on the margins of sulphide-rich micro-laminations. Sphalerite and galena occur as lamina and as disseminated grains. Lamina that contains high proportions of fine type-1 pyrite may commonly have a matrix of sphalerite and galena (Figure 6.3b).

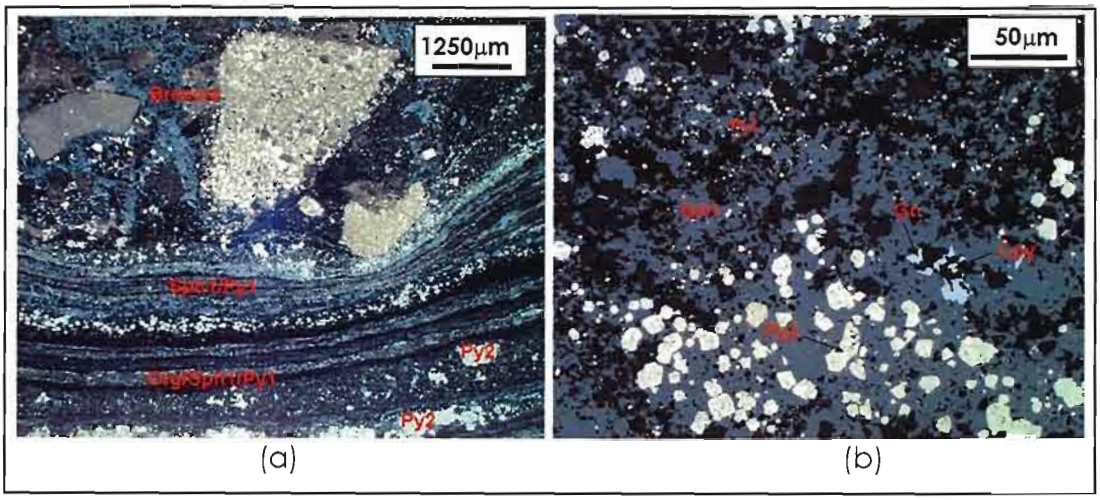

Figure 6.3. Reflected light photomicrographs of typical ore textures in 2 Orebody. (a) Light grey areas are lamina of fine-grained sphalerite and galena. Very fine grained type-1 pyrite is finely disseminated throughout. Type-2 pyrite forms large aggregates. Dark layers are a mixture of carbonate, silicate and organic material. (Sample MR01). Field of view: 8.2 x 6.4 mm (b) Closer view of view showing differences between type-1 and type-2 pyrite. (Sample MR39). Field of view: 0.3 x 0.2 mm.

The western margin of the deposit has been folded, faulted and dips steeply to the east (Figure 6.4). All current underground workings are located in the main shallowly east-dipping portion of the orebody to the east of the fault zone.

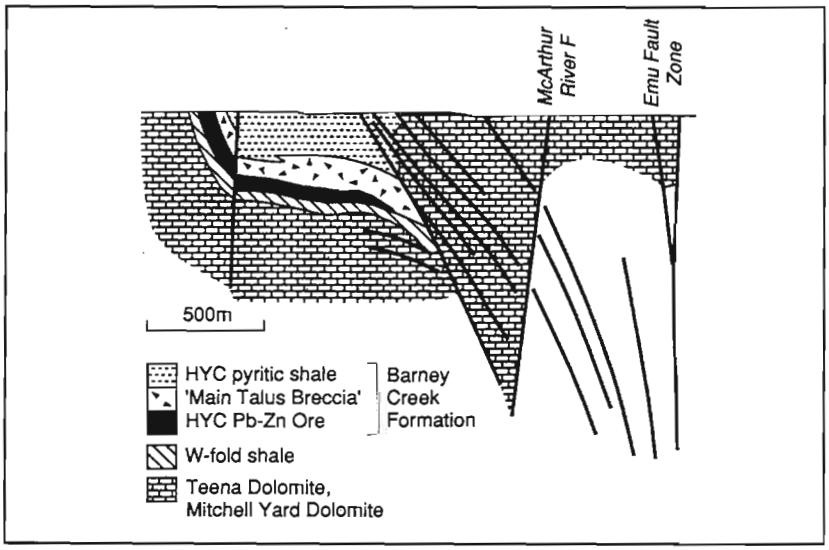

Figure 6.4. Schematic West-East cross section through the HYC orebody, showing the major structural controls of the deposit. From Large et al (1998).

The orebody is cut by a an array of faults with displacements from two to ten metres (Figure 6.5) and tight folding is locally developed adjacent to the major structures. Small scale normal faults (1 mm – 0.5 m) are common as are small scale bedding plane parallel thrust faults which may locally imbrecate the stratigraphy. Structural features do not significantly affect the grain size or the texture of the ore but thin late-stage galena-sphalerite-carbonate veins commonly crosscut stratigraphy.

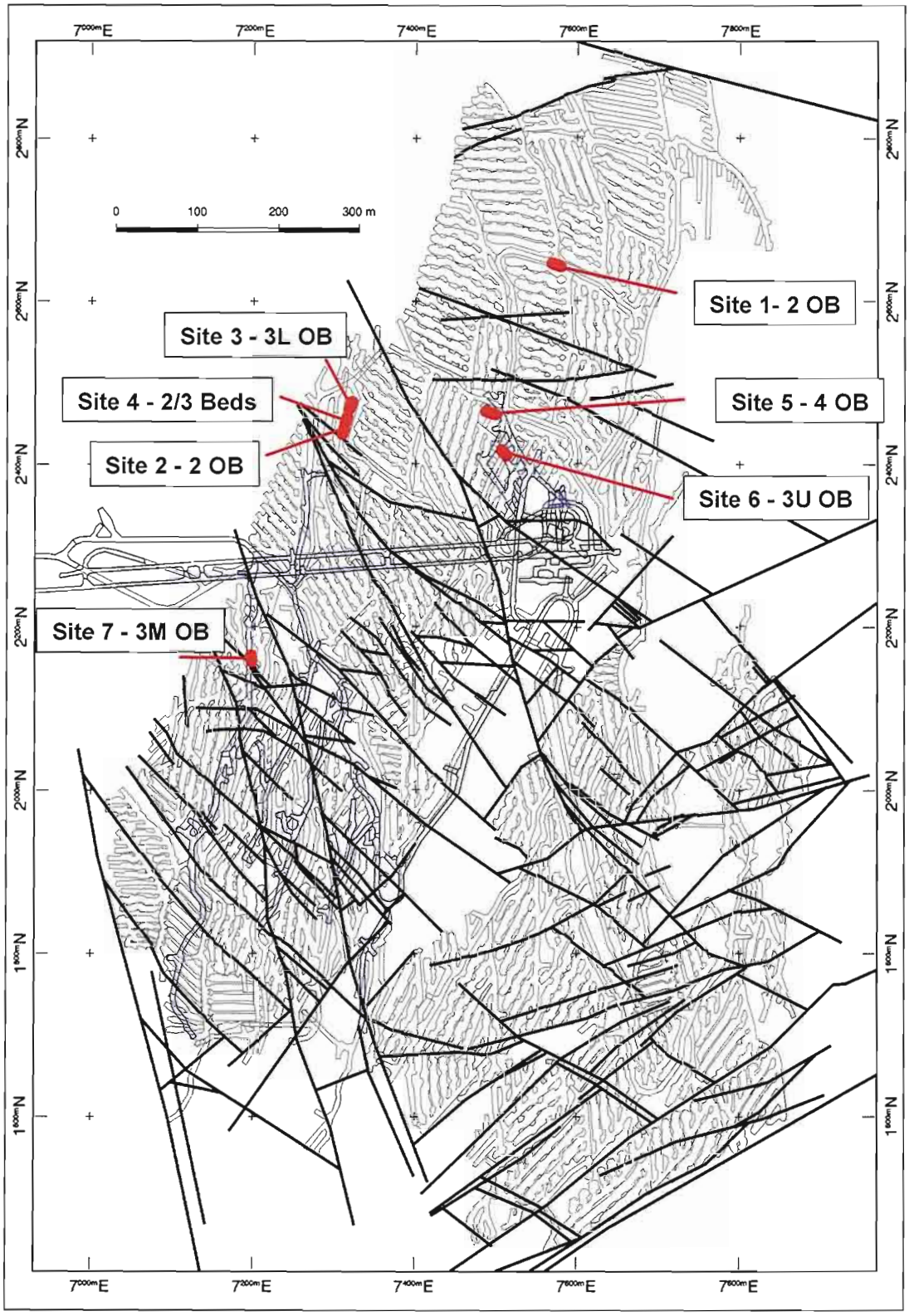

Figure 6.5. McArthur River Mine layout, showing distribution of measurement sites. Grey outlines are 2 Orebody workings, blue outlines are 4 Orebody workings. A large number of faults transect the deposit. Mine survey data provided by McArthur River Mine.

The HYC orebody was a geological discovery but geophysical methods were extensively used in the delineation phase (Shalley and Harvey, 1992). Surface resistivity, induced polarisation and electromagnetic surveys indicate that the ore and enclosing low-grade pyritic material is moderately conductive and chargeable.

6.4. Methodology

A generic discussion of the field and laboratory measurement techniques was described in chapter three. The following discusses the methodology specifically applied to the McArthur River Deposit.

6.4.1. Field Measurements (Insitu)

Seven underground sites of the HYC ore body were selected (Figure 6.5) for insitu electrical studies. Room and pillar workings in the HYC orebody are mainly developed in the No. 2 Orebody but limited exposures of other portions of the stratigraphy were accessible (No.2, 2/3 beds, 3L, 3M, 3U, 4L). There is little lateral variability within each HYC ore horizon and sites were selected to provide data primarily from a range of stratigraphic levels (Figure 6.6). Measurement sites were selected in consultation with the mine geologists. All sites were measured in sulphide-rich material. The criteria adopted for site selection included access to representative 6 x 3 metre exposures with smooth surfaces, little mining induced fracturing, absence of structural complexities such as faults and folding, absence of ground support (bolts and straps) and access to mining services.

The distribution of sites is shown in Figure 6.5. Site characteristics are summarised in Table 6.1 together with the chemical composition of samples collected from each site.

Stratigraphic Unit	Chemical Composition			Sites
4 Orebody	17% Zn (15-19)	9%Pb (7-10)	12% Fe (9-15)	5
3 Upper Orebody	18% Zn (13-20)	10%Pb(8-11)	11% Fe (8-15)	6
3 Middle Orebody	13% Zn (12-15)	8%Pb (6-9)	18% Fe (13-22)	7
3 Lower Orebody	15% Zn (10-18)	5%Pb (2-8)	14% Fe (7-19)	3
2/3 Beds	8% Zn (5-12)	2%Pb (1-4)	9% Fe (6-12)	4
2 Orebody	18% Zn (11-24)	7%Pb (4-10)	7% Fe (4-10)	1,2

Table 6.1. Stratigraphic units examined at the HYC ore body. Sulphide mineral composition is based upon chemical analyses of hand specimens. Average values listed (range shown in brackets).

At each site measurements were completed with electrode arrays orientated both parallel and perpendicular to sub-parallel bedding. Parallel insitu measurements of apparent resistivity and chargeability were completed using an expanding Wenner electrode array, with electrode spacings increasing systematically around a central location. The electrode "a" spacing (potential-potential electrodes) ranged from 0.11 metres to 2 metres for most sites, but for some sites with problematic geometry, geological or ground support factors the maximum current electrode spacing was reduced to 1 metre. Perpendicular insitu measurements were restricted to a maximum electrode spacing of 0.66 metres.

For large electrode spacings (greater than 0.33m) electrical contact was made using nickel-coated dynabolts. For small electrode spacings the mobile electrode array was employed. This instrument enabled sequential measurements at electrode spacings of 0.11, 0.22 and 0.33 metres. This array was also used to measure anisotropy by rotating the array about a central measurement location. (See Chapter 3 for further details).

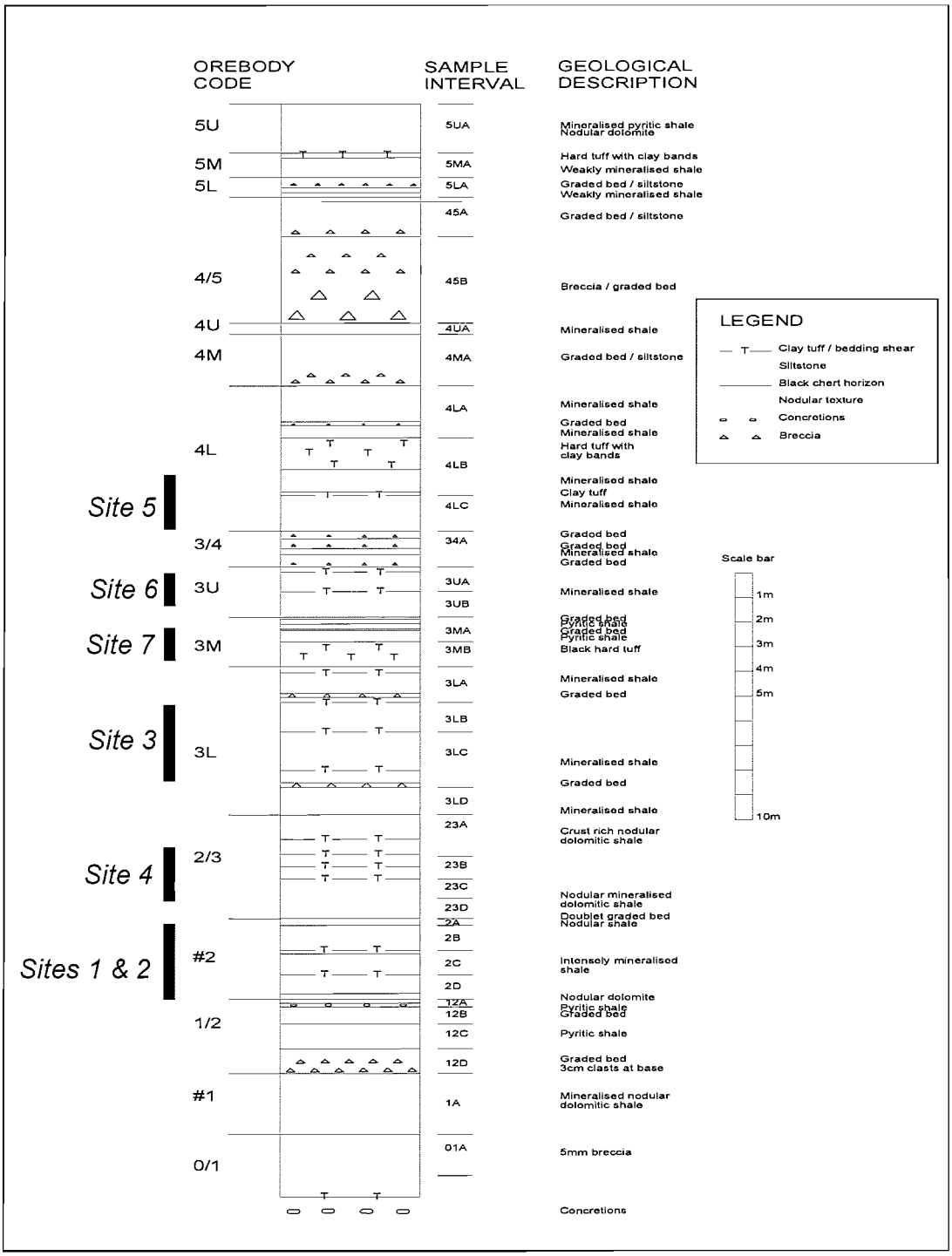

Figure 6.6. McArthur River Mine stratigraphy with sample sites indicated.

All measurements were collected using a Scintrex IPR12 receiver and IPC9 transmitter. A resistance shunt box was used to control and measure the current flow through the rock. A four second square pulse cycle was utilised for all insitu measurements. Chargeability was recorded in mV/V over the time interval 340-520ms after the current turn-off. Chargeability data was scrutinised and only those curves that showed a smooth monotonic decrease in voltage and contained no negative voltages at early or late times were accepted.

Prior to routine measurements at each site, a series of measurements were conducted to assess the variation of the electrical properties as a function of current density. These measurements were conducted using the maximum electrode spacing available at each site (1 or 2 metres). Plots of apparent resistivity and chargeability as a function of current density for a selection of sites are shown in Figure 6.7.

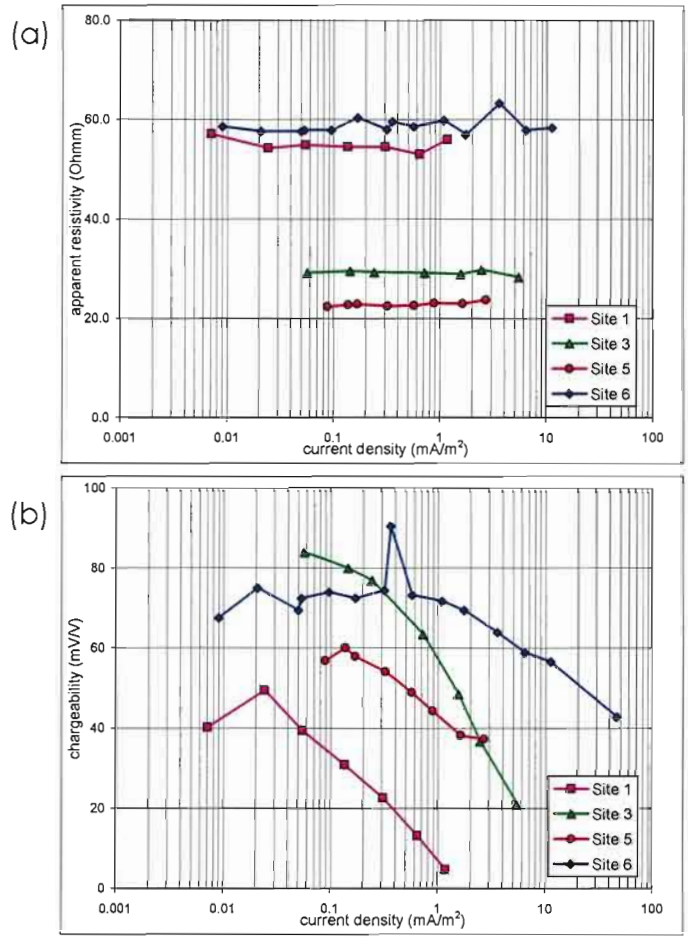

Figure 6.7. Insitu apparent resistivity (a) and chargeability (b) as a function of current density for a selection of McArthur River Sites. Apparent resistivity behaves linearly at these current densities; however chargeability significantly decreases with increasing current density. Routine measurements were conducted at current densities less than ~0.01 mA/m^2 (~currents of <0.1 mA), where practical. The current density is calculated as the maximum current density for a homogeneous half space based upon current and array dimensions.

Apparent resistivity shows no significant variation as a function of current density but chargeability decreases rapidly above a threshold value. For more resistive sites such as site 1 currents of ~1mA were employed (maximum current density ~ 0.1 mA/m^2). At highly conductive sites, such as 3 Lower Orebody (site 3) current densities near the threshold of 10mA/m^2 (applied current ~100 mA) were required to obtain an adequate signal.

Photographs of each site were taken to show variations of mineralogy, texture and structure and for qualitative comparison to the geophysical data. Lithological logs of each site were also completed to provide a stratigraphic context for the samples collected.

6.4.2. Laboratory measurements

A suite of forty-one large, mostly oriented rock samples was collected from the seven insitu sites for laboratory-scale testing. Samples were collected

during the initial preparation of each site, which involved the removal of loose or broken material to ensure electrical measurements were conducted on solid surfaces. Sample collection attempted to provide a record of the stratigraphic variability at each site.

Galvanic electrical measurements of resistivity and chargeability were collected for all samples (detailed procedures were described in Chapter 3). Electrical measurements of prismatic samples were taken in three orthogonal directions to quantify anisotropy (Figure 6.8). Multiple measurements were collected at three different current densities to check the linearity of the electrical results.

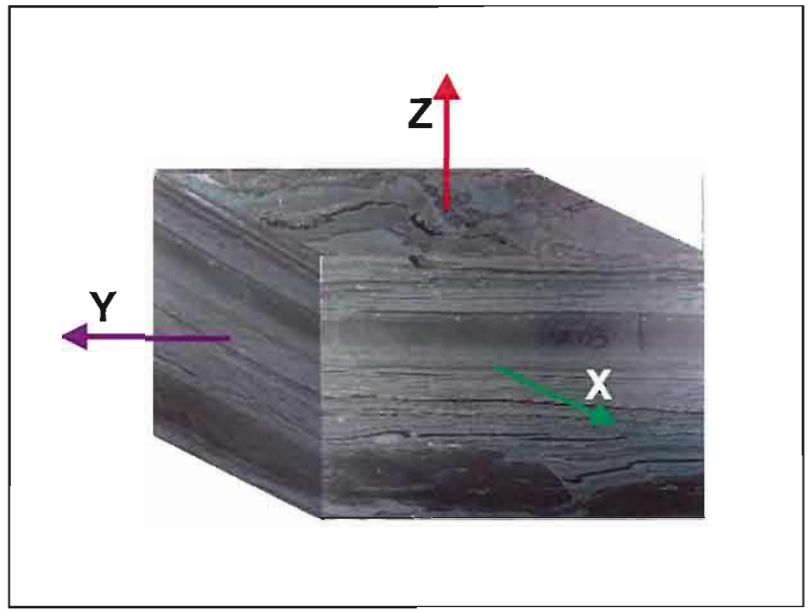

Figure 6.8. 3-D view showing the orientation of the three orthogonal laboratory resistivity measurements orientated with respect to the laminations in the McArthur River ore.

All samples were assayed for major and trace elements. Density and magnetic susceptibility measurements were also completed. A number of suitable samples were selected for mesoscopic continuity and current mapping techniques (refer Chapter 4). These techniques assist in assessing the electrical variation within each individual sample.

6.5. Discussion of results

The seven sites at McArthur River were all located within laminated lead-zinc ore. However, there are mineralogical and textural differences between them. The electrical measurements collected at Site 2 will be discussed in detail as an example, with a more abbreviated discussion of the measurements from the other sites.

6.5.1. Site 2 – No.2 Orebody

Site 2 was located in 2 Orebody. The well defined bedding of the orebody is clearly observed in a photograph mosaic of the site (Figure 6.9). 2 Orebody has high zinc content with low pyrite content. Assays of samples collected from the site average 20% zinc, 10% lead and less than 8% iron. A lithological log of the section at this site is shown in Figure 6.10 together with the location of samples and their important chemical characteristics. Photographs of several samples collected from Site 2 clearly show the mesoscopic layering of sulphides, carbonate and organic material (Figure 6.11).

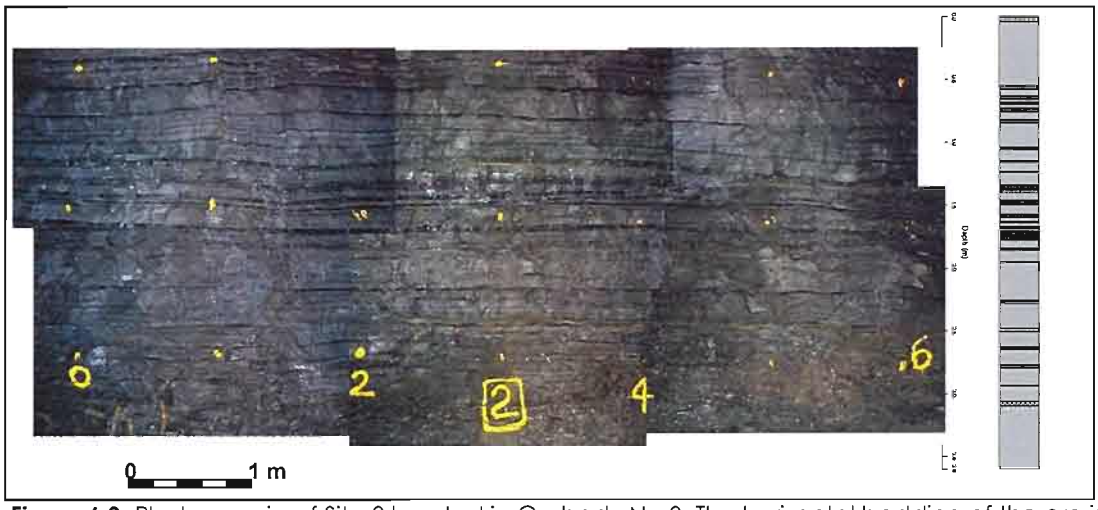

Figure 6.9. Photomosaic of Site 2 located in Orebody No.2. The horizontal bedding of the ore is clearly defined. Description of the stratigraphic log (shown in grey on the right) is explained in Figure 6.10.

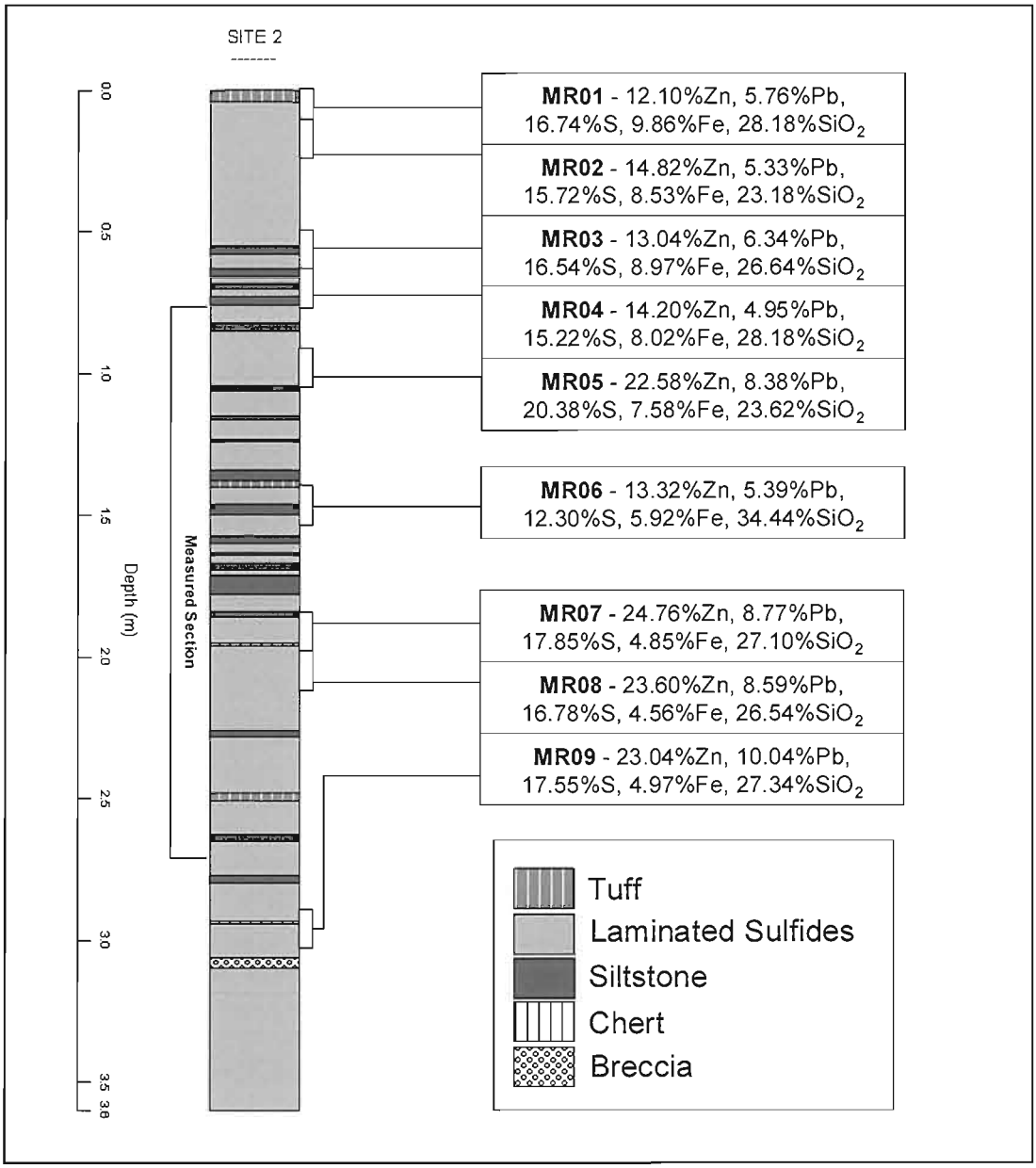

Figure 6.10. McArthur River Orebody No.2 lithological log and sample locations (Site 2). Samples were collected to provide representation of variability across stratigraphy. Assays of samples provided.

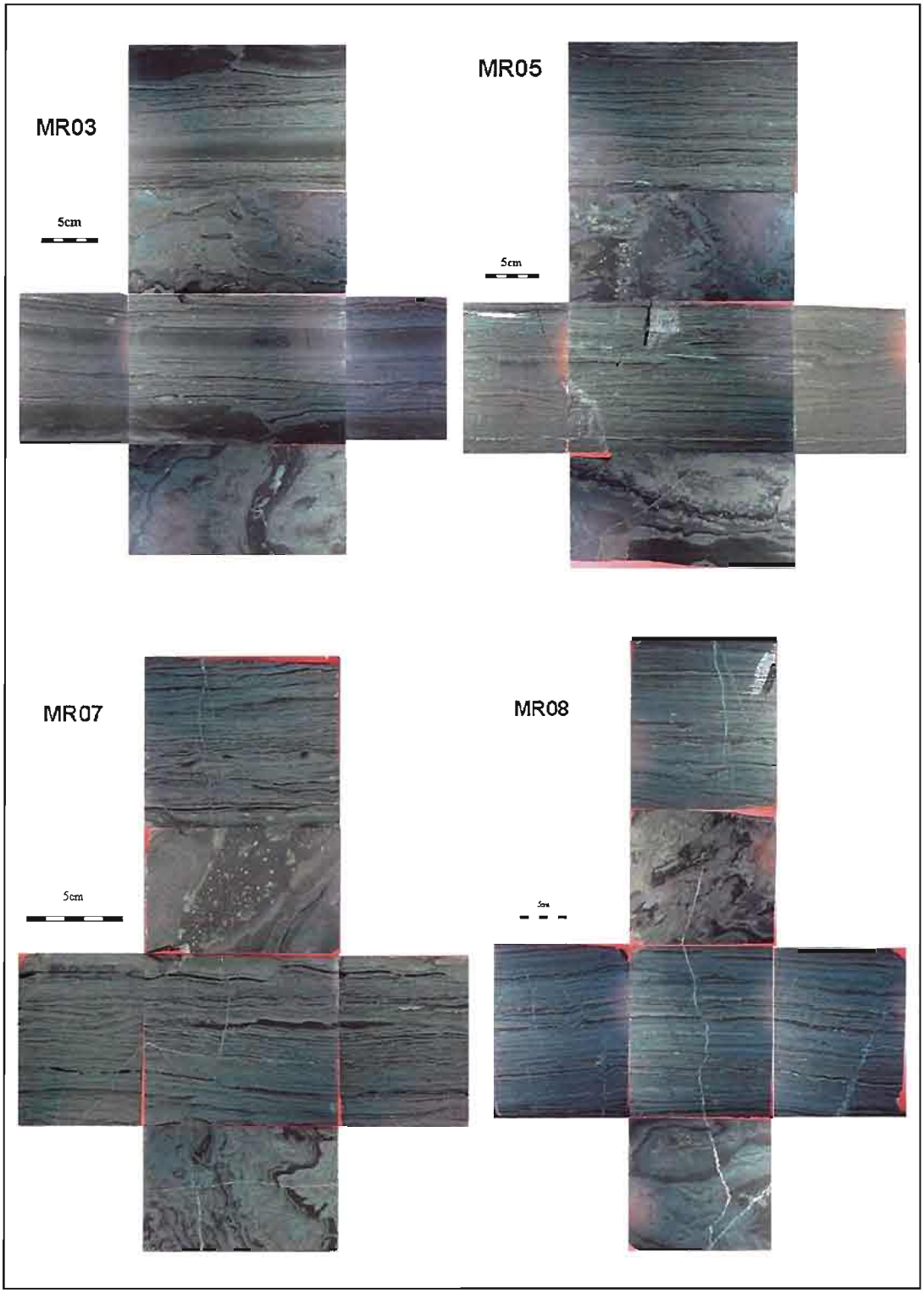

Figure 6.11. Samples (MR03, MR05, MR07 and MR08) collected from Site 2 in Orebody No.2, showing the distinct layers of sulphide, carbonate and organic material. Late stage cross-cutting carbonate, galena-sphalerite veins can be seen in samples MR07 and MR08. The photographs of the samples show an "exploded" view displaying all six sides of the prismatic sample.

6.5.1.1. Perpendicular measurements (longitudinal resistivity)

A series of electrical soundings, orientated perpendicular to bedding, were completed at Site 2. Apparent resistivity as a function of electrode spacing is shown in Figure 6.12. Scale effects are clear with apparent resistivity systematically decreasing with increasing electrode spacing (one order of magnitude) from ~200 Ωm to ~30 Ωm. The apparent resistivity data converges tightly at the largest spaced measurement (0.66 metres)

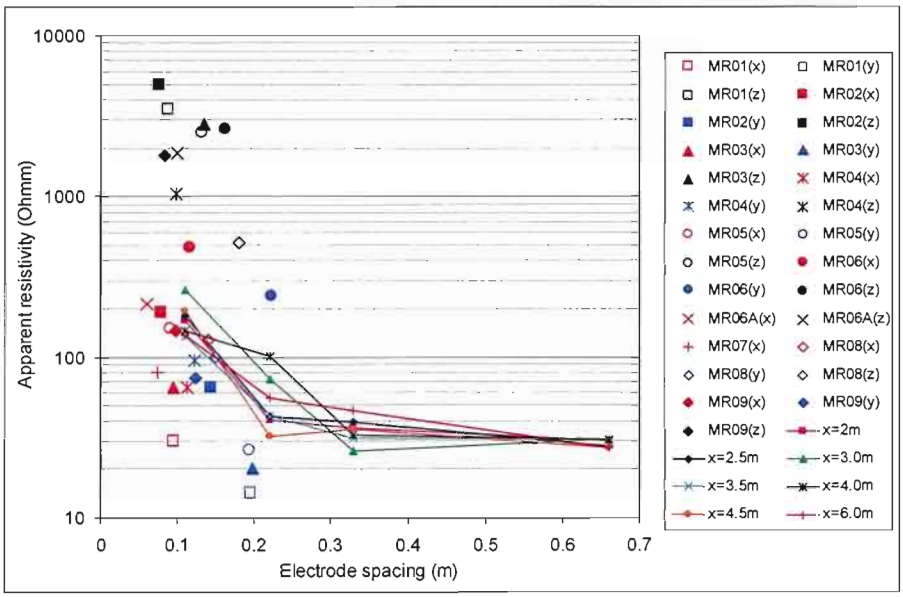

Figure 6.12. Apparent resistivity as a function of electrode spacing for Site 2, orientated perpendicular to bedding. Orthogonal measurements of samples are colour coded red (x), blue (y), and black (z).

The paradox of anisotropy states for an anisotropic medium, the apparent resistivity measured by an array orientated perpendicular to bedding ($\rho_{\perp measured}$) is directly equivalent to the longitudinal component of resistivity (ρ_l) as given by (Parasnis, 1997):

$$\rho_{\perp measured} = \rho_l \qquad (6.1)$$

Thus, the perpendicular measurements are directly comparable to longitudinal measurements on laboratory samples (marked as red and blue symbols on all diagrams, Figure 6.12). Laboratory longitudinal resistivity measurements (x & y) have a wide range from around 20 Ωm to less than 700 Ωm. But their median value (~100 Ωm) lies close to insitu values for small scale measurements.

Chargeability as a function of electrode spacing is shown in Figure 6.13. The scale variation of chargeability is not as pronounced as resistivity for all soundings, but all converge to a lower value (~80 mV/V) at the largest electrode spacing. In this case the chargeability at 0.11m electrode spacing lies near the lower bound defined by laboratory measurements (x & y). Samples with extremely high chargeability (>500 mV/V) all have high iron contents and hence higher pyrite concentrations (Figure 6.14).

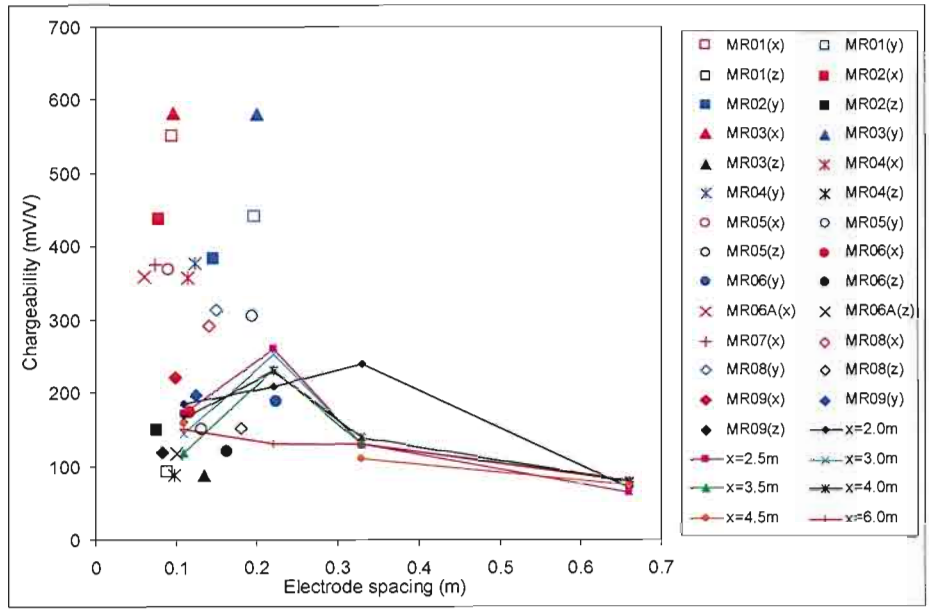

Figure 6.13. Chargeability as a function of electrode spacing for Site 2. Electrode array vertical, perpendicular to bedding. Orthogonal measurements of samples are colour coded red (x), blue (y), and black (z). Sample measurements in the x and y direction should be directly comparable to the insitu measurements.

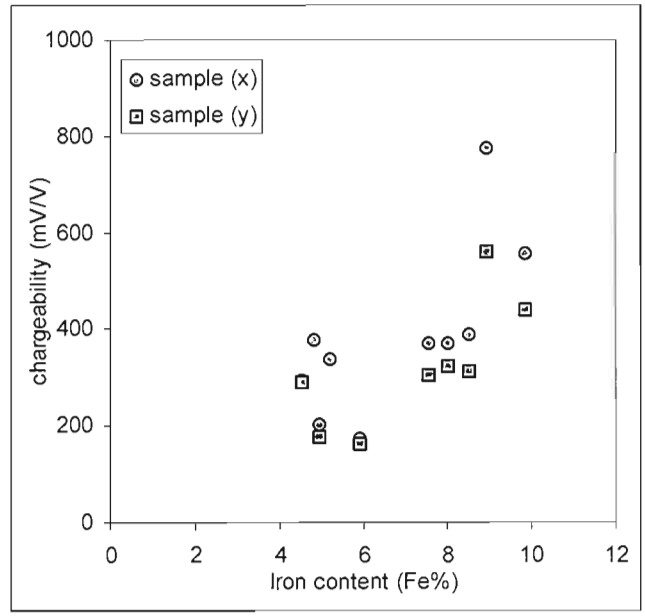

Figure 6.14. Samples from Site 2 show a positive trend between chargeability and iron content (r^2=0.45). These reflect an increase in pyrite concentration.

Histograms of log apparent resistivity for longitudinal insitu and laboratory measurements are shown in Figure 6.15. For longitudinal insitu measurements there is a clearly defined trend of decreasing apparent resistivity with increasing electrode spacing. Laboratory longitudinal resistivity measurements (x and y) span the range defined by insitu measurements with electrode spacings of 0.11 or 0.22m. On each graph in Figure 6.15 the dashed yellow line indicates the median value for measurements at the largest electrode spacing (up to 0.66m). The large-scale median lies below the lower quartile for 0.33m electrodes. The bulk insitu resistivity response is best predicted from the minimum of the laboratory data, rather than geometric mean or median.

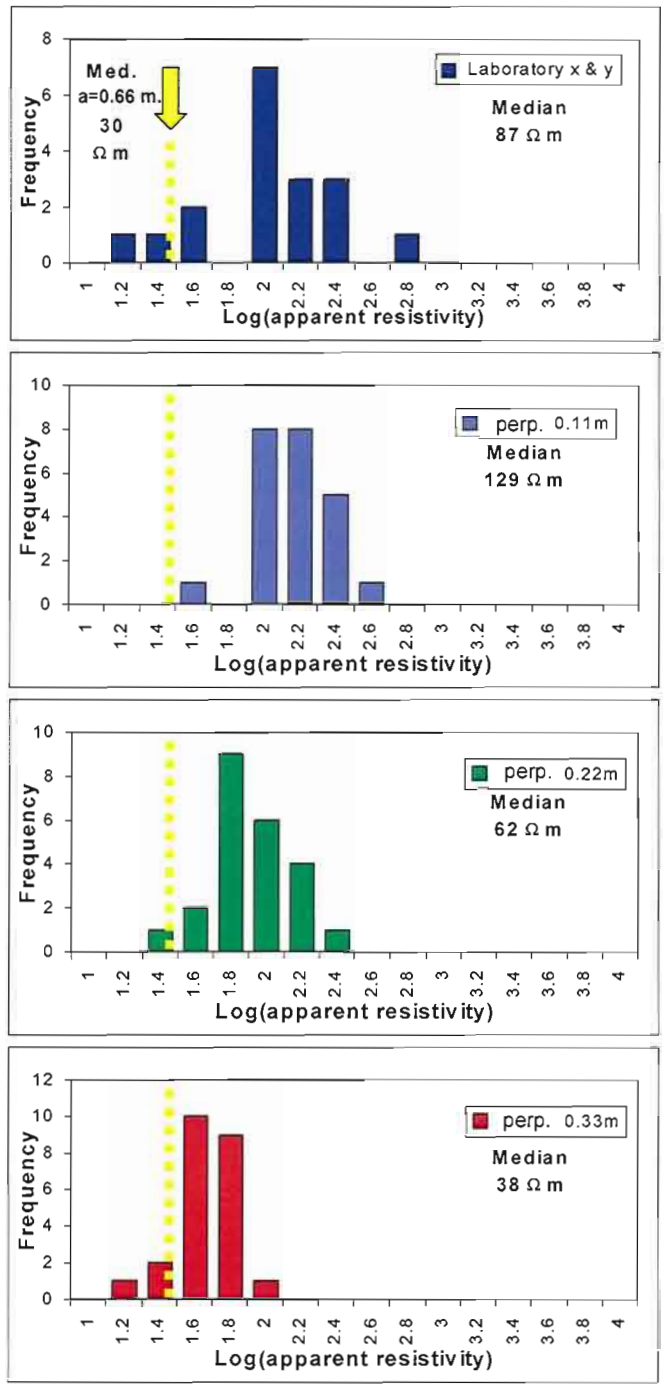

Figure 6.15. Histograms of longitudinal log(apparent resistivity) for Site 2 for insitu (perpendicular measurements) and laboratory measurements. The dashed yellow lines show the median values for large scale measurements at this site. Scale variations are clearly visible for the insitu data.

6.5.1.2. Parallel measurements (~transverse resistivity)

Four electrical soundings were completed at 0.66 metre intervals orientated parallel to bedding (Figure 6.9). Apparent resistivity as a function of electrode spacing is plotted in Figure 6.16. Laboratory measurements in three orthogonal directions are plotted with an electrode spacing corresponding to the length of the sample.

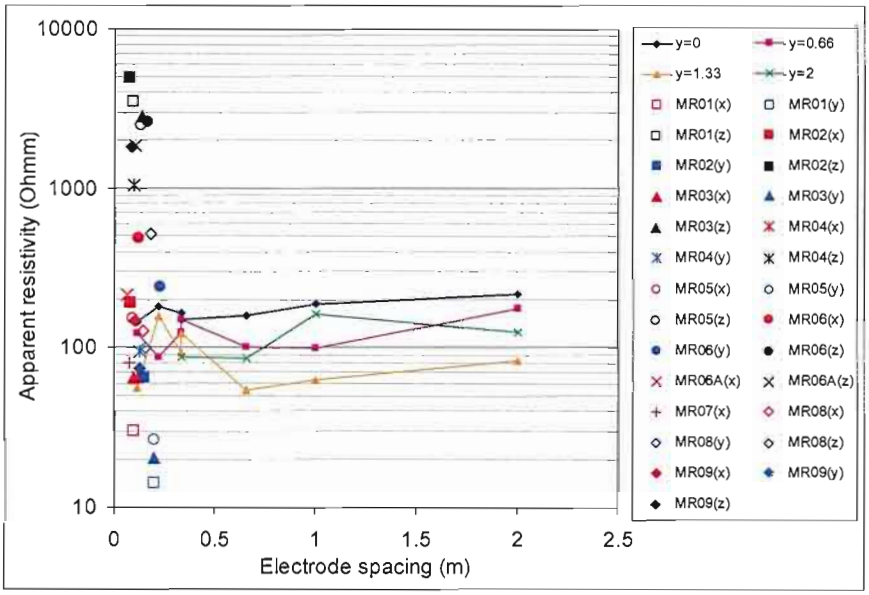

Figure 6.16. Apparent resistivity as a function of electrode spacing for Site 2, 2 Orebody. Electrode array orientated parallel to bedding. Orthogonal measurements of samples are colour coded red (x), blue (y), and black (z). Sample measurements in the x and y direction should be directly comparable to the insitu measurements.

There are no significant variations in apparent resistivity as a function of electrode spacing for parallel insitu measurements at this site (Figure 6.16). The different traverses reflect vertical variation across the site. Resistivity values for the four traverses range from 50 to 250 Ωm, with a median of ~100 Ωm.

It is not appropriate to directly compare sample resistivity measurements to the parallel insitu measurements. The paradox of anisotropy states for an anisotropic medium, the apparent resistivity measured by an array orientated parallel to bedding ($\rho_{\parallel}$) is related to a function of the transverse (ρ_t) and longitudinal (ρ_l) apparent resistivity as given by (Parasnis, 1997):

$$\rho_{\parallel measured} = \lambda \rho_l \qquad (6.2)$$

where $\lambda = \sqrt{\frac{\rho_t}{\rho_l}}$

Thus, the measured insitu resistivity derived from the parallel array does not directly relate to any of the orthogonal resistivity measurements of the samples.

However, we can rearrange equation 6.2 to solve for the insitu transverse resistivity, using both the parallel ($\rho_{\parallel}$) and perpendicular ($\rho_{\perp}$) measurements, given by:

$$\rho_t = \frac{\rho_{\parallel measured}^{\,2}}{\rho_l} \qquad (6.3)$$

where $\rho_l = \rho_{\perp measured}$

As the position of each array centre was not coincident between perpendicular and parallel arrays (Figure 6.17) the transverse resistivity could not be calculated for all measurements. However anisotropy resistivity measurements were completed with the mobile electrode array, located around a central mid-point. The anisotropy measurements can be used to calculate a transverse resistivity for small spaced measurements (0.11, 0.22, and 0.33m). Longitudinal and transverse resistivity calculated from the anisotropy measurements for Site 2, using equation 6.1 and 6.3 are listed in Table 6.2.

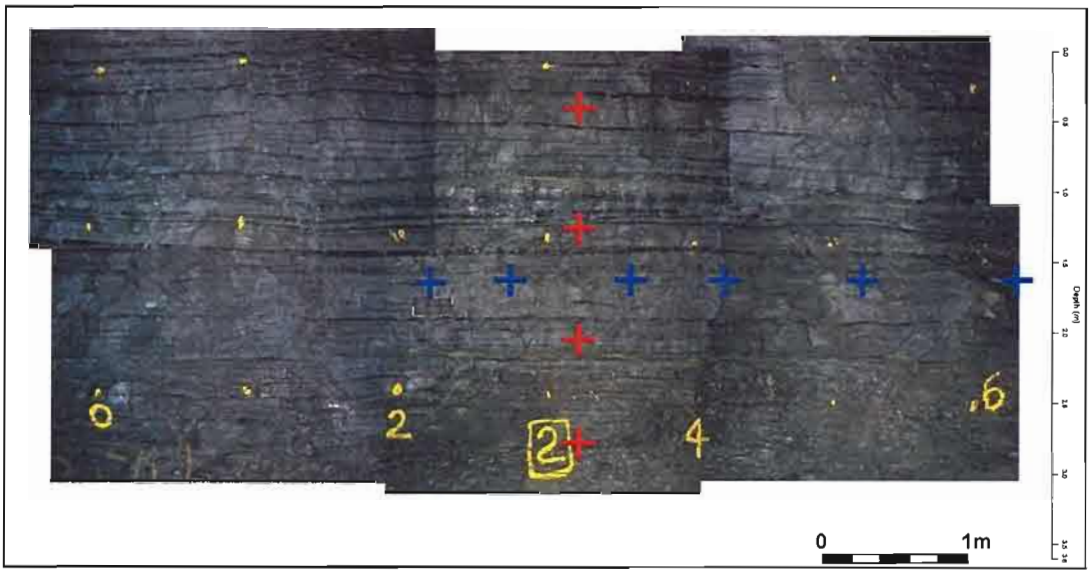

Figure 6.17. Positions of array centres for horizontal (red crosses) and vertical (blue crosses) measurements for Site 2.

Site	"a" spacing (metres)	Field measurements		Calculated components	
		$\rho_{\parallel}$ (Ωm)	$\rho_{\perp}$ (Ωm)	ρ_l (Ωm)	ρ_t (Ωm)
2	0.11	339.3	132	132	872
2	0.22	338.5	72.5	72.5	1580
2	0.33	429.4	26	26	7091

Table 6.2. Apparent resistivity measurements collected using the mobile electrode array orientated parallel ($\rho_{\parallel}$) and perpendicular ($\rho_{\perp}$) to layering within the ore, for Site 2. The longitudinal and transverse components of resistivity are calculated from these field measurement using equations 6.1 and 6.3.

The transverse resistivity derived from anisotropy mapping is plotted as a function of electrode spacing (Figure 6.18). Insitu transverse resistivity ranges from ~1000 to 7000 Ωm. The transverse laboratory resistivity of samples ranges from ~500 to 5000 Ωm (marked as black symbols on all diagrams) correlating well with the range of the insitu transverse measurements. The apparent resistivity for transverse measurements are clearly greater than apparent resistivity in the longitudinal direction, due to currents being impeded by the highly resistive layers of resistive volcanic sediments, as expected (Table 6.2).

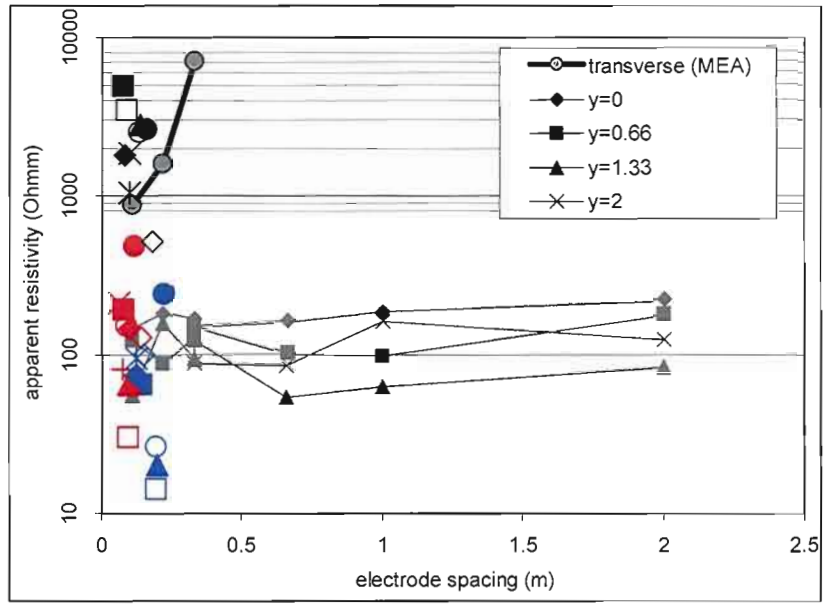

Figure 6.18. Transverse resistivity as a function of electrode spacing for Site 2, 2 Orebody. Transverse resistivity sounding is calculated from anisotropy mapping measurements. Parallel measurements shown in grey. Orthogonal measurements of samples are colour coded red (x), blue (y), and black (z). Sample measurements in the z direction should be directly comparable to median transverse sounding. See Figure 6.15 for legend for colour symbols.

Chargeability as a function of electrode spacing is plotted in Figure 6.19. Chargeability shows no obvious scale variation with insitu values ranging from 100 to 200 mV/V. Laboratory transverse chargeability of samples are generally consistent with the insitu chargeability data, ranging from 70 to 200 mV/V.

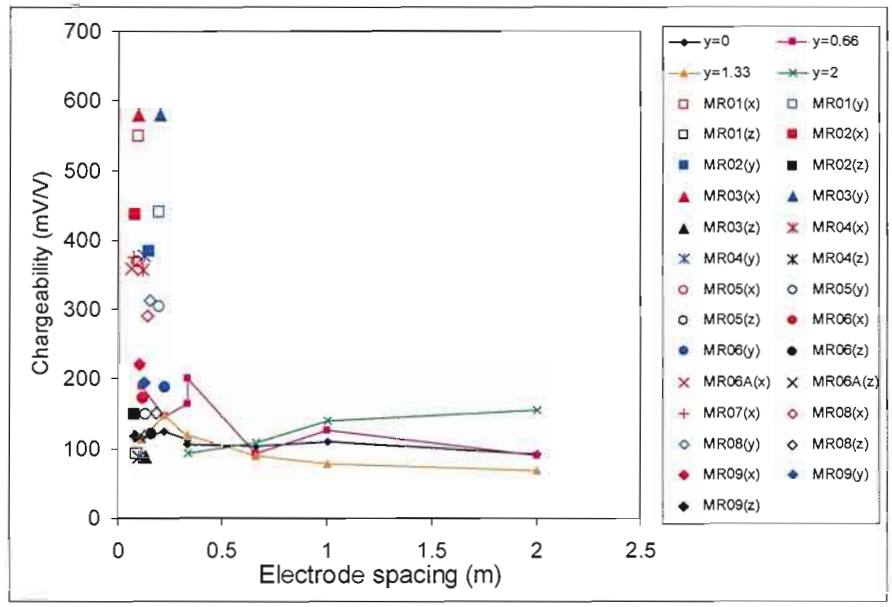

Figure 6.19. Chargeability as a function of electrode spacing for Site 2, 2 Orebody. Electrode array horizontal, parallel to bedding. Orthogonal measurements of samples are colour coded red (x), blue (y), and black (z). Sample measurements in the z direction should be directly comparable to z.

6.5.1.3. Anisotropy

Detailed measurements of anisotropy were completed using the mobile electrode array. Measurements were collected in 30 degree increments. Data are presented as resistivity and chargeability anisotropy maps as shown in Figure 6.20. The apparent resistivity anisotropy map reflects the markedly anisotropic nature of the ore, and clearly demonstrates the "paradox of anisotropy" (as described in Sections 6.4.4.1 and 6.4.4.2; equations 6.1 and 6.3). The resistivity anisotropy becomes more significant with increasing electrode spaced measurements at this site. Insitu chargeability is also anisotropic, but is less pronounced than resistivity anisotropy.

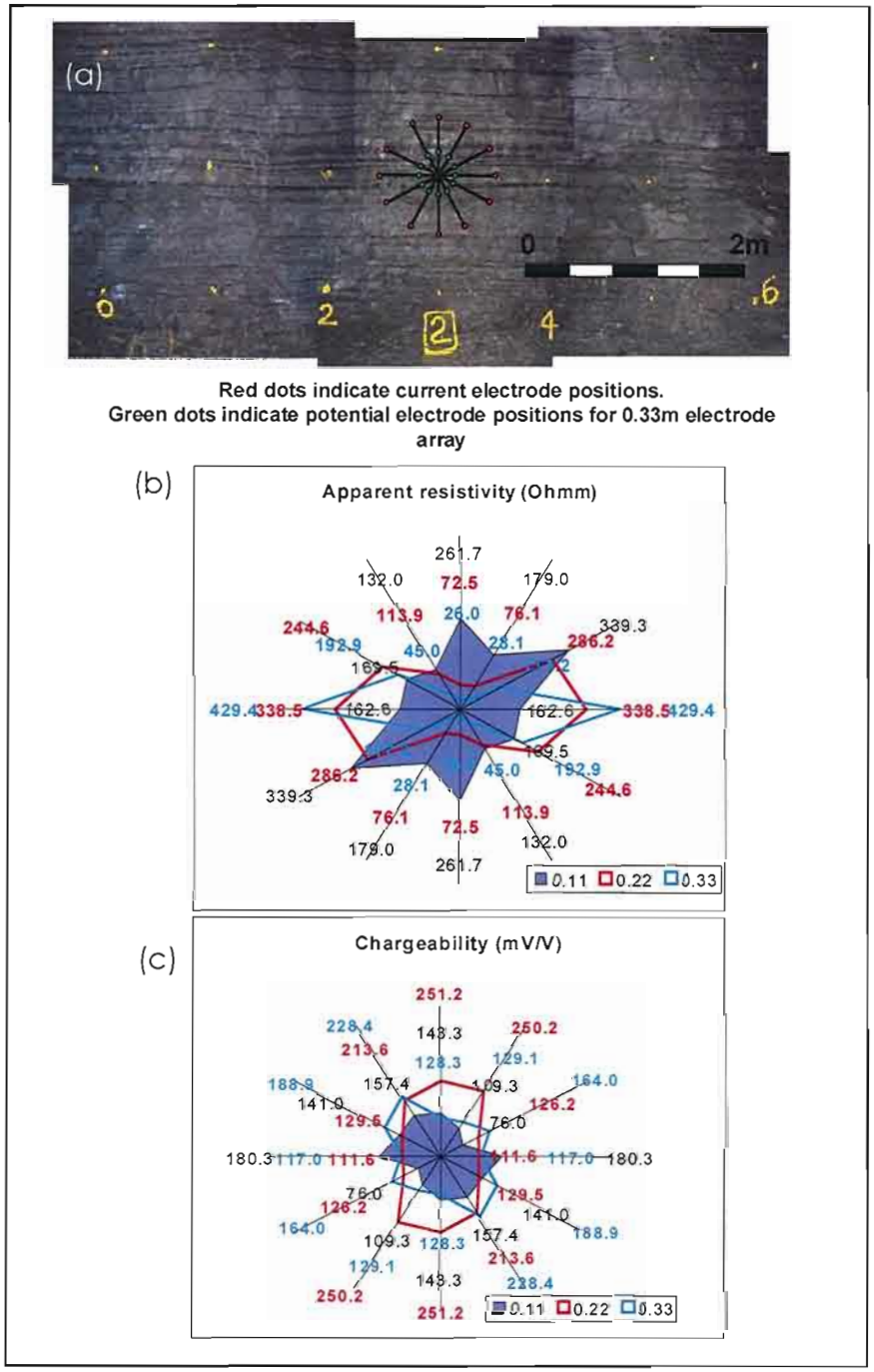

Figure 6.20. (a) Location of anisotropy measurements at Site 2 (b) Insitu apparent resistivity and (c) chargeability maps collected using the mobile electrode array (electrode spacings, of 0.11, 0.22 & 0.33m), as recorded in the field.

6.5.1.4. Mesoscopic properties of hand-samples

Continuity and current mapping were completed on a number of samples from McArthur River (Figure 6.21). The continuity map of sample MR05 collected from 2 Orebody (site 2) is shown in Figure 6.21b. A histogram equalisation contrast stretch has been applied to highlight the very poorly connected zinc-rich bands. The grade for this sample is 22.6% zinc and 8.4% lead. The continuity map clearly defines sulphide mineral bands interspersed within the resistive carbonates. Red zones within the continuity image indicate proportions of the sample that are well connected to the fixed electrodes, while black areas are not connected. Thin lamina rich in type-1 pyrite are generally well connected. However some aggregates of type-2 pyrite within carbonate or sphalerite rich bands are poorly connected in comparison.

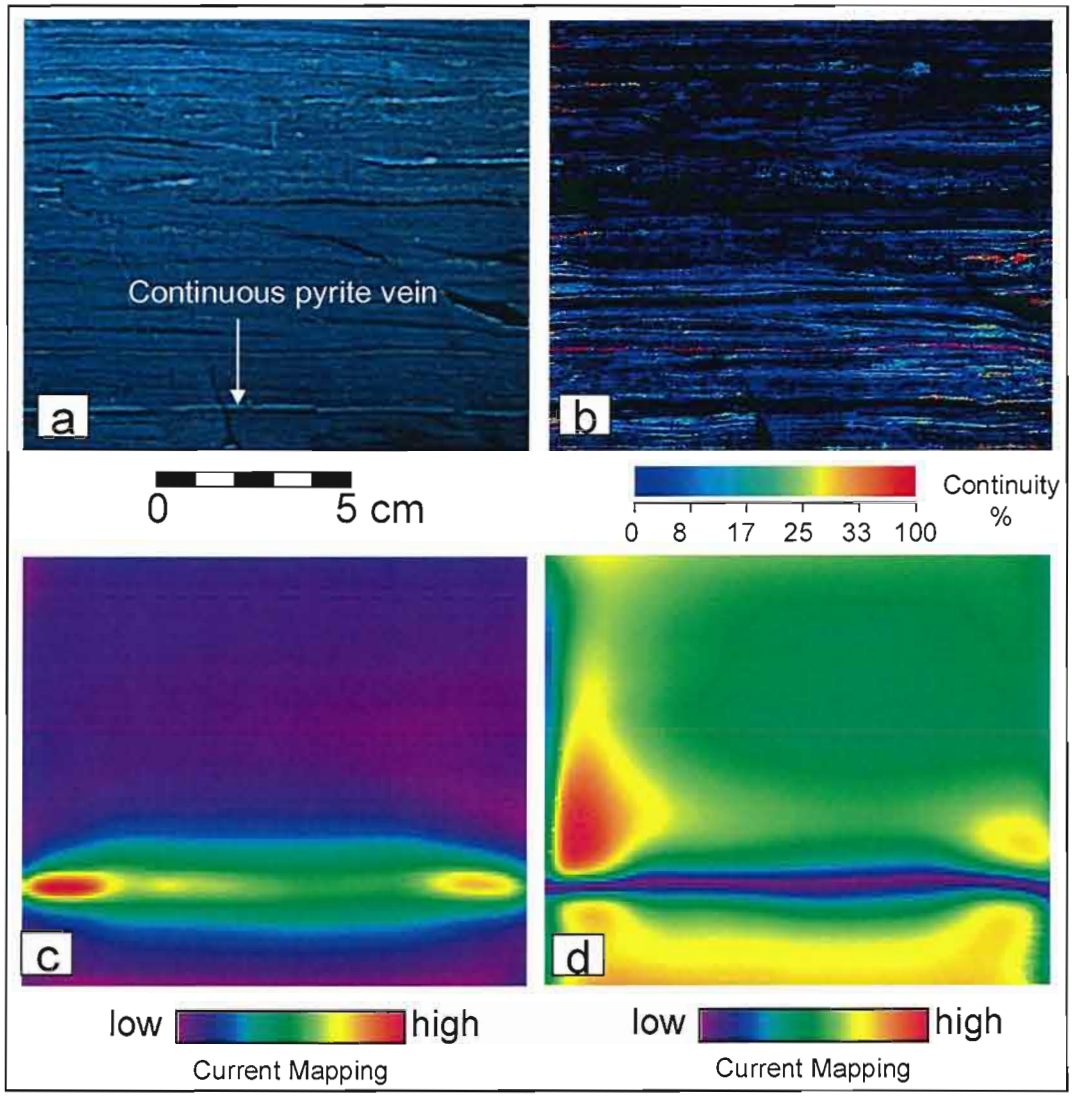

Figure 6.21. Continuity and current mapping results for sample MR05 collected from 2 Orebody. (a) Optical image. (b) Continuity image (histogram-equalised colour distribution). (c) Y component current map. (d) Z component current map. Maximum current flow is observed in the pyrite bands and indicated by Y-maximum and , Z-minimum.

The current maps of MR05 (Figure 6.21c and d) show that almost all of the current flows through a narrow band towards the bottom of the sample. This pathway coincides with the position of a thin (1 mm) yellow-brown band containing a high proportion of type-1 pyrite. Comparison of the current map and continuity map shows this band to be very well connected with the

fixed electrodes. Similar results are observed in other high zinc samples confirming that current predominantly flows in bands rich in type-1 pyrite and very little current flow occurs in more zinc rich bands.
Sample MR18 collected from 3 Lower Orebody has late stage sphalerite-galena-carbonate veins transecting the sample (Figure 6.22). Continuity and current mapping was conducted to assess the effects of these late stage features on the overall conductivity of the ore. The Continuity image reveals type-1 pyrite veins to be well connected, and zinc-rich layers to be poorly connected. The late stage veins are predominantly disconnected appearing as black zones within the image. The z current map reveals a number of current pathways in the sample. Although these current paths correspond to zones of elevated continuity, they are by no means the best connected region as indicated by the continuity image. The late stage crosscutting veins appear to have little effect on the flow of current through the sample.

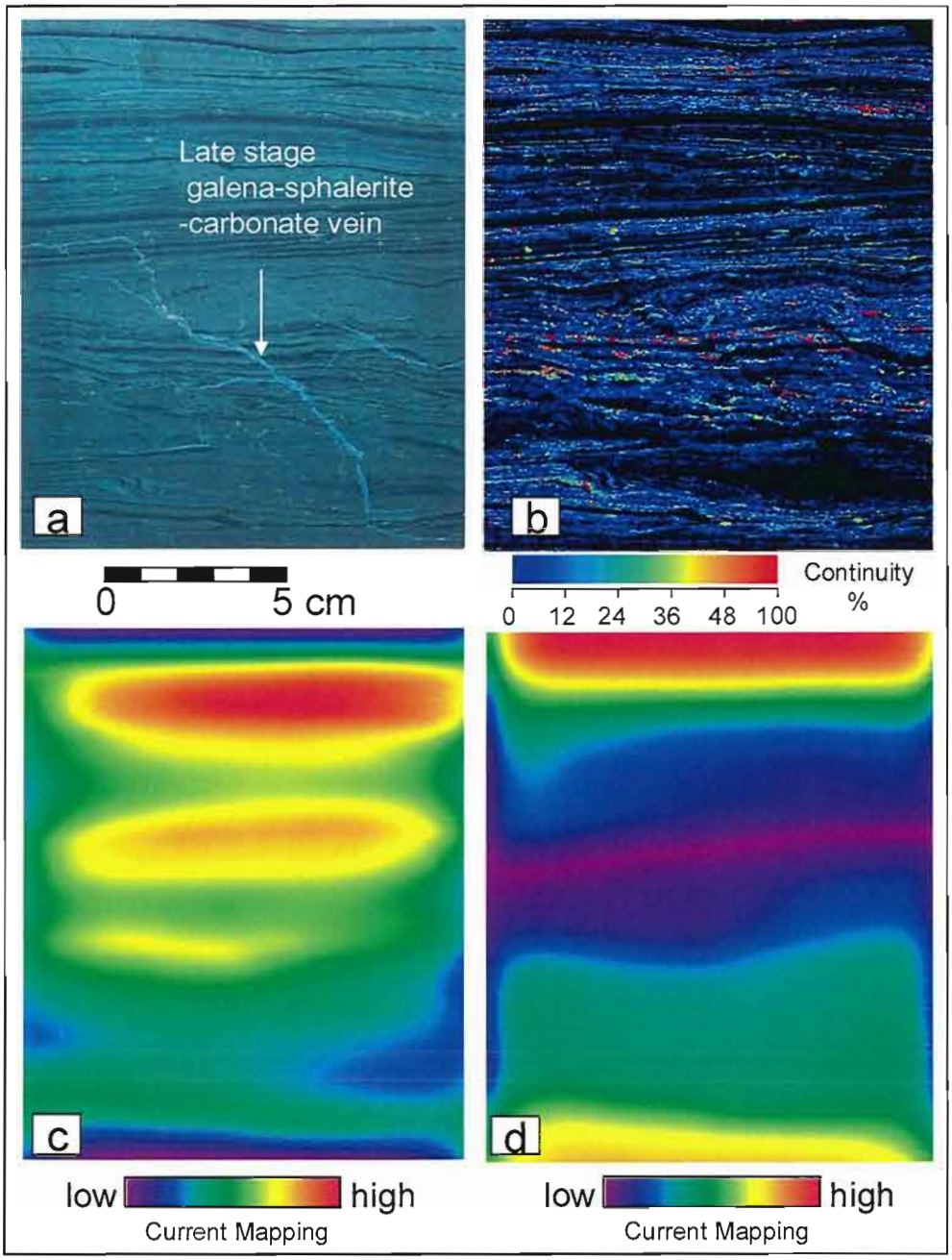

Figure 6.22. Photograph (a) and continuity (b) and current maps (c and d) for sample MR18 (3 Lower Orebody). Maximum current flow is of opposite magnitude between y and z components.

A photomicrograph of the late stage vein (Figure 6.23) in sample MR18 shows euhedral crystals of galena (light grey) projecting inward from the vein margin. The bulk of the vein is composed of coarse grain sphalerite (mid grey) with minor carbonate (dark grey-back). The galena within these veins may be in proportions as high as 40%, however the crystals are typically isolated.

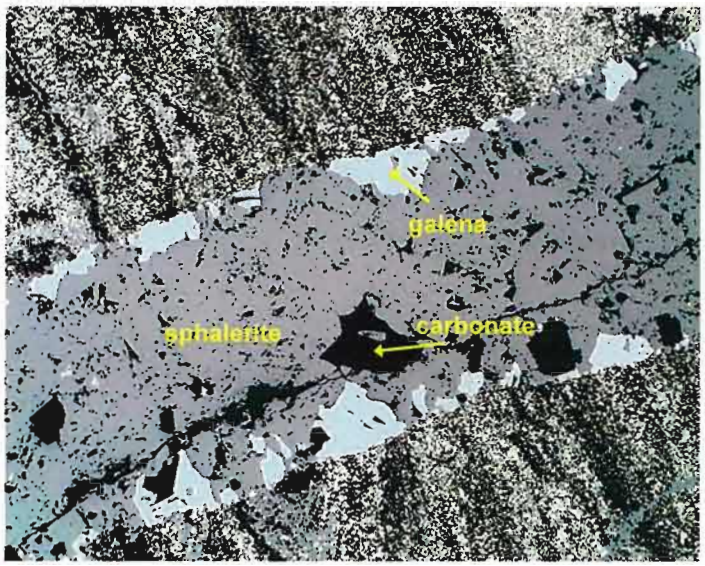

Figure 6.23. Reflected light photomicrograph of cross cutting late stage sphalerite-galena-carbonate veins. Large euhedral crystals of galena (light gray) project from the margin but do no form a connected network. Sample MR18, reflected light, field of view 4.1 x 3.2mm

6.5.2. Scale-dependent measurements: All Sites

6.5.2.1. Perpendicular array (longitudinal resistivity and chargeability)

The insitu measurements orientated perpendicular to bedding and laboratory measurements for all sites are presented in Figure 6.24. All sites show a consistent trend of apparent resistivity decreasing with increasing electrode spacing (one to two orders of magnitude) from 0.11 to 0.66 metres. Similar soundings recorded at each site indicate the vertical electrical homogeneity across the ore zone investigated. In the majority of cases, the multiple resistivity soundings at each site converge tightly at the largest-scale measurement.

The laboratory longitudinal resistivity measurements (x and y directions) can be directly compared to the insitu perpendicular measurements. The sample resistivity range typically lies within the range of the values recorded insitu at small electrode spacings, with moderate scattering.

There is a general decrease in insitu chargeability with increasing electrode spacing for most sites (Figure 6.24). Marked scale variation in chargeability is observed in Site 3 located within the 3 Lower Orebody. In almost all cases, longitudinal-chargeability measurements of samples (x and y directions) are typically a lot higher than those recorded insitu (by up to 4-5 times), with the exception of Site 3 (3 Lower Orebody) and Site 7 (3 Middle Orebody). For Site 3 and Site 7 laboratory chargeability of samples match insitu values for small scaled measurements. An interesting observation is that the transverse-chargeability of samples (z direction) correlates well to bulk insitu value for the majority of sites (Figure 5.24).

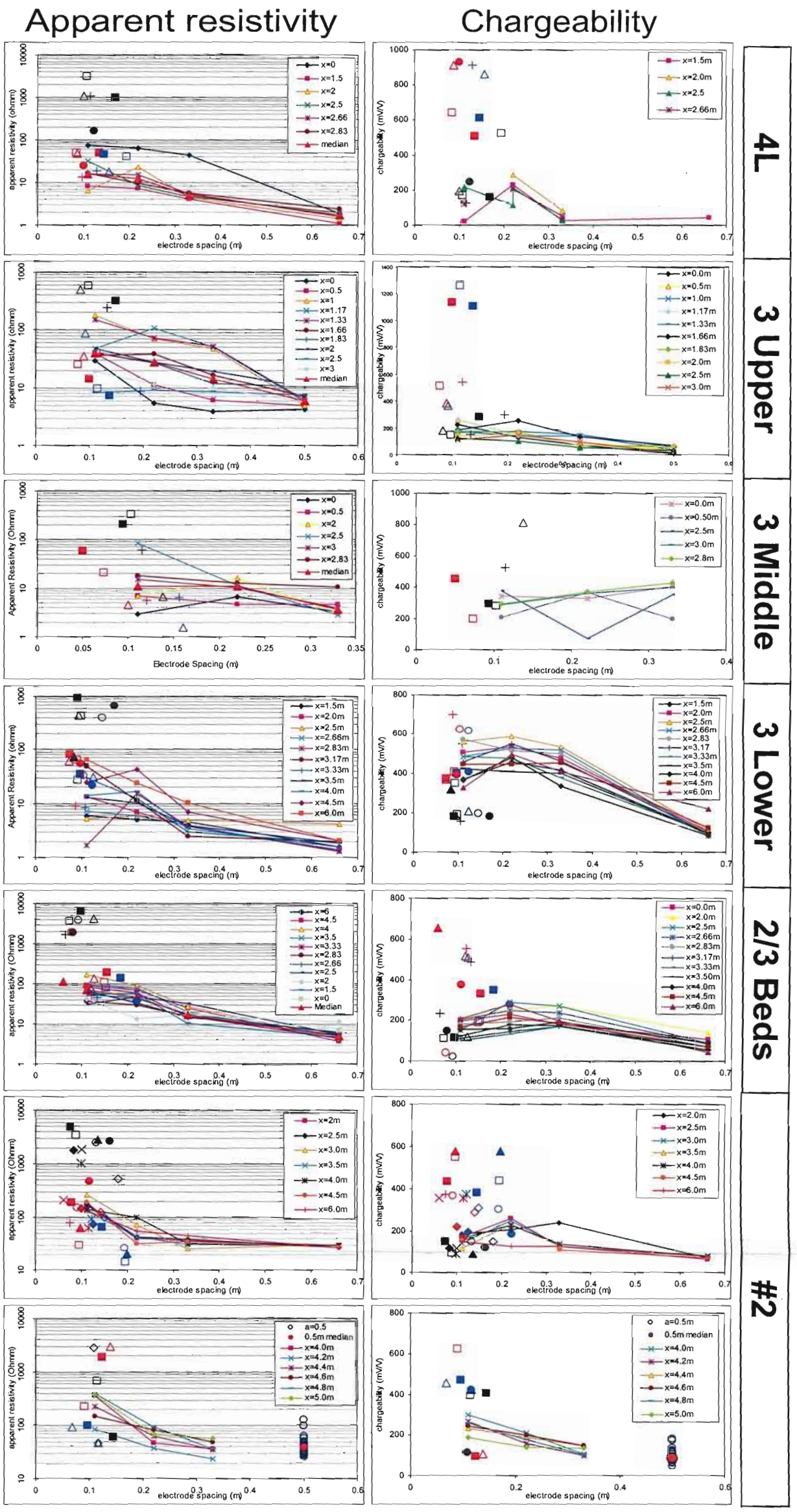

Figure 6.24. Insitu resistivity and chargeability measurements for all McArthur River sites, with the array orientated perpendicular to layering. Orthogonal measurements of samples are colour coded red (x), blue (y), and black (z). Sample measurements in the longitudinal direction (x,y) are directly comparable to insitu measurements.

The difference between longitudinal insitu and sample electrical properties for each site are summarised in the cross-plots of resistivity and chargeability for all McArthur River sites, as shown in Figure 6.25. The cross-plots highlight the problem in predicting the bulk electrical property from limited small-scale sampling. In all cases sample resistivity would overestimate the bulk resistivity response by one order of magnitude. Similarly laboratory chargeability measurements of samples would overestimate the bulk insitu response by up to 5 to 10 times in most cases.

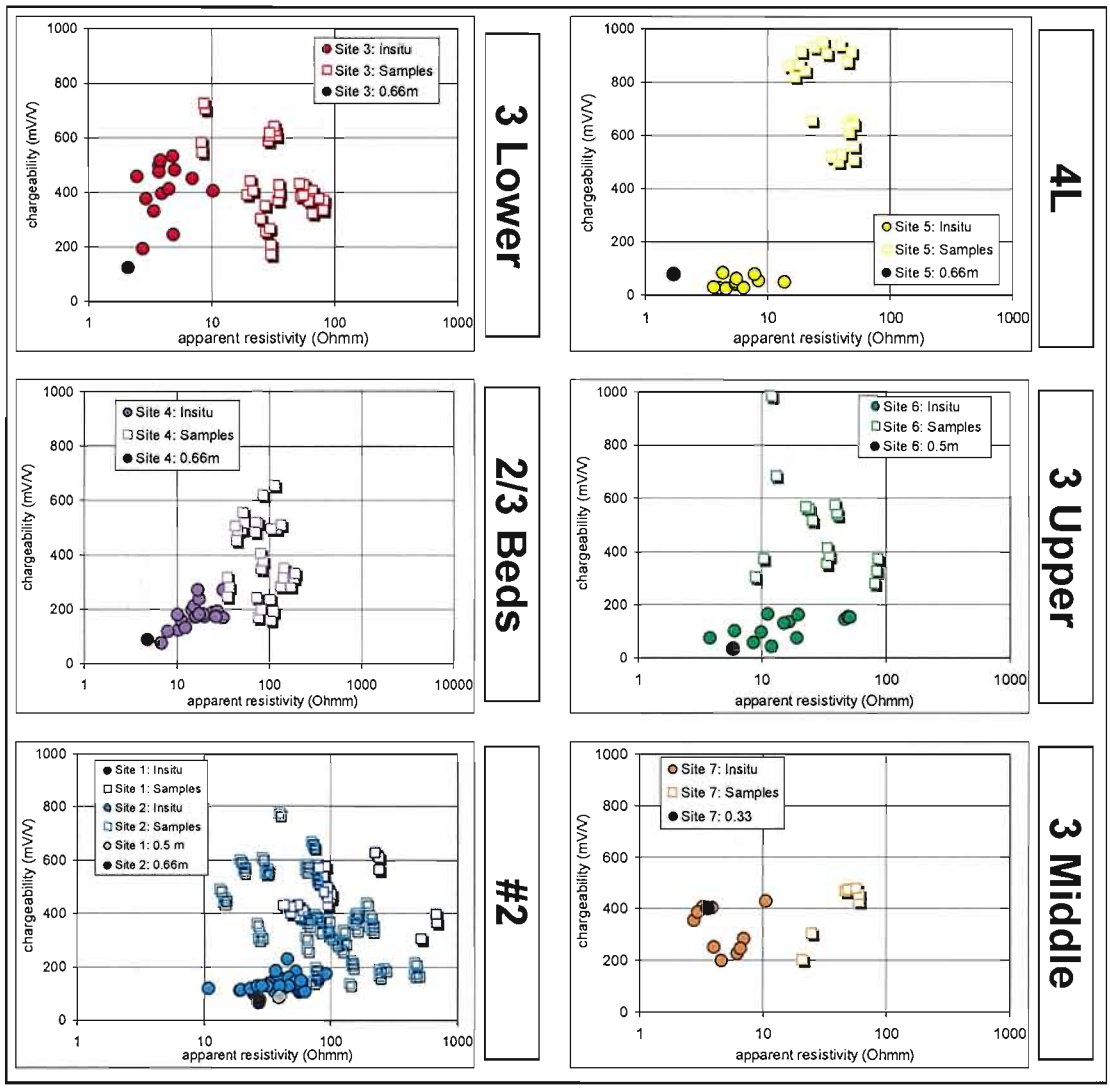

Figure 6.25. Longitudinal resistivity-chargeability cross-plots for insitu (perpendicular array) and laboratory measurements for all McArthur River sites. The insitu measurements (coloured dots) consist of all 0.11m, 0.22m and 0.33m measurements collected at each site. The black dot indicates the bulk median apparent resistivity, collected at the largest electrode spacing.

6.5.2.2. Parallel array (Transverse resistivity and chargeability)

The parallel insitu measurements and laboratory measurements for all sites are presented in Figure 6.26. There is little or no scale variation observed in apparent resistivity soundings for parallel measurements at all sites.

The multiple soundings at each site are collected at different stratigraphic intervals, thus provide an indication of the electrical variability observed, vertically across the ore horizon being investigated. Each site shows moderate variability in resistivity for the different parallel arrays.

Parallel array

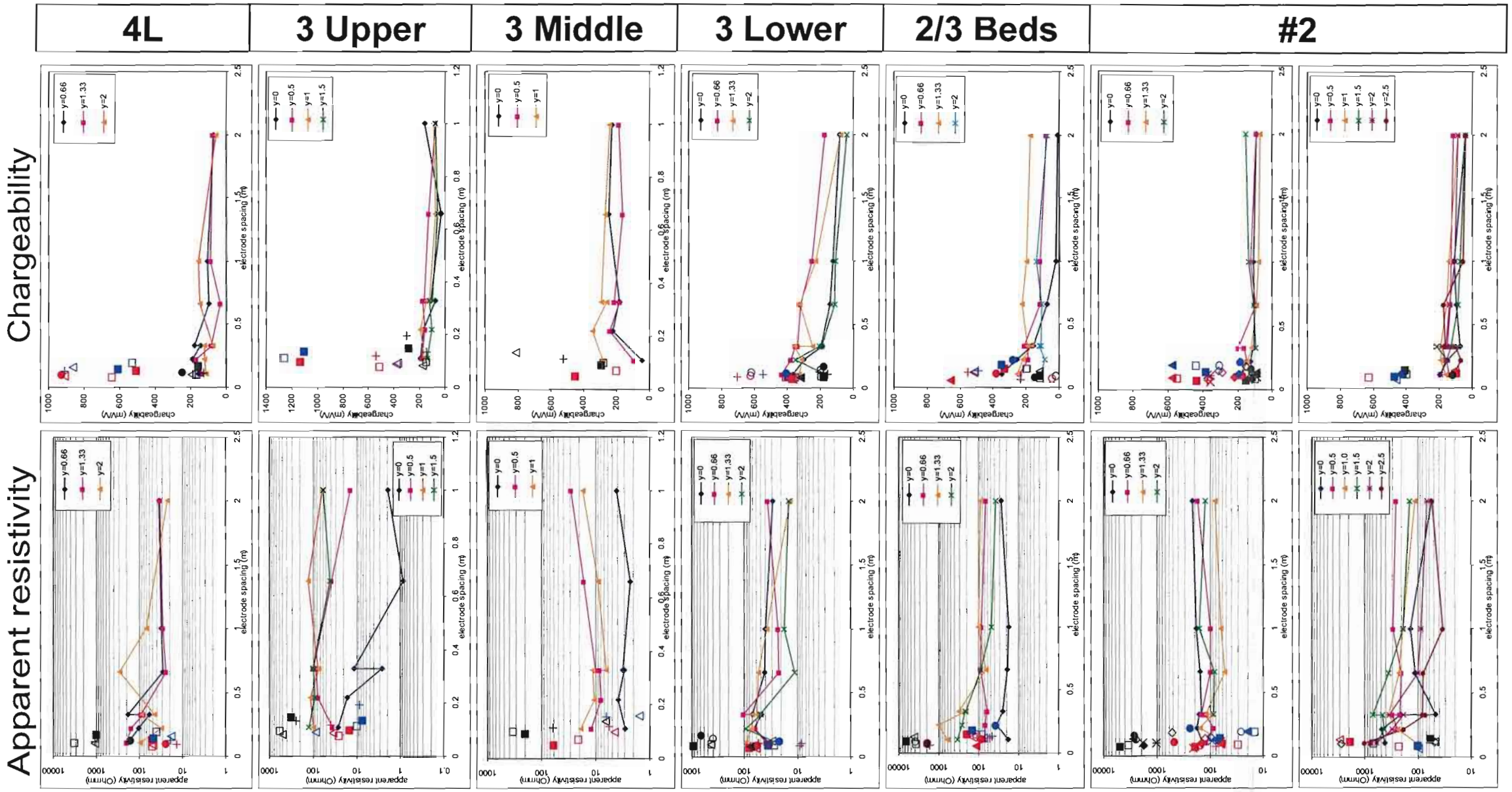

Figure 6.26. Insitu resistivity and chargeability measurements for all McArthur River sites with the array orientated parallel to layering. Orthogonal measurements of samples are colour coded red (x), blue (y), and black (z). Sample measurements in the longitudinal direction (x,y) are directly comparable to insitu measurements.

There is no consistent variation of chargeability as a function of electrode spacing for parallel insitu measurements (Figure 6.26). The transverse-chargeability measurements (z-direction) of samples coincide within the range of values measured insitu.

The transverse resistivity was calculated from parallel and perpendicular anisotropy measurements (using equation 6.3, section 6.4.1.2) collected at each site in order to be able to compare with transverse-sample resistivity data (Table 6.3). The calculated transverse resistivity soundings are plotted onto the original parallel-array sounding curves in Figure 6.27. The longitudinal resistivity data (derived from the perpendicular array measurements) are also plotted to provide an indication of the anisotropy between the two orthogonal components. The transverse resistivity soundings show no clear scale-dependent variation. The range of calculated insitu transverse resistivity lies within the range of transverse-resistivity of hand samples (z-direction). The transverse resistivity is much greater than longitudinal the resistivity, as the conduction is impeded by the highly resistive layers of siltstone and carbonate. Thus, there appears to be a lack of crosscutting conductive features that would connect the conductive sub-parallel pyrite veins.

Orebody	Site	measured		actual	
		$\rho_{parallel}$	$\rho_{perpendicular}$	$\rho_{longitudinal}$	$\rho_{transverse}$
4	5	142.2	2.2	2.2	9191.3
3U	6	91.2	11.2	11.2	742.6
3M	7	28.1	3	3	263.2
3L	3	18	2.8	2.8	115.7
2/3	4	92.3	6.9	6.9	1234.7
2	2	429.4	26	26	7091.7
2	1	943.1	51.7	51.7	17203.8

Table 6.3. Transverse and longitudinal resistivity components derived from parallel and perpendicular measurements from anisotropy mapping (0.33m).

6.5.2.3. Anisotropy mapping

Insitu anisotropy maps of resistivity and chargeability of each site are presented in Figure 6.28. All sites show a significant anisotropy in resistivity with larger values recorded with the array orientated parallel to laminations within the ore (obeying the paradox of anisotropy). The chargeability maps are typically isotropic for all sites, and do not appear to be significantly influenced by the layered nature of the ore.

The anisotropy ratio for parallel and perpendicular resistivity measurements (from 0.33 m spacing), along with the ratio for calculated transverse and longitudinal components (From Table 6.3) of resistivity are presented in Table 6.4. The transverse-longitudinal resistivity ratio is significant for all sites (~10:1 to ~100:1), and is extreme for Site 5, located in No.4 Orebody (~4000:1). The anisotropy for laboratory resistivity measurements of samples ranges from 5:1 to 250:1.

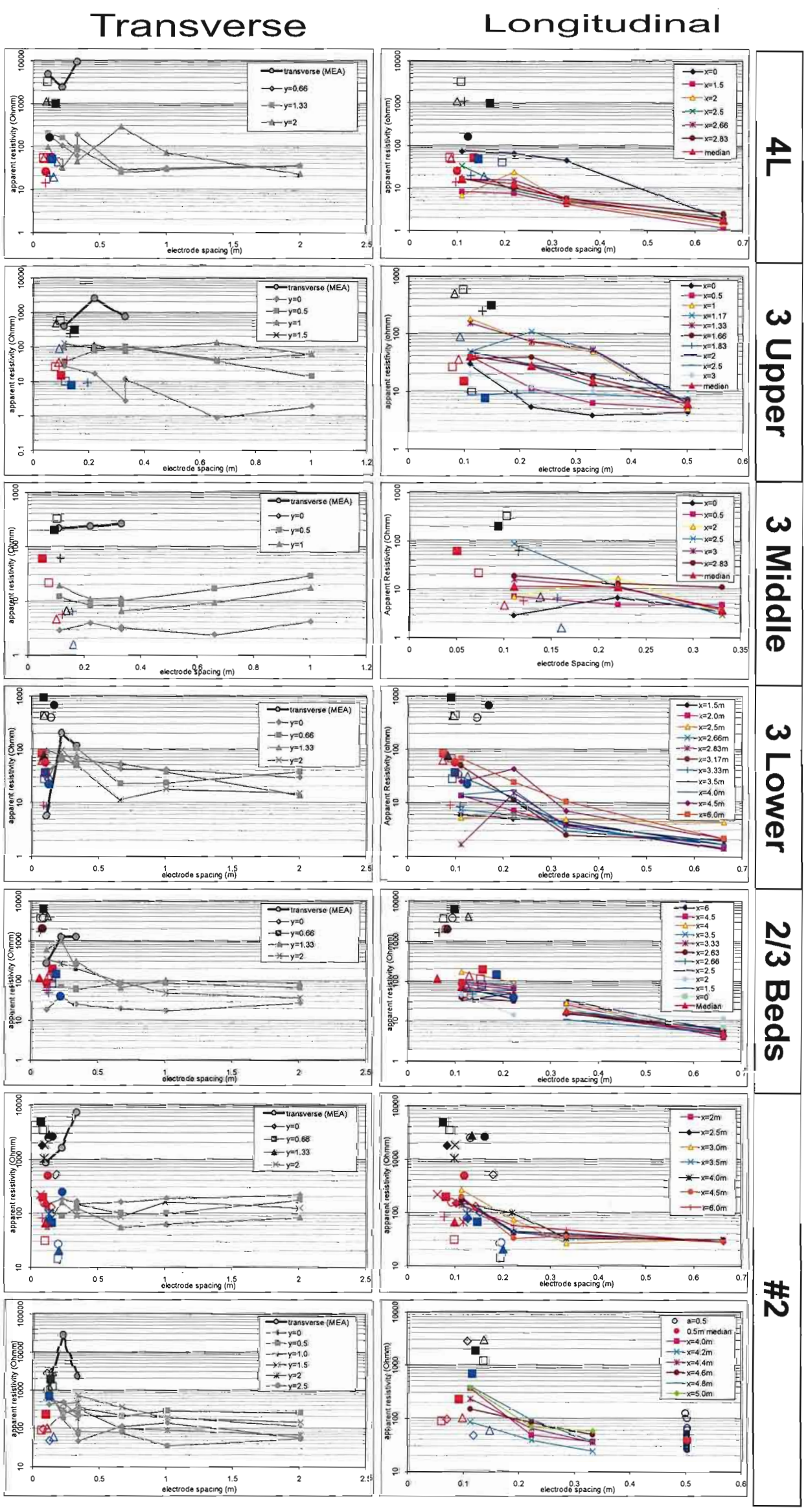

Figure 6.27. Transverse and longitudinal resistivity for all McArthur River sites. Transverse resistivity calculated using according to the paradox of anisotropy from anisotropy measurements, using the mobile electrode array (MEA). Orthogonal measurements of samples are colour coded red (x), blue (y), and black (z). Longitudinal components of samples are in the x,y plane, transverse component is in the z direction.

Anisotropy measurements

4L	3 Upper	3 Middle	3 Lower	2/3 Beds	#2

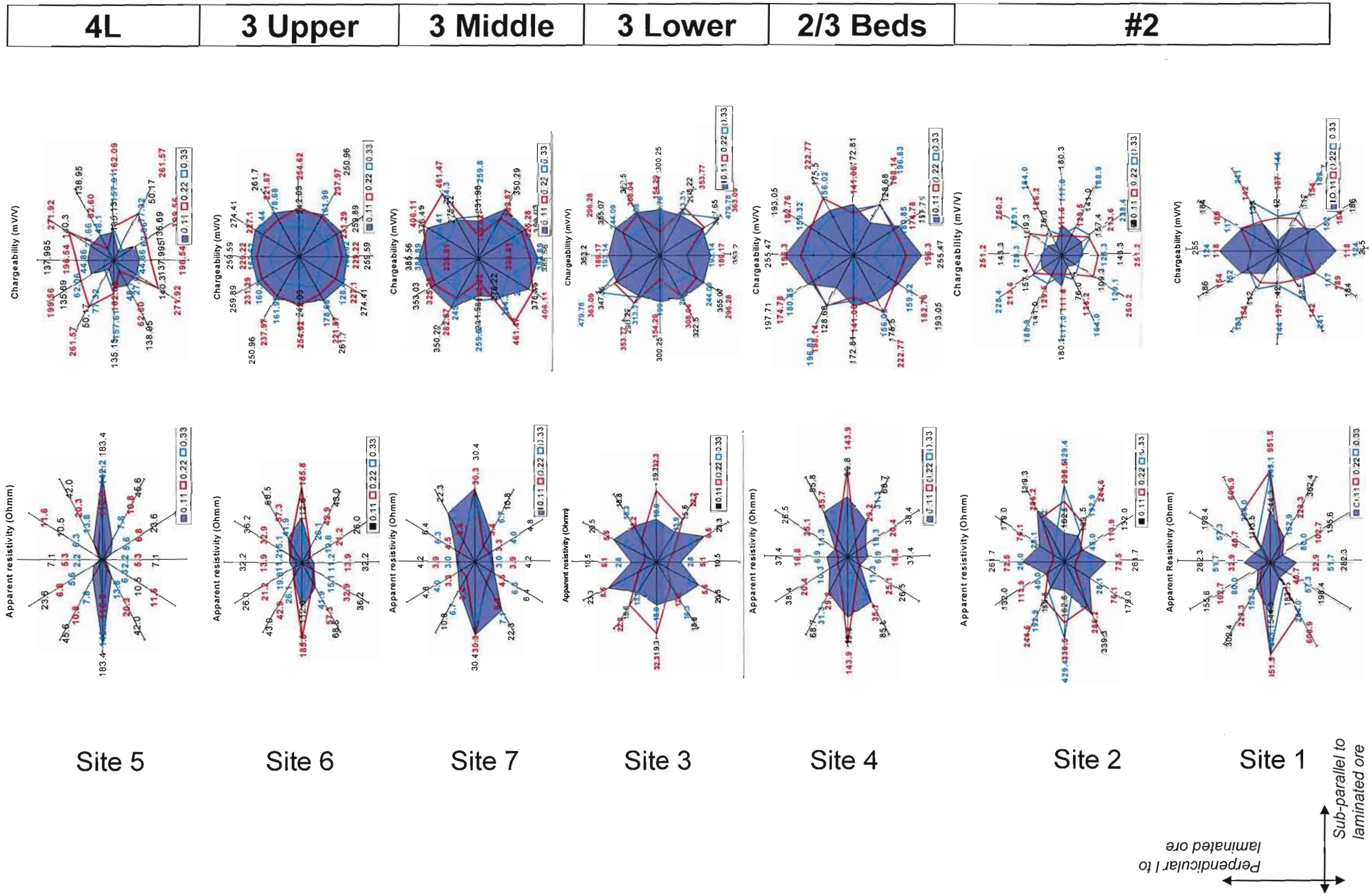

Figure 6.28. Resistivity and chargeability anisotropy maps for all McArthur River sites (0.11, 0.22, and 0.33 m electrode spacing).

Orebody	Site	parallel/perpendicular ratio	transverse/longitudinal ratio
4	5	65	4178
3U	6	8	66
3M	7	9	88
3L	3	6	41
2/3	4	13	179
2	2	17	273
2	1	18	333

Table 6.3. Anisotropy ratios for parallel-perpendicular orientated measurements (0.33 m electrode spacing) and calculated transverse-longitudinal components of resistivity for McArthur River sites.

6.5.2.4. Normalised Scale Variation

The longitudinal apparent resistivity soundings (perpendicular measurements) from all sites were normalised to show scale-variations with respect to the value measured at the minimum electrode spacing (0.11m). This was undertaken to assess whether a consistent scale variation was apparent and provide a measure of how well the properties at the largest electrode spacing (0.66m) could be estimated based on measurements at the smallest spacing.

The data from 63 vertical soundings is shown in Figure 6.29 together with median values. The general trend of decreasing resistivity with increasing spacing is apparent but the soundings do not appear to conform to a single well-defined scaling rule and considerable scatter is apparent. For each electrode spacing the apparent resistivity distribution is close to lognormal.

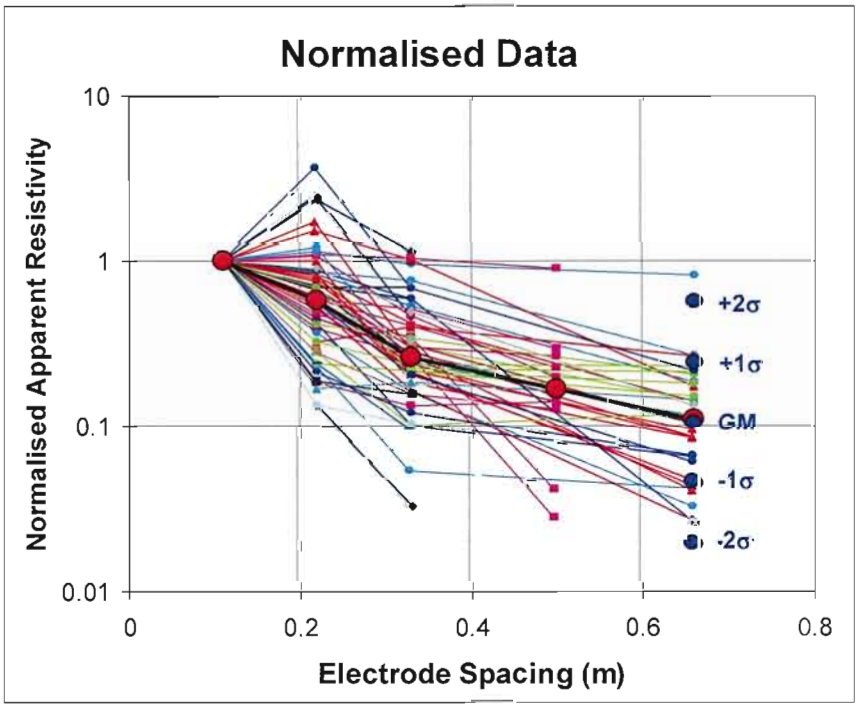

Figure 6.29. Normalised apparent resistivity as a function of electrode spacing for all longitudinal measurements (perpendicular array) collected at McArthur River Sites. Data has been normalised by the value at an electrode spacing of 0.11m. Large red dots mark the median values. Large blue dots mark the geometric mean and standard deviation limits for measurements with 0.66m electrode spacing.

The bulk insitu (electrode spacing of 0.66m) apparent resistivity median and geometric mean are 0.108 Ωm and 0.105 Ωm respectively. One and two standard deviations are also plotted in Figure 6.29. The graph in Figure 6.29 illustrates the extreme difficulty with accurately predicting the bulk apparent resistivity (at 0.66m) from small scale measurements (0.11m).

6.5.3 Electrical differentiation between ore horizons

Scatter plots of chargeability versus apparent resistivity for an electrode spacing of 0.33 m are shown in Figure 6.30, for perpendicular (a) and parallel (b) measurements, colour coded according to site number (ore horizon). Plots for other spacings show a similar pattern. Each ore horizon occurs in a well-defined resistivity-chargeability domain for perpendicular measurements, with minor overlap. The boundaries differentiating ore horizons in parallel measurements are apparent, but less distinct than perpendicular measurements.

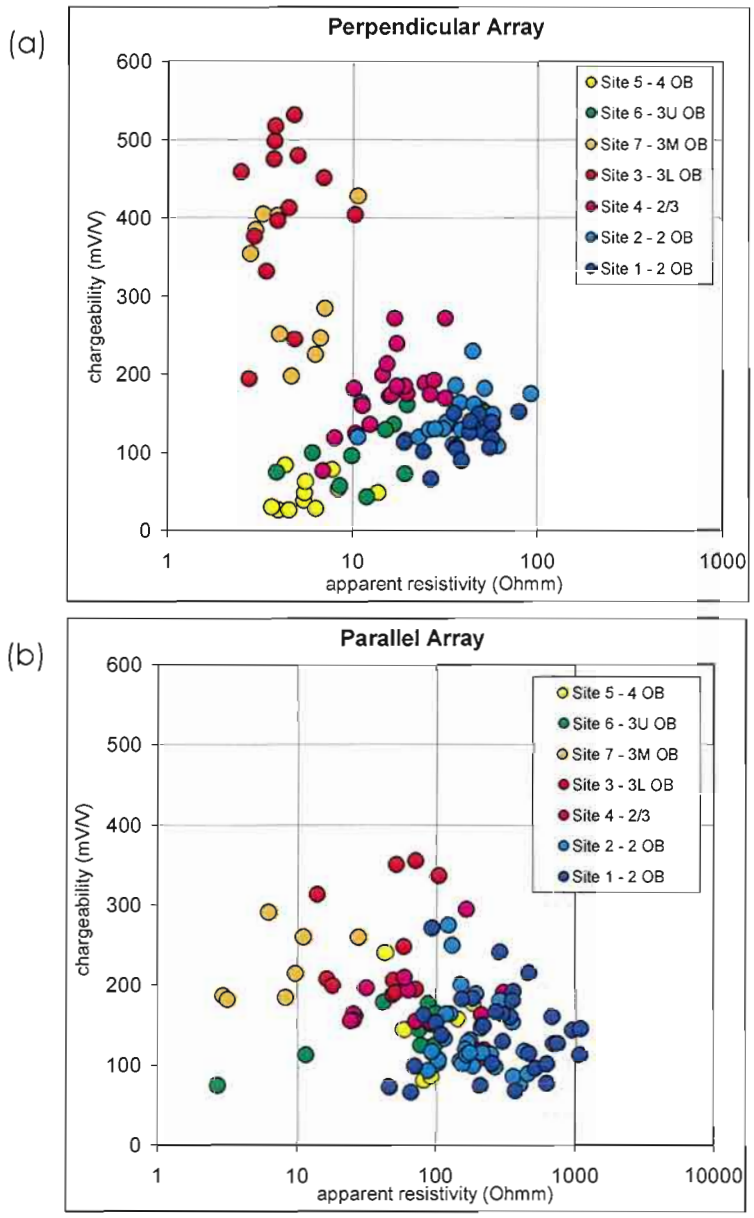

Figure 6.30. Scatter-plots of apparent resistivity-chargeability for McArthur River insitu measurements, for (a) parallel and (a) perpendicular array measurements. The different ore units (colour coded) plot in distinct domains, particularly for perpendicular measurements.

Measurements from 2 Orebody (Sites 1 and 2) consistently plot with high resistivity (20 - 100 Ωm perpendicular and 80-1000Ωm parallel) and low to moderate chargeability (70-200 mV/V) (Figure 6.30). The 3 Lower and 3 Middle Orebodies (Sites 3 and 7) plot together and show low resistivity (2-10 Ωm perpendicular and 2-80Ωm parallel) and high to very high chargeability (200-550mV/V). The marked difference between the 3 Lower and 2 Orebody does not result from a difference in zinc content, but is primarily due to the much higher proportion of type-1 pyrite in the 3 Lower and 3 Middle Orebodies (20-40% 3L/3M versus 5-10% for 2 Orebody). Samples from the 2/3 Beds (Site 4) have a moderate quantity of type-1 pyrite (10-15%) and the insitu data for this site lies intermediate between 2 Orebody and 3L/3M Orebodies in Figure 6.30.

Data from 4 Orebody (Site 5) and to a lesser extent 3 Upper Orebody, is anomalous in that it plots off the trend defined by 2 Orebody and 3 Lower Orebody end-members (Figure 6.30). This discrepancy is most apparent for perpendicular array measurements. Insitu measurements from 4 Orebody have similar apparent resistivity values to 3 Lower and 3 Middle Orebodies, but has significantly lower chargeability (<100 mV/V, as compared to 200-550 mV/V). Samples from 4 Orebody have almost the same zinc content and only slightly lower iron content than samples from the 3 Lower and 3 Middle Orebodies. The only significant geochemical difference between 4 Orebody and 3L Orebody samples is the relative proportion of lead in the form of galena. Samples from the 3 Lower Orebody have 4 to 5% Pb while those from 4 Orebody have 8 to 11.5% Pb. The 3 Upper and 4 Orebodies have higher proportions of lead than the 3 Lower Orebody. 3 Lower has 4 to 5 % lead as compared to 8 to 11.5% lead in Orebodies 4 and 3 Upper.

Galena in 3 Lower Orebody is primarily occurs as large irregular to rounded disseminated grains (20-40 μm) with only a small proportion present within the ground mass (Figure 6.31a). Sphalerite and carbonate make up the majority of the matrix enclosing the type-1 pyrite. The pyrite grains are evenly disseminated and are generally enclosed by resistive minerals.

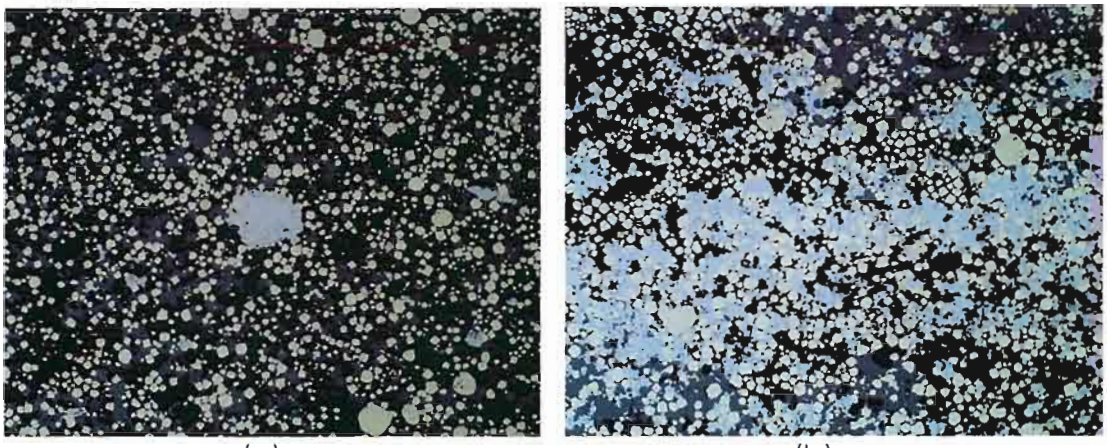

(a) (b)

Figure 6.31. Reflected light photomicrographs of; (a) typical ore texture in 3 Lower orebody (Site 3). Evenly disseminated type-1 pyrite in a matrix of sphalerite and carbonate. Galena is mainly present as "large" 20 – 40μm irregular grains (sample MR14). (b) typical ore texture in 4 orebody (Site 5). Evenly disseminated type-1 pyrite in a matrix of sphalerite, galena and carbonate (sample MR27). Field of view 180 x 136 μm.

In contrast, a significant proportion of the galena in samples from 3 Upper and 4 Orebodies forms bands connected interstitial to the type-1 pyrite (Figure 6.31b). Although this texture is not limited to samples from the 4 and 3 Upper Orebodies it is much more prominent than in samples from other stratigraphic levels. A proportion of the type-1 pyrite is enclosed in conductive galena, hence lowering the chargeability of the ore in compared to the 3 Lower Orebody. This observation may also help to explain the extremely high anisotropy of apparent resistivity observed for these ore horizons (3U and 4; Figure 6.28).

In summary the main cause for the marked difference in electrical properties between ore horizons is the variation in the proportion and textural association of type-1 pyrite (Figure 6.32). To a first order approximation the chargeability increases and the resistivity decreases roughly in proportion to the volume percentage of type-1 pyrite. A secondary effect is the presence of galena-rich zones in the groundmass which reduces the chargeability of the ore; this is characteristically featured in the 3 Upper and 4 Orebodies, which have high lead content.

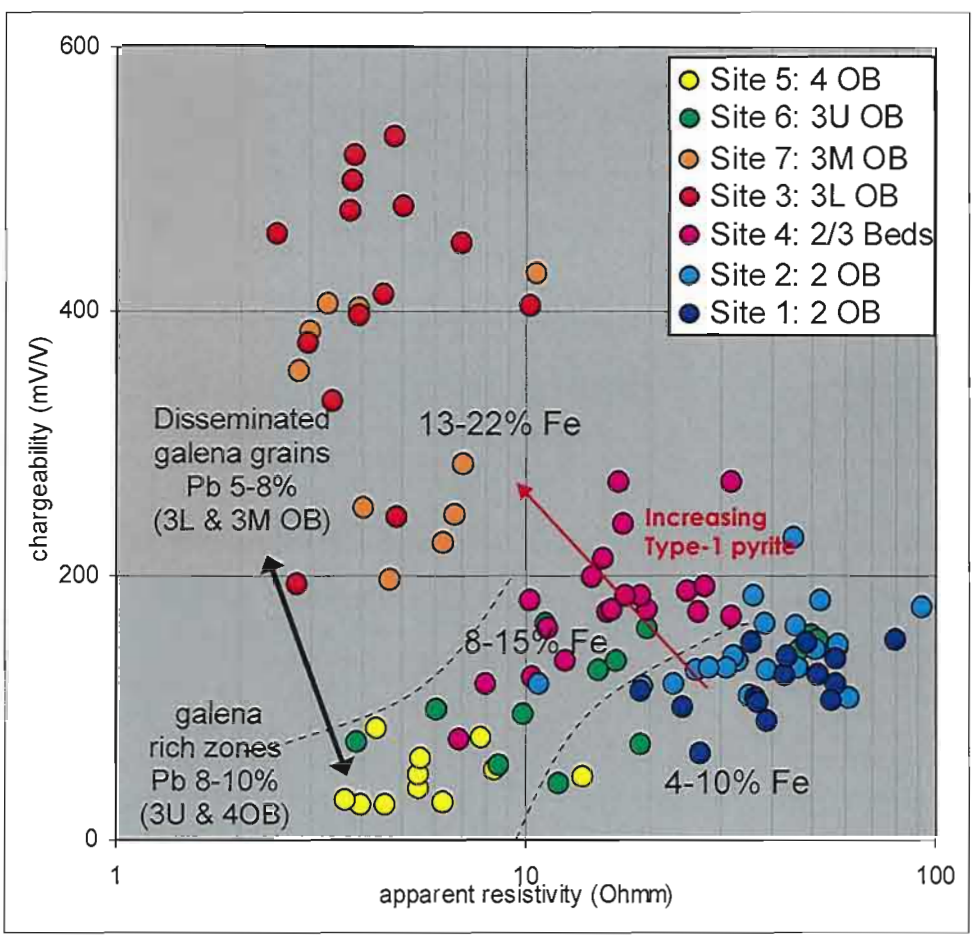

Figure 6.32. Resistivity-chargeability plot of all measurements showing the major differences between McArthur River ore horizons. Iron content which predominantly reflects type-1 pyrite explains the main difference between all the sites. 4 Orebody and 3 Upper Orebody have anomalously low chargeability, which is attributed to conductive galena veins which reduces the chargeability of the pyrite.

6.5.4. Chemical variations

The effects of chemical variations on the electrical properties of McArthur River ore samples were assessed using laboratory-scale electrical data. Samples were assayed for major elements.

A series of resistivity-chargeability plots for all laboratory measurements are shown in Figures 6.33-6.40. In each case data points are colour coded based upon major chemical characteristics including, zinc, lead, iron, sulphur, silicon and calcium oxide. Data is presented for both longitudinal measurements parallel to bedding (x and y) and transverse measurements perpendicular to bedding (z).

There are no systematic variations in apparent resistivity and chargeability with changes in zinc and lead content (Figures 6.33 & 6.34). Apparent resistivity decreases and chargeability increases with increasing iron content (Figure 6.35). This trend is more pronounced in transverse measurements, perpendicular to bedding. The increase in iron content largely reflects increasing type-1 pyrite content.

Variations in sulphur provide an indication of the total percentage of sulphide minerals. A clear trend of apparent resistivity decreasing and chargeability increasing coincides with increasing sulphur content (Figure 6.36)

The presence of silicate minerals appears to have little effect on the longitudinal (x and y) properties, but high silica samples are generally more resistive in the transverse direction (Figure 6.37). Silicate minerals are preferentially distributed in thin bands and the effects of these bands is greatest perpendicular to bedding. High carbonate content similarly affects the resistivity more significantly in the transverse direction (Figure 6.38).

Resistivity-chargeability plots were also colour-coded according to visual estimation of the two pyrite species; type-1and type-2 (Figure 6.39 & 6.40). There is a poorly defined relationship between electrical properties and visual estimates of the proportion of type-1 pyrite (Figure 6.39). Samples with a high proportion of type-1 pyrite typically have low resistivity and moderate to high chargeability. There is no clear correlation of electrical properties with type-2 pyrite (Figure 6.40).

The scatter in Figure 6.39 may reflect real bulk variations in type-1 pyrite, but is also influenced by the problems associated with extrapolating the modal percentage based upon visual estimates of single thin-sections (2-D) to large prismatic samples (15 x15 x15 cm). Estimates of mineralogy are based on bulk chemical composition provides a superior estimate, but unfortunately this method can not be used to differentiate between the two different pyrite types.

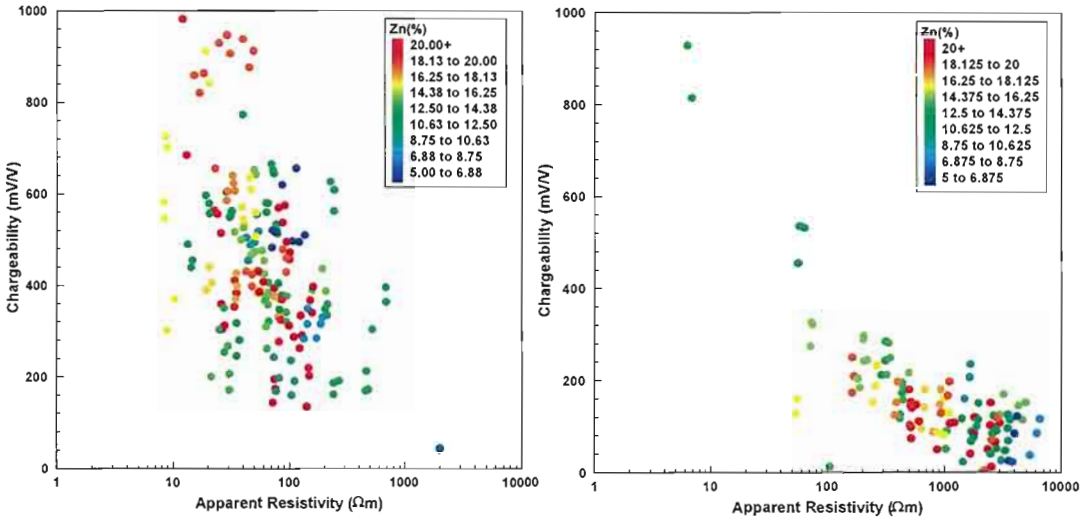

Figure 6.33. Cross plots of chargeability versus apparent resistivity for all laboratory measurements from McArthur River. Points have been symbolised based on Zn%. Data has been classified into longitudinal (bedding parallel) measurements (denoted x & y) and transverse measurements (denoted z).

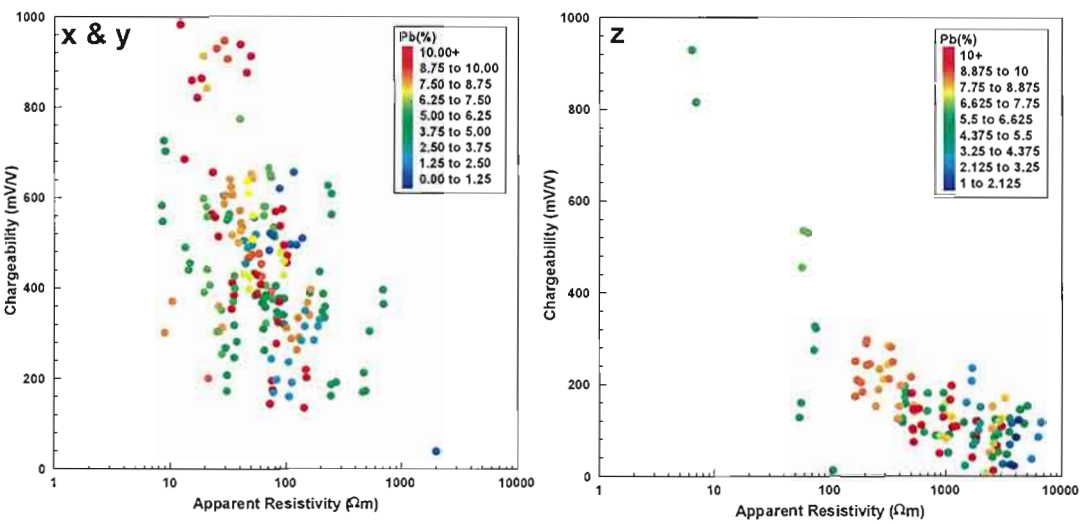

Figure 6.34. Cross plots of chargeability versus apparent resistivity for all laboratory measurements from McArthur River. Points have been symbolised based on Pb%. Data has been classified into longitudinal (bedding parallel) measurements (denoted x & y) and transverse measurements (denoted z).

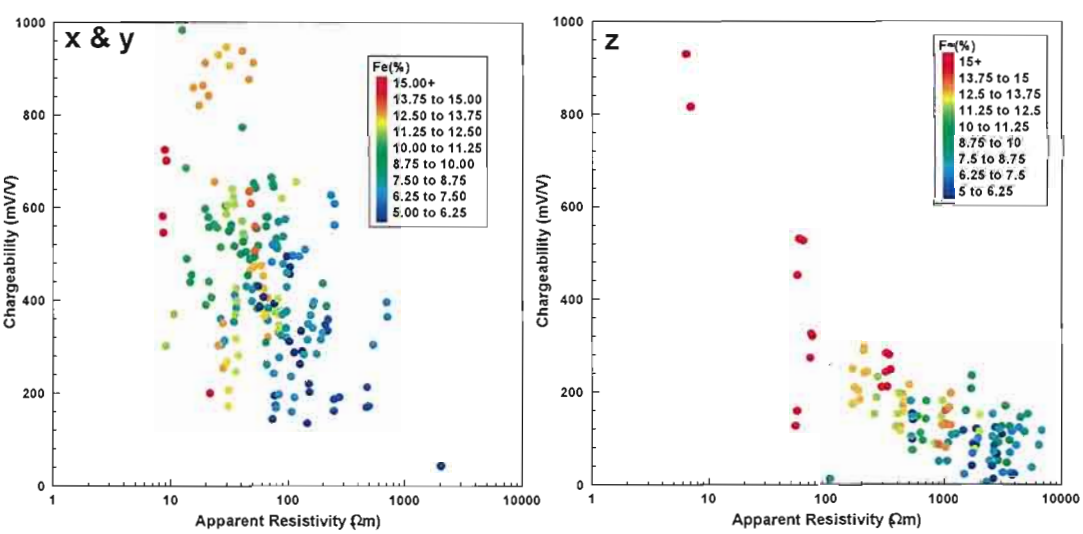

Figure 6.35. Cross plots of chargeability versus apparent resistivity for all laboratory measurements from McArthur River. Points have been symbolised based on Fe%. Data has been classified into longitudinal (bedding parallel) measurements (denoted x & y) and transverse measurements (denoted z).

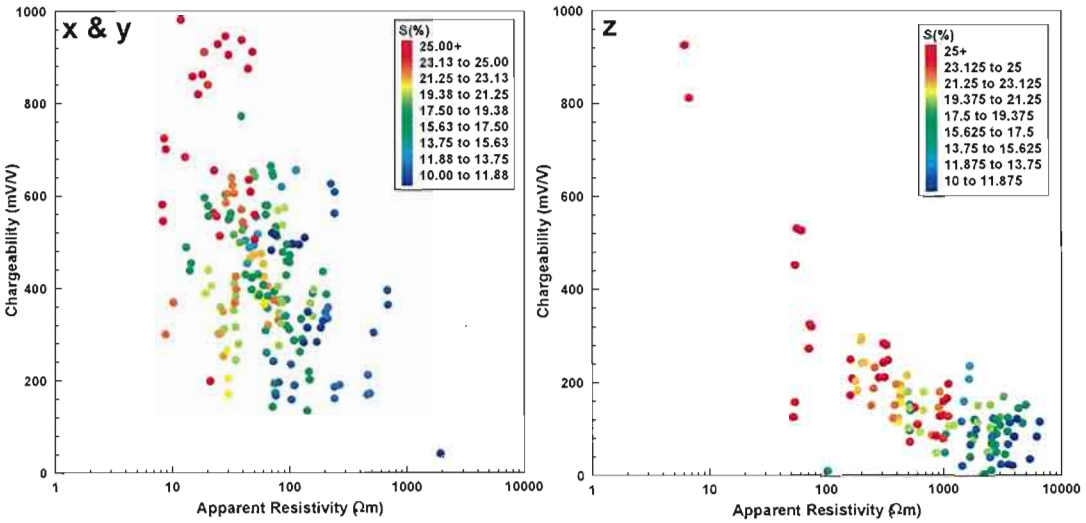

Figure 6.36. Cross plots of chargeability versus apparent resistivity for all laboratory measurements from McArthur River. Points have been symbolised based on S%. Data has been classified into longitudinal (bedding parallel) measurements (denoted x & y) and transverse measurements (denoted z).

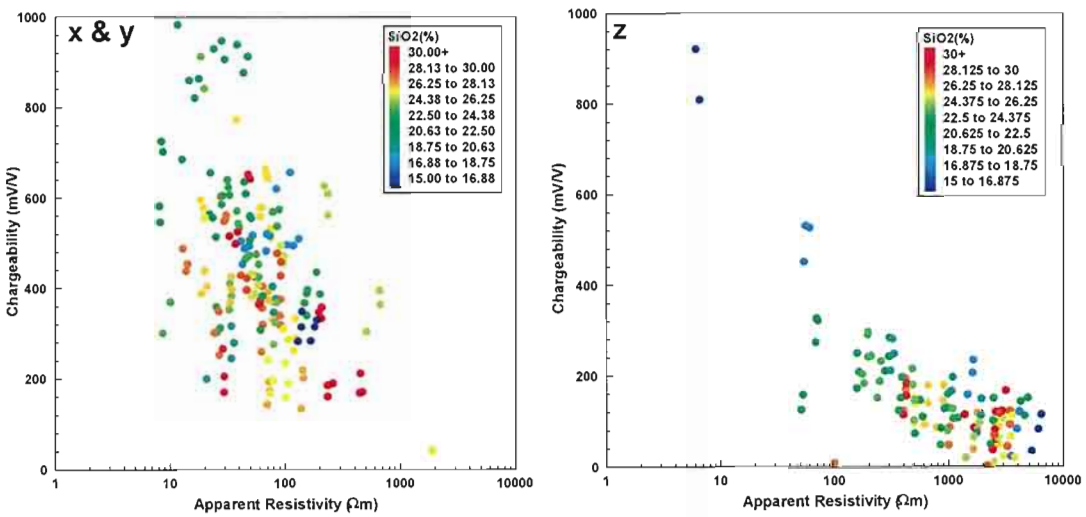

Figure 6.37. Cross plots of chargeability versus apparent resistivity for all laboratory measurements from McArthur River. Points have been symbolised based on SiO_2%. Data has been classified into longitudinal (bedding parallel) measurements (denoted x & y) and transverse measurements (denoted z).

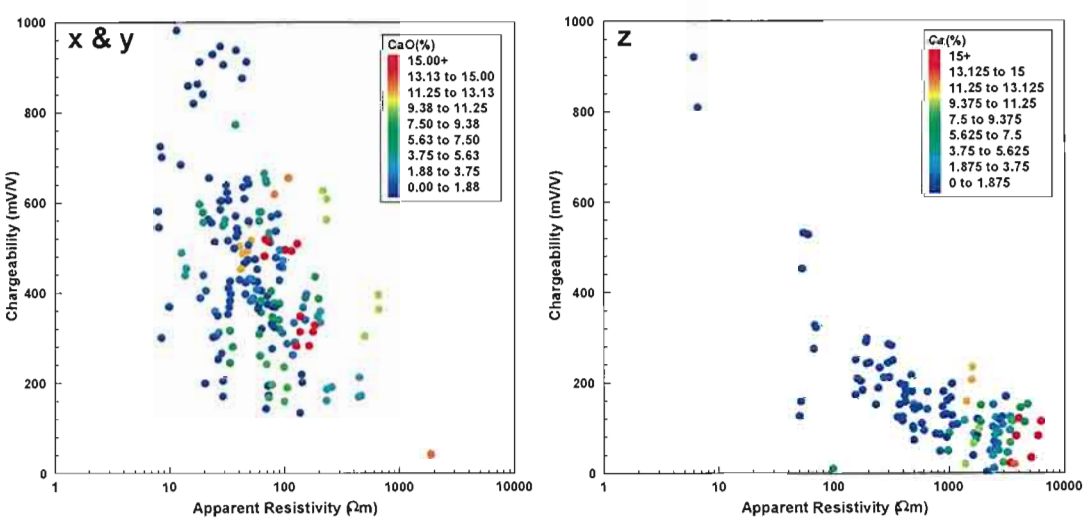

Figure 6.38. Cross plots of chargeability versus apparent resistivity for all laboratory measurements from McArthur River. Points have been symbolised based on Ca%. Data has been classified into longitudinal (bedding parallel) measurements (denoted x & y) and transverse measurements (denoted z).

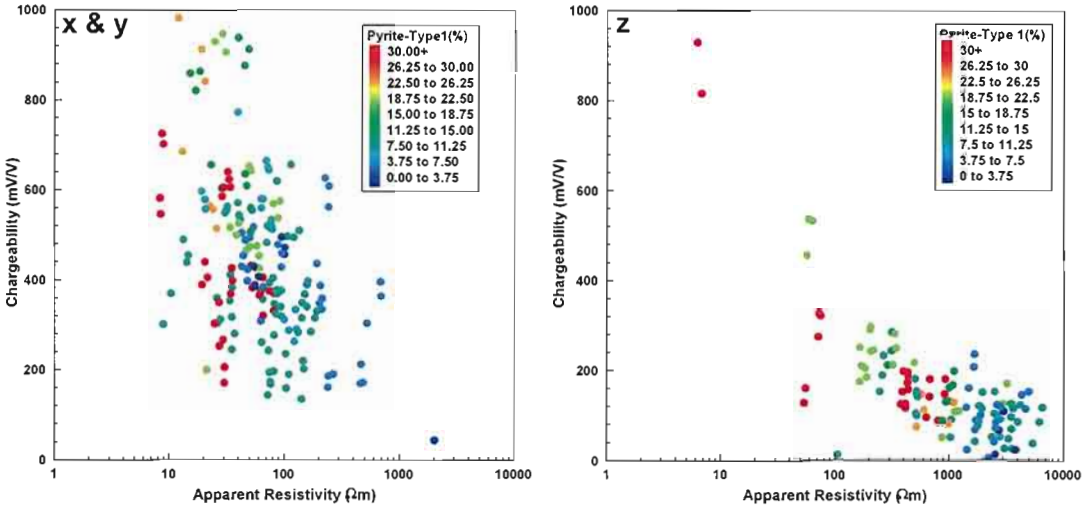

Figure 6.39. Cross plots of chargeability versus apparent resistivity for all laboratory measurements from McArthur River. Points have been symbolised based on type-1 pyrite%. Data has been classified into longitudinal (bedding parallel) measurements (denoted x & y) and transverse measurements (denoted z).

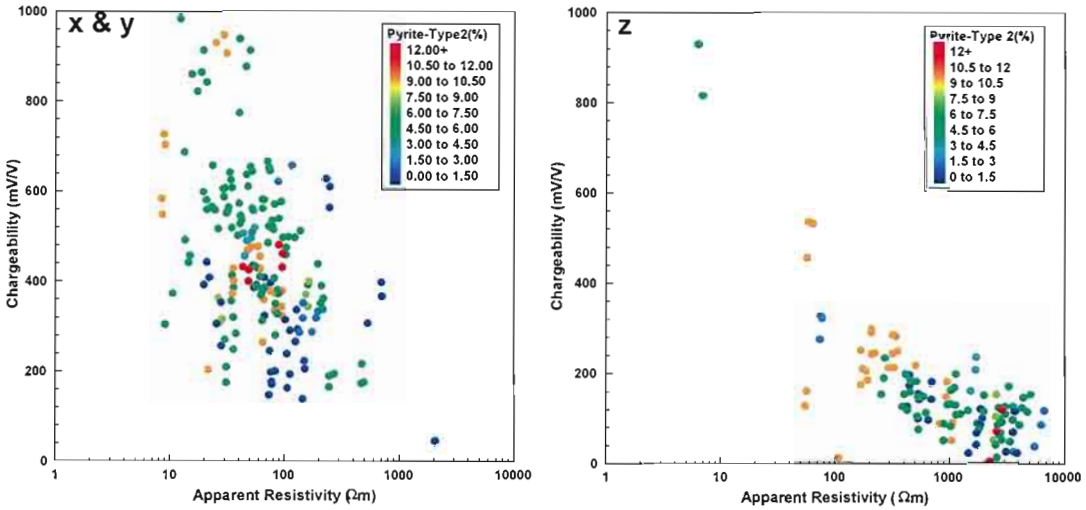

Figure 6.40. Cross plots of chargeability versus apparent resistivity for all laboratory measurements from McArthur River. Points have been symbolised type-2 pyrite %. Data has been classified into longitudinal (bedding parallel) measurements (denoted x & y) and transverse measurements (denoted z).

6.6. Summary

The McArthur River deposit clearly exhibits insitu scale-dependent variation in resistivity and chargeability. The banded nature of the ore causes significant anisotropy, which required orientated measurements to be collected both parallel and perpendicular to bedding. For all sites, scale variations in apparent resistivity and chargeability are most apparent for the perpendicular measurements. Parallel measurements show no clear evidence of scale dependent variation.

The perpendicular measurements (which effectively is the longitudinal resistivity) shows a consistent trend of decreasing apparent resistivity with increasing electrode spacing in all cases, typically by at least one order of magnitude from 0.11 to 0.66 metre spaced measurements (potential electrodes). However a single well-defined scaling relationship cannot be determined, due to significant scattering within the data. Longitudinal resistivity of samples plots over a significant range for each site, but predominantly lies within the range depicted by small-scale insitu measurements.

Perpendicular insitu measurements of chargeability decreases as a function of increasing electrode spacing, but significant scatter is also apparent. An interesting observation is that the bulk transverse chargeability is nearly identical for all ore horizons (~80mV/V). Longitudinal chargeability measurements of samples do no correlate well to the small-scale perpendicular-array measurements.

Apparent resistivity and chargeability derived from parallel measurements show no obvious scale-dependent variation. Insitu transverse resistivity was calculated from parallel and perpendicular measurements according to the "paradox of anisotropy". The range of the calculated insitu transverse apparent resistivity and transverse laboratory sample resistivity correlates well for all sites.

Insitu and sample transverse resistivity is greater than the longitudinal resistivity for each ore-horizon. Apparent resistivity anisotropy is significant for all sites with the ratio of longitudinal to transverse apparent resistivity ranging from 40:1 to 4000:1. Current in the transverse direction is impeded by the resistive carbonate material, whilst in the longitudinal direction current predominates in conductive pathways provided by the pyrite-rich sulphide bands.

Insitu chargeability which is inferred to be primarily due to finely disseminated type-1 pyrite is fairly isotropic across the orebody and is not greatly affected by the orientation of the continuous conductive sulphide bands. The bulk insitu chargeability of each ore horizon can be estimated from transverse measurements of samples.

The scale variation observed at McArthur River can be explained as a function of the number connected current pathways. Scale variation is observed in the longitudinal component and not the transverse component. As the size of investigation is increased the greater number of potential conductive pathways in the longitudinal direction increases, thus resistivity decreases. In the transverse direction there are effectively no current pathways, thus no scale variation is observed.

Current mapping of samples showed that all of the current may effectively flow through an individual pyrite-rich lamina 1mm thick, even in large specimens. Thus not all sulphide bands are effective predominant current pathways. Assessment of late stage cross-cutting sphalerite-galena-carbonate veins showed they are poorly connected and do not contribute to the flow of current through the rock-mass, nor do they significantly impede conduction.

The electrical differences between orebodies are predominantly due to differences in type-1 pyrite concentrations. Increase the type-1 pyrite content causes a decrease in resistivity and increase in chargeability.

2 Orebody has a high zinc and low iron content, and is relatively resistive and moderately chargeable. 3 Lower and 3 Middle have higher iron content (finely disseminate type-1 pyrite) and are quite conductive and highly chargeable.

The electrical properties of 4 and 3 Upper Orebodies are enigmatic, as they have high iron content, are quite conductive, but exhibit low chargeability. This effect is attributed to an increase in the galena content and its distribution within the rockmass. Galena in 4 and 3 Upper Orebodies occurs predominantly as diffuse connected zones in the groundmass, rather than as isolated galena grains as observed in 3 Lower and 3 Middle Orebody.

Chapter 7

North Parkes

7.1. Introduction

The North Parkes porphyry copper deposit was selected as a study site to examine the scale dependent electrical properties of a disseminated sulphide deposit with only a low overall proportion of sulphide minerals. Of the three deposit case studies presented, North Parkes shows the least variation in terms of primary lithologies and sulphide mineralogy. At North Parkes, only two lithologies were sampled; the monzonite porphyry hosting the majority of the economic mineralisation, and the enclosing volcanic rocks. Insitu measurements were conducted in the E27 open pit, as underground access to the E26 deposit was not possible. Mineralised rocks are typically low grade (<1.5% Cu) and contain only a small proportion of sulphides present predominantly as minor disseminated grains and occasionally associated with quartz stockwork veins.

The electrical properties of copper-porphyry deposits have been investigated by a number of authors (Van Voorhis et al., 1973; Pelton et al., 1983; Nelson and Van Voorhis, 1983 and Langore et al., 1989). Nelson and Van Voorhis (1983) completed insitu resistivity and IP measurements with electrode spacing ranging from two to ten metres at 99 sites in four open pit porphyry copper mines and conducted additional laboratory measurements on samples. They state *"insitu measurements provided a better basis for quantitative correlations between electrical parameters and mineralisation than laboratory measurements on small samples"*. Resistivity and phase lag was found to decrease with sulphide content (Figure 7.1a and b), but scatter in the data excluded the use of any empirical rules. However the ratio of phase to resistivity, labelled quadrature conductivity (Figure 7.1c) was found to increase with the square of sulphide content and could be used to estimate ore grade.

7.2. Geological Setting

The North Parkes deposits are located thirty kilometres north of Parkes, NSW, within the Goonumbla Volcanic Complex, in the western sub-province of the eastern Lachlan Fold Belt in New South Wales (Figure 7.2). The Lachlan Foldbelt consists of a widespread and thick succession of quartz-rich turbidites, which is interspersed with five Early to Late Ordovician belts of mafic volcanics (Heithersay et al., 1990; Heithersay and Walshe, 1995). These belts host a number of porphyry Cu-Au deposits with North Parkes situated in the Junee-Naroromine Belt.

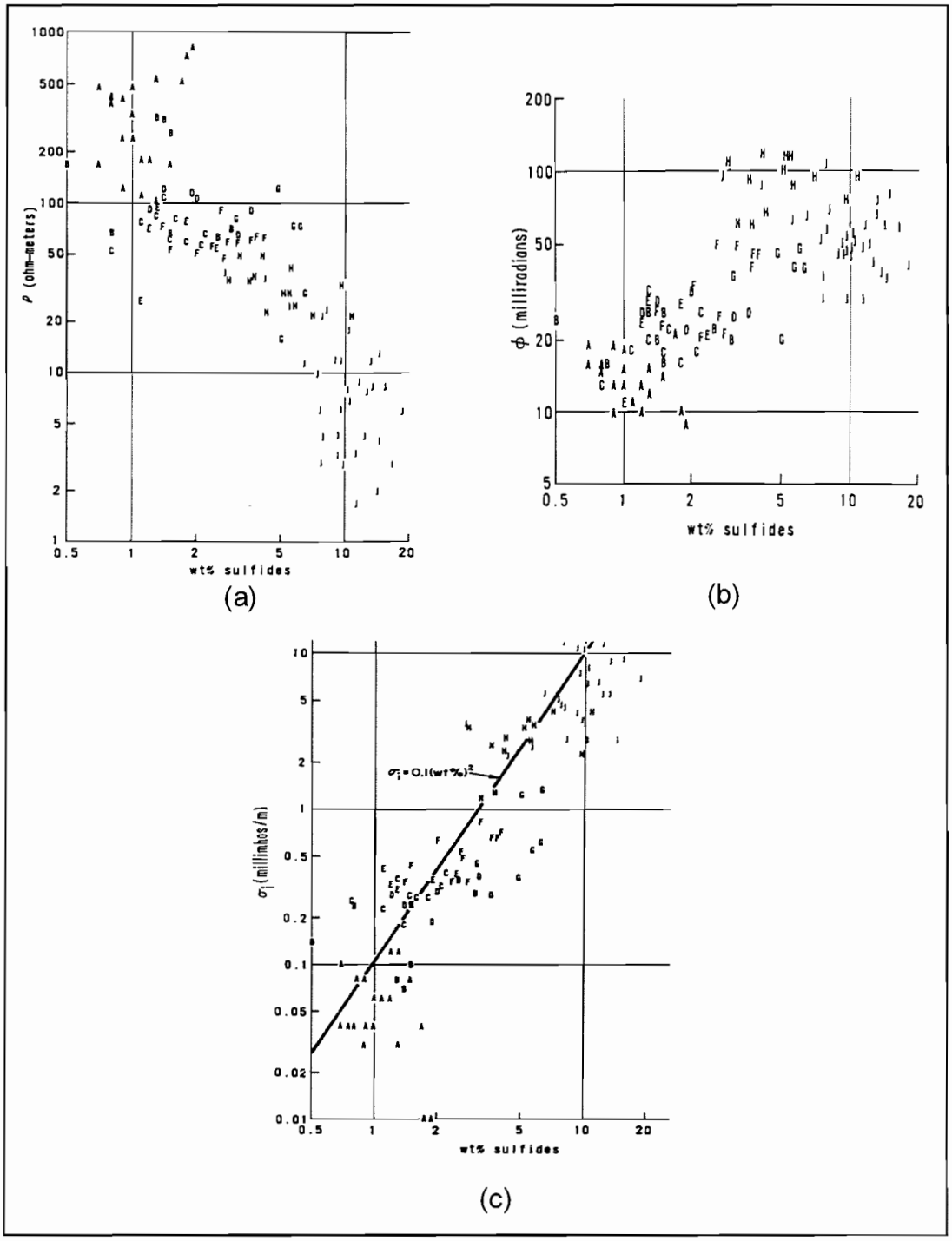

Figure 7.1. Observed relationship between; (a) resistivity (b) IP phase at 0.1 Hz and (c) quadrature conductivity and weight percent sulphide content for 109 porphyry copper insitu measurements (Sulphide content was derived from sample assays collected from sites). Quadrature conductivity is defined as the ratio of phase to resistivity. From Nelson and Van Voorhis (1983).

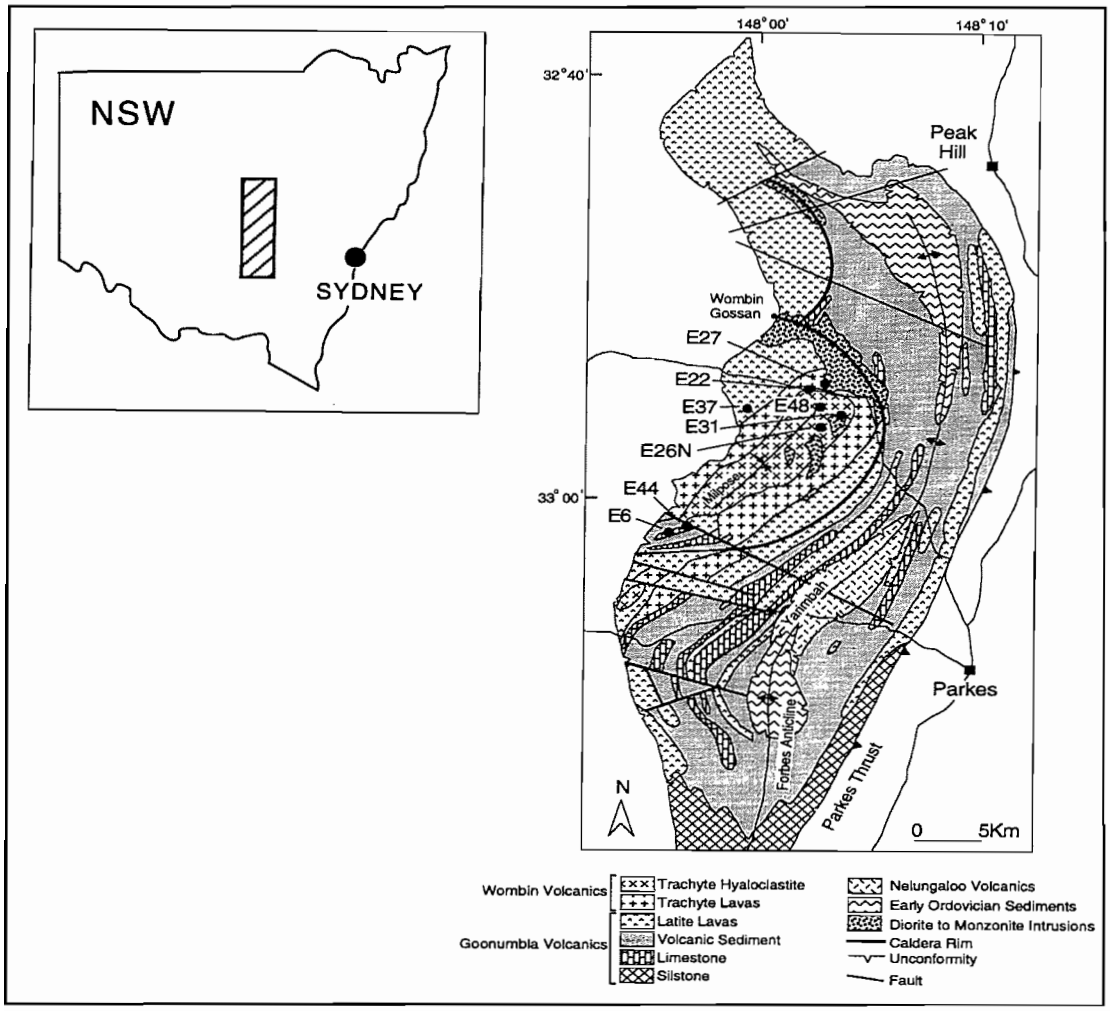

Figure 7.2. Locality and regional geology map of the North Parkes (Endeavour) porphyry Cu-Au deposits, Goonumbla district. The deposits are located in diorite to monzonite intrusions host in within the Goonumbla Volcanics. From Heithersay and Walshe (1995).

The North Parkes deposits consist of four significant porphyry copper-gold deposits called Endeavour 22, Endeavour 26, Endeavour 27 and Endeavour 48 (referred to as E22, E26, E27 & E48 respectively- see Figure 7.2). Mineralisation occurs within narrow, pipe-like intrusions of quartz, monzonite porphyry forming small satellite bodies to larger monzodioritic stocks (Heithersay and Walshe, 1995). All the deposits are sulphur poor systems, with sulphides typically less than 4% (Heithersay et al., 1990). Within the immediate vicinity of the deposits metamorphism is limited to lower greenschist facies (Lickfold, 2000). Detailed stratigraphy of the North Parkes deposits is described by Heithersay et al. (1990) and Duggan (1999).

The E27 porphyry ore body, as defined by the 0.6% copper equivalent has plan dimensions 150 by 200 metres. A schematic alteration diagram of the North Parkes deposits is shown in Figure 7.3. Magnetite and sericite alteration extends around the deposit. A resource of 9.5 million tonnes at an average grade of 0.5% copper and 0.6 g/t gold is indicated. Copper mineralisation (chalcopyrite) is disseminated and fracture-controlled (Figure 7.4 a, b, c and d). Gold occurs within and rimming bornite, typically as blebs less than 5μm in diameter (Heithersay et al., 1990) (Figure 7.4 e, f). Two varieties of bornite; orange-brown and mauve phases are present. The orange-brown phase is associated with co-precipitation of chalcopyrite whilst mauve phase is co-precipitated with chalcocite (Lickfold, 2000).

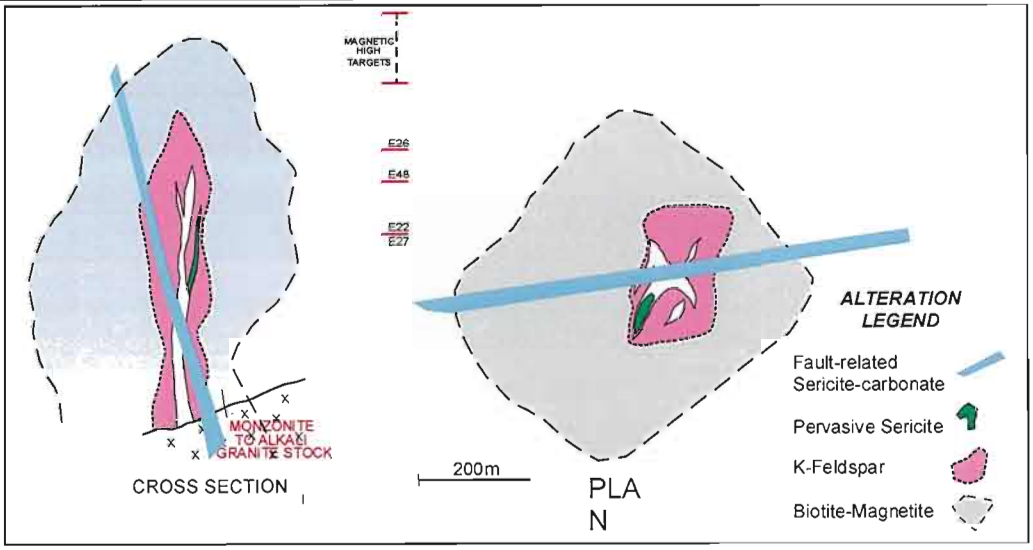

Figure 7.3. Schematic alteration diagram of the North Parkes (Endeavour; E26, E48, E22, E27) porphyry Cu-Au deposits (North Parkes per comms, 2001).

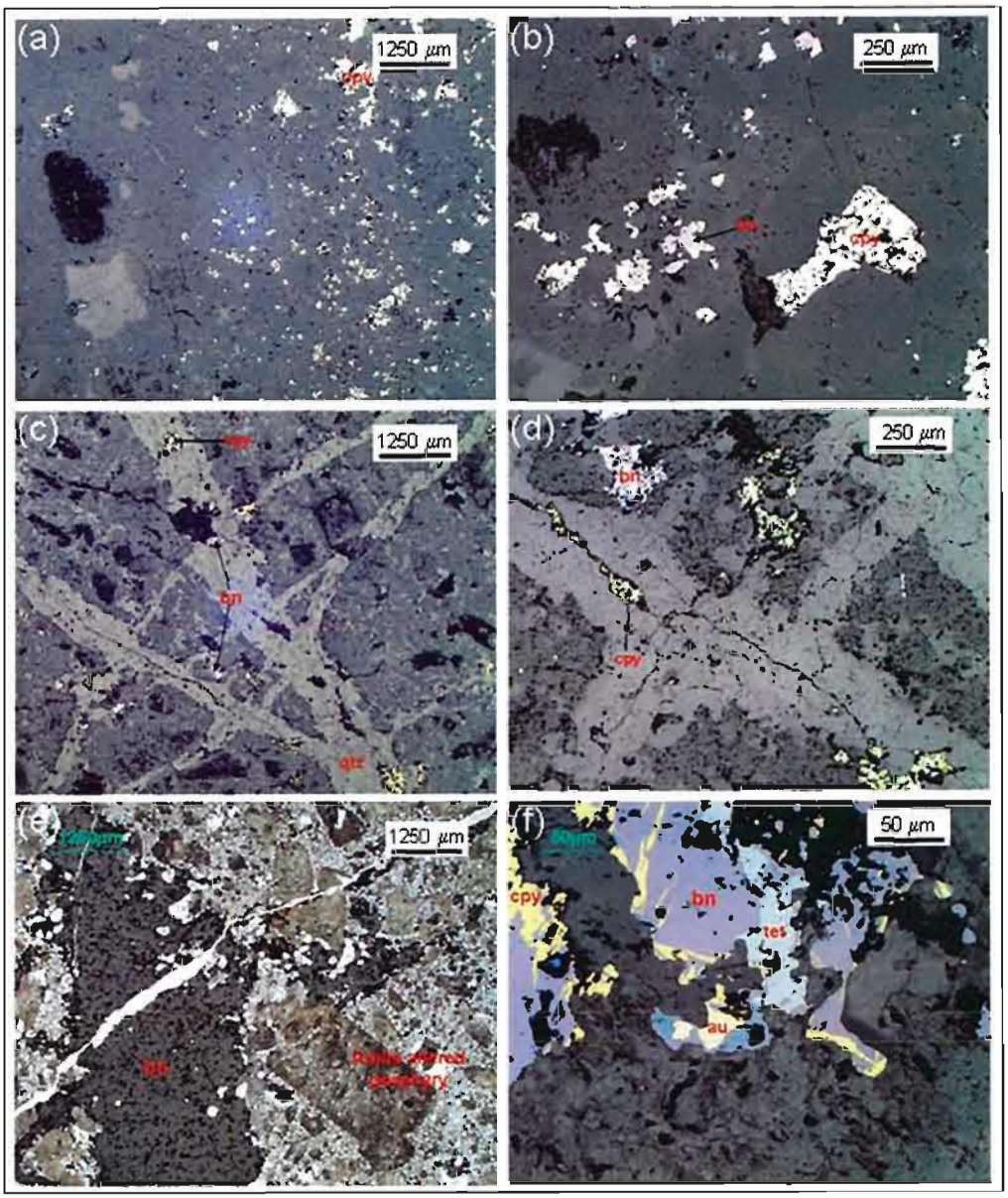

Figure 7.4. Reflected light microphotographs of mineralised feldspar porphyry samples from North Parkes E27 (a, b) Sample NP11; disseminated chalcopyrite and bornite mineralisation (c, d) Sample NP16; fracture controlled chalcopyrite mineralisation (e, f) NP01; gold occurring on the rims of bornite. cpy: chalcopyrite, bn: bornite, au: gold, qtz: quartz.

7.3. Methodology

A generic discussion of the field and laboratory measurement techniques was described in chapter three. The following discusses the methodology specifically applied to the North Parkes deposit.

7.3.1. Field Measurements (Insitu)

All in-situ measurements and samples were collected in the E27 open pit of North Parkes mine (Figure 7.5). The nature of the open-pit limited the number of suitable sites due to poor ground conditions along faces. Consultation with North Parkes geologists ensured type examples of characteristic features of the deposit were measured. The open pit contains low to high grade mineralised monzonite porphyry, host volcanics and magnetite altered volcanics. The main macroscopic variations that are apparent within these rock units are mainly due to variable degrees of alteration. Two sites were measured within the pit floor itself, and sampling from these proved difficult, with nearby representative samples collected after blasting. Due to mining practices at North Parkes measurements could not be made in the higher grade E26 ore body (underground), but two representative samples were collected for later macroscale measurements (Figure 7.6).

Figure 7.5. Site locations at the E27 Open-pit North Parkes (Endeavour) porphyry copper-gold deposit. (North Parkes per comms., 2001).

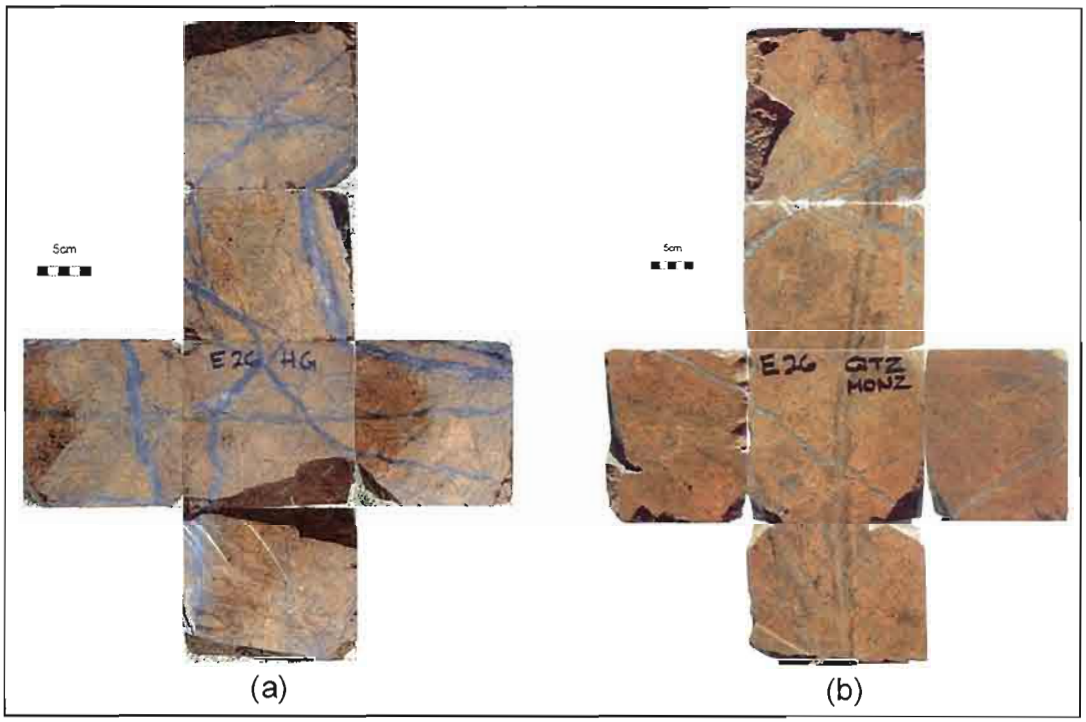

Figure 7.6. Representative sample of (a) high grade (1.93% Cu) and (b) moderate grade (1.67% Cu) monzonite porphyry sample from North Parkes E26 Deposit (underground). The photographs of the samples show an "exploded" view displaying all six sides of the prismatic sample.

A total of 457 in-situ measurements were recorded at ten sites within the porphyry and volcanic host sequence (Table 7.1). The majority of the sites were located in the mineralised monzonite porphyry (various grades); two sites were chosen in the magnetite altered volcanics, one site in sericite altered volcanics and one site in volcanics with minor porphyry veining. Examples of representative samples from the various lithologies at E27 are shown in Figure 7.7.

Site	Geology	Mining grade	Samples (grade)
1	Monzonite porphyry	moderate	0.5-0.85% Cu
2	Volcanics & minor porphyry	Low	0.1-0.3% Cu
3	Sericite alteration volcanics	low	0.2-0.5% Cu
4	Porphyry monzonite	high	1.10-1.15% Cu
5	Porphyry monzonite	moderate	0.6-0.69% Cu
6	Porphyry monzonite	moderate	0.4-0.7% Cu
7	Porphyry monzonite	high	~1.0%
8	Porphyry monzonite	low	0.18-0.21% Cu
9	Magnetite altered volcanics	low	0.05-0.42% Cu
10	Magnetite altered volcanics	low	0.1% Cu

Table 7.1. Site lithology and ore grade from mine control and sample assays from the North Parkes E27 deposit.

At each site galvanic electrical measurements (apparent resistivity and chargeability) were completed using an expanding Wenner array. The maximum potential electrode 'a' spacing was two metres for sites 1, 7, 8 and 9. For the remaining sites the maximum potential electrode spacing was limited to one metre. Anisotropy measurements were only conducted at selected sites, and these indicated that the deposit is effectively electrically isotropic.

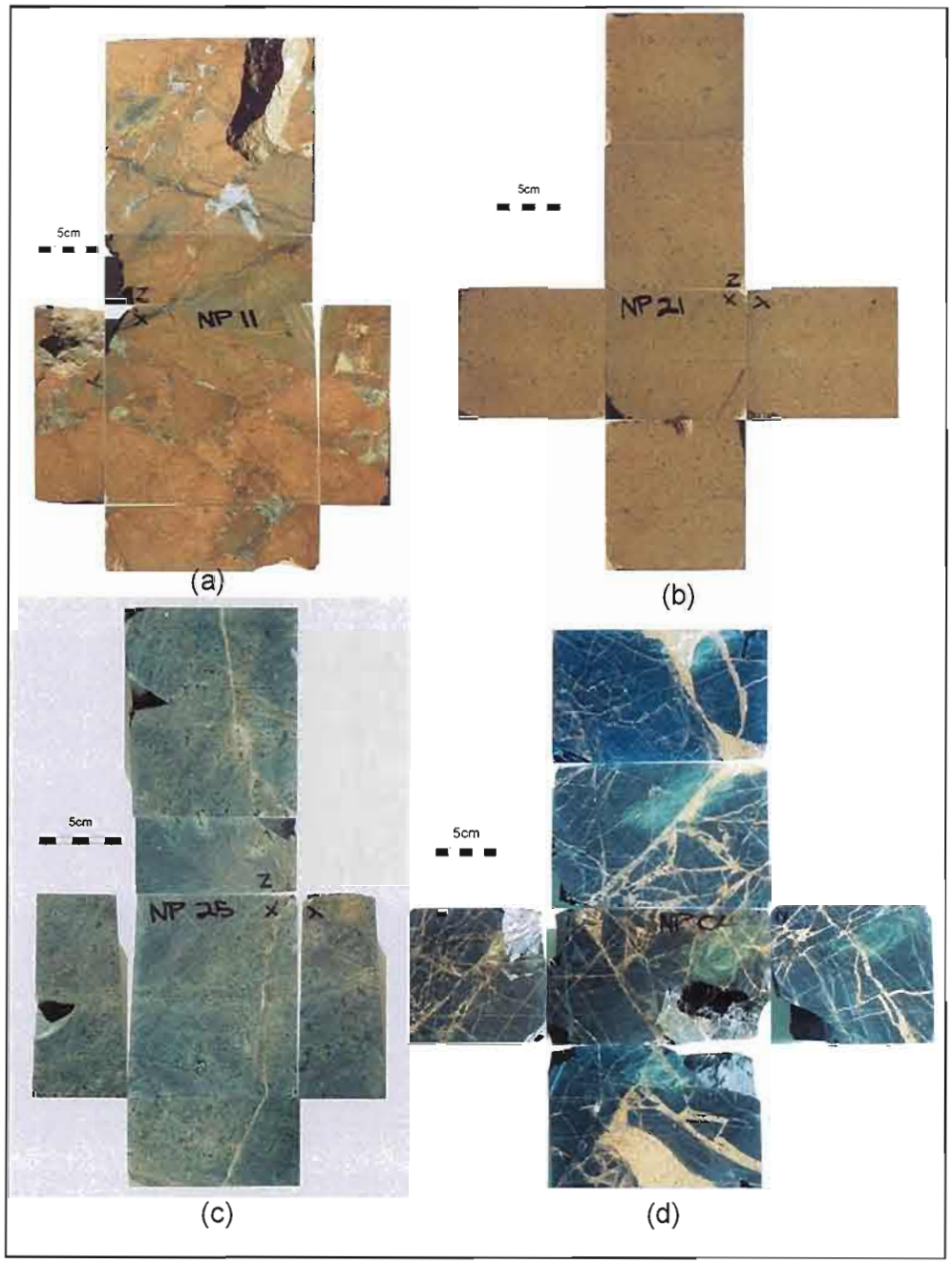

Figure 7.7. Representative samples from North Parkes E27 Deposit (open put) (a) high grade monzonite porphyry (NP11), (b) low grade monzonite porphyry (NP21), (c) low grade magnetite altered volcanics (NP25), and (d) mineralised sericite altered volcanics (NP04). The photographs of the samples show an "exploded" view displaying all six sides of the prismatic sample.

At all sites, where practical, traverses were undertaken using the mobile electrode array to map any lateral heterogeneity. Measurements were taken at electrode spacings of 0.11, 0.22 and 0.33 metre using the mobile array.

7.3.2. Laboratory measurements

Thirty-one samples were collected from the ten sites from the North Parkes deposit. The laboratory measurements were carried out as discussed in chapter 3. The highly resistive nature of many of the North Parkes samples meant that the combined sample and contact resistance approached or exceeded the input impedance of the Scintrex IPR12 (16 MΩ when inactive,

~1 MΩ when sampling). To avoid significant current flow through the measuring circuit approximately 50% of the samples were measured using a National Instruments DAQ 1200 12 bit PC data acquisition card with an input impedance of 2 GΩ that did not affect current flow through the samples. The acquired time series data recorded with the DAQ1200 were discretised into the standard IPR12 window time gates for comparisons with the valid IPR12 measurements. Due to the high sample impedance, a Faraday cage was used to attenuate electrical noise during measurements. Time series data was smoothed using a running average filter prior to binning.

Chargeability measurements recorded for approximately 80% of laboratory samples exhibited unusual IP decay curves (Figure 7.8a). The criteria adopted for acceptance of valid IP decays required a smooth monotonic decrease in voltage with time with no negative voltages recorded at any time (Figure 7.8b). Although a small proportion of laboratory measurements on samples produced "valid" chargeability decays, the majority of measurements on North Parkes samples produced decays that decreased monotonically for early times, but changed signs at later times. In addition a small proportion of samples exhibited decays that decreased from negative voltages, whilst other increased smoothly from initial negative voltages. The negative voltages were originally thought to be a product of incorrect self-potential removal by the IPR12. However additional comparative measurements conducted with the digital acquisition card (DAQ1200) and laboratory digital oscilloscopes produced similar decays. Despite considerable experimentation with laboratory conditions including altering the composition and concentration of the electrolyte, these unusual IP decay curves persisted.

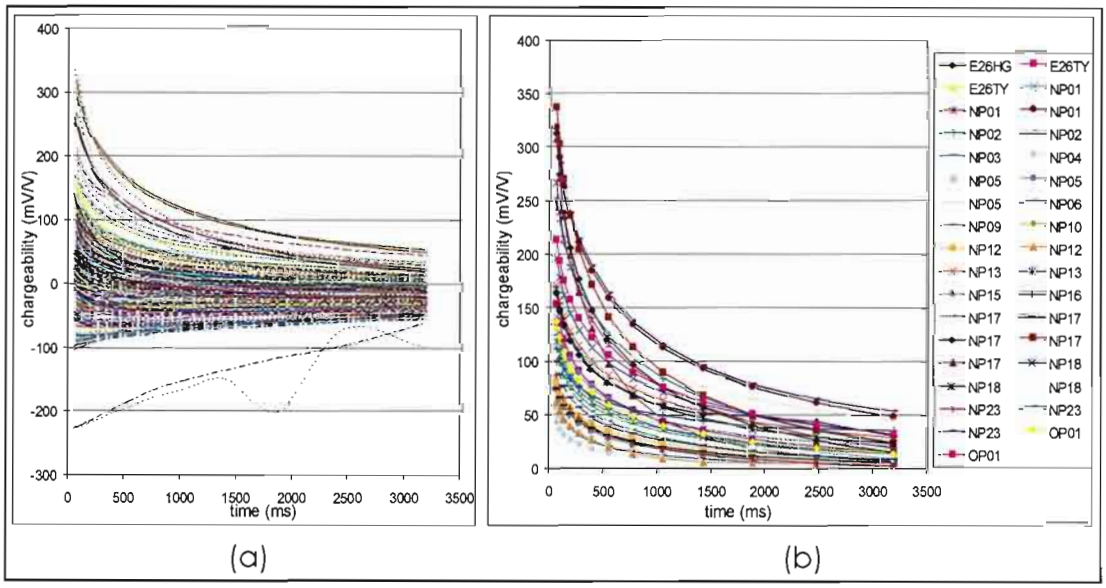

Figure 7.8. (a) IP decay curves for all laboratory measurement at North Parkes samples. Note that over 80% of all measurements recorded negative voltages at late times and a significant proportion of the decay curves were negative at all times. (b) IP decay curves satisfying the criteria of consisting of a smooth monotonic decrease and no negative voltages are shown.

The cause of the unusual decays could not be definitely determined. However, Nabighan and Elliot (1976) demonstrated negative IP effects could occur in layered media, where $\rho_1 < \rho_2 > \rho_3$ or $\rho_1 > \rho_2 > \rho_3$. It may be possible that for extremely resistive samples, the measuring system electrodes may act as thin layers which are orders of magnitude less resistive than the

sample; thus producing a negative polarising effect which saturates the sample's real decay (i.e. $\rho_1 < \rho_2 > \rho_3$, Figure 7.9). Only the laboratory IP decays which satisfied the acceptance criteria were considered valid for analysis.

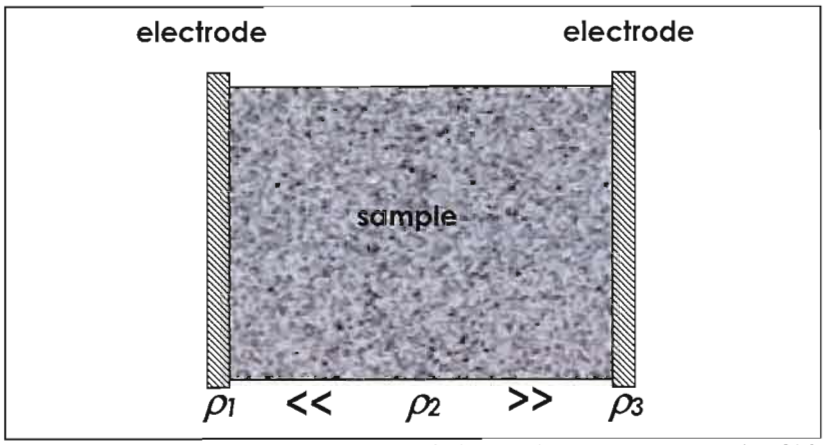

Figure 7.9. Negative IP decay effects observed in laboratory measurements of highly resistive sample could be a result of large contrast between rock and electrodes as shown above, in the case where $\rho_1 < \rho_2 > \rho_3$, as outlined by Nabighan and Elliot (1976).

7.4. Results

The results of two sites will be discussed in detail, followed by a summary of all site measurements.

7.4.1. Site 1: Mineralised porphyry

Site 1 was located in mineralised porphyry (Figure 7.10) at the base of the E27 pit on the western face. The rock mass consisted of monzonite porphyry of moderate copper grade; assays of samples collected from the site range from 0.5 to 0.85% copper. Stockwork veining was poorly developed with only thin fracture controlled quartz-bornite-chalcopyrite veins.

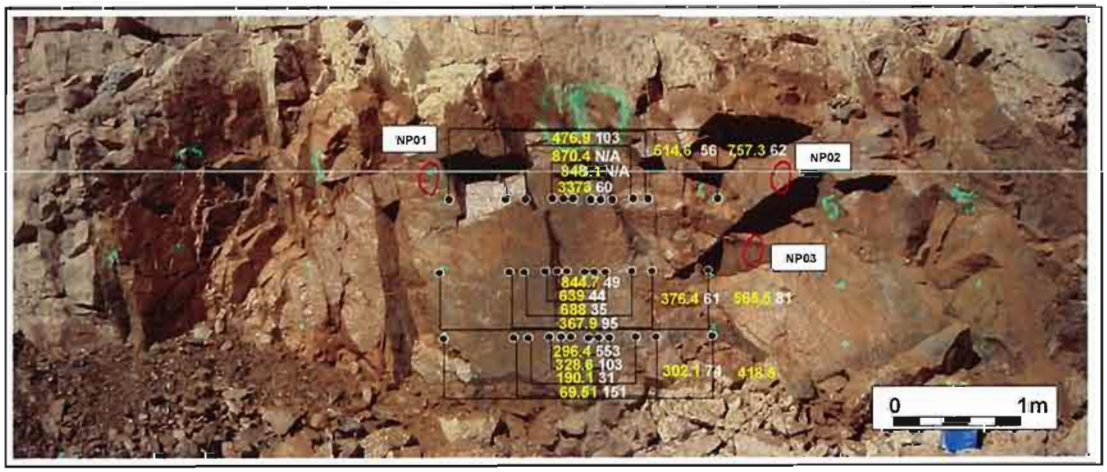

Figure 7.10. Photograph of Site 1 located in moderate grade porphyry monzonite. Black dots indicate potential electrode positions for three horizontal arrays. Yellow numbers are apparent resistivity Ωm). White numbers are chargeability (mV/V) (Time gate 340-520ms). Sample locations of NP01, NP02 and NP03 shown in red outline.

Three horizontal electrical soundings were completed at the site. Insitu apparent resistivity as a function of electrode spacing is shown in Figure 7.11a. Sample resistivity measurements in three orthogonal directions are shown as coloured points. In all cases there is an initial decrease with

apparent resistivity within increasing electrode spacing but the minimum insitu apparent resistivity (80-600 Ωm) occurs at 0.66 metre electrode spacing and not at the bulk scale measurement (2 metres). The magnitude of the scale variation is limited to one to two orders of magnitude.

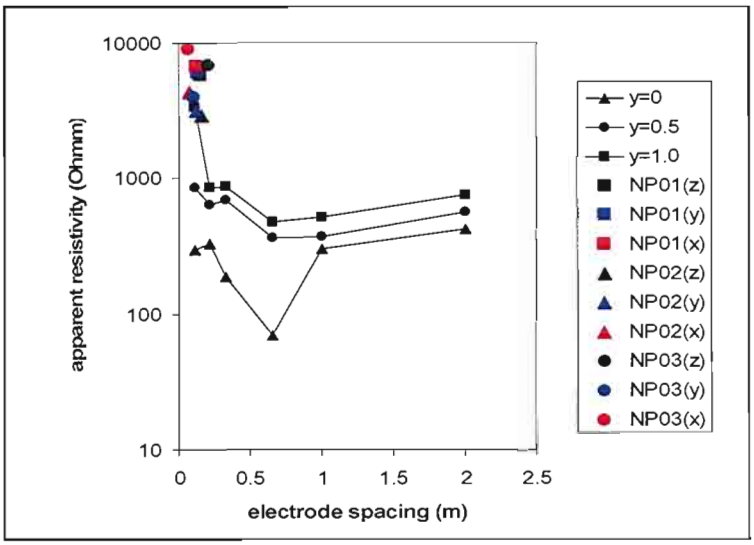

Figure 7.11. Site 1: Apparent resistivity versus electrode spacing for insitu electrical soundings. Colour symbols display sample measurements plotted against sample size, for three orthogonal measurements.

The resistivity of samples is typically one order of magnitude greater than the average insitu apparent resistivity recorded by small scale measurements (Figure 7.11). However, the laboratory data plots close to the projection of the trend defined by the y=0 traverse resistivity data. Resistivity of samples range from 2800 to 8700 Ωm. Samples collected from the site consist of a porphyritic rock with a finely granular groundmass and abundant plagioclase and K-feldspar phenocrysts (Figure 7.12). Sulphides (1-2%) are disseminated bornite and chalcopyrite (<1-8mm) and sulphide veinlets (1%; <1 mm).

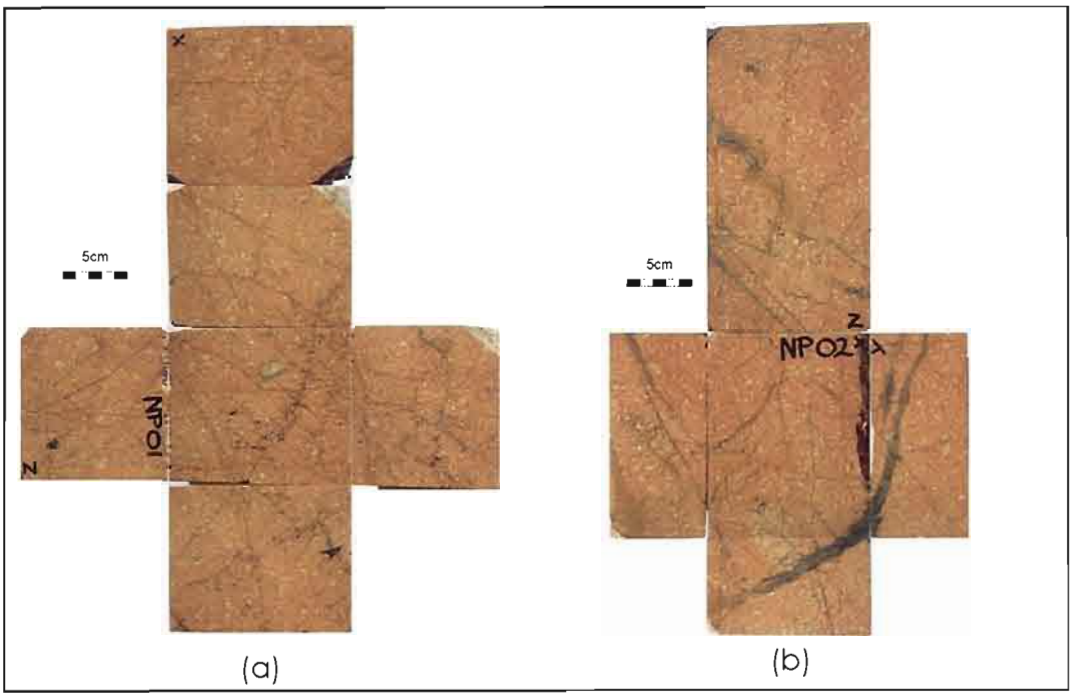

Figure 7.12. Samples (a) NP01 (0.53%Cu) and (b) NP02 (0.83%) collected from Site 1. Stockwork veining at small scales are observed in both samples. Sulphides are disseminated bornite and chalcopyrite (<1-7mm) and sulphide veinlets (1%; <1 mm).

The insitu chargeability of site 1 as a function of electrode spacing is shown in Figure 7.13. Chargeability data is quite irregular and shows no clear evidence of scale variation, although a maximum chargeability is recorded for the 0.66 m electrode spaced measurements, coincident with the insitu minimum resistivity. Insitu chargeability data range from 35 to 150 mV/V. The chargeability of samples (70-180mV/V) shows a similar spread as insitu values.

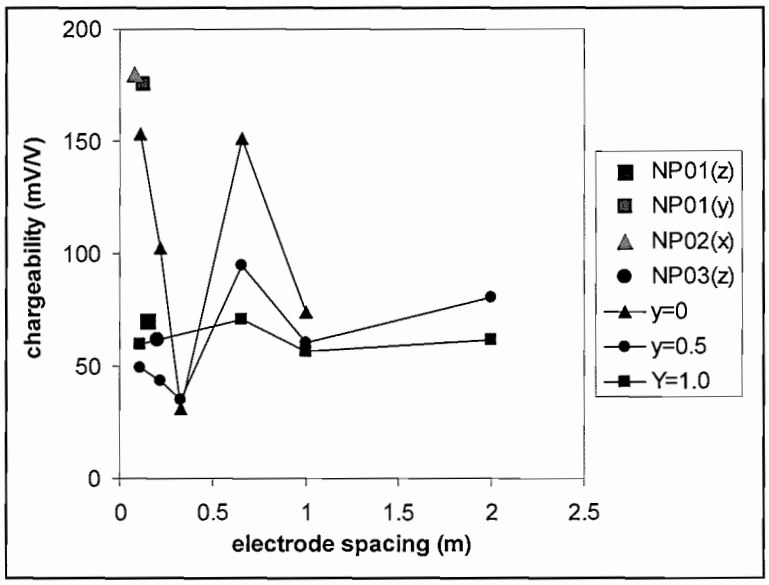

Figure 7.13. Chargeability versus electrode spacing for insitu electrical soundings. Colour symbols display sample measurements plotted against sample size, for 3 orthogonal measurements.

Site heterogeneity was assessed using 0.11, 0.22 and 0.33 metre measurements across the site face, using mobile electrode array. Apparent resistivity and chargeability are shown in Figure 7.14. There is considerable variation in electrical properties observed at this site. Apparent resistivity is predominantly low in the centre of the site and flanked by more resistive sections, apparent at all three measurement scales across the site (0.11, 0.22 and 0.33m). Chargeability data also displays significant variation, although the pattern and degree of variation is not consistent between measurements at different electrode spacings. The local variations at this site likely indicate irregularities in stockwork veining hence local variations in copper content.

The histograms of small scale insitu resistivity and chargeability measurements in Figure 7.15 show the variability observed across the site. There is no clear scale dependence in these measurements, as the distributions for each electrode spacing are similar. The median bulk insitu resistivity is displaced 1.5 standard deviations towards more conductive values than the median of smaller scale measurements.

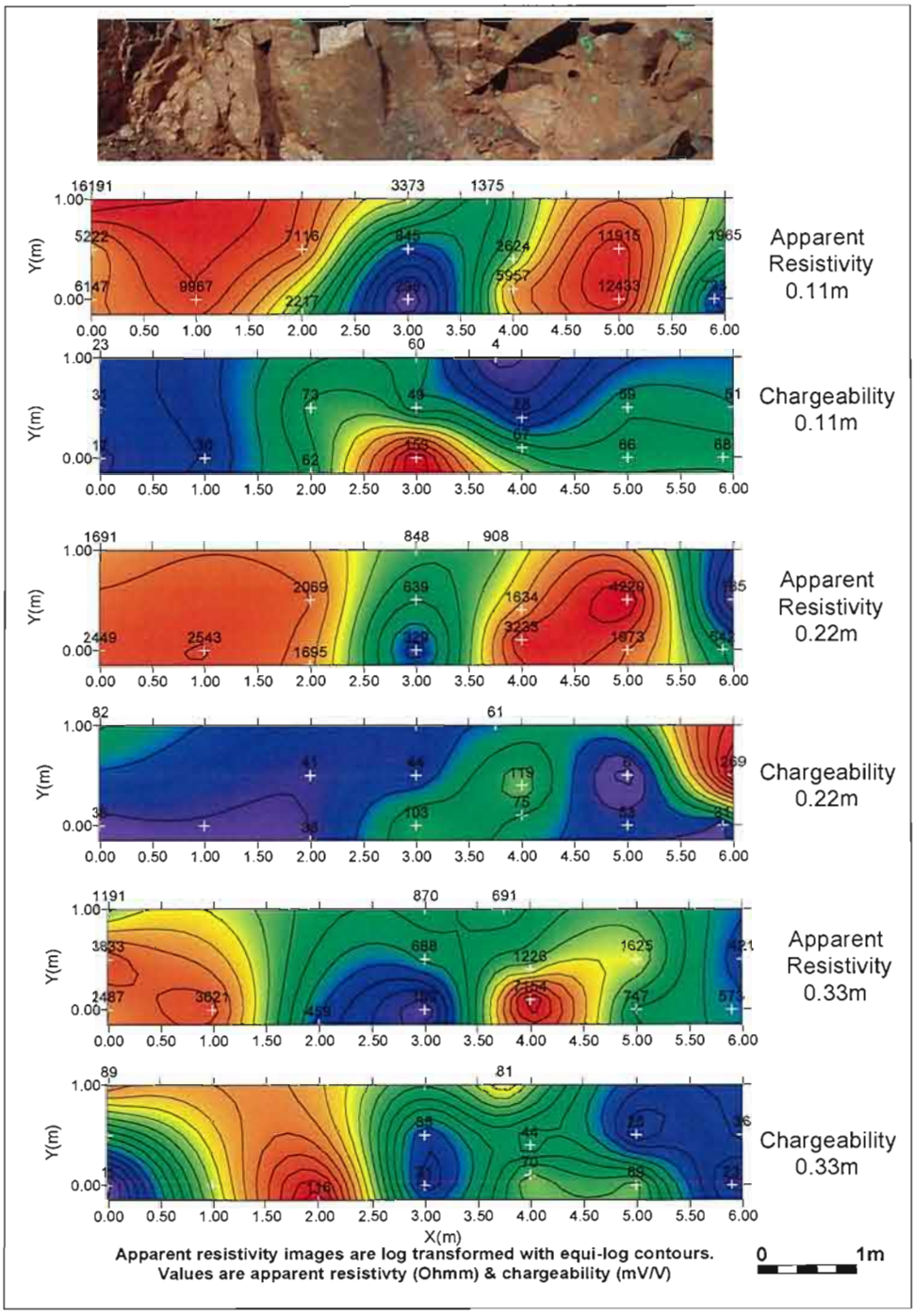

Figure 7.14. Apparent resistivity and chargeability maps of Site 1 for 0.11m, 0.22m and 0.33m electrode spacings at Site 1.

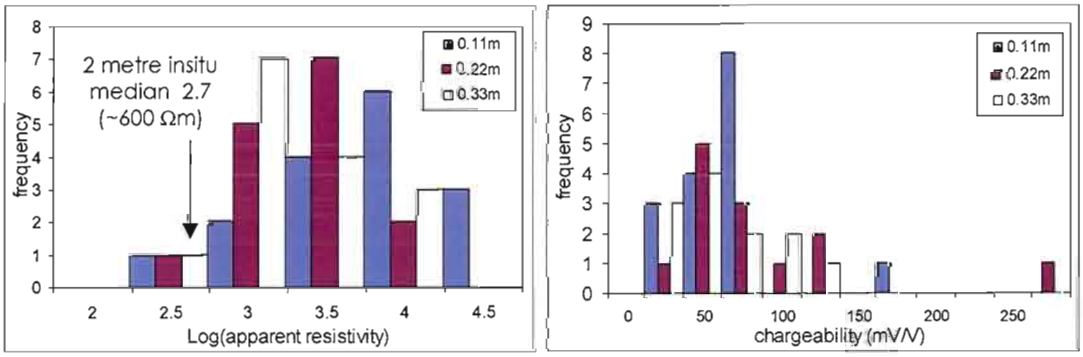

Figure 7.15. Distribution of LOG10(apparent resistivity) and chargeability for 0.11, 0.22 and 0.33 metre electrode space measurements of Site 1.

Petrographic examination of the three samples from site 1 reveals a similar porphyritic texture (Figure 7.16). Feldspar phenocrysts (15%) are enclosed in a fine grained (<0.1mm), equigranular, felsic framework. Phenocrysts are altered to albite and flecked with fine grained white mica and carbonate. Sulphides are mainly found in quartz veins, but also occur as fine disseminations in the groundmass. Sulphides (<1%) mainly occur as overgrowths on quartz crystals and as discontinuous aggregates (<5mm) in vein centres. Sulphides are predominantly bornite with intergrowths of chalcopyrite and digenite/ covellite. Fine, sparse disseminations (<0.2mm) of bornite and chalcopyrite occur in the groundmass. Chalcopyrite appears to be more common as groundmass disseminations; whereas bornite is more commonly a vein phase (Figure 7.16).

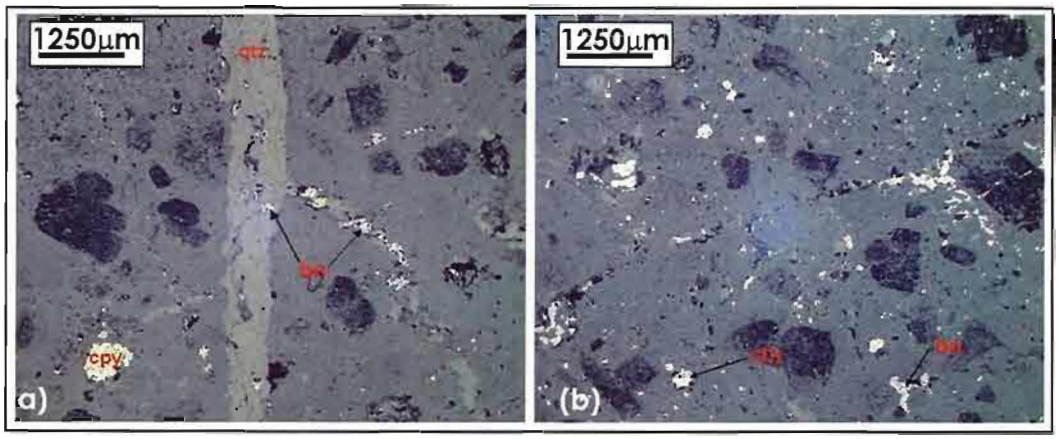

Figure 7.16. (a) Reflected light photomicrograph of sample NP02 showing chalcopyrite (cpy) dissemination in the groundmass and bornite (bn) in a quartz (qtz) vein (b) Reflected light photomicrograph of sample NP03- illustrating chalcopyrite (cpy) dissemination.

7.4.2. Site 9 Volcanics

Site 9 was located in volcanic host rocks located approximately half way down the E27 ramp. The rock mass at this site consisted of magnetite-biotite altered volcanics with thin carbonate-biotite-quartz-bornite-chalcopyrite veins (Figure 7.17). Assays of samples (Figure 7.18) collected from the site range from 0.05 to 0.42% copper.

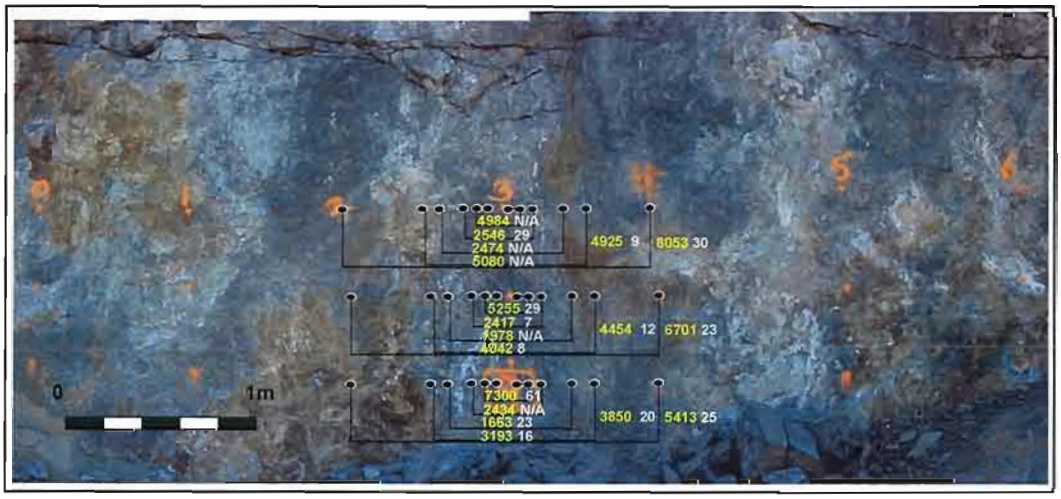

Figure 7.17. Photomosaic of Site 9 located in the volcanic host. Black dots indicate potential electrode positions for three horizontal arrays. Yellow numbers are apparent resistivity (Ωm). White numbers are chargeability (mV/V) (Time gate 340-520ms).

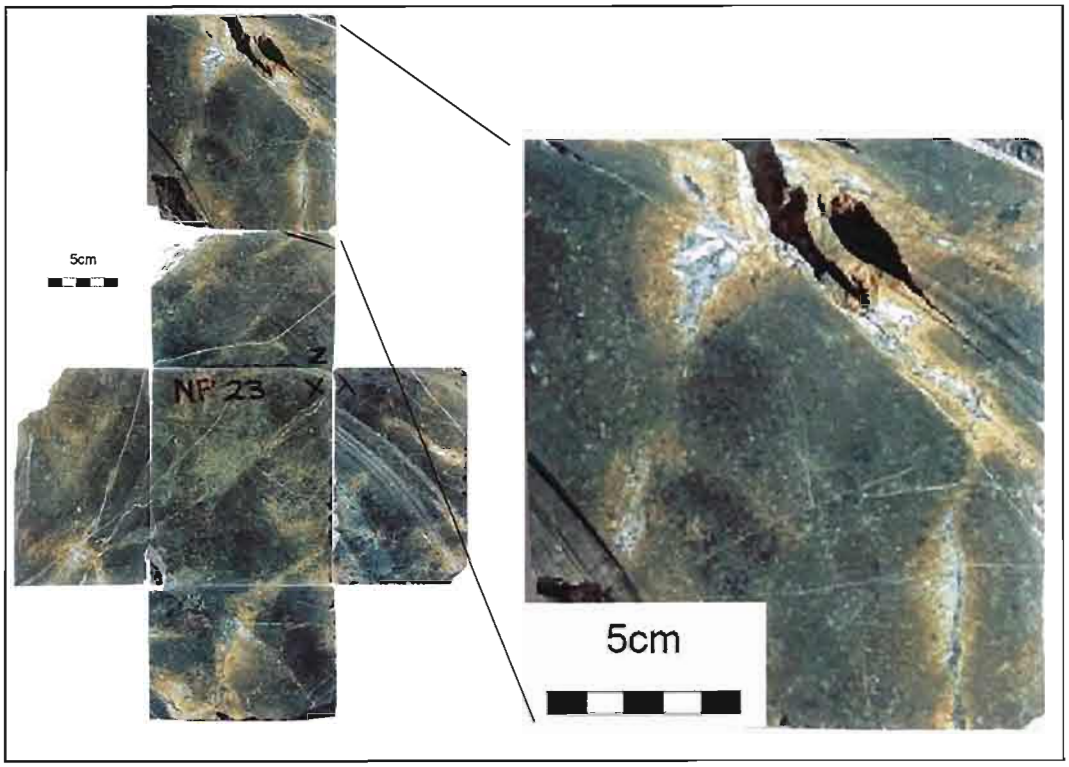

Figure 7.18. Sample NP23 (0.42%Cu): Strongly altered, porphyritic volcanic, with randomly oriented feldspar-clinopyroxene phenocrysts. Veins (chlorite-quartz-sulphides) cut the specimen (4%; <1-10mm) with K-feldspar alteration cleavages. Sulphides (1%; bornite-chalcopyrite) only occur in the veins. The photograph of the sample shows an "exploded" view displaying all six sides of the prismatic sample.

Three horizontal electrical soundings were completed at this site. Insitu apparent resistivity as a function of electrode spacing is shown in Figure 7.19. Sample resistivity measurements in three orthogonal directions are shown as coloured points. The insitu resistivity decreases to a minimum resistivity at an electrode spacing of 0.33 metres and then increases for larger scale measurements. The magnitude of the scale variation is within one order of magnitude.

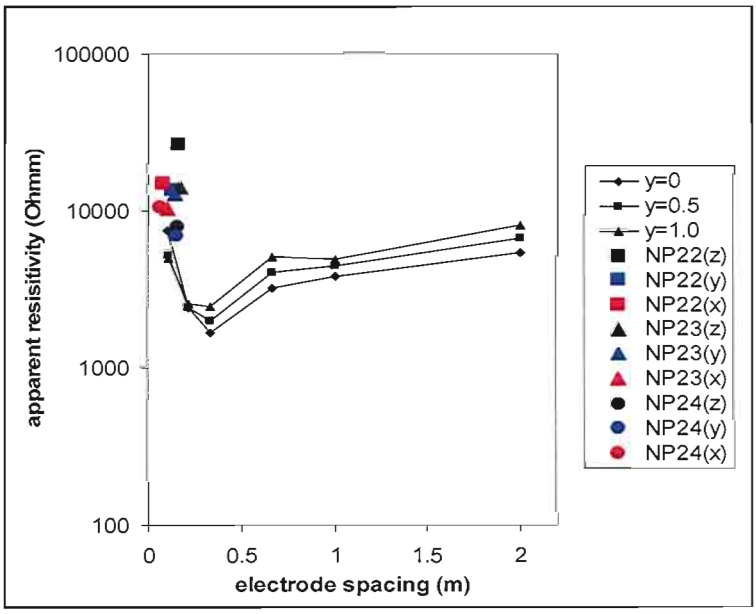

Figure 7.19. Apparent resistivity versus electrode spacing for insitu electrical soundings at Site 9 (volcanic host). Colour symbols display sample measurements plotted against sample size, for 3 orthogonal measurements.

The insitu chargeability of site 9 as a function of electrode spacing is shown in Figure 7.20. Chargeability data shows moderate scale dependence for electrode spacings less than 0.22 metre. Maximum chargeability was recorded for the 0.11 metre spaced measurements. Insitu chargeability data range from 6 to 60 mV/V.

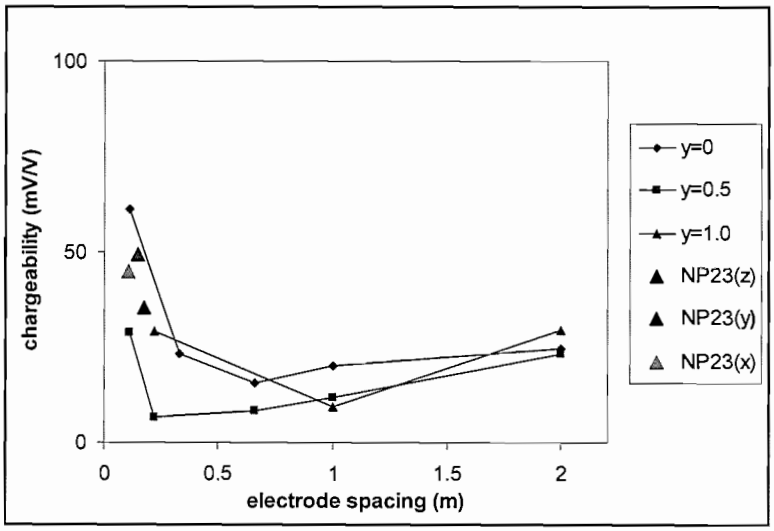

Figure 7.20. Chargeability versus electrode spacing for insitu electrical soundings at Site 9. Colour symbols display sample measurements plotted against sample size, for 3 orthogonal measurements.

The scale variation observed in the insitu resistivity likely reflects the nature of the fracturing and veining within the volcanic sequence. In this case, the well defined minimum at 0.33m electrode spacing indicates a characteristic length of connected pathways. The resistivity and chargeability measured on laboratory samples plots close to the projection of the trend defined by the insitu soundings (Figure 7.18 and 7.19). Resistivity of laboratory samples range from 6800 to 26500 Ωm. The chargeability of samples (35-50/V) lies close to the maximum values measured insitu (60mV/V) (Figure 7.20).

Site heterogeneity was assessed using 0.11m, 0.22m and 0.33 measurements across the site. Apparent resistivity, chargeability and magnetic susceptibility maps are shown in Figure 7.21. There is considerable variation in electrical properties observed at this site. Apparent resistivity is predominantly low in the centre and to the left side of the site and flanked by more resistive sections. This pattern is fairly coherent for all three measurements (0.11, 0.22 and 0.33m). Chargeability shows no significant variation across the site. The magnetic susceptibility image shows a similar pattern to the 0.33m resistivity image, and also shows an inverse correlation with the 0.33m chargeability image. The magnetic susceptibility image (Figure 7.21) largely reflects silicate alteration within the volcanics, and the general correlation with apparent resistivity suggests that alteration may significantly influence the electrical conductivity.

The histograms of small scale insitu resistivity and chargeability measurements are shown in Figure 7.22. They highlight the variability observed across the site. There is no clear scale dependence in these measurements, as distributions are similar for each electrode spacing. The average bulk insitu apparent resistivity in this case lies close to the median of the small scale (0.11m) measurements.

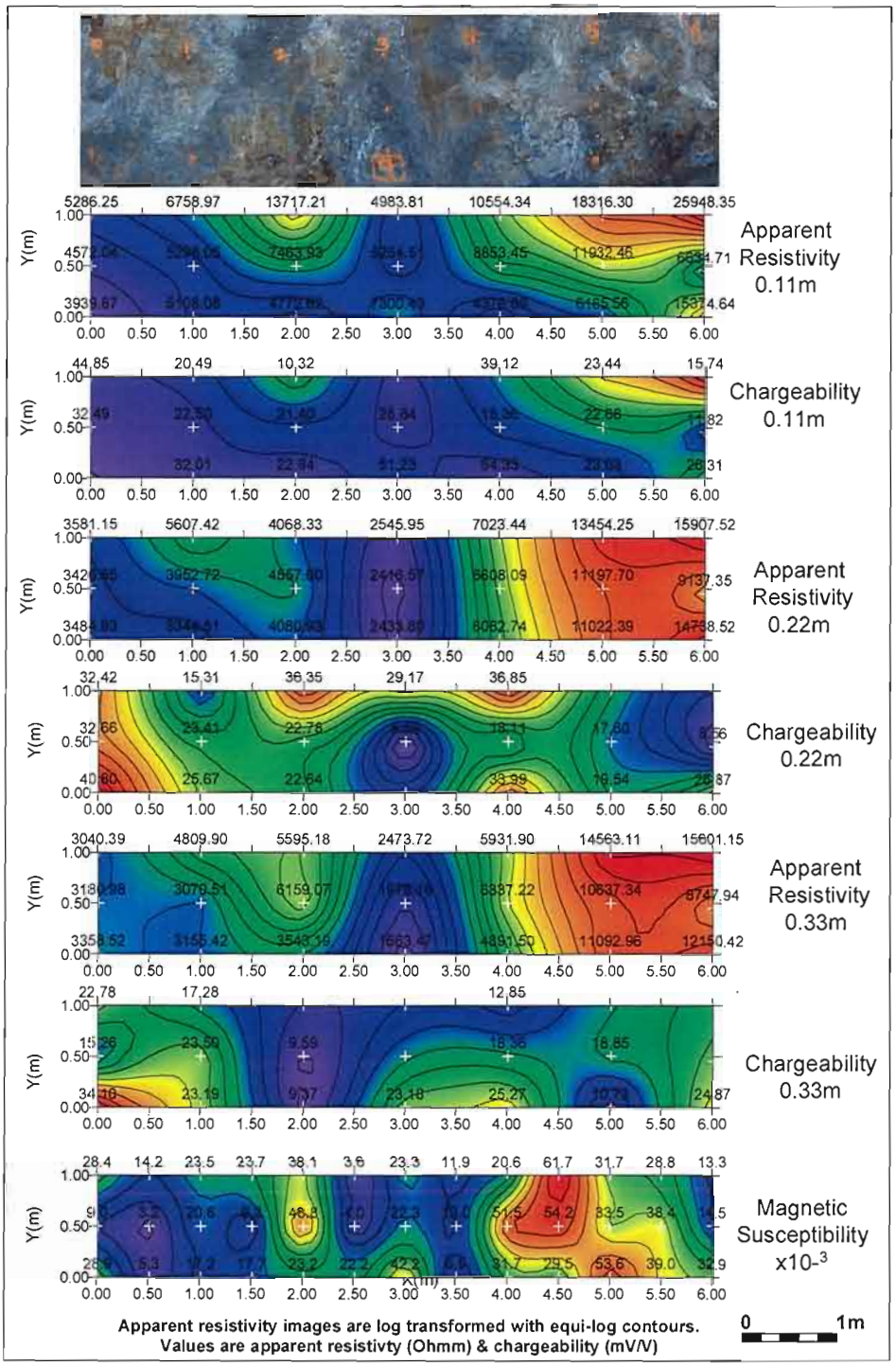

Figure 7.21. Apparent resistivity and chargeability maps of Site 9 for 0.11m, 0.22m and 0.33m electrode spacings. Magnetic susceptibility map.

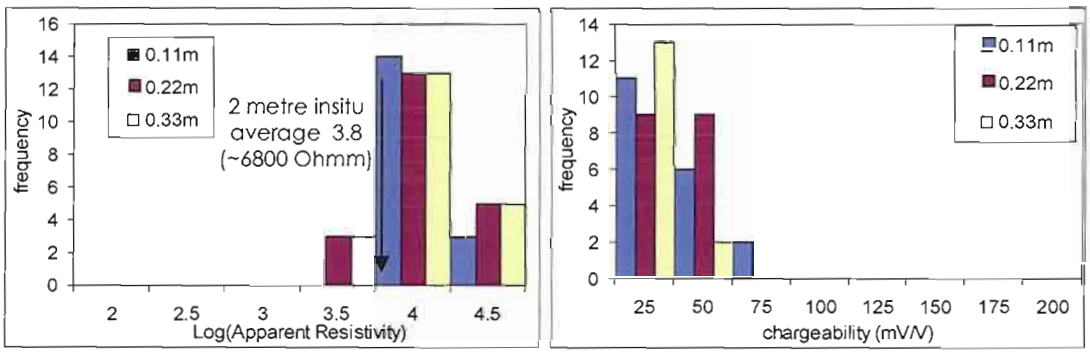

Figure 7.22. Distribution of LOG10(apparent resistivity) and chargeability for 0.11, 0.22 and 0.33 metre electrode space measurements of Site 9.

The three samples from Site 9 have similar petrographic composition and consist of porphyritic rock with feldspar phenocrysts (15%) enclosed in a fine grained (<0.1mm), equigranular, felsic framework. Phenocrysts are altered to albite, and flecked with fine grained white mica and carbonate. Magnetite phenocrysts are only partially replaced by hematite, around crystal rims. The fine grained ground mass is completely replaced by albite, tremolite-actinolite, quartz, magnetite and patches of biotite. Sulphides are mainly found in quartz veins, but also occur as fine disseminations in the ground mass (Figure 7.23).

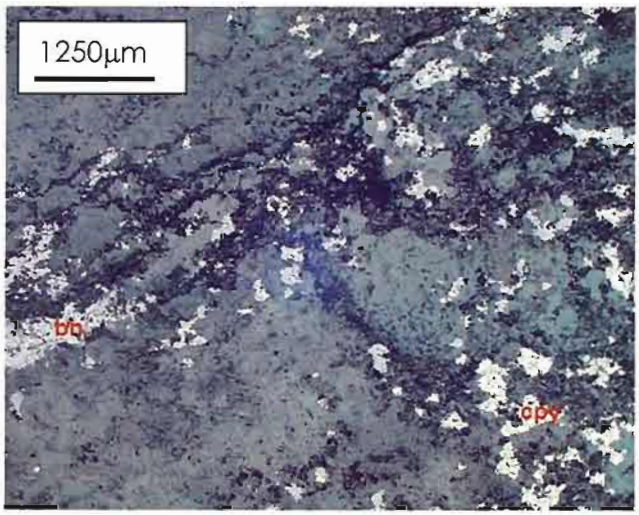

Figure 7.23. Photomicrograph of veins in sample NP23 collected from Site 9. Sulphides comprise <1% of the specimen and consists of chalcopyrite, and bornite. These are mainly found as anhedral disseminations in the veins. Bornite is partly replaced by digenite.

7.4.3. All Sites

Sections 7.4.1 and 7.4.2 provided detailed descriptions of the electrical properties of the only two primary lithologies examined at the North Parkes E27 Deposit (mineralised monzonite porphyry and the enclosing volcanic rocks). Three additional sites were also recorded in the volcanics and five additional sites were located in the monzonite porphyry of various grade.

Apparent resistivity soundings for all sites are shown in Figure 7.24. In each case laboratory samples are plotted as a function of the sample dimension. All graphs are plotted with consistent resistivity scales to readily enable direct comparisons between results from each site. The graphs are grouped into the two main lithologies (mineralised porphyry and host volcanics).

The scale variations observed for all sites at North Parkes do not show consistent patterns, and are not dependent on lithology. Several of the sites (1,3,6,7,8) exhibit well defined trends (Figures 7.24) of decreasing resistivity with increasing electrode spacing, although the variation is small, typically less than one order of magnitude.

In particular, sites 6 and 7 (Figures 7.24) show clear evidence of scale dependence, with resistivity consistently decreasing with scale. These two sites were located in the pit floor which represented the only opportunity to measure the high grade stockwork vein mineralisation. A sample of high grade ore (1.4%Cu) collected within the open pit is shown in Figure 7.25.

Volcanics

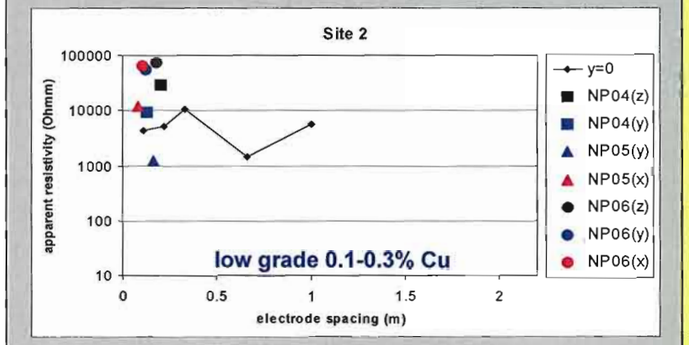

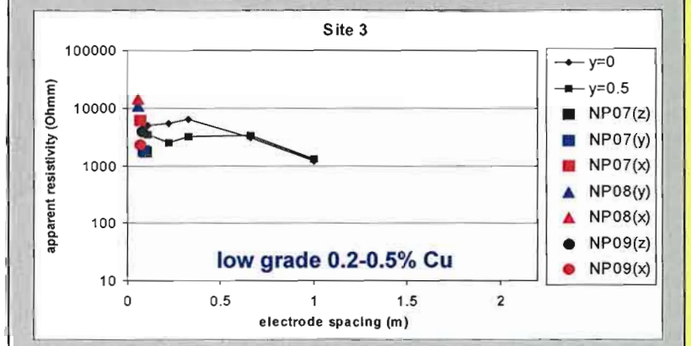

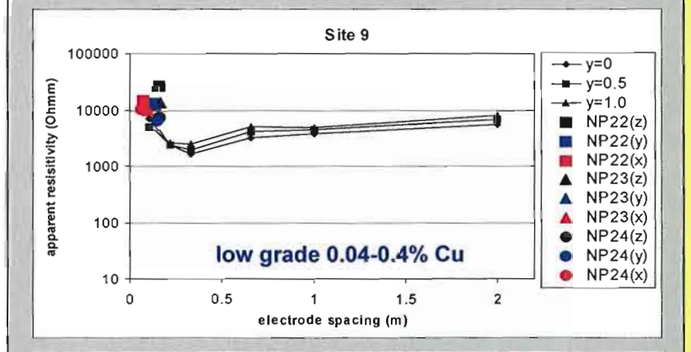

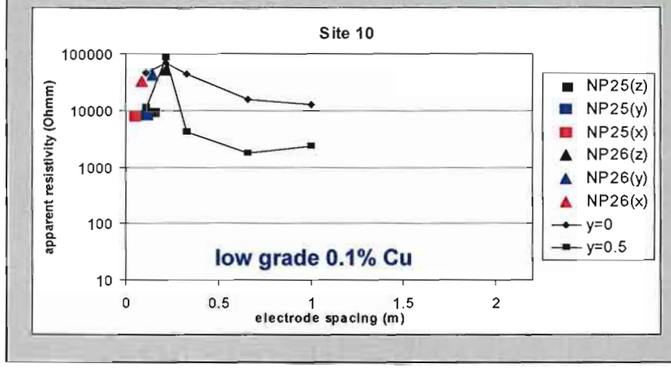

Porphyry Monzonite

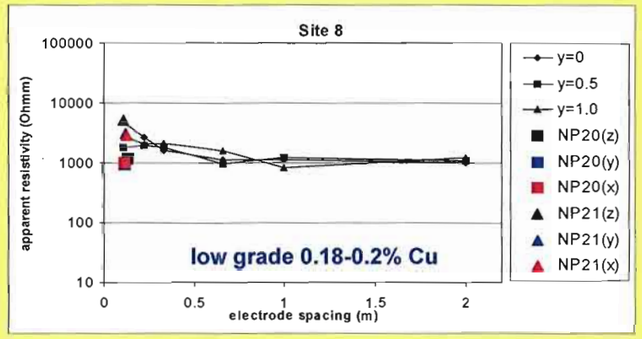

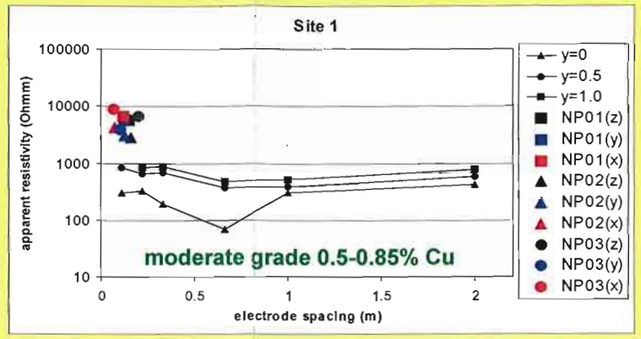

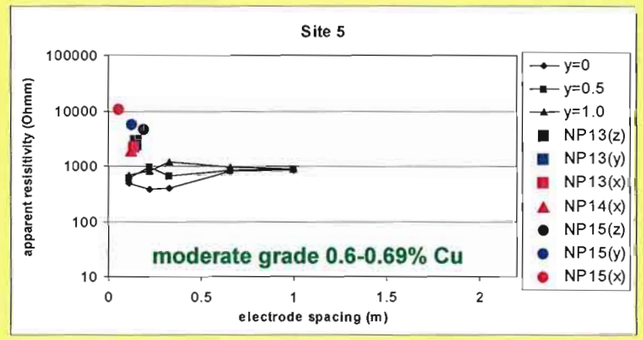

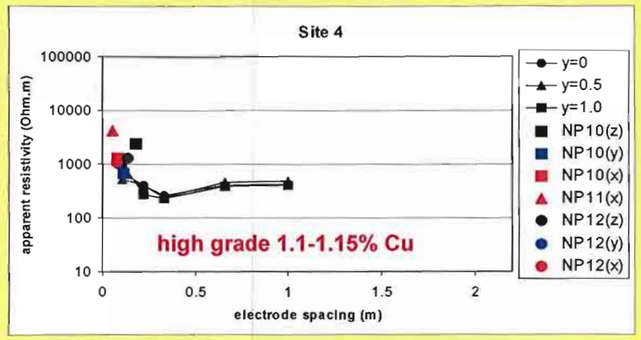

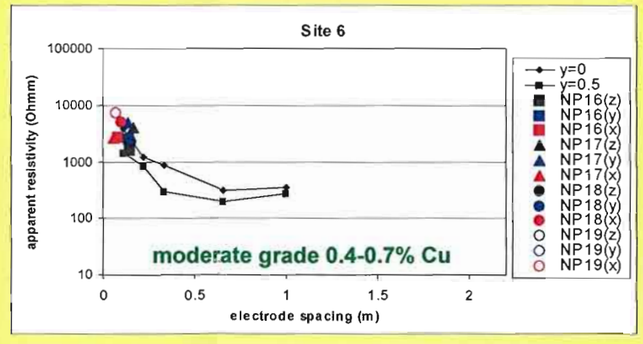

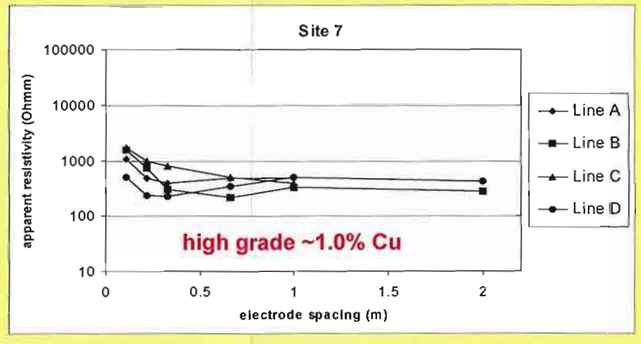

Figure 7.24. Apparent resistivity versus electrode spacing for insitu electrical soundings for all sites at North Parkes. Colour symbols display sample measurements plotted against sample size, for three orthogonal measurements.

Sulphides are disseminated bornite and chalcopyrite but occur mainly in quartz veins (5%; <1-7 mm). The more pronounced scale variation observed for these sites likely result from an increase in the density of veining and the overall proportion of sulphide minerals.

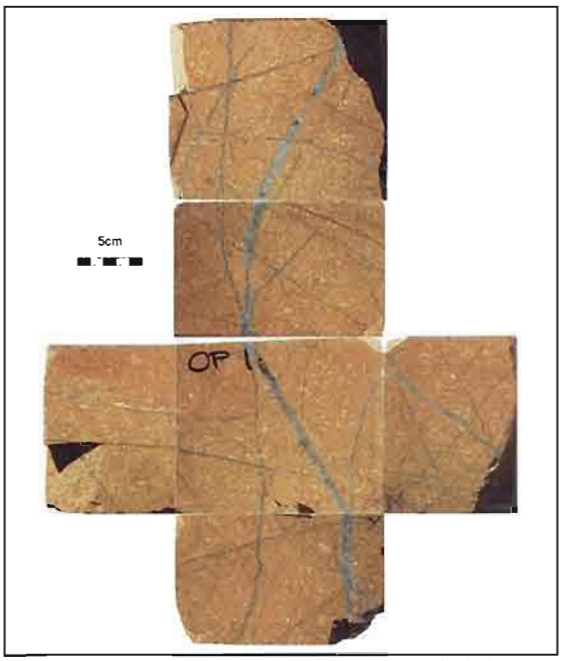

Figure 7.25. Sample OP1 collected from E27 is an example of high grade ore; assay 1.5%Cu. Sulphides are disseminated bornite and chalcopyrite but occur mainly in quartz veins (5%; <1-7 mm). The photograph of the sample shows an "exploded" view displaying all six sides of the prismatic sample.

Sites 9 and 4 (Figure 7.24) clearly show a minimum resistivity occurring at intermediate spaced measurements. The rock mass at site 9 consisted of magnetite-biotite altered volcanics with thin carbonate-biotite-quartz-bornite-chalcopyrite veins. The rock mass at site 4 consisted of a small wedge of volcanic "country" rocks intruded by thin "vein dykes". Sulphide mineralisation at this site was very minimal. This minimum apparent resistivity likely reflects the length-scale over which the mineralised veins are electrically connected.

For many sites (4, 6 and 9, 10) the laboratory data is tightly clustered and plots close to the projection of the trends defined by the insitu data at small scale measurements (Figure 7.24). Other sites (2, 3, 8) show a greater scatter in sample data but with values that are still close to the small scale insitu measurements. For sites 1 and 5, the sample resistivity measurements are significantly greater than the insitu data even at small electrode spacings. Both these sites were located in monzonite porphyry and the sample dimensions were smaller than the scale of the stockwork veining.

In all cases the insitu apparent resistivity at the largest electrode spacing is significantly less than the resistivity of the most conductive laboratory sample collected from the corresponding site.

Figure 7.24 clearly shows that there is little overall variation in apparent resistivity both within and between sites at North Parkes E27 deposit. This is due to the low overall proportion of sulphides within the rock mass (with low

grades equating to 0.2% Cu, and high grade equating to 1.5% Cu). The sulphur content in unmineralised altered volcanics is often similar to low grade ore. In these rocks the effects of very small volumes of sulphide minerals may be subsidiary to effects relates to more pervasive and volumetrically significant silicate alteration.

Despite the small resistivity contrast between volcanic and mineralised porphyry, the insitu resistivity of moderate to higher grade ore typically lies in the range 100-1000 Ωm, whereas low grade and unmineralised volcanic sequences have resistivity one order of magnitude higher (1000-10000 Ωm) (Table 7.2). The bulk rock apparent resistivity of moderate to high grade ore typically ranges between 300 to 500 Ωm, significantly less than very low grade or largely unmineralised material (typically >1000 Ωm).

Site	Grade		Insitu apparent resistivity		
			Min	Max	bulk
Volcanics- 2	low	0.1-0.3% Cu	1430	10400	**5450**
Volcanics- 3	low	0.2-0.5% Cu	1325	6350	**1325**
Volcanics- 9	low	0.04-0.3% Cu	1660	8050	**6700**
Volcanics- 10	low	0.1-0.4% Cu	1730	82300	**6000**
Porphyry- 8	low	0.1% Cu	815	1700	**350**
Porphyry- 5	moderate	0.6-0.69% Cu	375	1200	**870**
Porphyry- 6	moderate	0.4-0.7% Cu	200	5000	**300**
Porphyry- 1	moderate	0.5-0.85% Cu	70	870	**550**
Porphyry- 4	high	1.1-1.5% Cu	225	1050	**400**
Porphyry- 7	high	~1.0% Cu	215	1700	**300**

Table 7.2. Minimum, maximum and average bulk apparent resistivity at determined by insitu measurements. The resistivity of volcanic units is typically one order of magnitude higher than measured in mineralised porphyry sites.

Chargeability soundings for all sites are shown in Figure 7.26. In each case laboratory samples are plotted as a function of the sample dimension. All graphs are plotted with consistent chargeability scales to readily enable direct comparisons between results from each site. The graphs are grouped into the two main lithologies (mineralised porphyry and host volcanics).

Chargeability shows only minor scale variation, with a general but not universal trend of relatively higher values at small electrode spacings. Moderate to high grade material is characterised by higher chargeability than low grade and volcanic units. Valid laboratory chargeability was only available for 17 of 30 samples. Laboratory chargeability appears to lie within the range of insitu measurements for each site, although significant scatter is apparent in some sites.

Insitu apparent resistivity and chargeability plots for all measurements colour coded by site are shown in Figure 7.27. There is considerable overlap of data from different sites although primary lithologies are generally distinguished, with volcanics tending to be more resistive and less chargeable than porphyry sites. When broad copper grade estimates are superimposed on the graph, a clear trend showing sites becoming more conductive and chargeable with increasing copper and hence sulphide content.

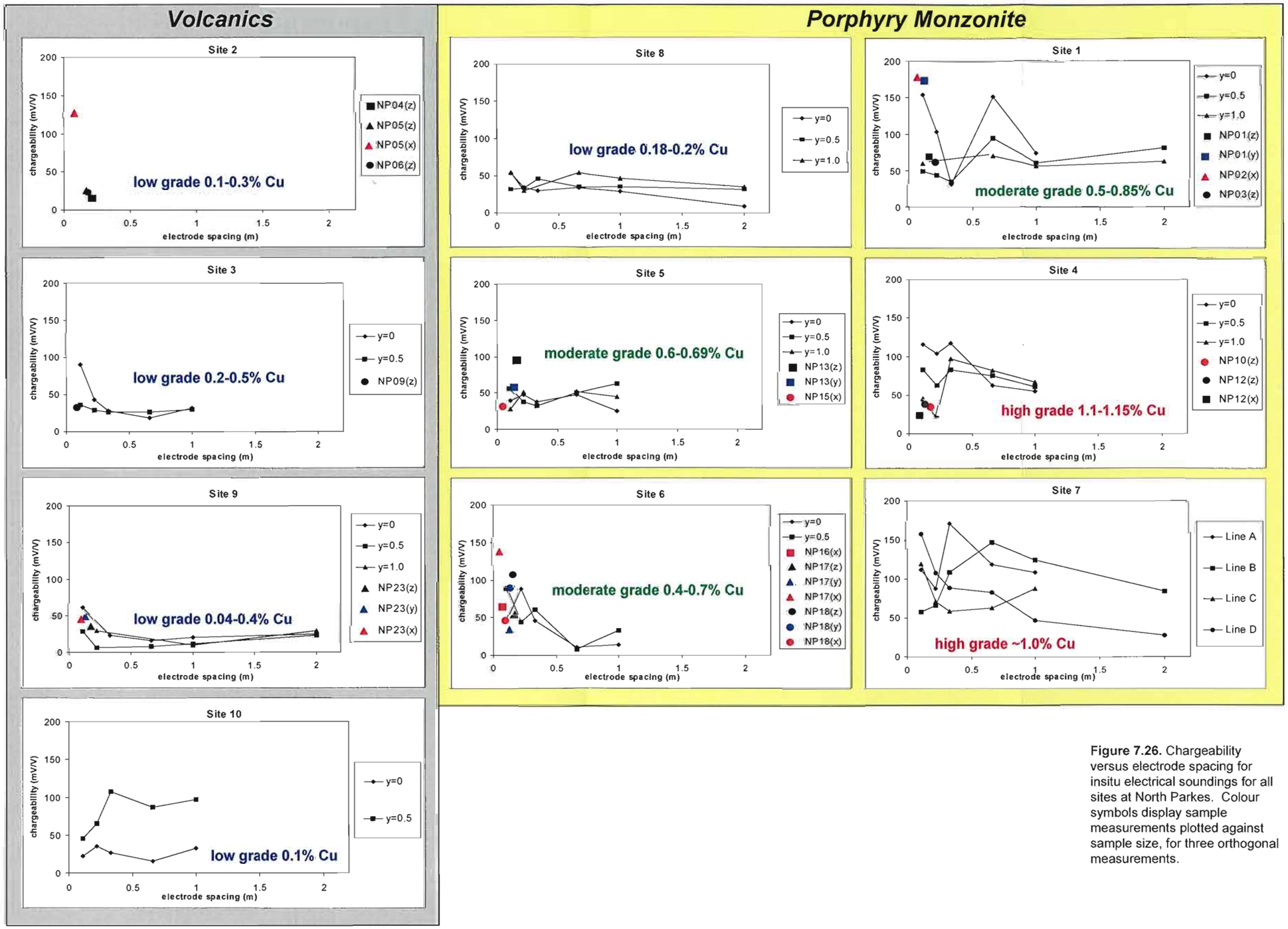

Figure 7.26. Chargeability versus electrode spacing for insitu electrical soundings for all sites at North Parkes. Colour symbols display sample measurements plotted against sample size, for three orthogonal measurements.

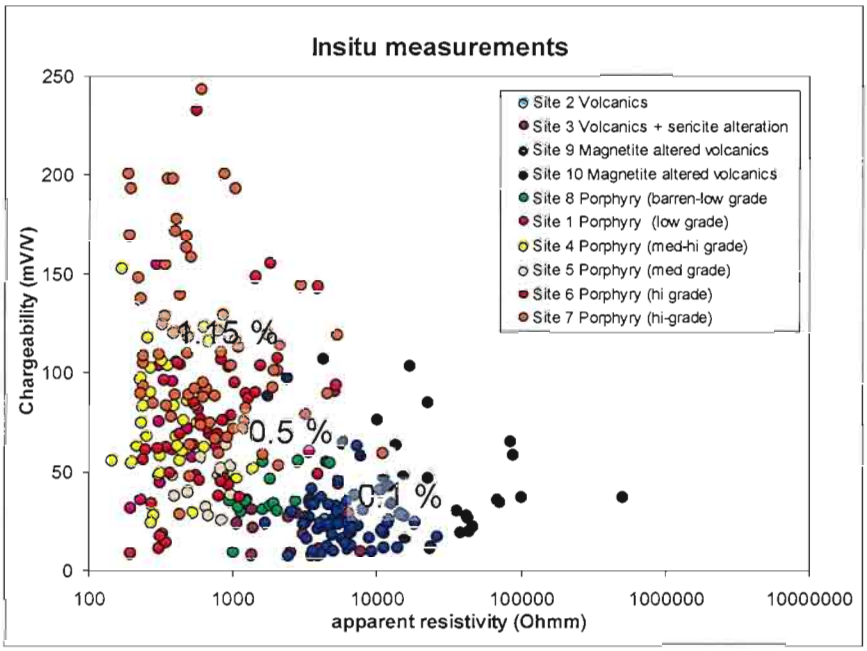

Figure 7.27. Apparent resistivity and chargeability plot for all North Parkes insitu measurements, colour coded by site. The percentage figures (0.1%, 0.5% and 1.15%) indicate approximate average copper grades. There is a general decrease in resistivity and increase in chargeability for higher copper content. Volcanic units have higher resistivity and lower chargeability than mineralised porphyry.

Laboratory resistivity and chargeability plots for samples where measurements could be obtained are shown in Figure 7.28. The laboratory measurements of volcanic samples are typically more resistive than porphyry samples. Laboratory chargeability is typically lower in volcanic samples, although two outliers exhibit unusually high values. Laboratory chargeability of samples for each site show similar values to insitu measurements. In comparison with insitu site measurements (Figure 7.27) the respective laboratory measurements tend to be more resistive by an order of magnitude, although a similar overall distribution is apparent.

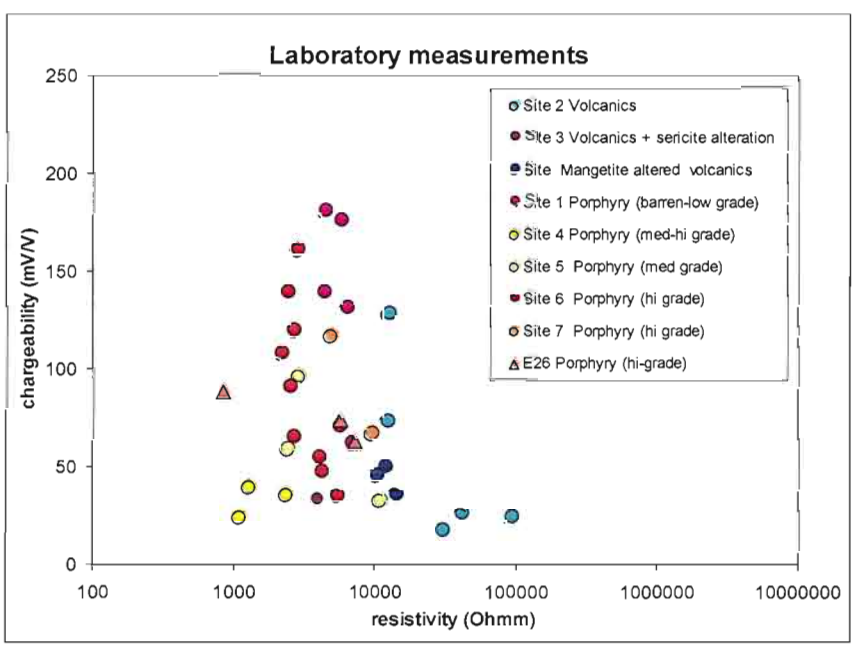

Figure 7.28. Resistivity and chargeability plot for all laboratory measurements from North Parkes, colour coded by site. High grade E26 ore samples are shown in triangles. The general pattern for insitu measurements (Figure 7.28) is also apparent for laboratory measurements with volcanic units having higher resistivity and lower chargeability than mineralised porphyry.

7.4.4. Chemical variations

The insitu apparent resistivity-chargeability plot in Figure 7.27 suggests copper content controls the distribution of data, with sites with high copper grade tending towards low resistivity and high chargeability, whereas the volcanic sites are resistive and with lower chargeability. This trend is also apparent in laboratory data, although recorded resistivity on samples is typically much greater. Since copper bearing sulphides were the main sulphide phases, copper basically reflects sulphide content and hence the total proportion of sulphides.

In order to examine chemical controls on the electrical properties of the North Parkes samples, laboratory electrical measurements were compared with geochemical assays. As previously described, valid chargeability measurements were available for only seventeen out of the thirty samples. The variation of major chemical parameters as a function of both resistivity and chargeability for these samples is shown in Figure 7.29. Copper and sulphur (Figure 7.29a and b) both show poorly defined trends, with higher values tentatively associated with lower laboratory resistivity. High levels of copper and sulphur are present in samples with both low and moderate chargeability.

Distinct patterns are evident in the chargeability versus resistivity cross plots for a number of major chemical constituents including iron oxide (Fe_2O_3) and silica (SiO_2) (Figures 7.29 c and 7.29d respectively). These patterns almost certainly reflect primary lithological variations with high silica and low iron typically corresponding to the monzonite porphyry rocks while the volcanic units are more basic, magnetite altered and usually have higher iron content (these units can be identified from Figure 7.27). Resistivity-chargeability plots colour coded for Na_2O (Figure 7.29 e) and K_2O (Figure 7.29f) do not mimic the lithological patterns delineated by iron oxide and silica. Na_2O decreases with decreasing resistivity while K_2O shows an opposite trend. These variations in mobile species are attributed to alteration rather than primary lithological variations.

The chemical variations detected in the valid subset of laboratory petrophysical data (Figure 7.29) are further reinforced by the resistivity-composition scatter plots shown in Figure 7.30. Very poorly defined trends of decreasing resistivity with increasing copper and sulphur content (Figure 7.30a,b) are observed, suggesting that variations in the small proportion of sulphide minerals present influence the measured resistivity to some extent. However better correlations are observed between decreasing resistivity and increasing K_20 or decreasing Na_2O Figure 7.30c,d) further suggest that the primary control on the electrical properties is probably pervasive silicate alteration rather than the distribution of a very small proportion of sulphide minerals. Similarly lithological differences as indicated by MnO, MgO, SiO_2 and Fe_2O_3 also influence the sample resistivity (Figure 7.30e,f,g,h).

Scatter plots of chargeability and chemistry showed no obvious trends.

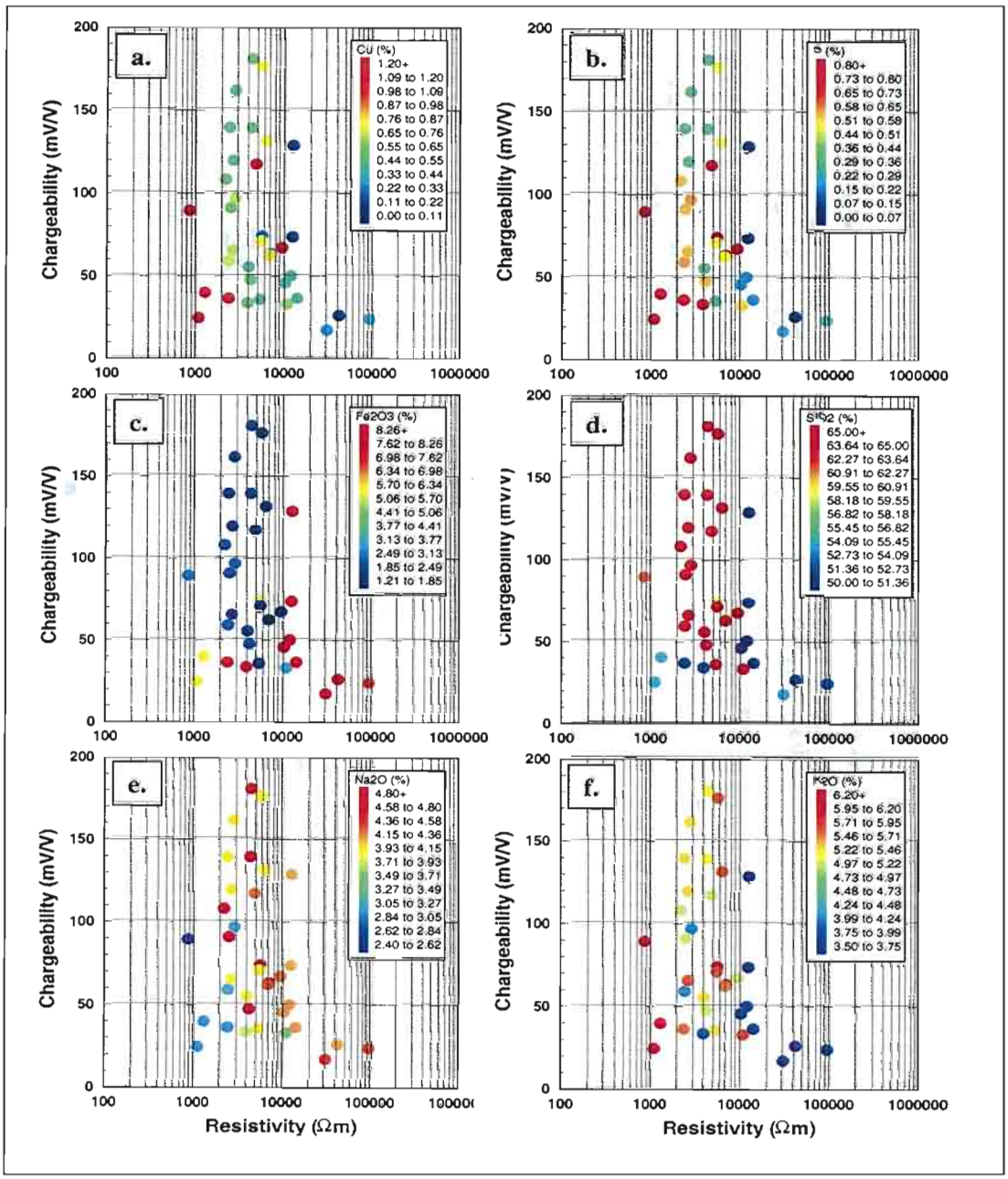

Figure 7.29. Resistivity and chargeability plots for North Parkes samples. Data samples colour coded by assay; (a) Cu%, (b) S%, (c) Fe_2O_3, (d) SiO_2, (e) Na_2O, (f) K_2O.

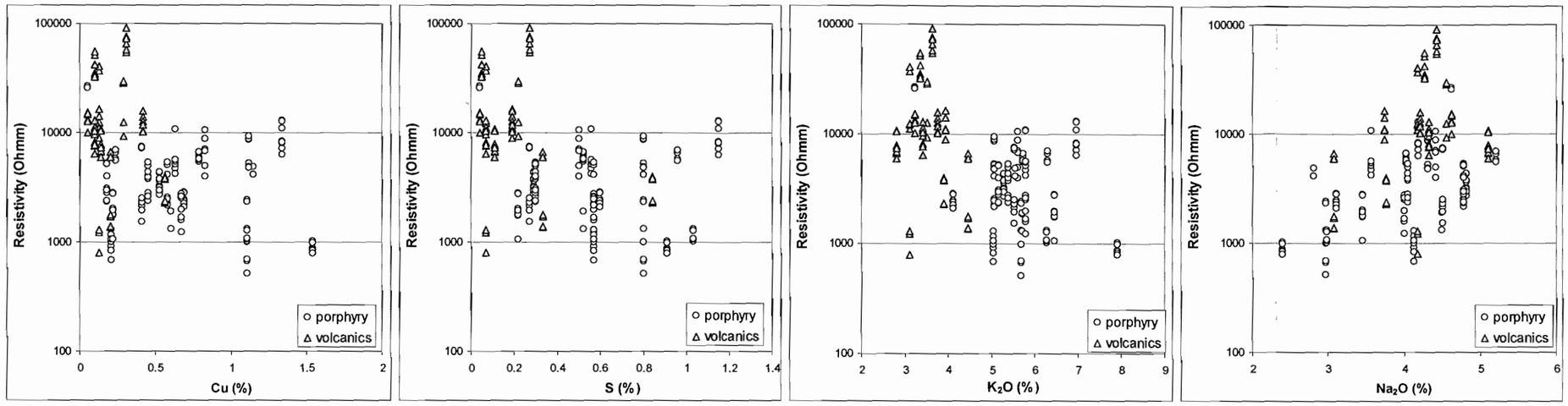

Figure 7.30. Scatter plots of resistivity and assays for (a) Cu, (b) S, (c) K_20, (d) Na_2O (e) MnO, (f) MgO, (g) SiO_2 and (h) Fe_2O_3 for all North Parkes samples.

7.5. Conclusions

North Parkes was selected as a study site as an example of a low grade, low sulphide content disseminated deposit. The very low proportions of sulphides and limited variations in lithology at North Parkes resulted in little overall change or scale variation in electrical properties. However the insitu and laboratory data generally showed a consistent pattern of decreasing apparent resistivity with increasing electrode spacing, although the variation is seldom greater than one order of magnitude. Some sites show a minimum resistivity at intermediate electrode spacing and this affect is likely a function of stockwork dimensionality. Sample measurements are generally more resistive than insitu values and lie along the projected trends plotted by insitu soundings.

Scale variations are most apparent for the higher grade material with a decrease in apparent resistivity of approximately a half to one order of magnitude with increase electrode spacing (from 0.11m to 1 to 2 metres). Chargeability measurements are typically less than 100 mV/V, and also reflect the low sulphide content with little scale variation measured across all sites.

Unmineralised or weakly mineralised rocks are highly resistive and have low chargeability. Apparent resistivity decreases significantly with increasing grade despite only a small increase in the percentage of sulphide minerals. High grade material is generally more chargeable than unmineralised or low grade ore but there is a large amount of scatter in the data.

Despite a poorly defined correlation between resistivity and copper or sulphide content, chemical correlations suggest that the variations observed may also be related to the effects of volumetrically pervasive alteration rather than the effects of the very small proportion of sulphide minerals.

Chapter 8
Synthetic models

8.1. Introduction

The insitu empirical studies at Scuddles, McArthur River and North Parkes show a consistent trend of decreasing apparent resistivity with increasing scale of investigation, despite the significant differences in mineralogy and ore texture between deposits. The insitu apparent resistivity calculated from the field measurements assumes a homogenous halfspace. However the majority of sites examined can be considered multiphase systems, consisting of conductive phases (sulphides and oxides) interspersed through a resistive matrix (silicate minerals).

Numerical modelling was undertaken to determine if synthetic systems demonstrated scale dependent behaviour similar to that observed in field measurements. A study by Jones (1989) demonstrated that two component numerical models could explain the scale behaviour observed for insitu resistivity measurements of granite. Jones' model consisted of conductive saturated fractures within resistive granite.

A series of three-dimensional synthetic rock textures were generated and apparent resistivity was calculated on the surface of the synthetic models, at various scales. These models were used to numerically assess the influence of factors such as variations in sulphide proportions, resistivity contrast between constituents, veining and variations in texture on apparent resistivity for a range of measurements at different scale.

8.2. Methodology

Cellular models were created using code generated in *Microsoft Visual Basic* (Roach, 2004). The code utilises a cellular automata approach for simulation of complex ore textures. Mineral phases in the three dimensional model grow around initial seed points subject to a set of user-defined rules. The code can be used to simulate a wide variety of textures including disseminated or massive ores and can reproduce features such as preferential orientation of individual minerals. Although the code allows for up to four conductive phases in the synthetic models, only one conductive phase was introduced in the models, to simplify the interpretation of results.

The prismatic model dimensions were; x - 120 cells, y - 80 cells and z - 40 cells (a total of 384 000 cells). Conductive cells are selected within a contrasting background by the program.

The scale variation of apparent resistivity was examined for a range of different synthetic rock textures, but the important characteristics of the synthetic models can best be illustrated for two end member models consisting of either random conductive cells in a resistive matrix or of penetrative conductive veins in a resistive matrix. Random cell models can simulate disseminated mineralisation textures, such as those observed at

North Parkes, or for higher proportions of conductive cells simulate textures observed for massive sulphide deposits, such as some sites at Scuddles. Vein models were selected to simulate layered or vein textures, commonly observed at sites at Scuddles and McArthur River.

Random models are the simplest type of three-dimensional model. A pre-defined number of random model cells are assigned resistivity values that differ from the background value. Two specific aspects were investigated using the random models. These were the effects of variable proportions of conductive minerals in a resistive background, and the variation in the resistivity contrast between conductive and resistive components of the system.

Vein models were generated, by simulating growth along the x-dimension from initial starting seeds. Veins could terminate, coalesce or make small changes in direction to simulate realistic geological textures. The vein geometry is 2.5 dimensional, since each vein extends throughout the length of model in the z direction. Three aspects of vein models were investigated; the effects of variations in the resistivity contrast between conductive and resistivity components, effects of variable proportions of conductive veins in a resistive background, and the variations in electrical anisotropy with electrode spacing and vein properties.

Apparent resistivity was calculated on the synthetic models using the finite-difference modelling program *RES3DMOD* (Loke, 2002). *RES3DMOD* automatically positions electrodes at every second grid node on the upper surface of the model providing a total of 2400 (60 x 40) electrodes. Potentials are calculated for each electrode position using a standard finite difference technique. Once calculated, these potentials can be combined to simulate measurements on the model surface using standard electrode arrays. Apparent resistivity was calculated for Wenner arrays to be consistent with insitu measurements.

The dimensions of the cells in the model were set to 1 metre and the minimum electrode spacing calculated by *RES3DMOD* is simply twice the cell dimension. With appropriate scaling the models could be used to simulate microscopic, mesoscopic and macroscopic systems, since the cell size and electrode separation scale in unison. For this reason, no dimensions have been designated for electrode separation in the results of the synthetic models. Theoretically, a cellular model could be produced to incorporate features at all scales, however this is not practical due to computational limitations. It is important to note that the minimum electrode measurement (2 units) is equivalent to twice the cell dimension (1 unit) in the models. For each model, resistivity is calculated with the Wenner array with electrode spacings from 1 to 20 units. In the instance where 1 unit was equal to 0.1 metre, measurements are effectively carried out from 0.2 metre electrode spacing to 2 metres (equivalent to field scale measurements, whose conductive features are of the scale of 0.1 metres). Or in the situation of the sample scale measurements the model of 1 unit could equal 1 millimetre, electrode spaced measurements would be effectively collected between 2 millimetres and 2 centimetres.

8.3. Results

8.3.1. Random Models

The results for a random cell model are presented, to firstly, demonstrate if scale variations are observed, and secondly, to provide an example for detail analysis. A section of the model is shown in Figure 8.1.

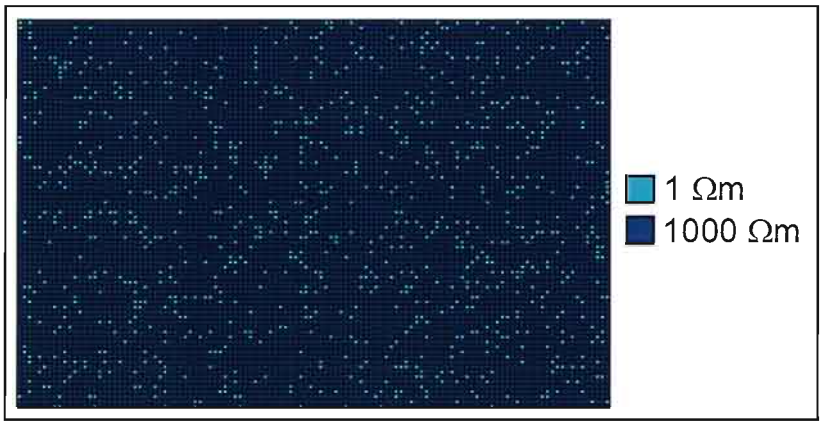

Figure 8.1. Top surface view of random cell model consisting of 10% proportion of conductive cells within resistive background (120 x 80 cells). Light blue cells: 1 Ωm, dark blue cells: 1000 Ωm.

The apparent resistivity derived from *RES3DMOD* can be displayed for any electrode array as either resistivity maps for different electrode spacings or as a series of apparent resistivity pseudsections for the x and y directions. The apparent resistivity and electrode position data was exported from *RES3DMOD* and histograms and statistics of the data were produced for the different electrode separations, for a Wenner array geometry.

An example of the results obtained for a random model consisting of 10% conductive (1 Ωm) cells in a resistive background (1000 Ωm) is displayed in Figure 8.2 (resistivity contrast- 1000:1). Surface apparent resistivity maps for the different electrode separations for both x and y directions show similar patterns indicating little or no anisotropy, as expected for a random cell model. The resistivity maps clearly show a decrease in apparent resistivity with increasing electrode separation, indicative of the increasing connectivity of random conductive paths with increasing scale of investigation.

Due to the large population of apparent resistivity data derived from the numerical modelling, scale variation of the models can be effectively presented statistically. The distribution of apparent resistivity for different electrode space measurements (1, 4 and 12 units) for the 10% random cell sample is shown in Figure 8.3, for all x and y data. For small scale measurements (1 unit) the distribution is distinctly bimodal with a mean of 409 Ωm and a modal peak at less than 10 Ωm. The bimodal distribution and apparent resistivity map for the smallest measurements (1 unit) are clearly reflecting the binary nature of the model, composing of a conductive and resistive population. The 4 and 12 unit electrode spaced data exhibit unimodal distributions with mean values decreasing to 156 Ωm and 73 Ωm respectively. The range of apparent resistivity values also becomes tighter at large electrode spacings, indicating less variability. The scale variation is

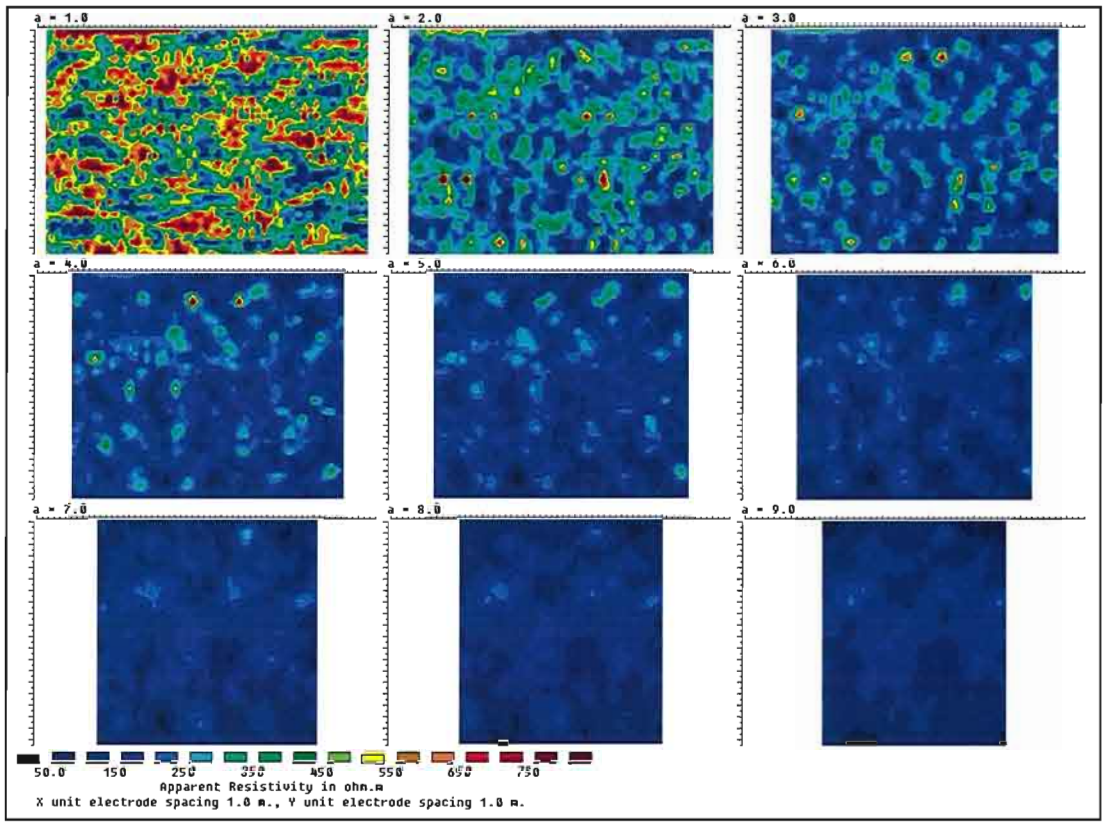

(a)

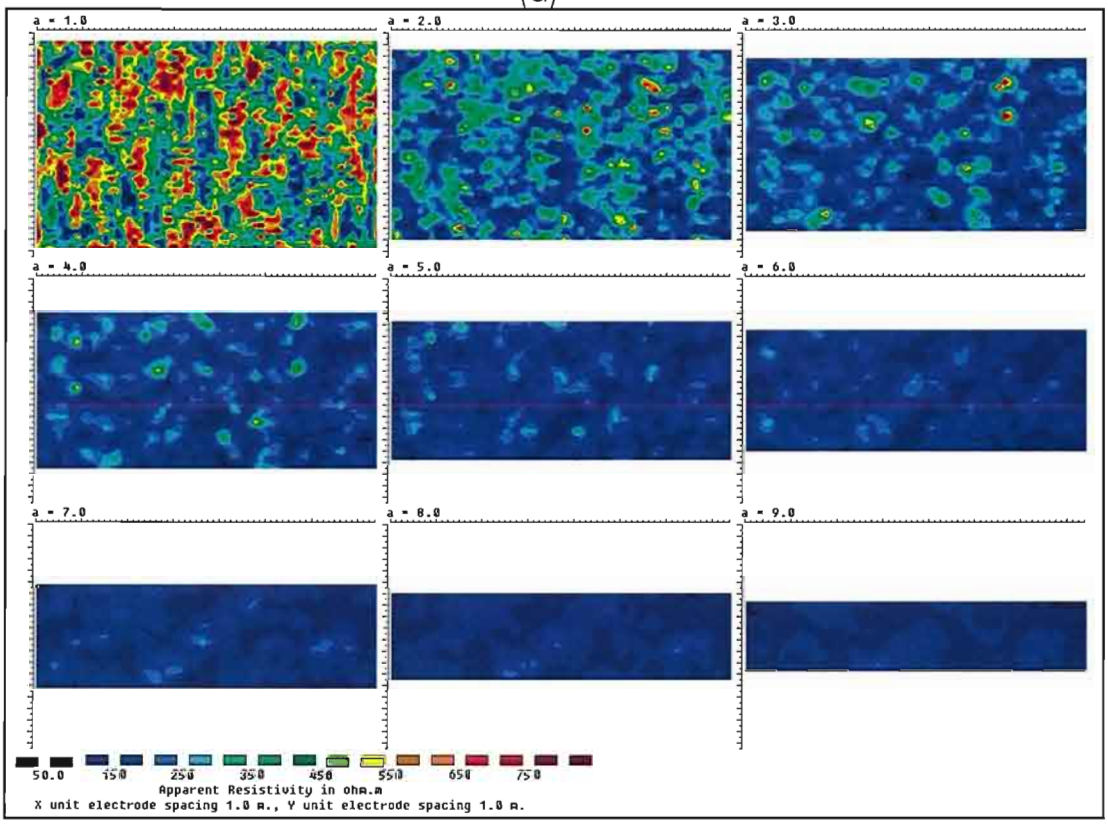

(b)

Figure 8.2. Apparent resistivity surface maps for different electrode spacings (Wenner measurements) for a random cell model containing 10% conductive cells,1 Ω cells in 1000 Ωm background (120 x 80 cells); (a) array orientated in the x direction, (b) array orientated in the y-direction. The same linear colour scheme has been applied to all resistivity maps. It is clear that apparent resistivity decreases with increasing electrode spacing, indicating greater connectivity between conductive grains at larger scales.

clearly observed by the shift in mean apparent resistivity between the three histograms. At larger scales the connectivity of the random conductive cells increases, reducing the bulk apparent resistivity.

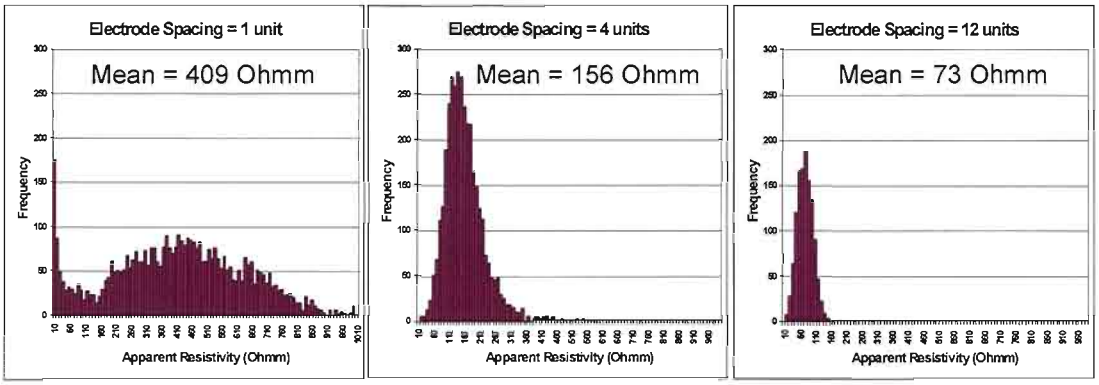

Figure 8.3. Histograms of apparent resistivity for three scale measurements for x and y directions, (1, 4 and12 units) for the 10% random cell model (1 Ωm conductive cells in 1000 Ωm background). The mean of apparent resistivity decreases for increasing electrode spacing.

The data distribution for calculations at all electrode spacings can be most effectively represented as a density image of data frequency in electrode spacing-apparent resistivity space. These plots are effectively two-dimensional histograms and show both the general trends of variations in apparent resistivity versus electrode spacing and also the degree of data scatter. Two-dimensional histograms of normal and log-transformed data for all x and y measurements for the 10% random cell model with 1 Ωm cells in a 1000 Ωm background is shown in Figure 8.4. The mean of apparent resistivity was calculated for both data sets and plotted on the images (arithmetic and geometric means respectively). Madden (1976) states the geometric mean is an accurate predictor of the physical properties of a mixture of different materials, especially for properties that may vary orders of magnitude for a given material.

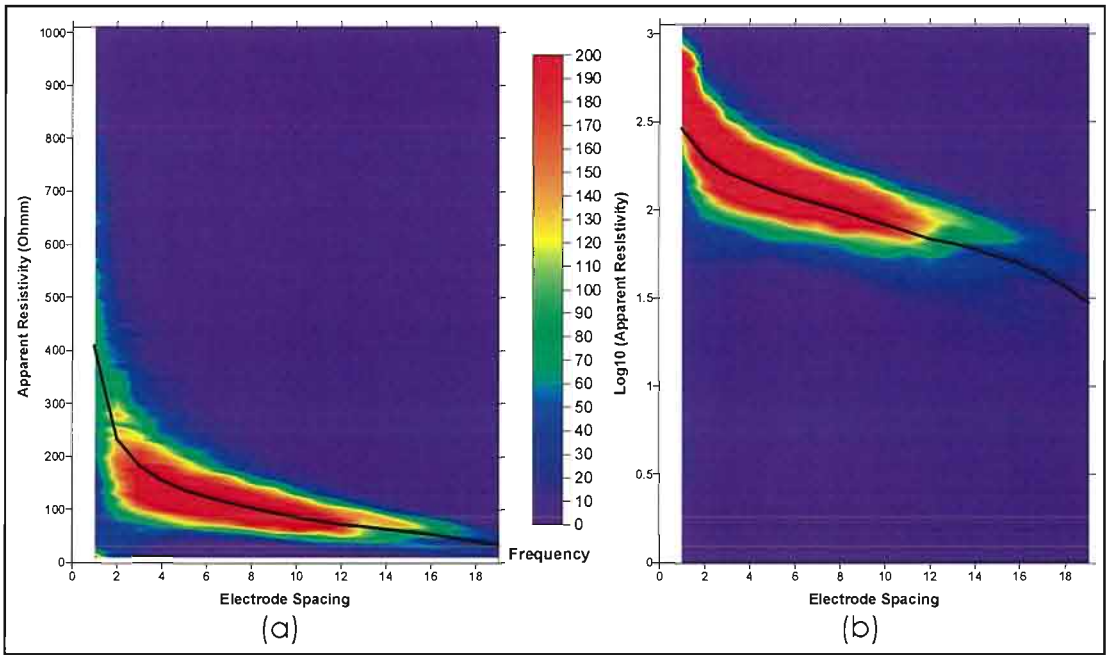

Figure 8.4. (a) Two-dimensional histograms of calculated apparent resistivity for measurements in the x and y direction for a 10% random cell model. (b) Log-transformed apparent resistivity histogram. The black lines indicate the average apparent resistivity value; (a) arithmetic mean and (b) geometric mean. Both plots clearly show a decrease in apparent resistivity with increasing electrode spacing.

The two means (Figure 8.4) produce almost identical curves, except for an electrode spacing of one unit where the mean of the log-transformed data provides a lower estimate. The geometric mean is used to provide an "average" for all further results. The scale variation in apparent resistivity is clearly observed in the data distribution and mean values. Apparent resistivity decreases with increasing electrode spacing, by one order of magnitude as the spacing increases from 1 to 20 metre. The data predominantly shows a unimodal distribution for all electrode separations, with the exception of small scale measurements. For small scale measurements, a bimodal distribution in resistivity is observed.

8.3.1.1. Random cell model: Variable Proportions

To assess the effects of varying the proportion of conductive cells in a random cell model, a series of models were produced, whose conductive cell content ranged from 0 to 60 percent by volume. Conductive cells were assigned a resistivity of 1 Ωm, while the background cells were assigned a resistivity of 1000 Ωm. Examples of random cell synthetic models are shown in Figure 8.5. These images clearly show that the connectivity of the conductive component becomes significant for models with greater than 20% conductive cells. For models with greater than 60% conductive cells, the model can be effectively considered as a single interconnecting conductive body, containing disconnected resistive bodies. Thus, high proportion random models may be suitable analogues for simulating textures of high grade sulphide samples, similar to those collected at Scuddles.

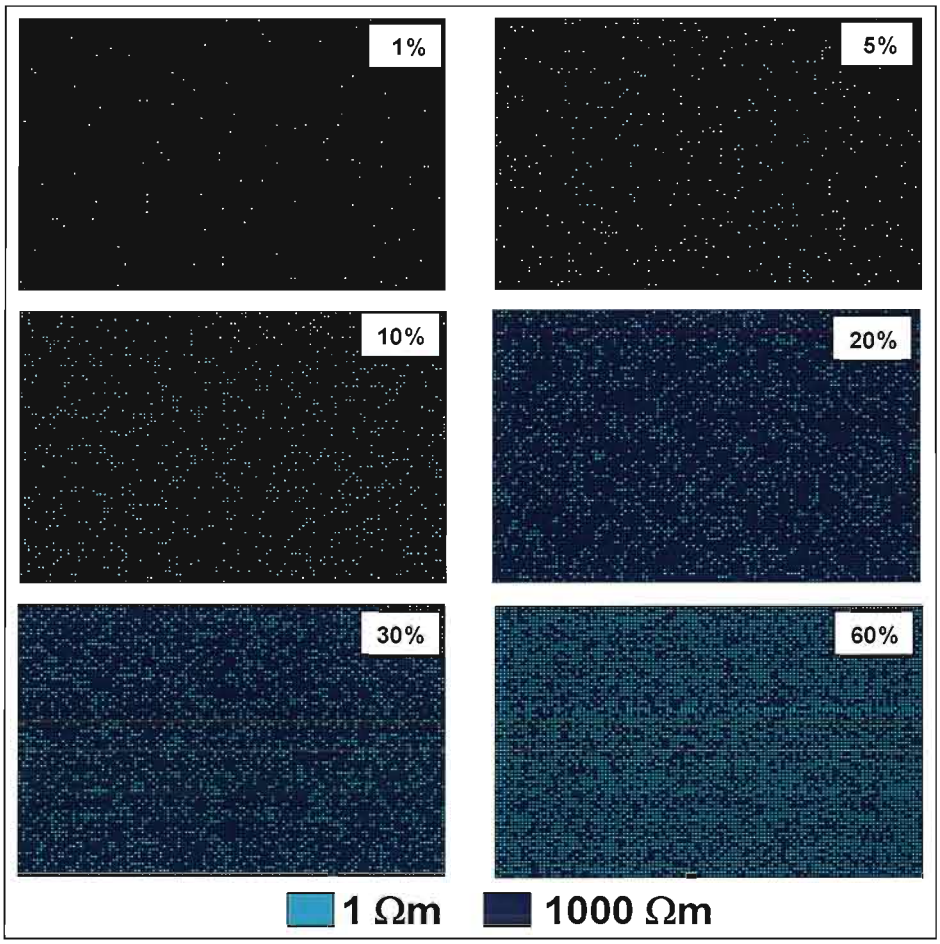

Figure 8.5. Example of random cell models of variable proportions. Each panel shows the top layer of the respective 3D random cell model. Percentage indicates the proportion of conductive cells in the model.

The geometric means of the log-transformed apparent resistivity were calculated from the *RES3DMOD* data for each electrode spacing, for all random cell models with variable proportions of conductive cells (Figure 8.6).

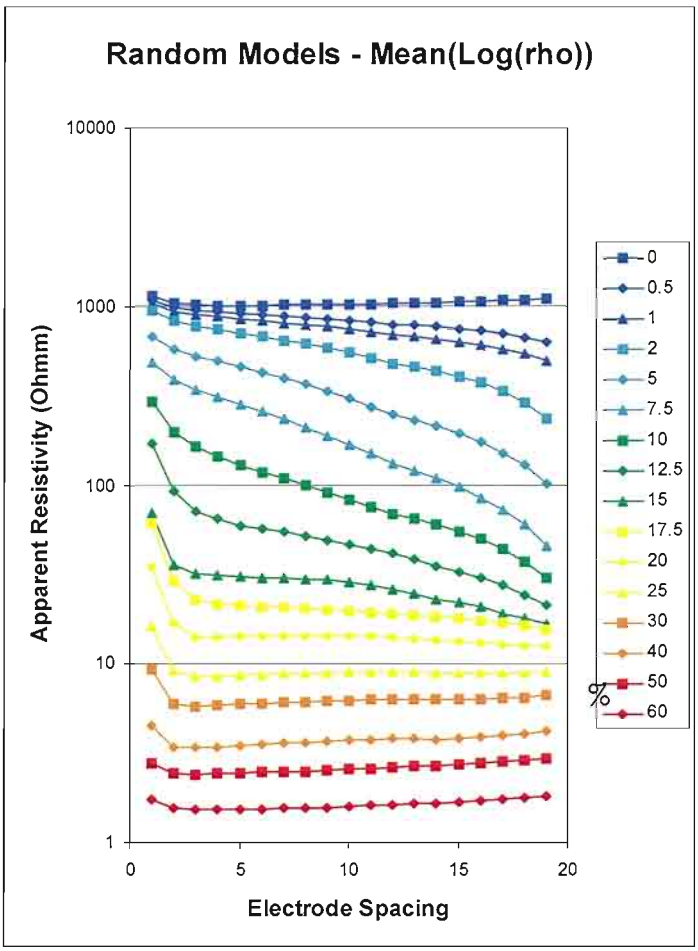

Figure 8.6. Graph of the calculated geometric mean of apparent resistivity versus electrode spacing for models with different proportions of conductive cells (1 Ωm cells in 1000 Ωm background). Scale variations are observed for all curves, with maximum scale variation occurring for 7.5% conductive cell content.

The apparent resistivity for the 0% model (i.e. 1000 Ωm homogeneous earth), diverges slightly from the expected 1000 Ωm result for all electrode spacings. This is attributed to an edge effect artefact in the numerical code in *RES3DMOD*, however, the variations are quite small (within 3%) and do not significantly detract from the overall pattern of variation.

Scale variations are most prominent for models with proportions of conductive cells ranging from 2 to 15%. The largest scale variation (~300-500 Ωm → 20-30 Ωm) is observed for models with between 7.5 and 10% of conductive cells. For greater proportions, the magnitude of the scale variation decreases, and becomes pronounced at only small electrode separations. This reflects the increasing connectivity for greater proportions of conductive cells.

A large number of models have been developed to attempt to predict the bulk resistivity of two component systems based upon the proportion of conductive cells to resistive background, geometry of the components and their respective resistivities. These models have evolved from direct measurements (experimentally or computationally), semi-empirical

relationships and theoretical techniques (Torquato, 1991; Banisi et al., 1993; Berryman, 1995; de Kuijper et al., 1996; Koleman and de Kuijper, 1997.). Although not explicitly described in some cases, these models ignore the effects of scale variation and make the assumption of large model volume in order to make a valid statistical prediction.

Grant and West (1965) provide equations for "extreme" end-member rock textures of variable proportions of randomly positioned conductive spheres, rods or plates in a resistive matrix (Figure 8.7). The effective resistivity for a mixture containing a small proportion of spheres dispersed in a medium was first shown by Maxwell (1891) to be approximately,

$$\rho_e = \frac{2\rho_1 + \rho_2 + v(\rho_1 - \rho_2)}{2\rho_1 + \rho_2 - 2v(\rho_1 - \rho_2)}\rho_2 \qquad (8.1)$$

where
ρ_e- effective bulk resistivity
ρ_1 - resistivity of sphere particles
ρ_2 - resistivity of matrix
v – volume ratio of spherical particles

For slender rods dispersed through the medium (Grant and West, 1965) the effective resistivity is approximately,

$$\rho_e = \frac{v\rho_1}{3} + (1-v)\rho_2 \qquad (8.2)$$

and for plates lying perpendicular to the z direction,

$$\rho_x = \rho_y = v\rho_1 + (1-v)\rho_2 \qquad (8.3)$$

and
$$\rho_z = \frac{\rho_1\rho_2}{v\rho_2 + (1-v)\rho_1} \qquad (8.4)$$

where
$\rho_{x,y}$ - effective bulk resistivity in x and y direction.
ρ_z - effective bulk resistivity in z direction.

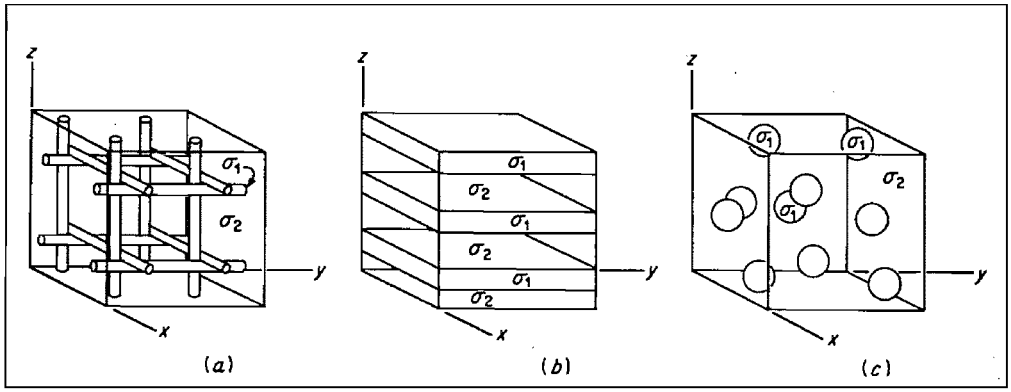

Figure 8.7. Extreme end member models of two component conductivity systems for (a) rods, (b) horizontal plates and (c) spheres, from Grant and West (1965).

Further intermediate models are described by Keller (1989), such as the Fricke model, which considers ellipsoidal particles suspended in a matrix. Other models are presented for different contrasts in resistivity between components. A more complex expression known as the Hanai-Bruggeman

method described by Bussian (1983) and Torquato (1991), approximates the bulk resistivity of multiphase mixtures and includes a "depolarisation factor" that reflects the texture (i.e. geometric arrangement of conductive constituents). The expression can be defined as,

$$\rho_e = \rho_2 v^{1/(1-d)} \left(\frac{1 - \rho_1 / \rho_2}{1 - \rho_e / \rho_2} \right)^{1/(1-d)} \qquad (8.5)$$

where d = depolarisation factor

This expression can be further simplified to,

$$\rho_e \cong (1/(1-d))\rho_2 (1 - v^{1/(1-d)}) + v^{1/(1-d)} \rho_1 \qquad (8.6)$$

The predictions of these models can be compared to the apparent resistivities calculated from *RES3DMOD* for the synthetic random cell models. The previous numerical results from the random cell model (Figure 8.6) can be alternatively presented as apparent resistivity plotted as a function of the proportion of conductive cells, with data grouped according to electrode spacing (Figure 8.8). The scale variation is indicated by the separation between the curves, most notably for conductive cell proportions between 1 and 10%. The curves converge for higher proportions indicating little or no scale variation. The predictions for the sphere, rod and plate models of Grant and West (1965) are superimposed on the results derived from the finite difference modelling. None of these simplistic models adequately fit the finite difference model results.

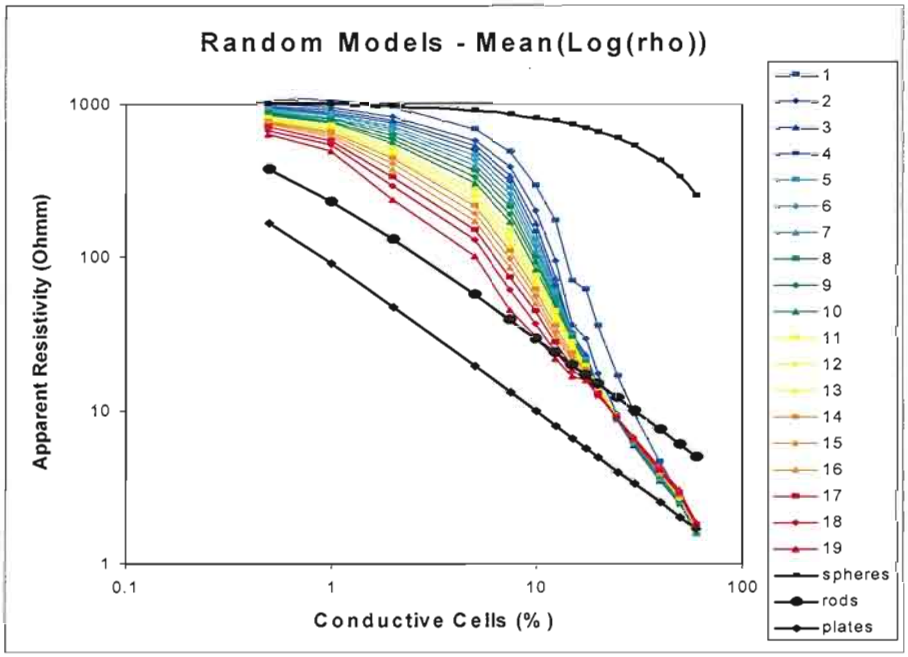

Figure 8.8. Calculated apparent resistivity versus percentage of 1Ωm conductive cells for different electrode spacings (colour coded) for a random cell model. The black lines represent the predictions of the Grant and West (1965) sphere, rods and plates model. Graphs are colour coded according to electrode unit spacing.

The sphere model (Figure 8.8) appears to systematically overestimate the resistivity of random cell models for all proportions of conductive cells. Grant and West (1965) comment that the sphere model is only valid for a small

volume percentage of random spheres and does not take into account the interconnection of multiple spheres to form a conductive network. This limitation results in an over-exaggeration of the predicted apparent resistivity for the sphere model when compared to the finite difference models, for proportions of conductive cells greater than 1%.

The rod and plate models (Figure 8.8) produce near-identical trends in log-log space of apparent-resistivity versus proportion of conductive cells, with the plate model displaced towards less resistive values. The rod model underestimates the apparent resistivity of random cell models for proportions less than ~10% and overestimates for higher proportions. The plate model predominantly underestimates the resistivity, except for very large proportions of the conductive component.

The predictions from the Hanai-Bruggeman method for several depolarisation factors were also compared to the numerical model results, as shown in Figure 8.9. The Hanai-Bruggeman curves have the same basic form as the random cell models, but the choice of the depolarisation factor varies with the scale of investigation. Despite the good fit, even for a particular scale measurement, there are discrepancies between the best model fit and the numerical data. A depolarisation factor of 0.04 best fits the data for intermediate proportions (10%). The small and large scale end-member numerical models are largely bound by depolarisation factors of 0.01 and 0.5 respectively.

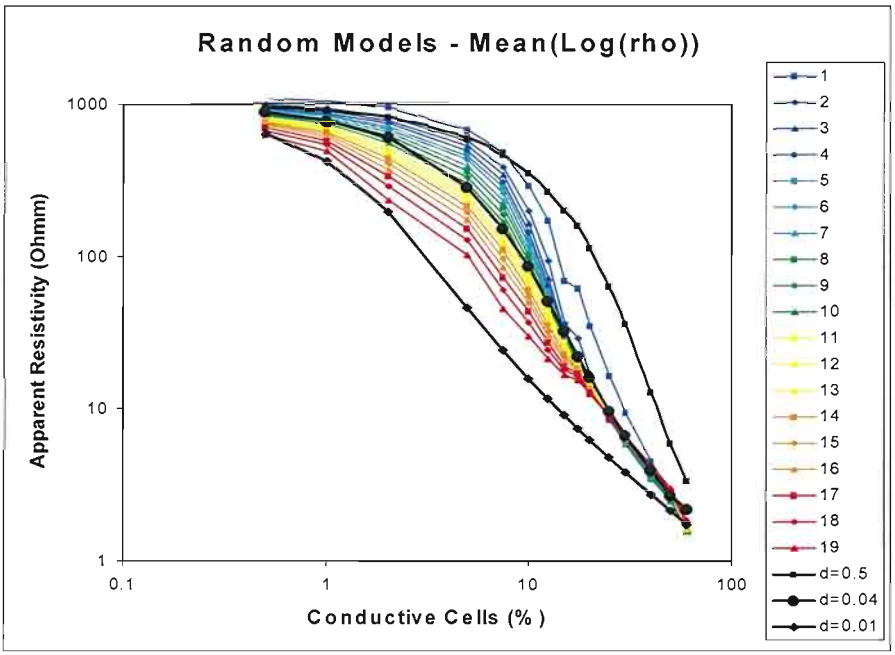

Figure 8.9. Calculated apparent resistivity versus percentage of 1Ωm conductive cells for different electrode spacings (colour coded) for a random cell model. The black lines represent the predictions of the Hanai-Bruggeman model for different depolarisation factors. Graphs are colour coded according to electrode unit spacing.

The Hanai-Bruggeman method provides a better fit to the form of the numerical data, compared to the end member models of Grant and West (1965). In the Hanai-Bruggeman method the depolarisation factor is used to describe the "texture" of the material. The form of the apparent resistivity-cell proportion curve, for a given electrode spacing can be closely matched

using the Hanai-Bruggeman equation but a different value of the depolarisation factor is required in order to fit curves generated for different electrode spacings. In this case variations in the depolarisation factor primarily reflect scale variability rather than variations in texture.

8.3.1.2. Random cell model: Variable contrast cell model

A 10% random cell model was selected to examine the effect of variations in resistivity contrast between conductive and resistive cells. The distribution of conductive cells was fixed, and the background model resistivity was set at 1000 Ωm. A series of models were generated with conductive cell resistivities varying between 0.001 Ωm and 100 000 Ωm.

The results are plotted as apparent resistivity versus electrode spacing for the various models (Figure 8.10). The degree of scale variation increases significantly as the resistivity contrast between background and the conductive cells increases. Scale variation first becomes clearly obvious for models with 30 Ωm conductive cells. For a 10% random cell model with 1 Ωm conductive cells, the scale variation is approximately one order of magnitude, between small and large electrode spacings. The scale variability increases to approximately three orders of magnitude for the model with 0.001 Ωm conductive cells in a 1000 Ωm background. There is no scale variability, when the cells are more resistive than the background. This would effectively represent a random model with a 90% "conductive" background (1000 Ωm) with 10% random resistive elements (>1000 Ωm).

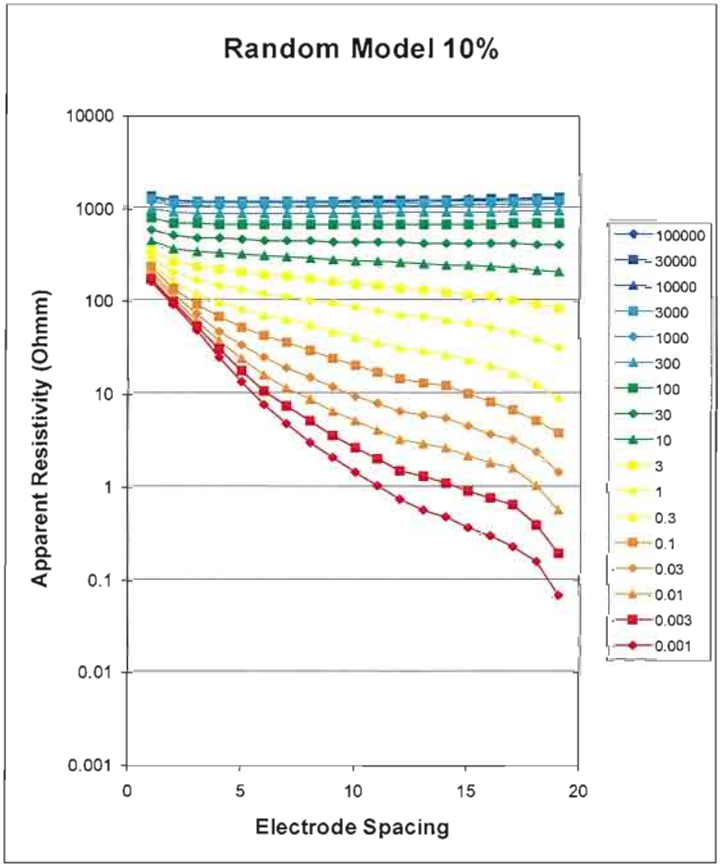

Figure 8.10. Geometric mean of apparent resistivity versus electrode spacing for 10% random cell models, with variable conductive cell resistivity. Graphs are colour coded according to the resistivity of the conductive cells. Background resistivity of model is 1000 Ωm.

8.3.2. Vein models

Three dimensional vein models were developed to simulate veins or irregular conductive layers which are frequent in mineralised environments. They may be either more or less resistive than the material through which they pass, thus may either provide direct pathways for electrical conduction, or impede electrical conduction. Thus, it is important to understand their influence on apparent resistivity at various scales. Vein models were generated as shown in Figure 8.11. The vein geometry is actually 2.5 dimensional, since each vein extends throughout the length of model in the z direction.

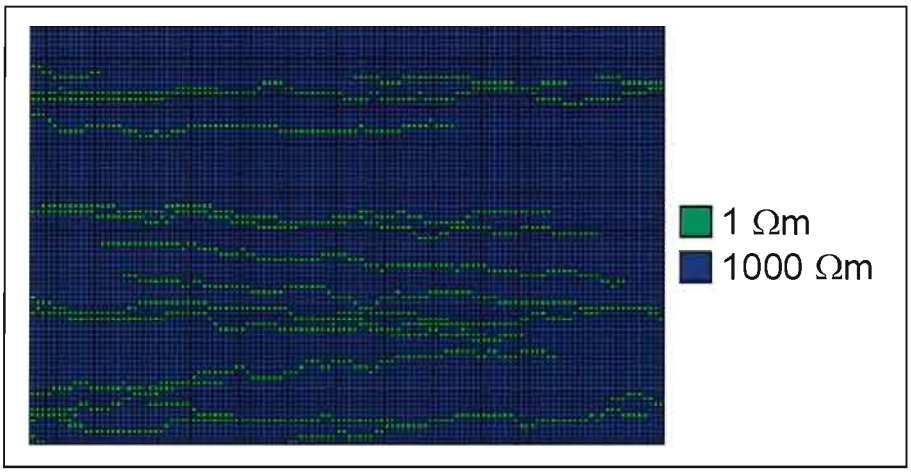

Figure 8.11. Top surface view of vein cell model consisting of 12.7% proportion of conductive cells within resistive background (120 x 80 cells).

Apparent resistivity maps for different electrode spacing measurements for both x and y directions of a 12.7% vein model are shown in Figure 8.12. The conductive vein cells were set to 1 Ωm in a 1000 Ωm background. The apparent resistivity maps clearly show significant scale variation and marked anisotropy, with the average resistivity measured in the x direction (sub-parallel to the veins) significantly higher than in the y direction. This model result is in agreement with the predictions of the "paradox of anisotropy" previously described in Section 3.2.5 and observations from the McArthur River case study (Chapter 6), where the measured minimum resistivity is observed perpendicular to the rock fabric.

Two-dimensional histograms of log-transformed data for all x and y measurements for the 12.7% vein model are shown in Figure 8.13. The apparent resistivity of the model for both measurement directions exhibits a bimodal distribution for small electrode spacings (up to 5 units). This distribution clearly shows the two components in the model at small scales. The distribution becomes unimodal at larger electrode spacings, due to increasing connectivity of conductive paths. At small scales in the x direction, sub-parallel to the vein network, the apparent resistivity populations, reflecting the end members of the model, lie significantly higher and lower (over an order of magnitude) than the bulk apparent resistivity recorded at the largest electrode spacing. For small scale measurements in the y direction, one of the resistivity populations lies close to the bulk value and the second population is two orders of magnitude higher.

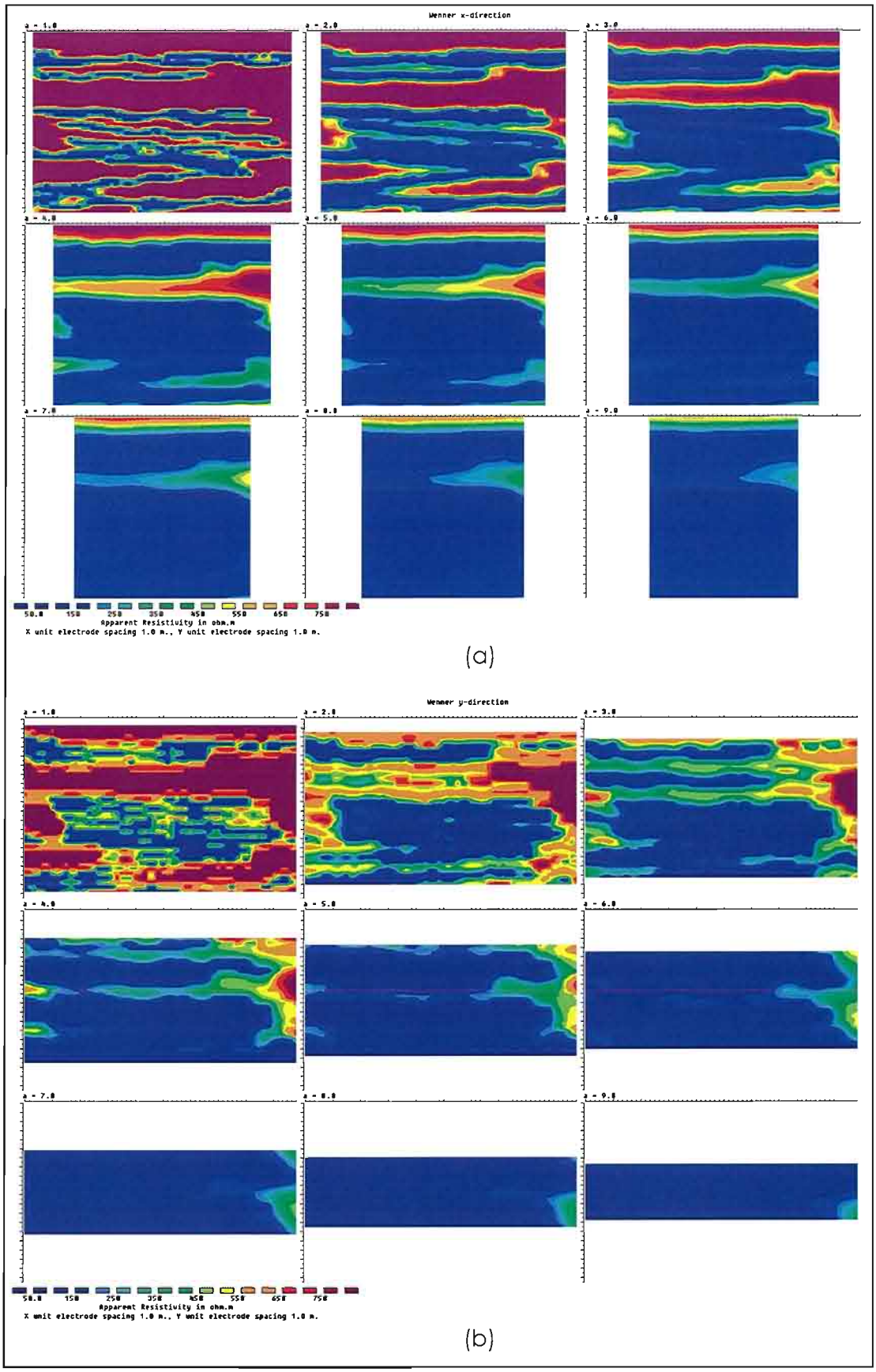

Figure 8.12. Apparent resistivity surface maps for different electrode spacings (Wenner measurements) for a vein cell model containing 12.7% conductive cells (1 Ωm cells in 1000 Ωm background) (a) x-direction (b) y-direction. The same linear colour scheme has been applied to all resistivity maps. It is clear that apparent resistivity decreases with increasing electrode spacing, indicating greater connectivity between grains at larger scales for both directions.

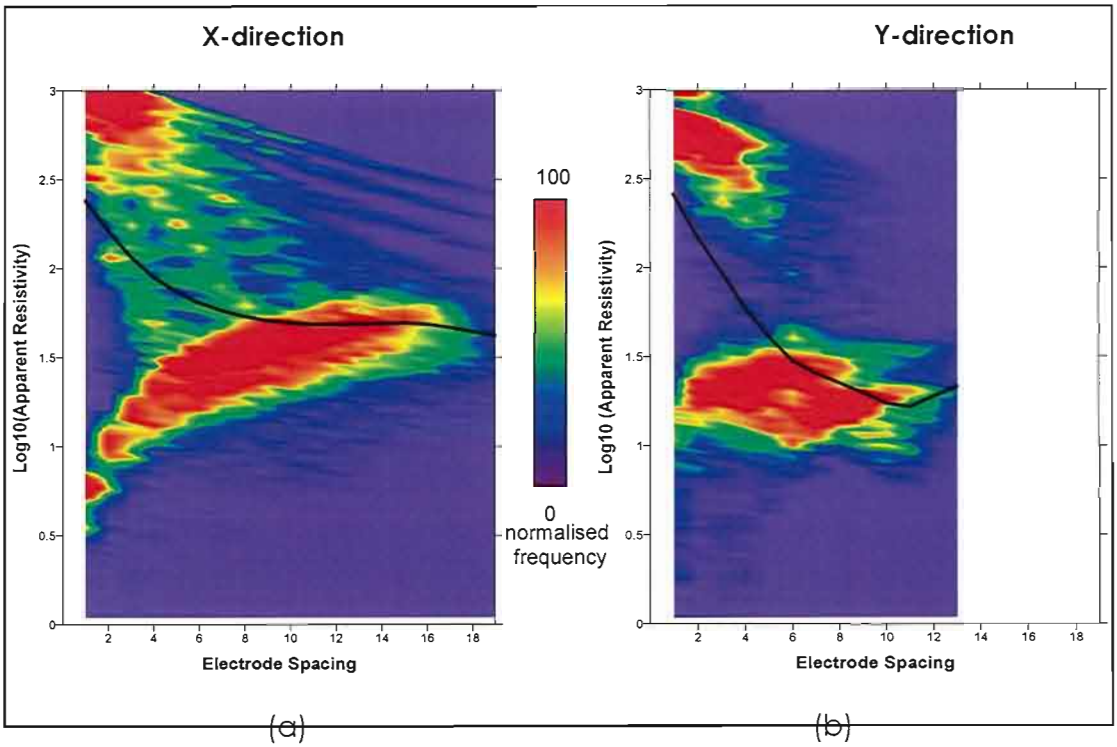

Figure 8.13. Two-dimensional histogram of calculated LOG apparent resistivity for measurements in the (a) x-direction and (b) y-direction for a 12.7% vein cell model (1 Ωm cells in 1000 Ωm background). The black line indicates the geometric mean of apparent resistivity. A bimodal distribution is clearly observed in both datasets. Both plots clearly show a decrease in "average" apparent resistivity with increasing electrode spacing from 0 to 8 units.

For irregular or bimodal distributions of apparent resistivity that span large ranges, such as calculated at small electrode spacings, it is difficult to characterise an "average" value. In these cases, each measure of central tendency such as arithmetic mean, median and geometric mean has significant limitations. The "average value" determined in all these cases will lie between the modal peaks. The geometric mean was selected to characterise the "average" apparent resistivity observed in the measurements. The geometric mean for the x and y data (Figure 8.13) show a decrease in apparent resistivity of 1 to 1.5 orders of magnitude over the range of measurements (18 and 12 units respectively).

8.3.2.1. Vein cell model: Variable proportions

The effects of variable proportions of veins on calculated resistivity were assessed by creating of a series of vein models. An initial model of 5.7% by volume of 0.1 Ωm vein material in a 1000 Ωm background was created. Other models (12.7, 17.5 and 22%) were created by continuation of pre-existing veins and creation of new vein seed cells in the models. Thus, the geometry of the vein network remains consistent for the different models, to simplify interpretation of results. The structure of the vein set results in significant anisotropy between the x and y directional measurements.

The mean apparent resistivity calculated from models with different proportions of vein cells is shown in Figure 8.14. The scale variation is more pronounced in the y direction measurements, orientated perpendicular to the vein network. For the 5.7% vein model the x direction apparent resistivity decreases monotonically for all electrode spacings. However, for higher

proportions of vein material, the scale variation is only pronounced for electrode spacings less than 10 units. The maximum scale variation observed for x-direction measurements is approximately one order of magnitude. For y-direction measurements, all proportions exhibit a similar pattern of apparent resistivity scale variation, decreasing monotonically for all electrode spacings. The scale variation observed for y direction measurements is over two orders of magnitude.

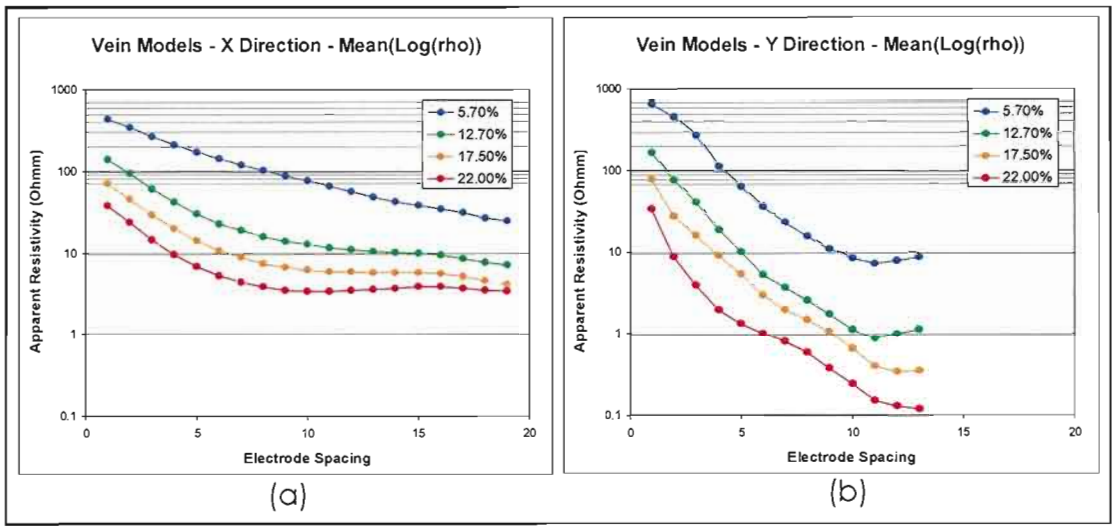

Figure 8.14. Geometric mean of apparent resistivity versus electrode spacing for varying proportions of vein material. The vein resistivity was 0.1 Ωm in a background of 1000 Ωm for all models. (a) x-direction data (sub-parallel to veins) (b) y-direction data (perpendicular to veins).

8.3.2.2. Vein cell model: Variable contrast

A 12.7% vein cell model was selected to examine the effect of varying the resistivity contrast between conductive and resistive cells. The distribution of conductive cells was fixed, with the background model resistivity set at 1000 Ωm, and the apparent resistivity of the conductive cells varied between 0.001 Ωm and 100 000 Ωm.

The geometric mean of apparent resistivity versus electrode spacing for the various models is shown in Figure 8.15. The degree of scale variation increases significantly for both x and y direction measurements, as the resistivity contrast between background and the conductive cells increases. In this case, highly resistive veins appear to have little influence on the bulk resistivity of the model, and show little or no scale variation. However highly conductive veins significantly contribute to the bulk response and exhibit a wider range of scale variation (up to 4 orders of magnitude for 0.003 Ωm veins). These effects are more pronounced for y directional measurements, orientated perpendicular to the vein network.

8.3.2.3. Vein cell model: Anisotropy

To assess the relationship between anisotropy and scale variations, the ratio of geometric mean apparent resistivity from the x and y-directional measurements was calculated for all electrode spacings for 12.7% vein models with different vein resistivity. The anisotropy data are presented as coloured contours of the log transformed ratio in log (vein resistivity) versus electrode spacing space (Figure 8.16). Anisotropy varies as a function of both scale of measurement, and resistivity contrast between components.

The electrical anisotropy is most significant for conductive veins at large spacings. The maximum anisotropy ratio for this model (y-direction resistivity: x-direction resistivity) is 260.

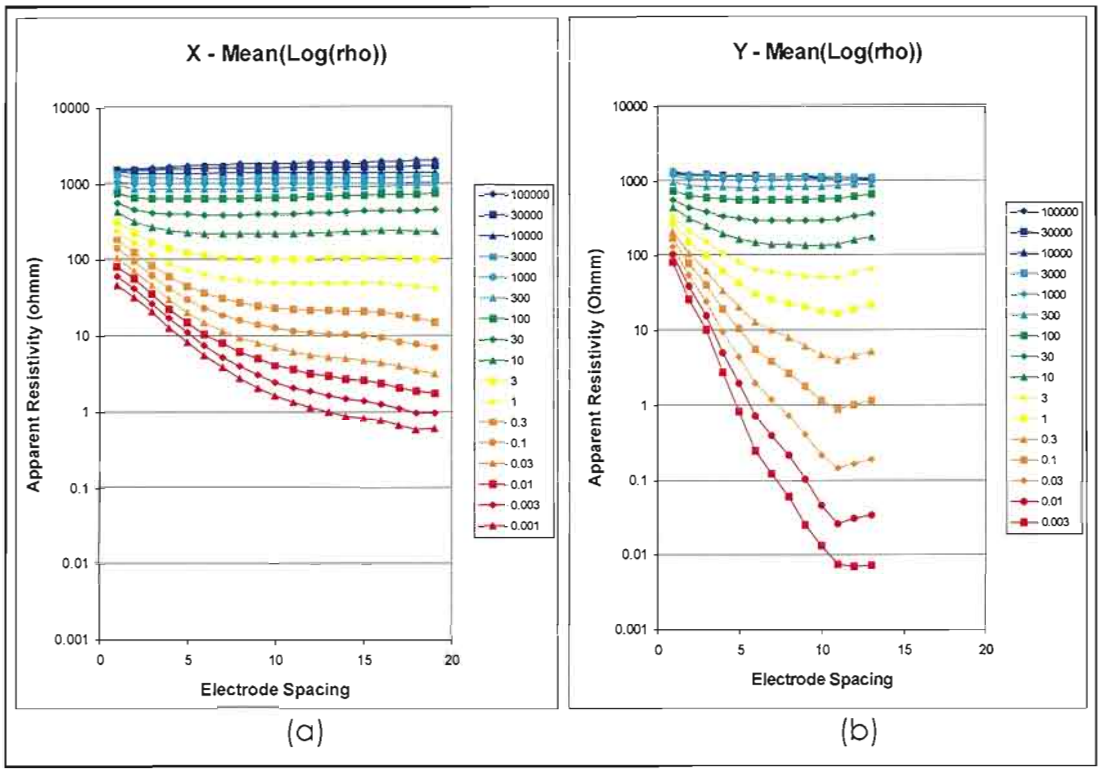

Figure 8.15 Geometric mean of apparent resistivity versus electrode spacing for 12.7% vein cell models, with variable resistivity of conductive cells. Graphs are colour coded according to the resistivity of the conductive cells. (a) x-direction data (sub-parallel to veins) (b) y-direction data (perpendicular to veins).

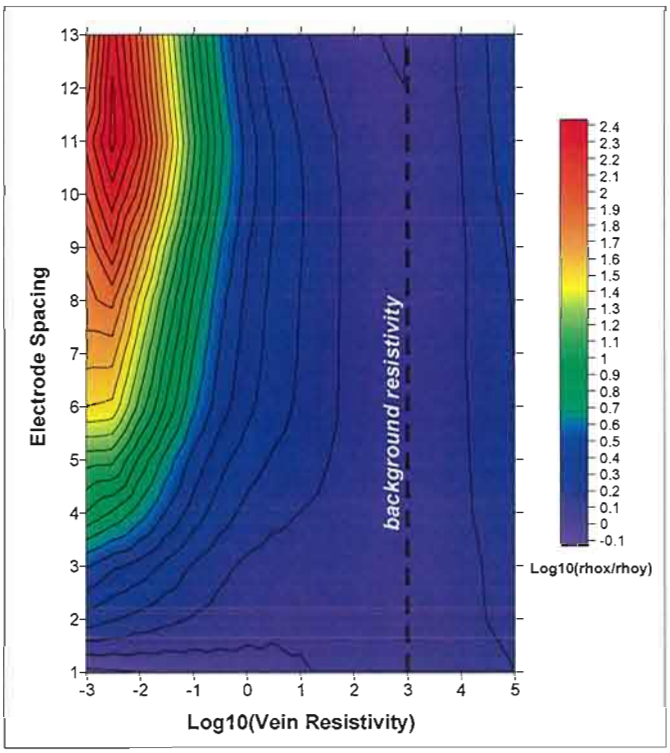

Figure 8.16. Anisotropy of surface apparent resistivity from the numerical models of 12.7% vein model with variable vein resistivity (in 1000 Ωm background). Resistivity anisotropy is expressed as the log to base 10 of the ratio of the geometric mean of the x and y direction measurements, for variations in both vein resistivity and electrode spacing.

8.4. Summary

Apparent resistivity calculated on the surface of 3D synthetic random and vein cellular models showed very similar patterns of scale variations to those that were observed insitu (Chapters 5, 6 and 7). Apparent resistivity decreases with increasing scale of investigation even for synthetic models incorporating a random distribution of conductive cells in a resistive matrix.

The detailed nature and magnitude of the scale variation was found to be dependent on a complex interaction of several variables. The results from both the random cell and vein models show that the resistivity contrast between the conductive and resistive components has the greatest influence on scale variations; with the magnitude of scale variation becoming more pronounced as the resistivity contrast between the two components increases. Small proportions of cells more resistive than the background appear to have little effect on scale variations.

The proportion of the conductive component also influences the scale behaviour. The scale variation initially increases as the proportion of the conductive phase increases in the model but then decreases when the system can be considered as irregular resistive zones in a conductive matrix. For a random cellular model, the scale variation is most pronounced for models containing moderate proportions of conductive cells (between 7 and 15%).

Texture has a major influence on the scale behaviour, with vein-like models showing more dramatic scale variations than random cellular models and also significant anisotropy.

Although only two types of synthetic models are described here, these models can be used to simulate a wide range of different ore textures. A random cellular model comprising small proportions of conductive sulphides (1-2%) simulates the disseminated sulphide ore at North Parkes. A veinlike (20-30%) model would simulate the layered ore texture observed at McArthur River. Scuddles ore samples would be simulated using a combination of vein like models or random cell models with large proportions of conductive cells (eg: 50% by volume conductive cells).

Despite the evident complexity of the scale relationships observed in the field, the numerical modelling has provided a better insight into the nature of these processes. The model results provide a qualitative indication of the geological environments in which scale variation will be most pronounced.

Chapter 9
Summary and Conclusions

9.1. Introduction

The electrical properties for a diverse range of sulphide ore deposits were investigated over a range of scales using electrical galvanic techniques. The three deposits examined consist of the Scuddles Cu-Pb-Zn orebody, McArthur River Pb-Zn orebody and North Parkes Cu-Au orebody.

9.2. Methodology

A methodology was developed to systematically measure the scale of electrical properties using insitu and laboratory techniques.

Conventional galvanic resistivity and chargeability soundings were completed insitu from centimetre to metre scales at various site exposures, using a Wenner array configuration. For large spaced measurements, electrodes consisted of 6.5mm Ni-plate masonry anchors (dynabolts) inserted into shallow holes drilled at each site. The contact resistance between the electrodes and rock surface was reduced using medical electrically conductive (MES Gel). For small scale measurements, a mobile multi-electrode array was developed. The array consisted of a number of spring loaded sponge-rubber electrodes, slotted in a wooden frame, which provided a good contact with the site exposure (0.11, 0.22, and 0.33 m electrode spacing). The mobile electrode array was used to collect small scale measurements, as well as map lateral variations and to measure electrical anisotropy.

A Scintrex IPR-12 receiver and IPC-9 transmitter were used for all measurements, which were completed at very low frequency (4 second on time). No problems were experienced with electrical interference from mining power infrastructure or communications. Difficulties were only encountered in highly conductive sites, where the receiver failed to synchronise with the low input signal. This is an inherent problem in the IPR-12 which relies on software synchronisation. A direct transmitter-receiver synchronisation would be more appropriate in such conductive environments.

Large samples, many which were orientated were collected and prepared for laboratory measurements by cutting into prisms. Galvanic laboratory measurements were mostly completed with a modified standard four-electrode method, with electrodes designed to make an electrolytic contact with opposing faces of a saturated prismatic sample. For highly conductive samples, a two electrode system consisting of burnished lead electrodes clamped to the sample surface was utilised. Most laboratory measurements were completed with the same instrumentation used for insitu measurements to enable direct comparison. Difficulties were encountered only with extremely conductive samples where receiver synchronisation failed, and for the most resistive samples, as the receiver's input impedance

was insufficient. In these cases measurements were completed using other standard laboratory electronic equipment.

Laboratory measurements were completed at low current densities, equivalent to those used for insitu measurements. It was found for higher current densities, resistivity measurements remained fairly consistent, whereas time domain chargeability measurements were highly sensitive to current variations. All measurements were completed with the minimum current levels required to record a clear decay without the effects of noise.

Continuity and current mapping methods are new laboratory methods that map the continuity and current flow on the surface of a thin flat specimen, using a modified flat-bed plotter. Continuity and current mapping was effective for studying the influence of ore textures on the electrical continuity of and current flow within sulphide ore samples. Continuity and current mapping have been instrumental in highlighting the extremely important contribution that well-connected highly conductive phases make to the overall electrical conductivity even when these phases are present in very small proportions.

9.3. Empirical Results

The major result from this empirical study was the observation of a consistent pattern of scale variation in resistivity occurring at all three deposits. In almost all cases, insitu apparent resistivity is observed to decrease with an increase in scale of investigation for each field site. The detailed results of the three deposits were presented as a series of case studies, outlined in the following summary.

The Scuddles deposit provided an excellent study site, allowing access to a wide range of ore styles and textures. Scale variability was most pronounced in the Scuddles deposit with some sites exhibiting differences in apparent resistivity of over three orders of magnitude between measurements collected at electrode spacings between 0.11 and 2 metres. For several sites, laboratory and small scale insitu measurements exhibit bimodal distributions. The two populations reflect the most resistive and conductive mineral end-members from the site. Sphalerite-rich portions of the deposit were unexpectedly found to display dramatic scale variations and to be quite conductive at large scales. Current mapping and petrographic analyses suggests that this can largely be attributed to the presence of a fine anastomosing network of pyrrhotite veinlets.

The McArthur River deposit provided access to varying grades of laminated lead-zinc ore. Scale variations observed in the insitu and laboratory data are systematic, but are smaller in amplitude than observed at Scuddles. This is inferred to reflect a lower contrast between the resistivities of the mineral constituents of the ore (sphalerite, shale and pyrite). The variable nature of the McArthur River orebodies allowed relationships between detailed ore mineralogy, texture and electrical properties to be investigated. The finely banded nature of the ore resulted in significant and consistent resistivity anisotropy.

The North Parkes deposit provided an example of a low grade sulphide deposit consisting of mineralised monzonite porphyry (less than 1.5% Cu). Data acquisition was limited at North Parkes as access was only possible with the E27 open cut pit. Despite this limitation the majority of the data acquired clearly shows a relatively consistent pattern of decreasing apparent resistivity with increasing electrode spacing, although the amplitude of the scale variation was typically limited to within one order of magnitude. The trends observed at North Parkes are mostly weakly displayed but this is expected since North Parkes ore contains only a very small proportion of widely disseminated sulphides and thin discontinuous sulphide veins. Geochemical analysis indicated that the primary control on scale variation may possibly be the degree of pervasive silicate alteration rather than variations in the sulphide content.

In all three case studies, scale variations are observed in insitu electrical resistivity for a range of measurements (Examples are shown in Figure 9.1). In some cases variations of up to several orders of magnitude are observed. The degree of scale variation differs from site to site, associated with variations in ore composition, texture and mineralogy.

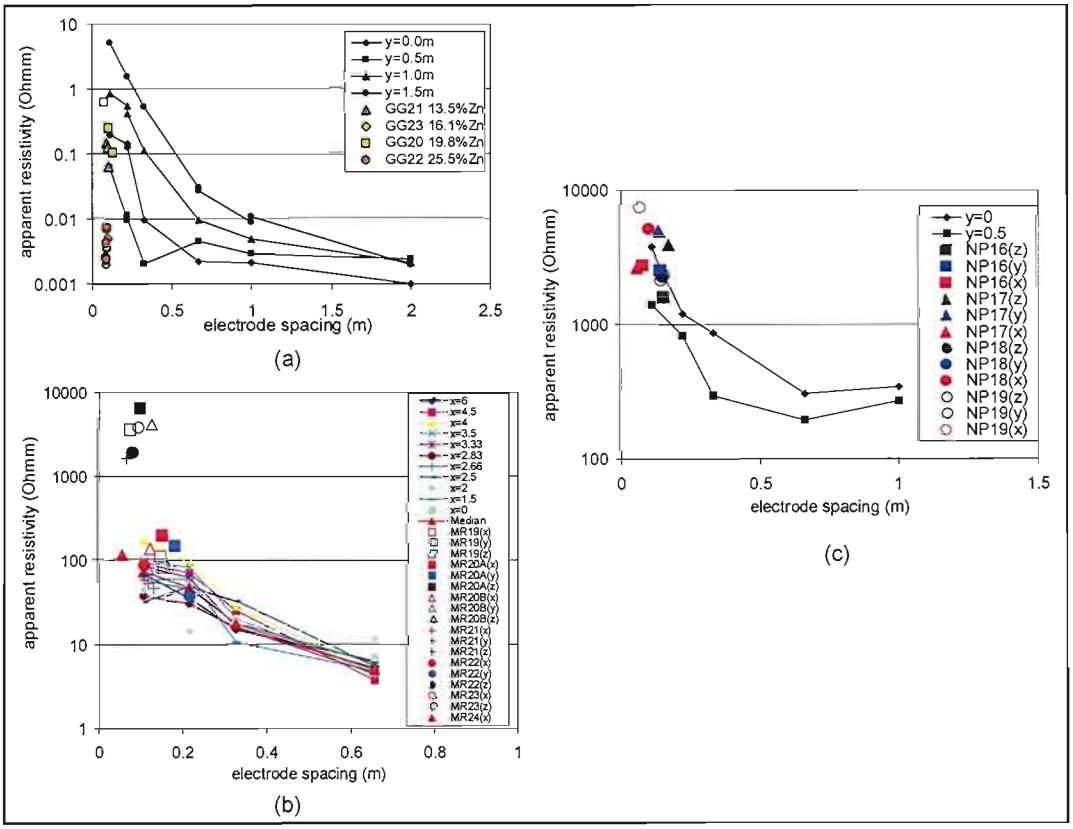

Figure 9.1. Examples of scale variations observed in apparent resistivity for sites from the three deposits. Insitu measurements are represented by the profiles, sample measurements are represented by point symbols. All sites show a decrease in apparent resistivity with increasing size of investigation for (a) Scuddles: Site 6, (b) McArthur River: Site 4, and (c) North Parkes: Site 6.

Despite the consistent pattern of decreasing apparent resistivity with increasing scale observed in the field data, no simple scaling rules could be systematically applied to all the data to enable prediction of the bulk response from small-scale insitu measurements.

Laboratory sample measurements were conducted for each measurement site to determine if laboratory data could be used to predict the bulk insitu

apparent resistivity. In many cases, sample resistivity displays a unimodal distribution, and values typically lie close to the smallest scale insitu measurements. Many of the samples from McArthur River and North Parkes displayed unimodal distributions plotting on the projection of the insitu apparent resistivity trend at small scales. In these cases, where no additional information is available to predict scaling behaviour, the bulk insitu resistivity cannot be easily predicted and all that can be inferred is that the bulk value is likely to be less than the mean of the laboratory samples.

In other cases laboratory sample resistivity exhibits a bimodal distribution, reflecting resistive and conductive end members (eg: Figure 9.1.a and 9.1.c). The bimodal distribution of resistivity in samples suggests the rock mass can be considered as a two-component system (conductive and resistive components) for which the volume percentages and distribution of the conductive component largely control the overall resistivity. The resistive specimens in this case have values that usually lie close to those of the small scale insitu measurements. For all sites at the three deposits studied, the best estimate of bulk apparent resistivity of the rock mass from laboratory samples would be provided by assuming the minimum laboratory resistivity, rather than a statistical measure such as the arithmetic mean, geometric mean or median. This empirical rule is applicable both for sites that display unimodal or bimodal distributions.

Insitu chargeability for sites at all three deposits appeared to show no significant systematic variation with scale of measurement. Laboratory chargeability measurements of samples typically lay close to the values observed insitu for all sites and deposits.

9.4. Numerical Modelling

The empirical observations from field measurements are supported by the results of numerical modelling of a number of synthetic models that simulate a variety of ore textures. These cellular models consist of two phases of contrasting resistivity, populating the entire model.

Apparent resistivity calculated on the surface of the three-dimensional random cell and veinlike models show generally similar patterns of scale variation to that recorded by insitu field measurements. The connectivity of the model increases with increasing electrode spacing, thus decreasing apparent resistivity. Even for a model containing random distribution of conductive cells significant scale variations were apparent.

The degree of scale variation in the synthetic models is primarily controlled by the resistivity contrast between conductive and resistive components, the texture (or geometry of the model) and proportion of sulphide (conductive component). The complex interaction of these variables inhibits the use of a simple equation to predict apparent resistivity for various scales. However, qualitative consideration of these factors can identify those geological environments susceptible to significant scale effects.

In particular:

- Scale variation becomes more significant as the resistivity contrast between conductive and resistive components increases. Small

proportions of components more resistive than the background appear to have little effect.

- For a disseminated sulphide (random cell) model the scale variation initially increases as the proportion of the conductive phase increases in the model but then decreases when the system can be considered as irregular resistive zones in a conductive matrix. For a random cellular model, the scale variation is most pronounced for models containing moderate proportions of conductive cells (between 7 and 15%).
- Scale variation is strongly affected by the geometry of the conductive phases, but the details of the relationship are complex. Modelling suggests that any departure from a random cell model will tend to increase the scale variation observed in the model, as observed when comparing vein models to random cell models.

The resistivity derived from numerical modelling of the synthetic textures, showed that the scale variation is confined over a particular range of scales. This range varies depending on the type and properties of the model. Apparent resistivity becomes constant at greater scales than the correlation length of the conducting system.

9.5. Comparisons with hydraulic parameters

Scale dependence is not only observed in electrical geophysical properties, but is also significant in studies of hydrological physical properties. Scale variations in hydraulic conductivity, permeability, transitivity, dispersivity and specific storativity have been documented since the 1970's (Dagan, 1986) showing inconsistencies between laboratory and field-scale measurements (Figure 9.2). A number of studies (Table 9.1) have shown scale dependent behaviour of hydraulic properties with values varying by up to five to six orders of magnitude from sub-metre to kilometre size measurements. Although some authors argued that the difference in scale may be attributed to the difference in measuring methods, Schulze-Makuch and Cherkauer (1995) demonstrated similar scale behaviour was evident using only pump tests for various volumes of an aquifer. Thus, their study suggests scale variations in hydraulic properties are real, and are independent of the measuring method.

Investigation	Property	Scale of investigation	magnitude of variation
Gelhar et al. (1992)	Dispersivity	1 to 100 000 metres	5 – 6 times
Neuman (1994)	Permeability	0.1 to 100 00 metres	3 – 6 times
Whitaker and Smart (2000)	Hydraulic conductivity	0.1 to 100 000 metres	4 – 5 times
(Schulze-Makuch and Cherkauer, 1995)	Hydraulic conductivity	0.02 to 1000 metres	3-4 times

Table 9.1. Scale variations observed in various studies of hydraulic properties by numerous authors.

Despite the clear scale variation observed in hydrologic parameters it is difficult to apply simple predictive rules to calculate bulk properties from small scale and laboratory methods (Gelhar et al.,1992; Neuman, 1994). This is largely attributed to the wide range of values measured at any one scale. Theoretical and geostatistical models can be applied to empirical data, but

local variations can not be predicted due to spatial variability of the geological unit or facies.

The scale dependence of hydraulic properties has not simply been shown from field and laboratory measurements, but has been verified by numerical modelling. For example, Khaleel (1989) developed numerical models to simulate fluid flow in fractured basalts for both regular and irregular joint patterns with lognormal aperture distributions. He calculated hydraulic conductivities in two principle directions and plotted these as a function of measurement scale (Figure 9.2). Both models showed hydraulic conductivity to increase rapidly before asymptotically approaching a maximum value, as observation scale increases (Khaleel, 1989).

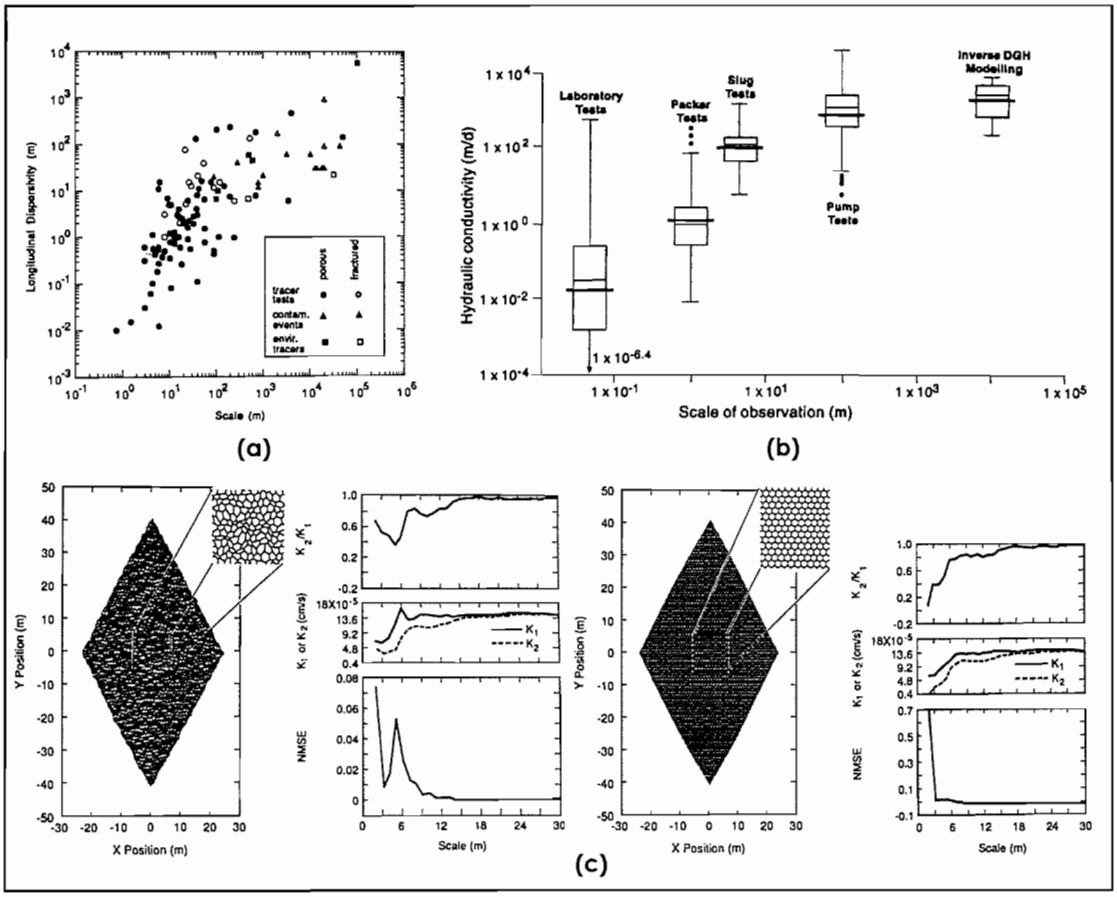

Figure 9.2. Examples of scale variations observed in hydraulic parameters. (a) Longitudinal dispersitivity versus scale of observation for both porous and fracture aquifers. Data is from 59 sites in widely varying geological environments (from Gelhar et al., 1992), (b) Hydraulic conductivity versus scale of observation for Pleistocene carbonate aquifers in the Bahamas (from Whitaker and Smart, 2000). (c) Irregular and regular hexagonal fracture network used to simulate fluid flow in jointed basalt together with simulation results. K1 and K2 are the principal hydraulic conductivities. NMSE is the Normalised Mean Squared Error between the fitted data and numerical results (from Khaleel, 1989).

The empirical and numerical results from this study show that electrical resistivity displays similar scale variability to that as exhibited by hydraulic properties, with variations of up to several orders of magnitude possible for a range of measurements from centimetre to metre scale. As with the numerous hydraulic studies, it is difficult to apply simple generic scaling rules due to the complexity of the system.

9.6. Implications for Exploration

This study was initially motivated by the common observation of marked discrepancies between the apparent resistivity measured on samples and drill cores, and the values inferred from modelling or inversion of field scale electrical and/or electromagnetic datasets. Although the scaling properties of hydraulic properties are extensively reported in the literature, there has been little or no systematic study of scale variant electrical phenomena in sulphide-bearing rocks. This study has addressed this deficiency by completing a comprehensive empirical study of the insitu and laboratory properties in a diverse range of sulphide ore deposits. In addition, numerical modelling of a range of ore textures support the scale variations observed in field data.

The most significant single result from this empirical study is the observation that insitu apparent resistivity decreases with increasing scale of investigation for almost all measurement sites in a wide range of geological settings and for a diverse range of ore deposits. In many cases, laboratory samples lie close to the values determined insitu at small electrode spacings, but in some cases they display a bimodal distribution with the resistive end-member lying close to the small scale insitu measurements and the conductive end member approximating the bulk rock resistivity.

This observation is related to the scale of connectivity of conductive grains or vein networks throughout the rock. Laboratory samples may significantly over-estimate the bulk insitu apparent resistivity if they do not contain representative examples of the conductive pathways. In the case where the distribution of sample resistivity is unimodal and there is no additional information that may assist in determining the extent of the scale variation, than all that can be concluded about the material is that its insitu bulk resistivity is always less than the mean of the laboratory measurements and in almost all cases less than the minimum value. There is no simple means to accurately predict the scale of the variation, or the bulk resistivity from the laboratory data.

Bimodal distributions in laboratory sample resistivity indicate both conductive and resistive end members have been adequately sampled. In this case the best estimate of the bulk resistivity can be estimated from the average (and often the minimum value) of the conductive population. This approach originally based upon the results of empirical measurements is supported by the results of the numerical modelling.

The field results and numerical modelling show that scale variation of resistivity is a complex function of the proportion and distribution (texture) of a conductive element within a resistive medium and the resistivity contrast between components. Scale variability may arise due to the effects of very minor but well connected highly conductive constituents of the rock mass. At large scales, the conductive element becomes better connected, thus lowering the bulk resistivity. The magnitude of the scale variability depends on the complex interaction of these controlling variables.

Estimation of bulk rock resistivity directly from laboratory data is extremely unreliable and estimates may be in error by several orders of magnitude. A very large number of laboratory measurements may be required to

adequately characterise the conductive component of the system that predominantly controls the bulk properties. This study recommends that insitu measurements are preferable than sample measurements in estimating bulk resistivity. Resistivity data, acquired using downhole tools provides a more reliable measure of the bulk properties than laboratory measurements since these tools sample a much larger volume of the rock mass, but in many cases downhole measurements may still systematically overestimate the bulk rock resistivity.

Although this study has concentrated on scaling of electrical properties in sulphide rocks where there are pronounced contrast in the resistivities of the ore and gangue minerals, it is likely that scale variability also affects unmineralised rocks in which there are several constituents with contrasting resistivity. In the case of engineering and environmental geophysics typical ground would consist of two-component (sand and water) or three-component (sand, clay and water) systems. From the numerical modelling results, it is speculated that in instances where there is a considerable resistivity contrast between these components that significant scaling may occur. For example, in the case of conductive pore-waters hosted in a resistive matrix, scaling is expected to occur, but most likely will happen over a very small distance related to the dimensions of the pore network. However in the case of clay materials interconnecting through sands, electrical scaling effects may be similar to the observations for sulphide mineralisation in this study. The numerical modelling showed even small proportions of disseminated conductive particles could result in scaled behaviour; so even clays dispersed through sands may produce scaling effects. A more significant scenario is likely to occur in fractured rock aquifer systems, where scaling effects are likely to be more pronounced from centimetre to metre scale.

The observation of scale-dependent resistivity also has significant implications for inversion and interpretation of electrical geophysical data. The apparent resistivity recorded in an isotropic material comprised of both resistive and conductive constituents will in almost all cases decrease with increasing electrode spacing. In a standard electrical pseudosection the upper levels will thus likely display higher resistivity values. Subsequent inversion of these data will then result in a geoelectrical section which appears to have a layered structure with resistive upper layers and more conductive lower layers even though the material sampled is effectively isotropic. Given the scales of the geoelectrical textures that may influence the scale variability, this effect is likely to be most noticeable in shallow geoelectrical measurements for engineering or environmental projects.

Although this thesis demonstrated that the majority of measurements from centimetre to metre scale showed strong scale-dependence in electrical resistivity it is important to speculate as to what scale-lengths the scale-dependence is important. For some systems the scale dependence is likely to occur over small scales; for example for low grade disseminated mineralisation or conductive pore fluids in a sandstone, the scale dependence is likely to be over short distances only several more times greater than the size of the conductive grain size or pore dimensions. There were some examples from North Parkes where the minimum resistivity occurred at intermediate spacings (at 0.66m), suggesting that this was the threshold where the maximum number of electrical connections occurred. In

addition, for most sites at each deposit studied there was a tendency for the degree of scale variability to decrease at the larger electrode spacings, suggesting little scale variability may occur at larger scales. There is the possibility at larger scales, the conductive networks may become isolated, thus increasing the bulk resistivity, however it is likely that in reality saturated large scale fractures are more likely to aid in electrical connection at large measurement lengths. Regardless of the scale lengths the study demonstrated that larger scale insitu measurements were preferable to laboratory measurements of samples.

This study has demonstrated that the apparent resistivity of sulphide ores exhibit marked scale dependent variations which can be described using binary mixture models comprising of conductive and resistive phases. The results highlight the importance of understanding the key geological factors that influence electrical petrophysical measurements and provide a cautionary note for practitioners who attempt to estimate bulk properties from laboratory petrophysical measurements.

References

Alvaraz, R., 1973, Complex dielectric permittivity in rocks: a method for its measurement and analysis: Geophysics, **38**, 1769-1779.

Anderson, L. A., 1960, Electrical properties of sulphide ores in igneous and metamorphic rocks near East Union, Maine: Short Papers in the Geological Sciences, Paper 400B, 125-128.

Angoran, Y., and Madden, T., 1977, Induced polarisation: A preliminary study of its chemical basis: Geophysics, **42**, 788-803.

Appararo, A., Sivarama Sastry, R., and Subrahmanya Sarma, V., 1994, Spectral IP studies on buried scale models incorporating surface and volume polarisation: Exploration Geophysics, **25**, 31-37.

Banisi, S., Finch, J. A., and Laplante, A. R., 1993, Electrical conductivity of dispersions: A review: Minerals Engineering, **6**, 369-385

Berryman, J. G., 1995, Mixture theories for rock properties, rock physics and phase relations, *in* Ahrens, T. J., Ed., AGU Handbook of Physical Constants: American Geophysical Union, 205-228.

Bhattacharya, B. B., and Sen, M. K., 1981, Depth of investigation of collinear electrode arrays over homogeneous anisotropic half-space in direct current methods: Geophysics, **46**, 768-780.

Bhattacharyya, B. K., and Morrison, H. F., 1963, Some theoretical aspects of electrode polarisation in rocks: Geophysical Prospecting **11, 176-191.**

Bishop, J. R., and Emerson, D. W., 1999, Geophysical properties of zinc-bearing deposits: Australian Journal of Earth Sciences, **46**, 311-128.

Bleil, D. F., 1953, Induced polarisation: A method of geophysical prospecting: Geophysics, **18**, 636-661.

Boyd G., and Francombe, K. F., 1994, Geophysical response over the Scuddles VMS deposit, *in* Dentith M. C., Eds., Geophysical signatures of Western Australian mineral deposits: ASEG Special Publication No.7.

Brace, W. F., Orange, A. S., and Madden, T. R., 1965, The effect of pressure on electrical resistivity of water-saturate crystalline rocks: Journal of Geophysical Research, **70**. 5669-5678.

Bussian, A.E., 1983, Electrical conductance in a porous medium: Geophysics **48**, 1258-1268.

Chelidze, T. L. Gueguen, Y., and Ruffet, C., 1999, Electrical spectroscopy of porous rocks: a review-II. Experimental results and interpretation: Geophysical Journal International, **137**, 16-34.

Christensen, N. B., 2000, Difficulties in determining electrical anisotropy in subsurface investigations: Geophysical Prospecting, **48**, 1-19.

Clark, D. A., Emerson, D. W., and Kerr, T. L., 1988, The use of electrical conductivity and magnetic susceptibility tensors in rock fabric studies, Australian Society of Exploration Geophysicists Conference, Adelaide, 244-248.

Clennell, M. B., 1997, Tortuosity, *in* Lovell, M. A., and Harvey, P. K., Eds., Developments in Petrophysics: Geological Society Special Publication, No. 122, 299-344.

Clifford, B. A., 1992, Facies and palaeoenvironment analysis of the Archaean volcanic-sedimentary succession hosting of the Golden Grove Cu-Zn massive sulphide deposits, Western Australia, Unpublished PhD Dissertation, Monash University.

Collett, L. S., 1959, Laboratory investigation of overvoltage- chapter 5, *in* Wait, J. R., Ed., Overvoltage Research and Geophysical Applications: Permagon Press, 50-83.

Collett, L. S., and Katsube, T. J., 1973, Electrical parameters of rocks in developing geophysical techniques: Geophysics, **38**, 76.

Dagan G., 1986, Statistical theory of groundwater flow and transport: pore to laboratory, laboratory to formation and formation to regional scale: Water Resources Research, **22**, 120-134.

DaRocha, B. R. P., and Habashy, T. M., 1997, Fractal geometry, porosity and complex resistivity: from rough pore interfaces to hand specimens, *in* Lovell, M. A., and Harvey, P.K., Eds., Developments in Petrophysics: Geological Society Special Publication, No. 122, 277-286.

de Kuijper, A., Sandor, R. K. J., Hofman, J. P., and de Waal, J. A., 1996, Conductivity of two-component systems: Geophysics, **61**, 162-168.

DeLima, O. A. L., and Sharma, M. M., 1990, A generalised Maxwell-Wagner theory for membrane polarisation in shaly sands: Geophysics, **57**, 431-440.

deWitt, G. W., 1979, Parameter studies of induced polarisation spectra. MSc. Dissertation, University of Utah, Salt Lake City.

Dias, C. A., 1972, Analytical model for a polarisable medium at radio and lower frequencies: Journal of Geophysical Research, **77**, 4945-4956.

Dias, C. A., 2000, Developments in a model to describe low-frequency electrical polarisation of rocks: Geophysics, **65**, 437-451.

Duckworth, K., and Calvert, H. T., 1995, An examination of the relationship between time-domain integral chargeability and the Cole-Cole impedance model (short note): Geophysics, **60**, 1249-1252.

Duggan M. B., Lyons P., Raymond O. L., Wallace D. A., Wyborn D., Young G. C., Krynen J. P., Scott M. M. and Sherwin L., 1999, Forbes Geology – Sheet S155-7: Australian Geological Survey Organisation.

Emerson, D. W., 1969, Laboratory electrical resistivity measurements of rocks: Proceedings of Australian Institute of Minerals and Metallurgy, No.230.

Emerson, D. W., and Smith, M. J., 1969, A Laboratory study of the induced polarisation response of some New South Wales sulphide ores: Proceedings of Australian Institute of Minerals and Metallurgy, No.230.

Emerson, D. W., and Yang Y. P., 1998, Physical properties of fractured rock-bulk resistivity: Preview, **77**, 26-27.

Emerson, D. W., 2001., The conductivities of komatiitic nickel ores are Kambalda, W.A.: Preview, **77**.

Fraser, D. C., Keevil, N. B., and Ward, S. H., 1964, Conductivity spectra of rocks form the Craigmont ore environment: Geophysics, **29**, 832.

Gelhar L. W., Welty C., and Rehfeldt K. R., 1992, A critical review of data on field-scale dispersion in aquifers: Water Resources Research, **28**, 1955-1974.

Grant F. S., and West, G. F., 1965, Interpretation theory in applied geophysics, McGraw-Hill, New York.

Gunn, P. J. and Chisholm, J., 1984, Non-conductive volcanogenic massive sulphide mineralisation in the Pilbara area of Western Australia: Exploration Geophysics, **15**, 143-153.

Guptasarma, D., 1983, Effect of surface polarisation on resistivity modeling, *Geophysics* **48**, 98-106
Harvey, R. D., 1928, Electrical conductivity and polished mineral surfaces: Economic Geology, **23**, 778-801.

Hawk, P. J., and Brooker P. I., 2001, Can sphalerite be a polarisable mineral? An example from the Century Zn-b deposit: Extended Abstracts, Australian Society of Exploration Geophysicists15th Geophysical conference and Exhibition.

Heithersay, P. S., and Walshe J. L., 1995, Endeavour 26 North: a porphyry copper-gold deposit in the late Ordovician, shoshonitic Goonumbla Volcanic Complex, New South Wales, Australia: Economic Geology, **90,** 1506-1532.

Heithersay P. S., O-Neill W. J., van der Helder P., Moore C. R., and Harbon P. G., 1990, Goonumbla porphyry copper district; Endeavour 26 North, Endeavour 22 and Endeavour 27 copper-gold deposits, *in* Hughes, F .E., Ed., Geology of the mineral deposits of Australia and Papua New Guinea,

Monograph Series: Australasian Institute of Mining and Metallurgy, Special Publication, No. 14, 1385-1398.

Hill, D. G., 1972, A laboratory investigation of electrical anisotropy in Precambrian rocks: Geophysics, **37**, 1022-1038.

Hone, I. G., 1980, Geoelectric properties of the Elura Prospect, Cobar, NSW, *in* Geophysics of the Elura orebody: Exploration Geophysics, **11**, 178-182.

Humphreys, M., Chappell, J., Harris, M. F., and Pitt, J. N., 1991, Golden Grove discovery case histories, *in* Hollister, V. F., Porphyry copper, molybdenum, and gold deposits, volcanogenic deposits (massive sulphides), and deposits in layered rock: Society of Mining, Metallurgy and Exploration, USA.

Jackson, P. D., Gunn, D. G., Flint, R. C., Beamish, D., Meldrum, P. I., Lovell, M. A., Harvey, P. K., and Peyton, A., 1997, A non-contacting resistivity imaging method for characterising whole round core at the well site, *in* Lovell, M. A., and Harvey, P. K., Eds., Developments in Petrophysics: Geological Society Special Publication, No. 122, 299-344.

Johnson, I. M., 1984, Spectral induced polarisation parameters as determined through time domain measurements: Geophysics, **49**, 1993-2003.

Jones, J. W., 1989, An examination of scale-dependent electrical resistivity measurements in Oracle granite, PhD Dissertation, University of Arizona.

Katsube, T. J., Ahrens, R. H., and Collett, L.S., 1973, Electrical nonlinear phenomena in rocks: Geophysics, **38,** 106-124.

Katz, A. J., and Thompson, A. H., 1985, Fractal sandstone pores: Implications for conductivity and pore formation: Physical Review Letters, **54,** 1325-1328.

Keevil, N. B., and Ward, S. H., 1962, Electrolyte activity: its effect on induced polarisation: Geophysics, **27**, 677-690.

Keller, G. V., 1959, Analysis of some electrical transient measurements on igneous, sedimentary and metamorphic rocks, Wait, J. R., Ed., *in* Overvoltage Research and Geophysical Applications: Permagon Press, 92-111.

Keller, G. V., 1966, Electrical Properties of Rocks and Minerals, *in* Clark, S. P., Ed., Handbook of Physical Constants: Memoir 97, Geological Society of America.

Keller, G. V., and Frischknecht, F.C., 1966, Electrical Methods in Geophysical Prospecting: London Permagon Press.

Keller, G. V., 1988, Rock and Mineral Properties, *in* Nabighian, M. N., Electromagnetic methods in applied geophysics, Volume 1: Society of Exploration Geophysicists, 11-52.

Keller, G. V., 1989, Electrical properties, *in* Carmichael, R. S., Ed., Practical handbook of physical properties of rocks and minerals: CRC Press, 359-427.

Keys. J. D., Horwood, J. L., Baleshta, T. M., Cabri, L. J., and Harris, D. C., 1967, Iron-iron interaction in iron-containing zinc sulphide: Canadian Mineralogist. 453-467.

Khaleel R., 1989, Scale-dependence of continuum models for fractured basalts: Water Resources Research, **25,** 1847-1855.

Klein, J. D., Biegler, T., and Horne, M. D., 1984, Mineral interfacial processes in the method of induced polarisation: Geophysics, **49**, 1105-1114.

Koleman, J. M. V. A. and de Kuijper, A., 1997, An effective medium model for the electrical conductivity of an N-component anisotropic and percolating mixture: Physica A, **247**, 10-22.

Langore, L., Alikaj, P., and Gjovreku, D., 1989, Achievements in copper sulphide exploration in Albania with IP and EM methods: Geophysical Prospecting, **37**, 975-992.

Large R. R., Bull S. W., Cooke D. R. and McGoldrick P. J., 1998, A genetic model for the HYC deposit, Australia: Based on regional sedimentology, geochemistry, and sulphide-sediment relationships: Economic Geology, **93** 1345-1368.

Lee, T., 1981, Short Note: The Cole-Cole model in time domain induced polarisation: Geophysics, **46**, 932-933.

Lewis, R. J. G., 1985, The determination of spectral parameters with pulse train induced polarisation, Geophysics, **50**, 870-871.

Lewis, R. J. G., and Bishop, J. R., 1988, Inversion of time domain spectral IP data: Exploration Geophysics, **19**, 303-305.

Lickford, V., 2000, The intrusive history of the Goonumbla porphyry Cu-Au deposits, NSW, *in* Understanding Planet Earth; searching for a sustainable future; Abstracts of the 15th Australian Geological Convention. Geological Society of Australia, 303.

Loke, M. H., 2002, RES3DMOD online users manual. http://appliedgeophysics.berkeley.edu:7057/dc/r3dmod/

Logan R. G., Murray W. J., and Williams N., 1990, HYC silver-lead-zinc deposit, McArthur River, *in* Hughes, F. E., Ed., Geology of the mineral deposits of Australia and Papua New Guinea, Monograph Series: Australasian Institute of Mining and Metallurgy, **14**, 907-911.

Losito, G., Schnegg, P., Lambelet, C., Viti, C., and Trovea, A., 2001, Microscopic scale conductivity as explanation of magnetotelluric results from the Alps of Western Switzerland: Geophysical Journal International, **147**, 602-609.

Lydon, J. W., 1988, Volcanogenic massive sulphide deposits, Part 1: a descriptive model, *in* Roberts, R. G., and Sheahan, P. A., Deposit Models: Geological Association of Canada, Reprint Series 3.

Madden, T. R., and Cantwell, T., 1967, Induced Polarisation, A Review Rocks *in* Mining Geophysics, Volume II Theory: Society of Exploration Geophysics, 373-400.

Madden, T. R., 1976, Random networks and mixing laws: Geophysics, **41**, 1104-1125.

Mahan, M. K., Redman, J. D., and Strangway, D. W., 1986, Complex resistivity of synthetic sulphide bearing rocks: Geophysical Prospecting, **34**, 743-768.

Maillot, E. E., and Sumner, J. S., 1966, Electrical properties of porphyry deposits at Ajo, Morenci and Bisbee, Arizona, *in* Mining Geophysics Volume 1 Case Histories: Society of Exploration Geophysics, 273-287.

Mandel, P., Berg, J. W., and Cook, K. L., 1957, Resistivity studies of metalliferous synthetic cores: Geophysics, **22**, 398-411.

Marshall, D. J., and Madden, T. R., 1959, Induced Polarisation, A study of its causes: Geophysics, **24**, 790-816.

Markushin, Y. V., Bortsov, V. D., and Chuprin, I.S., 1973, Comparative characteristics of induced polarisation of certain ore and rock-forming minerals: Earth Physics, No.2, 51-61.

Matias, M. J. S., and Habberjam G. M., 1986, The effect of structure and anisotropy on resistivity measurements: Geophysics, **51**, 964-971.

Mayper, V., 1959, The Normal Effect – Part I, *in* Wait, J. R., Ed., Overvoltage Research and Geophysical Applications: Permagon Press,125-141.

McEuen, R. B., Berg, J. W., Cook, K. L., 1959, Electrical properties of synthetic metalliferous ore: Geophysics, **24**, 510-530.

Mill, J. H. A., Clifford, B. A., Dudley, R. J., and Ruxton, P. A., 1990, Scuddles zinc-copper deposit at Golden Grove, Australian Institute of Mining and Metallurgy Mon. 14, 583-590.

Murray, W. J., 1975, McArthur River H.Y.C lead-zinc and related deposits, N.T., *in* Economic geology of Australia and Papau New Guinea; 1 Metals, AUSIMM Monograph Series 328-338.

Nabighan, M. N., and Elliot, C. L., 1967, Negative induced-polarisation effects from layered media: Geophysics, **41**, 1236-1255.

Nelson, P. H. and Van Voorhis, G. D., 1983, Estimation of sulphide content from induced polarisation data: Geophysics, **48**, 62-75.

Neuman S. P., 1994, Generalised scaling of permeabilities: validation and effect of support scale: Geophysical Research Letters, **21**, 349-352.

Normandy Golden Grove Operations, 1999, Scuddles and Gossan Hill Archaean deposits. Hand out and field excursion guide, 22 pages plus figures.

North Parkes Copper deposit, 2001, Personal communication.

Olhoeft, G. R., 1977, Nonlinear complex resistivity: Geophysics, **42**,1530.

Olhoeft, G. R., 1981, Electrical properties of granite with implications for the lower crust: Journal of Geophysical Research, **86**, 931-936.

Olhoeft, G. R., 1985, Low frequency electrical properties: Geophysics, **50**, 2492-2503.

Ovchinnikov, I. K., Zhavoronkova, V. V., and Kormil'tsev, V. V., 1968, The nature of polarisation for the principle natural sulphides: Earth Physics, No.3, 95-101.

Palacky, G. J., 1988, Characteristics of geological targets, *in* Nabighian, M. N., Ed., Electromagnetic methods in applied geophysics, Volume 1: Society of Exploration Geophysicists, 53-130.

Parkhomenko, E. I. 1967, Electrical Properties of Rocks: Plenum Press.

Parkhomenko, E. I. 1982, Electrical resistivity of minerals and rocks at high temperature and pressure: Revisions of Physics and Space Physics, **29**, 193-218.

Parasnis, D. S., 1957, The electrical resistivity of some sulphide and oxide minerals and their ores: Geophysical Prospecting, **4**, 249-278.

Parasnis, D. S., 1997, Principles of Applied Geophysics, 5th Edition: Chapman and Hall.

Pelton, W. H., Sill, W. R., and Smith, B. D., 1983, Interpretation of complex resistivity and dielectric data, Part I: Geophysical Transactions, **29**, 297-330.

Pelton, W. H., Ward, S. H., Hallof, P. G., Sill, W. R., and Nelson, P. H., 1978, Mineral discrimination and removal of inductive coupling with multifrequency IP: Geophysics, **43**, 588-609.

Petrov, A. A., and Fedorov, A. N., 1988, Estimation of nonlinear behaviour of time domain induced polarisation with current density: Prikladnaya Geofizika No. 119, 55-60.

Pridmore, D. F., and Shuey, R. T., 1976, The electrical resistivity of galena, pyrite and chalcopyrite: American Mineralogist, **61**, 248-259.

Rauen, A., and Soffel, H. C., 1995, Determination of electrical resistivity, its anisotropy and heterogeneity on drill cores: a new method: Geophysical Prospecting, **43**, 283-298.

Roach, M. R., 2004, Visual basic code for production of multiphase 3-D cellular models (personal communication).

Roach, M., Lewis, R., and Jablonski, W., 1997, Scale-dependent electrical properties of sulphide rocks- New methods and techniques: Exploration Geophysics, **28**, 123-126.

Roach, M. R., and Fitzpatrick, A. D., 2001, Continuity and current mapping - new laboratory techniques for the study of the electrical properties of sulphide rocks, 71st Annual International Meeting: Society of Exploration Geophysics, 1517-1520.

Ruffet, C., Gueguen, Y., and Darot, M., 1991, Complex conductivity measurements and fractal nature of porosity: Geophysics, **56**, 758-768.

Saint-Amant, M., and Strangway, D. W., 1970, Dielectrical properties of dry, geologic materials: Geophysics, **35**, 624.

Saloheimo, K., 1990, Model Studies on spectral induced polarisation, Acta Polytechnica Scandinavia: Applied Physics Series, 167.

Schulze-Makuch, D., and Cherkauer , D. S., 1995, Scale behaviour of hydraulic conductivity during a pumping test, *in* Osterkamp, W. R., Ed., Effects of Scale on Interpretation and Management of Sediment and Water Quality: International Association of Hydrological Sciences, Publication No. 226, 141-146.

Schneider, M. N., and Emerson, D. W., 1980, Physical properties of the Elura Prospect, Cobar, NSW: Exploration Geophysics, **11**, 184-185.

Scott, W. J., and West, G. F., 1969, Induced polarisation of synthetic, high-resistivity rocks containing disseminated sulphides: Geophysics, **34**, 87-100.

Seigel, H. O., 1959, Mathematical formulation and type curves for induced polarisation: Geophysics, **24**, 547-565.

Seigel, H. O., Vanhala, H., and Sheard, S. N., 1997, Some case histories of source discrimination using time-domain spectral IP: Geophysics **62**, 1394-1408.

Sen, P. N., 1981, Relation of certain geometrical features to the dielectric anomaly of rocks: Geophysics, **46**, 1714-1720.

Sen, P.N., 1984, Grain shape effects on dielectric and electrical properties of rocks: *Geophysics*, **49** 1714-1720

Shalley, M. J. ,and Harvey, T. V., 1992, Geophysical responses of the HYC deposit: Exploration Geophysics, **23**, 299-304.

Shaub, Y. B., 1965, Use of the non-linear conductivity effect in rocks for electrical prospecting: Earth Physics, No. 6. 76-81.

Shaub, Y. B., 1969, Use of effects of non-linear electrical conductivity in the detection of disseminated sulphide ores: Earth Physics, No. 1. 89-94.

Shaub, Y. B., and Ivanov, V.A., 1971, Experimental discrimination of sulphide ores and graphites by the use of the effects of non-linear electrical conductivity: Earth Physics, No.3, 101-104.

Sharpe, R., 1999, Mineralisation, alteration and structure of the Gossan Hill Cu-Zn VHMS deposit, Western Australia: implications for ore genesis and exploration: PhD Dissertation, University of Tasmania.

Shuey, R. T., 1975, Semiconducting Ore Minerals: Elsevier Scientific Publishing Company, 415.

Siegesmund, S., Vollbrecht, A., and Nover, G., 1991, Anisotropy of compressional wave velocities, complex electrical resistivity and magnetic susceptibility of mylonites from the deeper crust and their relation to the rock fabric: Earth and Planetary Science Letters, **105**, 247-259.

Song, L., and Vozoff, K., 1985, The complex resistivity spectra of models consisting of two polarisable media of different intrinsic properties, Geophysical Prospecting, **33**, 1029-1062.

Sumner, J. S., 1976, Principles of Induced Polarisation for Geophysical Exploration: Elsevier, 277.

Telford, W. M., Geldart, L. P., and Sheriff, R. E., 1990, Applied Geophysics, 2nd Edition: Cambridge University Press.

Torquato, S., 1991, Random heterogeneous media: Microstructure and improved bounds on effective properties: Applied Mechanics Revisions, **44**, 37-77.

Tyne, E. D., Idnurm, M., and Malone, J., 1981, The physical properties of the Woodlawn Orebody and Surounding Rocks, *in* Whiteley, R. J., Geophysical case study of the Woodlawn Orebody, New South Wales, Australia: Pergamon Press, 99-111.

Vanhala, H., 1997, Laboratory and field studies of environmental and exploration applications of the spectral induced-polarisation (SIP) methods: PhD Dissertation, Geological Survey of Finland.

Vanhala, H., and Peltoniemi, M., 1992, Spectral IP studies of Finnish ore prospects: Geophysics, **57**, 1545-1555.

Van Voorhis, G. D., Nelson, P. H., and Drake, T. L., 1973, Complex resistivity spectra of porphyry copper mineralisation: Geophysics, **38**, 49-60.

Wait, J. R., 1959, A phenomenological theory of overvoltage for metallic particles, *in* Wait, J. R., Ed., Overvoltage Research and Geophysical Applications: Permagon Press, 22-28.

Ward, S. H., and Fraser, D. C., 1967, Conduction of Electricity in Rocks, *in* Mining Geophysics, Volume II Theory: Society of Exploration Geophysics, 197-223.

Waxman, M. H., and Smits, L. J. M., 1968, Electrical conduction in oil-bearing shaly sands: Society of Petroleum Engineers Journal, **243**, 107-122.

Whitaker F. F. and Smart P. L., 2000, Characterising scale-dependence of hydraulic conductivity in carbonates: evidence from the Bahamas: Journal of Geochemical Exploration, **69-70**, 133-137

White, R. M. S., 1974, A study of non-linear electrical effects in mineralised rocks: MSc. Dissertation, Macquarie University.

Wong, J., 1979, An electrochemical model of the induced polarisation phenomenon in disseminated sulphide ores: Geophysics, **44**, 1245-1265.

Wong, P., Howard, J., and Lin, J., 1986, Surface roughening and the fractal nature of rocks: Physical Review Letters, **57**, 637-640.

Wong, J., and Strangway, D. W., 1981, Induced polarisation in disseminated sulphide ores containing elongated mineralisation: Geophysics, **46**, 1258-1268.

Wyller, J., Wellander, N., Larson, F., and Parasnis, D., 1992, Burger's equation as a model for the IP phenomenon: Geophysical Prospecting, **40**, 325-342.

Yang, Y. P. and Emerson, D. W., 1997, Electromagnetic conductivities of rock cores: theory and analogue results: Geophysics, **62**, 1779-1793.

Yin, C., 2000, Geoelectrical inversion for a one-dimensional anisotropic model and inherent non-uniqueness: Geophysical Journal International, **140**, 11-23.

Yuval and Oldenburg, D. W., 1997, Computation of Cole-Cole parameters from IP data, *Geophysics* **62**, 436-448.

Zonge, K. L., 1972, Electrical parameters of rocks as applied to geophysics. PhD Dissertation, University of Arizona, Tuscan.

Zonge, K. L. and Wynn, J. C., 1975, Recent advances and applications in complex resistivity measurements, Geophysics, **40**, 851-864.

Appendix-A

Slice #	Width (ms)	Start (ms)	End (ms)	Midpoint (ms)
2	20	40	60	50
3	40	60	100	80
4	40	100	140	120
5	80	140	220	180
6	80	220	300	260
7	160	300	460	380
8	160	460	620	540
9	280	620	900	760
10	280	900	1180	1040
11	460	1180	1640	1410
12	460	1640	2100	1870
13	720	2100	2820	2460
14	720	2820	3540	3180

Time slices recorded for all measurements using the IPR-12

Appendix-B.1

Calculation of potentials in anisotropic half space (From Telford, et al., 1990)

The equipotenital surfaces generated by a current electrode in a homogeneous, anisotropic half-space can be calculated using the following expression:

$$U = \frac{-I\rho_l\lambda}{2\pi(x^2 + y^2 + \lambda^2 z^2)^{1/2}} \qquad \lambda = \sqrt{\frac{\rho_t}{\rho_l}}$$

where U = potential (V)
I = current (A)
ρ_l = longitudinal resistivity (Ωm)
ρ_t =longitudinal resistivity (Ωm)
x,y,z = distance away from current electrode (m)

Lamba (λ) is referred to as the coefficient of anisotropy.

Appendix-B.2

Calculation of maximum current density for electrical sounding (From Telford, et al., 1990)

The following equation and diagram were used to calculate the maximum current density for insitu measurements, by substituting known values of I (current) and L (half-length distance of current electrodes).

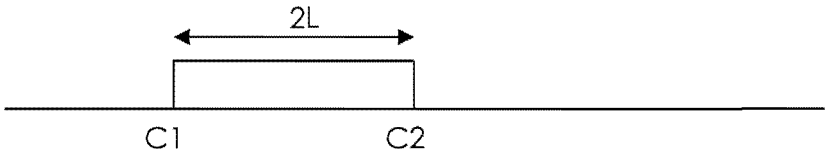

$$J_x = \frac{I}{2\pi}\frac{L}{(z^2 + L^2/4)^{3/2}}$$

J_x = current density
I = current (A)
L = distance from electrode to centre of array (m)
z = depth (m)

J_x is a maximum when L = $\sqrt{2}$ z